ALFRED-WEGENER-INSTITUT
HELMHOLTZ-ZENTRUM FÜR POLAR-
UND MEERESFORSCHUNG

Universität Potsdam

Dissertation

ON THE LINKAGE BETWEEN FUTURE ARCTIC SEA ICE RETREAT, THE LARGE-SCALE ATMOSPHERIC CIRCULATION AND TEMPERATURE EXTREMES OVER EUROPE

zur Erlangung des akademischen Grades

„doctor rerum naturalium "(Dr. rer. nat.)

in der Wissenschaftsdisziplin „Klimaphysik "

eingereicht an der Mathematisch-Naturwissenschaftlichen Fakultät

der Universität Potsdam

von ***Johannes Riebold***

Potsdam, den 10. Juli 2023

Mentorin: Dr. Dörthe Handorf
1. Gutachter: Prof. Dr. Markus Rex
2. Gutachter: Prof. Dr. Uwe Ulbrich
3. Gutachter: Prof. Dr. Joaquim Pinto

Published online on the
Publication Server of the University of Potsdam:
https://doi.org/10.25932/publishup-60488
https://nbn-resolving.org/urn:nbn:de:kobv:517-opus4-604883

ABSTRACT

Extreme weather and climate events are one of the greatest dangers for present-day society. Therefore, it is important to provide reliable statements on what changes in extreme events can be expected along with future global climate change. However, the projected overall response to future climate change is generally a result of a complex interplay between individual physical mechanisms originated within the different climate subsystems. Hence, a profound understanding of these individual contributions is required in order to provide meaningful assessments of future changes in extreme events. One aspect of climate change is the recently observed phenomenon of Arctic Amplification and the related dramatic Arctic sea ice decline, which is expected to continue over the next decades. The question to what extent Arctic sea ice loss is able to affect atmospheric dynamics and extreme events over mid-latitudes has received a lot of attention over recent years and still remains a highly debated topic. In this respect, the objective of this thesis is to contribute to a better understanding on the impact of future Arctic sea ice retreat on European temperature extremes and large-scale atmospheric dynamics. The outcomes are based on model data from the atmospheric general circulation model ECHAM6. Two different sea ice sensitivity simulations from the Polar Amplification Intercomparison Project are employed and contrasted to a present day reference experiment: one experiment with prescribed future sea ice loss over the entire Arctic, as well as another one with sea ice reductions only locally prescribed over the Barents-Kara Sea.

The first part of the thesis focuses on how future Arctic sea ice reductions affect large-scale atmospheric dynamics over the Northern Hemisphere in terms of occurrence frequency changes of five preferred Euro-Atlantic circulation regimes. When compared to circulation regimes computed from ERA5 it shows that ECHAM6 is able to realistically simulate the regime structures. Both ECHAM6 sea ice sensitivity experiments exhibit similar regime frequency changes. Consistent with tendencies found in ERA5, a more frequent occurrence of a Scandinavian blocking pattern in midwinter is for instance detected under future sea ice conditions in the sensitivity experiments. Changes in occurrence frequencies of circulation regimes in summer season are however barely detected. After identifying suitable regime storylines for the occurrence of European temperature extremes in winter, the previously detected regime frequency changes are used to quantify dynamically and thermodynamically driven contributions to sea ice-induced changes in European winter temperature extremes. It is for instance shown how the preferred occurrence of a Scandinavian blocking regime under low sea ice conditions dynamically contributes to more frequent midwinter cold extreme occurrences over Central Europe. In addition, a reduced occurrence frequency of a Atlantic trough regime is linked to reduced winter warm extremes over Mid-Europe. Furthermore, it is demonstrated how the overall thermodynamical warming effect due to sea ice loss can result in less (more) frequent winter cold (warm) extremes, and consequently counteracts the dynamically induced changes.

Compared to winter season, circulation regimes in summer are less suitable as storylines for the occurrence of summer heat extremes. Therefore, an approach based on circulation analogues is employed in order to quantify thermodyamically and dynamically driven contributions to sea ice-induced changes of summer heat extremes over three different European sectors. Reduced occurrences of blockings over Western Russia are detected in the ECHAM6 sea ice sensitivity experiments; however, arguing for dynamically and thermodynamically induced contributions to changes in summer heat extremes remains rather challenging.

When compared to other characteristics of future climate change, such as the thermodynamical impact of globally increased sea surface temperatures, it is shown that the detected effects on European temperature extremes related to Arctic sea ice loss are of secondary relevance. Nevertheless, the results of this this thesis can help to better understand current and near future changes in European temperature extremes. In addition, the present thesis provides a useful and a new methodological perspective on the research field of Arctic-mid-latitude linkages, and consequently further contributes to a consensus on this highly debated scientific topic.

KURZZUSAMMENFASSUNG

Wetter- und Klimaextreme stellen eine der größten Gefahren für die heutige Gesellschaft dar. Daher ist es essentiell verlässliche Aussagen darüber zu treffen, welche Änderungen solcher Extremereignisse im Zuge des zukünftigen globalen Klimawandels zu erwarten sind. Die projizierten Klimaänderungen, welche mit dem zukünftigen Klimawandel einhergehen, sind jedoch im Allgemeinen das Ergebnis komplexer Wechselwirkungen von verschiedenen physikalischen und dynamischen Prozessen in den verschiedenen Subsystemen des Klimasystems. Daher ist ein tiefgreifendes Verständnis dieser einzelnen Prozesse erforderlich, um aussagekräftige Einschätzungen für die Zukunft abgeben zu können. Ein Aspekt des globalen Klimawandels über die letzten Dekaden ist das Phänomen der arktischen Verstärkung und der damit verbundene dramatische Rückgang des Arktischen Meereises, welcher sich voraussichtlich in den nächsten Jahrzehnten auch fortsetzen wird. Die Frage, inwieweit der Rückgang des arktischen Meereises die atmosphärische Dynamik sowie Wetter- und Klimaextreme über den mittleren Breiten beeinflussen kann, wurde in den letzten Jahren von einer Vielzahl von Studien adressiert, bleibt jedoch bis zum heutigen Tage ein kontrovers diskutiertes Thema. Aus diesem Grund zielt die vorliegende Arbeit darauf ab einen Beitrag zu einem besseren Verständnis der Auswirkungen des zukünftigen arktischen Meereisrückgangs auf europäische Temperaturextreme, sowie auf Änderungen der relevanten großräumigen atmosphärischen Zirkulationsbedingungen zu leisten. Die Ergebnisse dieser Arbeit basieren auf Modelldaten des atmosphärischen Zirkulationsmodells ECHAM6. Zwei unterschiedliche Meereissensitivitätsexperimente aus dem Polar Amplification Intercomparison Project werden analysiert: ein Experiment mit vorgeschriebener zukünftiger Meereisreduktion über der gesamten Arktis, sowie ein Weiteres, in dem jediglich das Meereis über der Barents- und Karasee verringert wird. Beide Experimente werden einer Referenzsimulation gegenübergestellt, welche gegenwärtige Meereisbedingungen repräsentiert.

Zunächst wird analysiert, inwieweit der zukünftige arktische Meereisrückgang Einfluss auf die großräumige atmosphärische Zirkulation über der nördlichen Hemisphäre hat. Dazu werden im Rahmen dieser Arbeit die Häufigkeitsänderungen von fünf bevorzugten atmosphärischen Zirkulationsregimen bestimmt. Beide Sensitivitätsexperimente zeigen diesbezüglich ähnliche Änderungen in den Auftrittswahrscheinlichkeiten der Regime. In Übereinstimmung mit Ergebnissen, welche auf der ERA5-Reanalyse basieren, zeigt sich beispielsweise ein häufigeres Auftreten eines skandinavischen Blockierungsmusters im Mittwinter unter reduzierten Meereisbedingungen. Änderungen in der Auftrittswahrscheinlichkeit verschiedener Zirkulationsregime in der Sommersaison werden hingegen kaum detektiert. Anschließend werden jene Regime identifiziert, welche mit einem häufigerem Auftreten von winterlichen Temperaturextremen über Europa in Verbindung gebracht werden können. In Kombination mit den zuvor erfassten meereisbedingten Änderungen in den Auftrittswahrscheinlichkeiten der Regime werden dann dynamisch und thermodynamisch induzierte Beiträge zu meereisbedingten Än-

derungen europäischer Temperaturextreme quantifiziert. Es zeigt sich beispielsweise, dass das bevorzugte Auftreten des skandinavischen Blockierungsmusters unter zukünftigen Meereisbedingungen dynamisch zu häufigeren Kälteextremereignissen im Winter über Mitteleuropa beiträgt. Darüber hinaus kann eine reduzierte Häufigkeit des Auftretens eines Regimes, welches mit einem Trog über dem westlichen Atlantik assoziiert werden kann, mit einer verringerten Anzahl von sehr warmen Wintertagen über Mitteleuropa in Verbindung gebracht werden. Es wird zudem gezeigt, wie der in den Modellsimulationen thermodynamisch induzierte Erwärmungseffekt infolge der reduzierten Meereisbedingungen zu einem häufigeren (weniger häufigeren) Auftreten von extrem warmen (kalten) Wintertagen führen kann. Dieser thermodynamische Effekt kann folglich den dynamisch induzierten Veränderungen entgegenwirken.

Zirkulationsregime in der Sommersaison können nur bedingt mit einem häufigeren Auftreten von europäischen Hitzeextremen im Sommer in Verbindung gebracht werden. Aus diesem Grund wird ein zusätzlicher methodischer Ansatz verwendet, der auf der Identifikation von Zirkulationsmustern basiert, welche große Ähnlichkeit zu typischen atmosphärischen Blockierungen während vergangener Hitzewellen über verschiedenen europäischen Regionen aufweisen. Dies ermöglicht es meereisbedingte Änderungen im Auftreten von Hitzeextremen über drei verschiedene europäische Sektoren in thermodynamisch und dynamisch induzierte Beiträge zu zerlegen. In den Meereissensitivitätsexperimenten kann beispielsweise ein selteneres Auftreten von Blockierungen über Westrussland detektiert werden. Eine in sich geschlossene physikalische Argumentation bezüglich der dynamisch und thermodynamisch induzierten Beiträge zu den detektierten Änderungen in der Häufigkeit von sommerlichen Hitzeextremen stellt jedoch weiterhin eine Herausforderung dar.

Im Vergleich zu anderen Aspekten des zukünftigen Klimawandels, wie beispielsweise dem thermodynamischen Einfluss global erhöhter Meeresoberflächentemperaturen, zeigt sich, dass die meereisinduzierten Auswirkungen auf europäische Temperaturextreme wahrscheinlich von untergeordneter Bedeutung sind. Nichtsdestotrotz können die Ergebnisse dieser Arbeit zu einem besseren Verständnis gegenwärtiger und zeitnah zu erwartender Änderungen von Temperaturextremereignissen über Europa beitragen. Zusätzlich dazu bietet die vorliegende Arbeit eine nützliche und ergänzende Perspektive auf die wissenschaftliche Fragestellung, inwieweit der Arktische Klimawandel mit Änderungen in der atmosphärischen Zirkulation und Extremereignissen über den mittleren Breiten in Verbindung gebracht werden kann. Folglich trägt diese Arbeit damit dazu bei einem allgemeinen Konsens in diesem stark debattierten Forschungsgebiet einen Schritt näher zu kommen.

MANUSCRIPTS ASSOCIATED WITH THIS DISSERTATION

Riebold, J., A. Richling, U. Ulbrich, H. Rust, T. Semmler and D. Handorf (2023). "On the linkage between future Arctic sea ice retreat, Euro-Atlantic circulation regimes and temperature extremes over Europe." In: *Weather and Climate Dynamics* 4.3, pp. 663-682 , DOI: 10.5194/wcd-4-663-2023.

Contributions: **Johannes Riebold** and Dörthe Handorf developed the original idea for the paper. **Johannes Riebold** conducted the entire analysis, interpreted the results, wrote the original paper draft and handled the review process. Andy Richling contributed the blocking frequency plots and provided feedback and comments to the manuscript. Henning Rust, Uwe Ulbrich and Dörthe Handorf supervised and also provided scientific feedback to the manuscript. Tido Semmler conducted the ECHAM6 model experiments and also provided feedback to the paper draft.

CONTENTS

1 SCIENTIFIC BACKGROUND AND RESEARCH QUESTIONS

1.1 EXTREME EVENTS AND ATTRIBUTION

Weather and climate extremes pose a considerable source of danger for modern-day society. Indeed, recent surveys on global risk perceptions of business leaders and global change scientists revealed that climate extremes are among, if not the top ranked risk for both likelihood and impact (World Economic Forum, 2021; Future Earth, 2020). Especially extreme events related to unprecedented temperature anomalies, such as the Russian heat wave in 2010 (Barriopedro et al., 2011), the European heat wave in 2003 (De Bono et al., 2004), or even winter cold spells like 2010 in Europe (Cattiaux et al., 2010) or over central North America in 2021 (Bolinger et al., 2022) can result in significantly increased mortality rates, severe economic losses and ecological damages. Hence, a major interest for human society nowadays is given by the question to what extent the recently observed trend towards more frequent and severe extreme events (Coumou et al., 2012) can be expected to continue in the future. Indeed, some of the more pessimistic shared socioeconomic pathways (SSP) used in the latest phase of the Coupled Model Intercomparison Project CMIP6 show that the severity of heat extremes over land areas is expected to increase until the end of the century (Almazroui et al., 2021). And moreover, the recently increased frequency and intensity of heat extremes over European regions (Lorenz et al., 2019; Sulikowska et al., 2021) is predicted to continue in future as well (Carvalho et al., 2021).

The attribution of recent extreme events to anthropogenic global warming is not only an important contribution to raise the public awareness of climate change; it is also closely related to the question what changes in extreme events can be expected in the future.

The main idea of classical extreme event attribution (e.g. Naveau et al., 2020) is to define a so-called factual world (a world as it is) and a counterfactual world (e.g. a world that might have occurred without climate change), both based on appropriately designed model experiments or different periods in observational data. Questions such as " how likely does an extreme event as the current one occur in a world with climate change compared to a world without climate change " are then answered by comparing the occurrence probability for a class of events[1] between both worlds.

Nevertheless, Trenberth et al. (2015) and Shepherd (2016) stressed that such a purely probabilistic '*risk-based approach*' can only provide a meaningful attribution statement if changes in the occurrence frequency of some extreme event are mainly a result of thermodynamical aspects of climate change. On a continental scale it seems indeed reasonable that, from a thermodynamical perspective, global warming leads to more (less) frequent and intense warm (cold) extremes. In this respect, also the latest sixth IPCC assessment report (Arias et al., 2021) stated that it is "very likely that human influence is the main contributor to the observed increase in the intensity and frequency of hot extremes and the observed decrease in the intensity and frequency of cold extremes on continental scales". However, recent occurrences of severe cold extremes like the aforementioned cold spells over Europe or the central US might be considered as contradictions to this simplified thermodynamical perspective.

Especially on a regional scale the vast majority of climate extremes are indeed dynamically driven by specific synoptic- to large-scale flow configurations of the atmospheric circulation. For instance, cold European winters commonly occur during pronounced negative phases of the North Atlantic Oscillation (e.g. Vihma et al., 2020; Rust et al., 2015), and summer heat waves are typically co-located with persistent anticyclones (e.g. Pfahl et al., 2012). In this respect, Cattiaux et al. (2010) demonstrated that the European winter cold spell in 2010 was, from a thermodynamical point of view, perfectly in line with recent global warming when accounting for the prevailing negative state of the North Atlantic Oscillation during this winter. Consequently, changes in the occurrence frequencies and characteristics of the dynamical drivers conducive to an extreme event can potentially mask the thermodynamical impact of global warming. In contrast to the well-established thermodynamical aspects of climate change, forced circulation changes found in climate model simulations typically suffer low signal-to-noise ratios. Hence, they can usually be hardly separated from internal atmospheric variability (Trenberth et al., 2015)

For this reason, Trenberth et al. (2015) and Shepherd (2016) advocated the so-called *storyline approach* as a useful complementary perspective to the ordinary risk-based approach. The storyline approach generally aims to provide a physically consistent narrative on how the occurrence of a past extreme event can be unfolded into different thermodynamical and dynamical contributing factors, and asks how climate change can impact these factors that led to the specific event at hand. As risk-based and storyline approaches were originally aimed to tackle distinct research questions, there is no "right" or "wrong" between both perspectives in any absolute sense (Lloyd et al., 2018). Indeed, Shepherd (2016) argued that both approaches can be unified into a common framework. Thus, changes in occurrence frequencies of a class of extreme events could be decomposed into different contributions: one that is related to changes in the dynamical situation leading to the class of extreme events[1], and another one which assumes no changes in the relevant dynamics (also termed thermodyamical contribution). As mentioned above, there is relatively high confidence in thermodynamical aspects of climate change, while impacts on atmospheric dynamics are more uncertain. Consequently, changes regarding the dynamical situation leading to a certain class of extreme events[1] should only be considered when there is solid evidence that such changes can be expected or reliably detected (Trenberth et al., 2015; Shepherd, 2016).

1.2 ARCTIC CLIMATE CHANGE AND MID-LATITUDE LINKAGES

Recent global warming includes a phenomenon called Arctic Amplification that comes along with an up to four times faster warming of Arctic regions compared to global average over recent decades (Rantanen et al., 2022). This amplified Arctic warming is predominantly observed in winter time and is accompanied by an unprecedented shrinkage of summer Arctic sea ice concentration and thickness (Stroeve et al., 2018). Model projections forced under different greenhouse gas scenarios show clear evidence of a continuation of sea ice decline, with some models suggesting a seasonally ice-free Arctic by the mid of the century (Notz et al., 2020).

Aside from local ecological and economical impacts (Meredith et al., 2019) the question to what extent Arctic climate change and related sea ice loss may impact mid-latitude

1 e.g. "all events at least as extreme as the current one"

weather and general atmospheric dynamics has received a lot of attention over the last years and decades (e.g. Cohen et al., 2020; Screen, 2017b; Handorf et al., 2015; Cohen et al., 2014a). A large variety of potential hemispheric-wide atmospheric winter responses have been detected and hypothesized in connection to Arctic sea ice loss. Such responses include for instance a commonly observed response pattern similar to the negative phase of the North Atlantic Oscillation (e.g. Screen, 2017b; Nakamura et al., 2015; Jaiser et al., 2012), a highly debated weakening and stronger meandering of the jet stream that may result in more stationary and slower propagating large-scale Rossby waves (Francis et al., 2012; Barnes et al., 2015; Riboldi et al., 2020), as well as an intensification of the Scandinavian and Ural highs leading to continental winter cooling over Eurasia (Cohen et al., 2018). In this respect, dynamical pathways have been proposed relating for instance sea ice and snow cover anomalies in autumn to enhanced vertical wave activity fluxes and a weakened stratospheric polar vortex. These stratospheric disturbances can subsequently propagate downward (Baldwin et al., 1999) and finally result in a late winter response resembling the negative phase of the North Atlantic Oscillation (Cohen et al., 2014a; Nakamura et al., 2016; Jaiser et al., 2016; Sun et al., 2015). Especially the Barents-Kara Sea region, being a hotspot of recent Arctic sea ice retreat, has been argued to play an essential role for triggering such dynamical pathways (Screen, 2017a; Jaiser et al., 2016; Kretschmer et al., 2016).

Nevertheless, no overall consensus about linkages and the underlying dynamical pathways has been reached until now (Cohen et al., 2020), mostly due to discrepancies between observational and modeling studies. A recent study by Siew et al. (2020) highlighted for instance that the intermittent and state-dependent character of the aforementioned stratospheric pathway might be a potential reason for the typical low signal-to-noise ratios of atmospheric responses to sea ice changes. Furthermore, Petoukhov et al. (2010) showed how the modeled atmospheric response can depend on the magnitude of prescribed sea ice loss in the Barents-Kara Sea in a highly nonlinear way. Although most studies on Arctic-mid-latitude linkages focus on the role of sea ice changes, several recent studies (He et al., 2020; Labe et al., 2020) also highlighted the importance of the vertical extent of Arctic warming into the upper troposphere compared to sea ice loss alone.

In contrast to winter season, relatively few studies investigated linkages between Arctic climate change and mid-latitude weather and dynamics in summer (e.g. Coumou et al., 2018). Hypothetical links include for instance a weakened storm track (Coumou et al., 2015), amplified quasi-stationary waves (Coumou et al., 2014) or a shift of the jet stream.

1.3 RESEARCH QUESTIONS

As already mentioned in the very beginning there is a need for a better comprehension of future developments of extreme events. As such future changes are governed by different dynamical and non-dynamical factors that could be modified global climate change, it is essential to gain a better understanding of these different factors and their expected changes. However, the overall projected response to future climate change is generally a result of a complex interplay between individual contributions from different local subsystems of the climate system. Therefore, it is essential to acquire deeper insights into these individual contributions in order to make reliable statements about what to expect in the future. Especially changes in atmospheric dynamics are usually triggered by more

localized forcings, such as the aforementioned Arctic sea ice loss which has been proven to be potentially able to affect large-scale atmospheric dynamics.

In this respect, the overreaching objective of this thesis is to contribute to a better understanding of the impact of future Arctic sea ice retreat on mid-latitude extremes and the relevant atmospheric dynamics. Hence, the results of this thesis might also provide a complementary and useful perspective on the controversial topic of Arctic-mid-latitude linkages (e.g. Cohen et al., 2020). In particular, a focal point of this thesis is to assess sea ice-induced changes in European temperature extremes and the associated dynamically and thermodynamically induced contributions to these changes.

In order to isolate the impact of Arctic sea ice changes the analysis in this thesis is predominantly based on ECHAM6 atmosphere-only simulations from the Polar Amplification Intercomparison Project (PAMIP, Smith et al., 2019). ECHAM6 is the latest version of a global atmospheric general circulation model that was developed at the Max-Planck-Institute for meteorology in Hamburg. The different model experiments that are considered here are forced under present day and reduced future sea ice conditions over the entire Arctic, as well as under sea ice conditions only locally reduced over the Barents-Kara Sea. The latter allows for assessing the role of sea ice loss specifically in the Barents-Kara Sea region.

The overreaching objective of this thesis can be addressed by stating three main research questions (**RQ**s), which are studied in the different result sections in Chapter 4.

RQ1: *What changes in the atmospheric large-scale circulation over the Euro-Atlantic sector can be expected under future Arctic sea ice retreat in ECHAM6?*

Motivated by the large variety of previous studies on Arctic-mid-latitude linkages, one major objective is to assess the impact of future Arctic sea ice changes on the atmospheric large-scale circulation over the Euro-Atlantic domain.

From a large-scale and regime-oriented perspective atmospheric dynamics can be viewed in a variety of conceptual frameworks (Hoskins et al., 2015), including for instance jet stream states, blockings or atmospheric circulation regimes. In this thesis, the framework of atmospheric circulation regimes is mainly employed, which has been utilized in several previous studies (e.g. Crasemann et al., 2017; Horton et al., 2015) in order to characterize the atmospheric circulation. Circulation regimes provide physically meaningful categorizations (Hochman et al., 2021) of atmospheric low-frequency variability into different regime states and have also been considered as preferred or quasi-stationary states of the underlying nonlinear atmospheric system (Hannachi et al., 2017). It has been hypothesized that weak external forcings imposed to the atmospheric system are able to modify the occurrence probability of such regime states (Corti et al., 1999), while not effecting the overall regime structure (Palmer, 1999). Indeed, Crasemann et al. (2017) compared atmosphere-only model experiments forced under low and high sea ice conditions relative to the recent past and showed how the occurrence probability of certain Euro-Atlantic circulation regimes can be significantly affected by such Arctic sea ice changes.

To address **RQ1**, Sec. 4.2.2 will initially assess the impact of recent Arctic sea ice change on the occurrence probability of atmospheric circulation regimes over the Euro-Atlantic region in winter and summer. Section 4.2.3 will investigate how the

regime occurrence frequency changes under future sea ice conditions in the respective ECHAM6 PAMIP experiments. In Sec. 4.6, the summer analysis is extended by a circulation analogue-based approach. This allows to assess how future Arctic sea ice changes affect the occurrence frequency of blocking patterns that are commonly associated with summer heat waves over different European regions.

RQ2: *What overall changes in temperature extremes over the continental Northern Hemisphere can be expected in response to future Arctic sea ice loss in ECHAM6?*

Again motivated by earlier studies (e.g. Screen, 2017b; Cohen et al., 2014b; Francis et al., 2012), that linked Arctic sea ice retreat to changes in mid-latitude extremes, Sec. 4.3 investigates to what extent changes in temperature extremes over continental parts of the Northern Hemisphere can be attributed to future Arctic sea ice loss. Similar to the probabilistic risk-based approach in extreme event attribution Sec. 4.3.1 studies temperature extreme occurrence frequency changes under future sea ice conditions in the ECHAM6 PAMIP experiments. This analysis is extended by a comparison of temperature return level between the different experiments (Sec. 4.3.2).

RQ3: *What are dynamically and thermodynamically induced contributions to frequency changes of European temperature extremes that are related to future Arctic sea ice loss in ECHAM6?*

Several previous studies (e.g. Screen, 2017b; Deser et al., 2016; Chripko et al., 2021) investigated how changes in mid-latitude weather can be dynamically and thermodynamically attributed to Arctic sea ice changes. Screen (2017b) compared large ensembles of atmosphere-only experiments forced under low and high sea ice conditions relative to the recent past. They observed that despite an intensification of negative winter NAO events under low Arctic sea ice conditions an expected dynamically induced European cooling response was absent, mostly due to compensation effects related to an overall thermodynamical warming. A further study by Deser et al. (2016) investigated the large-scale hemispheric circulation response to Arctic sea ice loss in different coupled model setups. They compared model simulations with Arctic sea ice conditions constrained to the late 21th and to the 20th century. On the one hand they argued that under reduced sea ice conditions elevated sea level pressures over northern Siberia and Arctic regions are associated with anomalous northeasterly advection of cold Arctic air masses towards central Eurasia. This may dynamically induce a cooling response over central Eurasian regions. On the other hand, this dynamical cooling effect may be thermodynamically counteracted by increased sea surface temperatures. Recently, Chripko et al. (2021) studied fully coupled model experiments where the sea ice albedo parameter was reduced to an albedo value representative of the ocean. This yielded mostly ice-free conditions from July to October and moderate sea ice reductions in winter due to the negligible influence of albedo in polar winter. When compared to a control simulation they detected winter warming signals over Europe and North America in the sensitivity experiment. By applying a dynamical adjustment method (Deser et al., 2016) they showed that these overall responses can be explained by a combination of a dynamical response and a residual contribution.

Motivated by these previous studies, Sec. 4.5 aims to decompose the previously (in **RQ2**) detected changes in temperature extreme occurrence frequencies over the

European region into dynamically- and thermodynamically induced contributions. The decomposition is based on a framework for conditional extreme event attribution (Yiou et al., 2017), that assumes suitable circulation regime storylines identified in Sec. 4.4. Dynamical contributions will be related to changes in the occurrence frequencies of atmospheric circulation regimes that are investigated in **RQ1**. For summer heat extremes, an approach based on circulation analogues is finally employed (Sec. 4.6).

When studying the impact of Arctic sea ice changes on the mid-latitude circulation and extremes, the question may arise how such impacts compare to atmospheric responses induced by more global facets of future climate change. Therefore, in order to assess the relative importance of sea ice loss on future changes in extremes, the analysis will be complemented by investigating the impact of a globally increased future sea surface temperatures background state that is prescribed in one of the experimental setups. Although the main focus of this thesis is on temperature extremes, some parts of the analysis were also conducted for wind extremes.

The current introduction is followed by a review of the most relevant topics related to the different **RQ**s in Chapter 2, including general atmospheric large-scale dynamics, the concept of circulation regimes, Arctic climate change and Arctic-mid-latitude linkages, as well as temperature extreme events. Chapter 3 subsequently describes the reanalysis and ECHAM6 PAMIP data that are used for the analysis in this thesis. Chapter 4 presents and discusses results that aim to answer the different **RQ**s. This thesis ends up with a summary of the main findings and answers to the different **RQ**s and concludes with a final discussion and future outlook.

FOUNDATIONS 2

This Chapter reviews the most relevant topics related to the research questions and analyses in this thesis. One main objective of this thesis is to link Arctic climate change to changes in the Northern Hemispheric large-scale dynamics. Therefore Sec. 2.1 first starts to summarize some essential concepts of large-scale atmospheric dynamics and variability patterns. Subsequently, Sec. 2.2 provides an overview on the topic of atmospheric circulation regimes, as this conceptual framework is mainly employed for the analysis of this thesis. Section 2.3 afterwards present recent Arctic climate developments and the relevant feedback mechanisms that contribute to the phenomenon of Arctic Amplification. As an additional main objective of this thesis is to assess the impacts of Arctic sea ice retreat on climate extremes over Europe, Sec. 2.3 ends up by providing a state-of-the-art review on the topic of Arctic-mid-latitude linkages. Finally, Sec. 2.4 concludes with an overview over climate extremes with a primary focus on recent developments and relevant dynamical drivers of temperature extremes.

2.1 ATMOSPHERIC BASICS

This Section provides a concise overview over some basic concepts of general atmospheric circulation. Therefore, the governing equations of atmospheric motion are initially outlined, which form the basis for all present-day climate models. Afterwards, a description of some of the most prominent atmospheric large-scale and synoptic circulation features is provided, including atmospheric waves, instabilities, blockings and dominant modes of atmospheric variability over the Euro-Atlantic region.

2.1.1 *Governing equations*

Basically, the general dynamics of moving air parcels within the atmosphere can be conceptually treated in the same way as all other hydrodynamical applications. Many phenomena and specialties of atmospheric motions compared to ordinary problems in fluid dynamics arise however from the fact that atmospheric dynamics evolve within the reference frame of a rotating sphere. Consequently, the conservation of momentum is given by the *Navier-Stokes* equations in Eulerian form as

$$\underbrace{\rho(\frac{\partial}{\partial t} + \vec{v}\,\nabla)\vec{v}}_{1} = \underbrace{-\nabla p}_{2} + \underbrace{\rho g}_{3} \underbrace{- 2\rho\,\vec{\Omega} \times \vec{v}}_{4} + \underbrace{\vec{F}_{\text{ext}}}_{5}, \tag{2.1}$$

where an additional term (4) is included that accounts for the Coriolis force. Here, $\vec{v} = (u, v, w)$ is the velocity vector, ρ is air density, ∇p is the pressure gradient, g is the gravitational constant, Ω is the Earth's rotational velocity and $\vec{F}_{\text{ext}}$ describes all forms of frictional or external volume forces. The Navier-Stokes equations state the balance between inertia forces (1), pressure forces (2), gravity forces (3), Coriolis force (4) and other forms of external forces (5).

Additional balance relations that form the basis of general atmospheric dynamics are given by

- the conservation of mass that is described by the continuity equation

$$\frac{\partial \rho}{\partial t} = -\nabla(\rho \vec{v}) \tag{2.2}$$

- as well as the conservation of thermal energy given by the first law of thermodynamics:

$$\dot{Q} = c_\mathrm{p} \frac{\mathrm{d}T}{\mathrm{d}t} - \frac{1}{\rho}\frac{\mathrm{d}p}{\mathrm{d}t}, \tag{2.3}$$

  where T is temperature, c_p is the specific heat capacity and $\dot{Q}$ is the heating rate per unit mass.

The previous set of primitive equations are commonly extended by

- the equation of state for an ideal gas:

$$p = \rho R T, \tag{2.4}$$

- as well as the conservation of specific humidity q[1]:

$$\frac{\partial \rho q}{\partial t} = -\nabla(\rho \vec{v} q) + \rho(\dot{E} - \dot{C}), \tag{2.5}$$

where R is the ideal gas constant, $\dot{E}$ and $\dot{C}$ are water vapor sources (e.g. evaporation and sublimation rates) and sinks (e.g. condensation and deposition rates), respectively. Equations 2.1–2.5 would form a closed system, if the quantities $\dot{E}$, $\dot{C}$, $\dot{Q}$ or $\vec{F}_\mathrm{ext}$ were perfectly known. These quantities typically rely on a huge variety of complex physical processes. For instance, dissipative shear forces near the Earth's surface and within the lower atmospheric boundary layer may contribute to $\vec{F}_\mathrm{ext}$ in the momentum balance 2.1 and generally highly depend on orography and surface roughness. The atmospheric thermal energy budget in Eq. 2.3 is modified by additional energy sinks and sources $\dot{Q}$, such as fluxes at the air-sea interface (see Sec. 2.3.2), but also by complex absorption and emission processes of shortwave and longwave radiation at the Earth's surface, in clouds, or by radiative interactions with chemical species or aerosol particles. The atmospheric water vapor balance 2.5 is affected by moisture fluxes through land, ice and ocean surfaces, as well as for instance by condensation processes in clouds.

Nevertheless, a detailed understanding of most of these processes is still lacking. Indeed, even if all these processes were physically fully understood and quantifiable, they typically occur on too small temporal and spatial scales to be directly resolved in present-day climate models.

1 Defined as the weight of water vapor contained in a unit weight of air

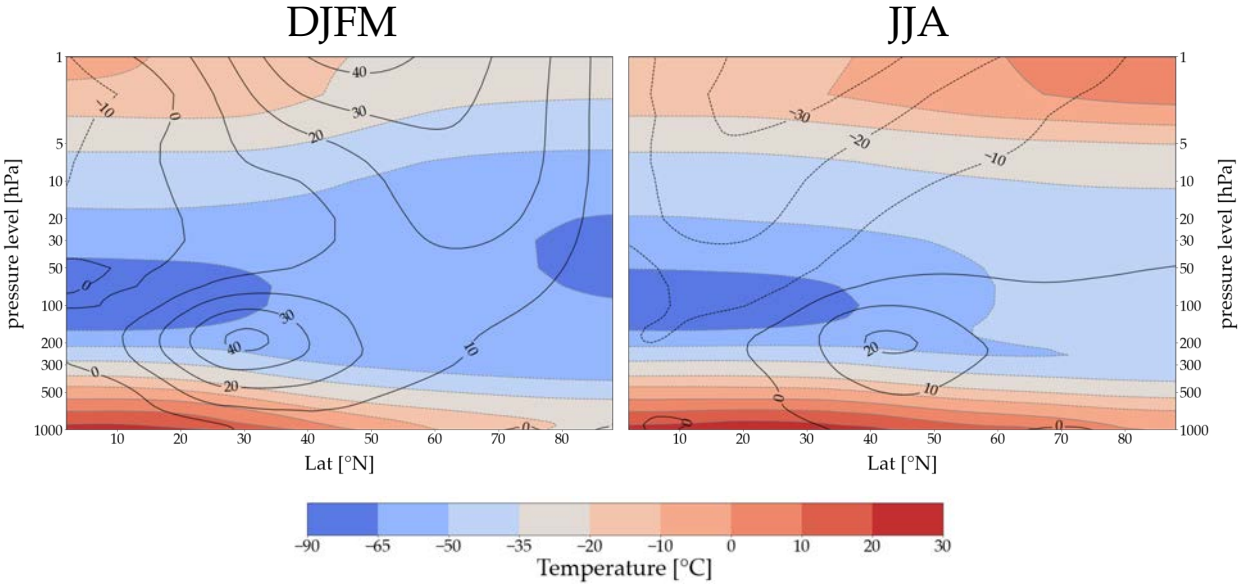

Figure 2.1: Latitude-Height climatologies of zonal wind (black contour lines with contour interval of 10 m s^{-1}) and temperature (colors) for DJFM and JJA, calculated from monthly ERA5 data (see Sec. 3.1) over the period 1979–2018.

2.1.2 *Zonal wind and temperature profiles*

Figure 2.1 shows the latitude-height profile of zonally averaged zonal wind and temperature for the extended winter (December, January, February, March; denoted by DJFM) and summer season (June, July, August; denoted by JJA) over the Northern Hemisphere NH. The plots were calculated from monthly ERA5 data (see Sec. 3.1) averaged over the period 1979–2018.

The vertical temperature profile in the troposphere is generally determined by increased absorption of Earth's emitted longwave radiation in lower atmospheric layers. This results in decreasing temperatures with height, also referred to as a positive lapse-rate. This positive lapse rate continues up to the extremely cold tropopause that is located at a height of around 8 km over polar and around 17 km over equatorial regions. Above the tropopause, the stratosphere initially exhibits a constant vertical temperature profile until temperatures actually start to increase with altitude. This temperature inversion or negative lapse rate is mainly attributed to the direct absorption of UV radiation by a high amount of ozone in the stratospheric ozone layer, located between 15–30 km altitude. The stratospheric vertical temperature profile results in very stable stratification; consequently, less turbulence and mixing occurs compared to more chaotic tropospheric layers.

An important driver of the general atmospheric circulation is provided by the differential surface heating by the sun, resulting in lower temperatures at the poles and higher temperatures at the equator. From a coarse point of view the resulting equator-to-pole temperature gradient $\frac{\partial T}{\partial y}$ gives rise to meridional air motions that are zonally deflected by the Coriolis force. This equator-to-pole gradient is weaker in summer compared to winter season. As the strength and variability of the general circulation however depends on the magnitude of such gradients, atmospheric circulation in summer months is weaker compared to winter (see Fig. 2.1).

The horizontal components of the *Navier-Stokes equations* 2.1 can be simplified by making a steady state assumption, as well as by neglecting any frictional forces. The resulting *geostrophic equations*

$$f\vec{v}_g = \frac{1}{\rho}\vec{k} \times \nabla_h p \tag{2.6}$$

describe the balance between pressure and Coriolis force for large-scale atmospheric motions. Here, $\vec{v}_g = (u_g, v_g)$ is the geostrophic wind vector, $\vec{k}$ is a vertically directed unit vector and ∇_h is the horizontal component of the nabla operator. Thus, some negative equator-to-pole pressure gradient $\frac{\partial p}{\partial y}$ gives rise to westerly winds, which are indeed commonly observed in the upper mid-latitude troposphere. Deviations from the geostrophic wind vector $\vec{v}_g$, typically averaged out in climatological mean plots like Fig. 2.1, are referred to as the ageostrophic wind. The ageostrophic wind components are a consequence of non-stationarities in the atmospheric flow, frictional forces, as well as of flow divergence that is closely linked to the grow and decay of atmospheric weather systems.

As also deducible from Fig. 2.1, a vertical strengthening of tropospheric zonal winds can be observed in connection with horizontally decreasing temperatures towards the poles. The latter is also referred to as a baroclinic stratification[2]. When incorporating the hydrostatic approximation[3] $\frac{\partial p}{\partial z} = -\rho g$ into the geostrophic wind Equations 2.6, this observation can be expressed by the *thermal wind equations*

$$\vec{v}_T = \frac{\partial \vec{v}_g}{\partial z} \approx \frac{g}{fT}\vec{k} \times \nabla_h T \tag{2.7}$$

These equations relates the vertical strengthening or weakening of horizontal wind components with altitude z (also referred to as the *thermal wind* $\vec{v}_T$) to meridional and latitudinal temperature gradients. As a result, strongest zonal winds in the lower atmosphere are typically found near the tropopause, also referred to as jet streams. Nevertheless, beyond this zonally averaged picture in Fig. 2.1, different more regional jet stream systems actually exist. Indeed, different mechanisms and explanation approaches about the formation of different types of jets are established nowadays. First, the subtropical jet stems mostly from planetary angular momentum transport from the tropics into the subtropics via the thermal Hadley circulation. This thermally driven jet is usually located at around 30°N in winter and is shifted polewards in summer due to the northward shift of the Inter-Tropical Convergence Zone (ITCZ). Secondly, the eddy-driven jet stream emerges from the momentum flux convergence of zonal momentum by atmospheric waves in mid-latitude regions of enhanced baroclinic activity. Although for instance the North Atlantic jet is supposed to be mostly eddy-driven (Li et al., 2012), both jet formation processes can generally co-occur and contribute to the emergence of other regional jet stream systems.

As additionally evident in Fig. 2.1, a very strong circular belt of westerly winds enclosing an area with very low temperatures (and pressures) can be found in the polar strato-

2 Baroclinicity is generally present when surfaces of constant pressure and constant density are not parallel. Hence, the temperature can vary along isobars. In contrast, a barotropic atmosphere is characterized by parallel surfaces of constant pressure and constant density or temperature.

3 which states the balance between gravity and pressure forces. It is a reasonable approximation when vertical accelerations and therefore the vertical intertia terms in the Navier-Stokes Equations 2.1 are negligibly small compared to vertical gravity and pressure forces.

sphere in winter. The so-called polar stratospheric vortex forms in fall when the polar regions begin to be completely located in the Earth's shadow and lack solar heating. The resulting strong meridional gradients in temperature and pressure between polar and mid-latitudinal regions give rise to strong westerly winds that maximize at around 60°N. The polar vortex starts to breakdown in early spring, when incoming solar radiation begins to compensate the meridional temperature gradient between low and high latitudes.

2.1.3 *Atmospheric waves and instabilities*

Atmospheric waves

Atmospheric waves describe spatially periodic disturbances in fields of atmospheric variables that may propagate over time and in space. Probably the most relevant type of atmospheric waves responsible for shaping the large-scale circulation is termed *Rossby waves*. Their typical zonal wave numbers k_x correspond to wavelengths on synoptic scales ($O \sim 1000\,\mathrm{km}$, $k_x = 6 - 10$), or even larger planetary scales (see e.g. Pichler, 1997).

Assuming a purely non-divergent and barotropic flow, the formation of Rossby waves is a consequence of the conservation of the vertical component of absolute vorticity. Absolute vorticity is defined as the sum of the relative vorticity of the flow $\frac{\partial v}{\partial x} - \frac{\partial u}{\partial y}$ and planetary vorticity $2\Omega \sin(\varphi)$, where Ω is the Earth's rotational velocity and ϕ is latitude. For instance, a northward displacement of an air parcel increases its planetary vorticity, which in return has to result in a decrease of relative vorticity by curving the parcel's trajectory southwards. The resulting meandering circumpolar wave patterns with high pressure ridges and low pressure troughs form characteristic and essential features of the circulation over mid-latitudes (see for instance Fig. 2.4a).

An expression for the zonal phase speed c_x of *free* Rossby waves can be derived when applying linear perturbation theory to the vorticity equation of a horizontal, non-divergent and barotropic atmospheric flow. For given zonal and meridional wave numbers (k_x and k_y), the phase speed of Rossby waves in a zonal background flow u_0 is given by (e.g. Pichler, 1997)

$$c_x = u_0 - \frac{\beta}{k_x^2 + k_y^2}. \tag{2.8}$$

Here, β describes the linearly approximated meridional variation of planetary vorticity at some reference latitude (also termed *beta-plane approximation*). It is evident from Eq. 2.8 that a single Rossby wave always propagates westwards relative to the mean flow. For a typical value of $u_0 = 10\,\mathrm{m\,s^{-1}}$ at 45°N, stationary waves with zero phase speed are characterized by a stationary wavelength of around 5000 km. Rossby waves with wavelengths shorter than the stationary wavelength propagate eastwards. The direction and strength of energy transport associated with Rossby waves is determined by the group velocity of Rossby wave packets, that is, the velocity of the resulting envelope of a superposition of different Rossby waves with varying spatial and temporal frequencies. In this respect, the meridional energy transport of Rossby waves requires a non-zero meridional wave number k_y and therefore a tilt of the troughs and ridges with respect to the north-south direction.

In contrast to free Rossby waves that do not require any external forcing and are an inherent feature of atmospheric dynamics, *forced* Rossby waves are mainly generated by diabatic and orographic forcings. Their wave numbers are consequently typically determined by the land-sea distribution and orography. Owing to the large-scale and mostly stationary nature of these forcings, forced Rossby waves tend to have smaller wave numbers (k_x<6) and are considered quasi-stationary.

Forced Rossby waves are of primary importance for understanding northern hemispheric large-scale dynamics, especially the energetic coupling between the troposphere and the stratosphere. In this respect, Charney et al. (1961) stated a criterion for the upward propagation of stationary Rossby waves, which can be derived from the linearized quasi-geostrophic equations of potential vorticity on a beta-plane:

$$0 < u_0 < \frac{\beta}{k_x^2 + k_y^2 + \frac{f_0^2}{4N^2H^2}} \equiv U_c \tag{2.9}$$

Here, f_0 is the Coriolis parameter at some reference latitude, N is Brunt–Väisälä frequency of the unperturbed motion and H is the scale height of the atmosphere. Thus, only extremely long-wave Rossby waves (commonly with wavenumber 1 or 2) can propagate upward and disturb the stratospheric circulation. However, this upward propagation and energy transport can only proceed in a westerly background flow until a critical westerly wind velocity U_c is reached. Due to the more complex orography and land-sea contrast on the NH, an overall stronger wave forcing is provided compared to the Southern Hemisphere SH. This consequently results in enhanced wave activity and upward fluxes of energy and momentum in Northern Hemispheric regions.

The relatively strong wave activity over the NH is supposed to be responsible for so-called sudden stratospheric warming (SSW) events (Matsuno, 1971). Such events are accompanied by stratospheric temperature increases of up to 30–40°C within a few days. In the most extreme cases, even a reversal of stratospheric westerly winds and an immediate breakdown of the polar vortex is possible, also referred to as major sudden stratospheric warmings. Major SSW events have been linked to cold winter weather over the NH, such as to more severe cold extremes over Scandinavia (King et al., 2019). A recent study by Butler et al. (2017) identified 41 major events in different reanalysis products over the time period 1958–2014. Although normally only observed over the NH, a major SSW event has been recognized for the first time in September 2002 over Antarctica as well, probably related to an anomalously high prevalence of strong planetary waves during this period (Varotsos, 2004).

Atmospheric instabilities

Depending on the atmospheric background flow configuration atmospheric waves and perturbations may either decay, grow or remain stable over time. The associated amplification and instability processes play an important role for atmospheric dynamics, especially for the formation of synoptic weather systems (see e.g. Pichler, 1997).

The most essential form of atmospheric instability involved in the genesis of extratropical cyclones and storm systems over mid-latitudes is termed *baroclinic instability*. This form of instability requires the baroclinic stratification typically found over mid-latitudes, and consequently horizontal temperature gradients and the associated vertical wind shear

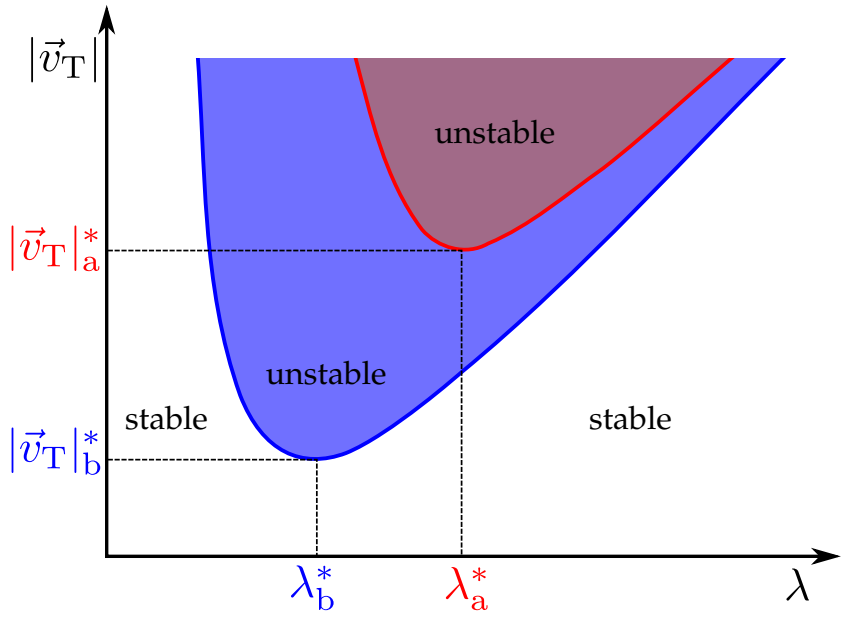

Figure 2.2: Schematic illustration of the baroclinic instability criteria as a function of the wavelength λ and the absolute thermal wind $|\vec{v}_T|$ (based on Pichler (1997)). Until a certain threshold of the vertical wind shear $|\vec{v}_T|^*_a$ is reached waves remain stable for all wavelengths. When $|\vec{v}_T|^*_a$ is reached waves with a critical wavelength λ^*_a start to amplify and become unstable. The blue curve (subscript "b") exemplary illustrates the consequences for the instability criterion for a more unstable atmospheric stratification. Compared to a more stable stratification (red curve), instability in a less stable atmosphere requires lower critical wind shears $|\vec{v}_T|^*_b$, and waves with shorter critical wavelengths λ^*_b are amplified first.

$|\vec{v}_T|$ (see Eq. 2.7). Linear perturbation theory shows that until a critical vertical wind shear $|\vec{v}_T|^*$ is reached atmospheric waves remain stable (see Fig. 2.2). After exceeding this critical wind shear instability and amplification occurs first for waves with a certain critical wavelength λ^* on synoptic scales. However, these critical wavelength and vertical wind shear thresholds are typically shifted towards lower values for more unstable atmospheric stratifications (see the two different curves in Fig. 2.2). From an energetic point of view, such baroclinic amplification processes of atmospheric waves and disturbances gain their kinetic energy from the available potential energy supplied by the baroclinic stratification.

Another form of atmospheric instability is termed barotropic instability, that already occurs in a barotropic atmosphere with horizontal wind shear. Contrary to the baroclinic instability, a kinetic energy exchange occurs between the perturbations and the zonal mean flow. Especially in mid-latitudes waves with shorter wavelength restore their energy back and help to maintain the zonal mean flow against friction.

2.1.4 *Large-scale variability patterns and blocking*

Large-scale low frequency variability patterns

Low-frequency variability of the large-scale atmospheric circulation can be characterized by a set of dominant variability patterns (Wallace et al., 1981), typically determined by

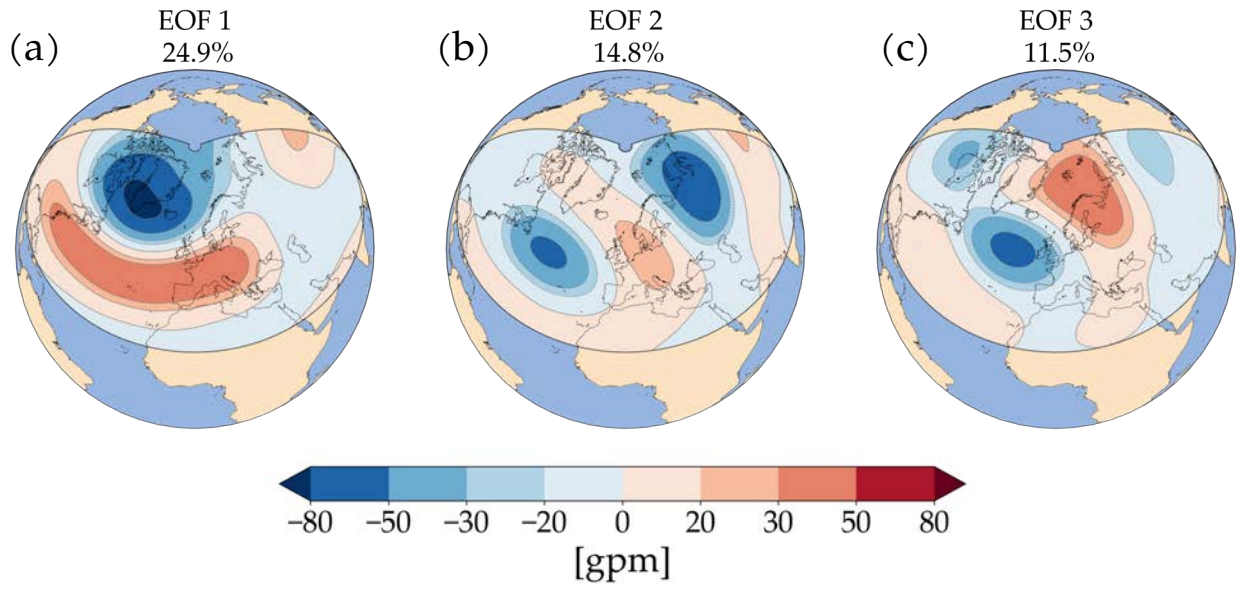

Figure 2.3: First three leading EOF patterns for the extended winter season with a focus on the Euro-Atlantic region. The variability patterns are computed from monthly averaged ERA5 gph500 anomalies over the period 1979–2018. The percentages of explained variance by the respective pattern are given above the plots. Note, that these three patterns already explain about 51% of monthly low frequency gph500 variability over the displayed region. Units are given in geopotential meter.

correlation analysis or given by the leading Empirical Orthogonal Functions EOF of a Principal Component Analysis (see Sec. A.1).

In this respect, Fig. 2.3 displays the dominant modes of atmospheric month-to-month variability of geopotential height anomalies at the 500 hPa pressure level gph500 over the Euro-Atlantic region (-115°W–115°W, 20°N–88°N) and for the extended winter season. The patterns were computed with a Principal component Analysis PCA. It should be noted that the pattern structures, especially for higher EOFs, typically depend on the analyzed height level, the time period, but also on the analyzed region due to the multivariate character of PCA. Nevertheless, the leading and always robustly detected EOF pattern explains around 25% of interannual low-frequency month-to-month variability in the middle troposphere and is termed the *North Atlantic Oscillation* (NAO, see Walker, 1923; Hurrell et al., 2003). The NAO is characterized by a meridional sea-saw of pressure anomalies over the North Atlantic region. In its positive index phase this results in positive pressure anomalies over mid-latitudes and negative pressure anomalies over the Arctic (see Fig. 2.3a), and vice versa for a negative NAO state. The current index state of the NAO is typically given as the corresponding Principal Component PC of the respective EOF pattern, but it is also commonly defined as the difference of normalized sea level pressure SLP anomalies between Iceland and the Azores. The NAO is an important driver of European weather; e.g, it strengthens Atlantic wind speeds in its positive phase. In winter this results in enhanced transport of warm (and moist) maritime air masses towards northern Europe, and consequently in an anomalous convergence of latent heat transport over Scandinavia (Vihma et al., 2020). Additionally, the NAO is also typically associated with a northward displacement or tilt of the Atlantic stormtrack (see e.g. Fig. B.8).

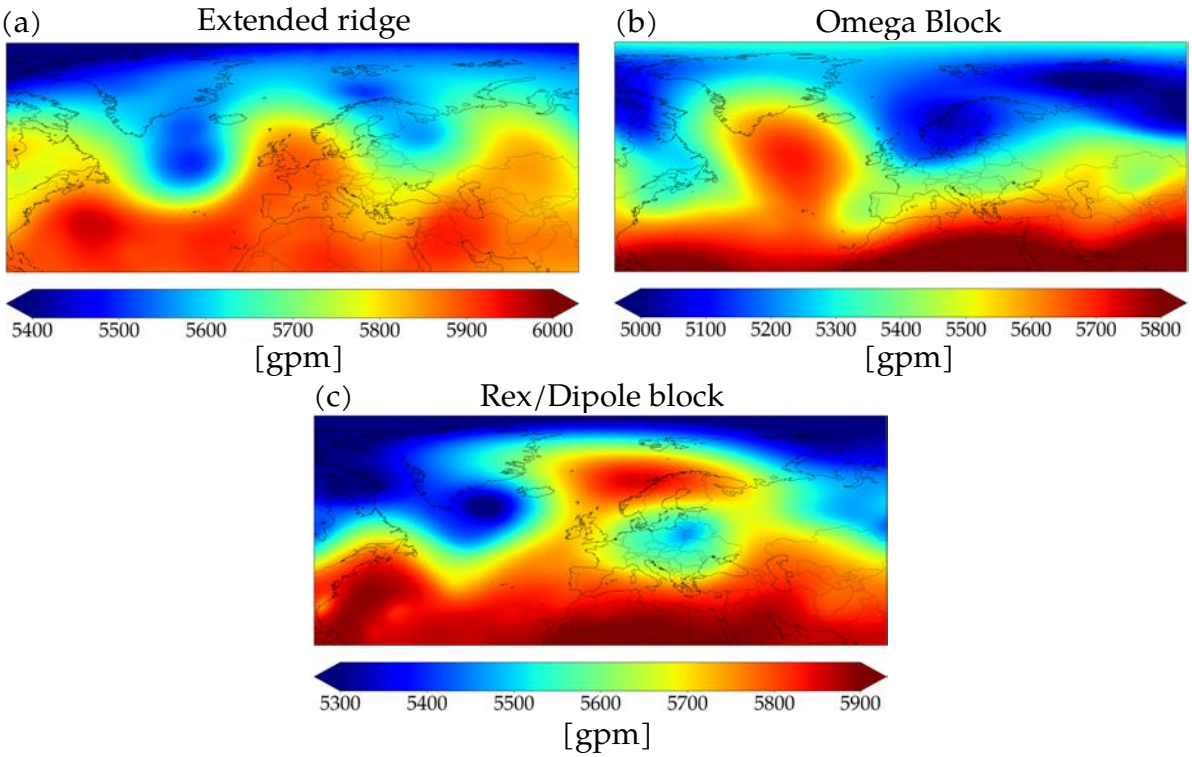

Figure 2.4: Examples of typical atmospheric blocking structures. Shown are ERA5 gph500 fields for selected days: a) Extended Summer ridge (8th August 2003), b) Omega Block (25th February 2004) and c) Rex or Dipole Block (8th October 2016). Selected dates are the same as in Woollings et al. (2018).

The second and third EOFs shown in Fig. 2.3b and c have been previously termed the *East Atlantic* pattern and the *Scandinavia* pattern, respectively (see e.g Wallace et al., 1981; Handorf et al., 2012). Together they also explain more than 25% of mid-tropospheric variability. They reveal phase shifted wave structures similar to stationary Rossby wave trains (see Sec. 2.1.3). Variability patterns as shown before are also commonly referred to *teleconnections patterns*, which in general describe all forms of direct or indirect climatic linkages between geographically separated regions.

Atmospheric blocking

Atmospheric blockings are commonly referred to as persistent and quasi-stationary tropospheric structures that typically obstruct and split the prevailing zonal jet, sometimes even leading to a flow reversal towards slightly easterly winds in the blocked region. Although there is still no definite and generalized definition, blocking systems are commonly assigned to one of following suggested categories (see e.g. Woollings et al., 2018; Kautz et al., 2022):

- *Extended Ridges* can be associated with stationary Rossby waves (see Fig. 2.4a). Here, an anticyclone is flanked by two cyclones that are respectively located upstream and downstream of the ridge. This results in an omega-shaped structure.

- *Omega Blocks* (see Fig. 2.4b) bear a strong resemblance with amplified ridges, however, they typically exhibit a more poleward extension of the anticyclone and sometimes even closed contours in the stream function.
- A *Rex* or *Dipole Block* is characterized by an anticyclonic center located poleward of a cyclone (see Fig. 2.4c). It has been shown that the cyclonic and anticyclonic breaking of Rossby waves can result in such meridional dipole patterns (Masato et al., 2012).

Owing to the complexity and variety of atmospheric blocking systems, a huge number of indices for blocking detection have been defined over the years. Such indices are for instance based on the reversal of meridional gradients in gph500 (e.g. Tibaldi et al., 1990; Scherrer et al., 2006), or in potential temperature at a surface of constant potential vorticity (e.g. Pelly et al., 2003). In addition, blocking indices have also been based on the detection of persistent negative potential vorticity anomalies (e.g. Schwierz et al., 2004). Although successive improvements have been reported for climate models from the latest Coupled Model Intercomparison Projects CMIP, contemporary state-of-the-art climate models still underestimate blocking frequencies compared to observation, especially in key regions such as over Europe in winter (Davini et al., 2020). Due to their stationarity and persistence over several days or even more than a week, atmospheric blockings are closely tied to extreme events such as summer heat waves or winter cold spells (see also Sec. 2.4.2).

2.2 ATMOSPHERIC CIRCULATION REGIMES

Starting several decades ago, it has been already recognized that certain preferred and recurrent states of atmospheric circulation may exist (e.g. Rossby et al., 1939; Rex, 1950). Starting in the mid 20th century, a catalogue of the most common and persistent weather patterns over Europe, called "Großwetterlagen", has been summarized (Baur et al., 1944; Hess et al., 1952). Later on, probability density estimates of low-dimensional phase spaces revealed multimodal distributions in observed low frequency geopotential height variability (e.g. Molteni et al., 1990), and hence provided additional statistical evidence of the existence of preferred atmospheric circulation states.

2.2.1 *Dynamical concepts*

Despite an overall consensus on the existence of preferred states within the highly nonlinear atmospheric system (see e.g. Eqs. 2.1-2.5), understanding their dynamical origins still remains a challenging task (Hannachi et al., 2017). One of the first approaches was to investigate simplified equations that govern the atmospheric flow and check for stationary solutions. In one of the pioneering studies Charney et al. (1979) described a simplified barotropic channel model with variable surface height, aiming to explain persistent large-scale atmospheric flow states. They demonstrated the existence of multiple stable equilibria under topographic and thermal forcings. Indeed, one of these states could actually be associated with a large wave amplitude or blocking pattern. Many future studies have been inspired and extended the multiple equilibria approach (Legras et al., 1985; Charney et al., 1980). In this context, Sempf et al. (2007a) and Sempf et al. (2007b) employed a quasigeostrophic three-level model, as well as a spectral barotropic model in order to

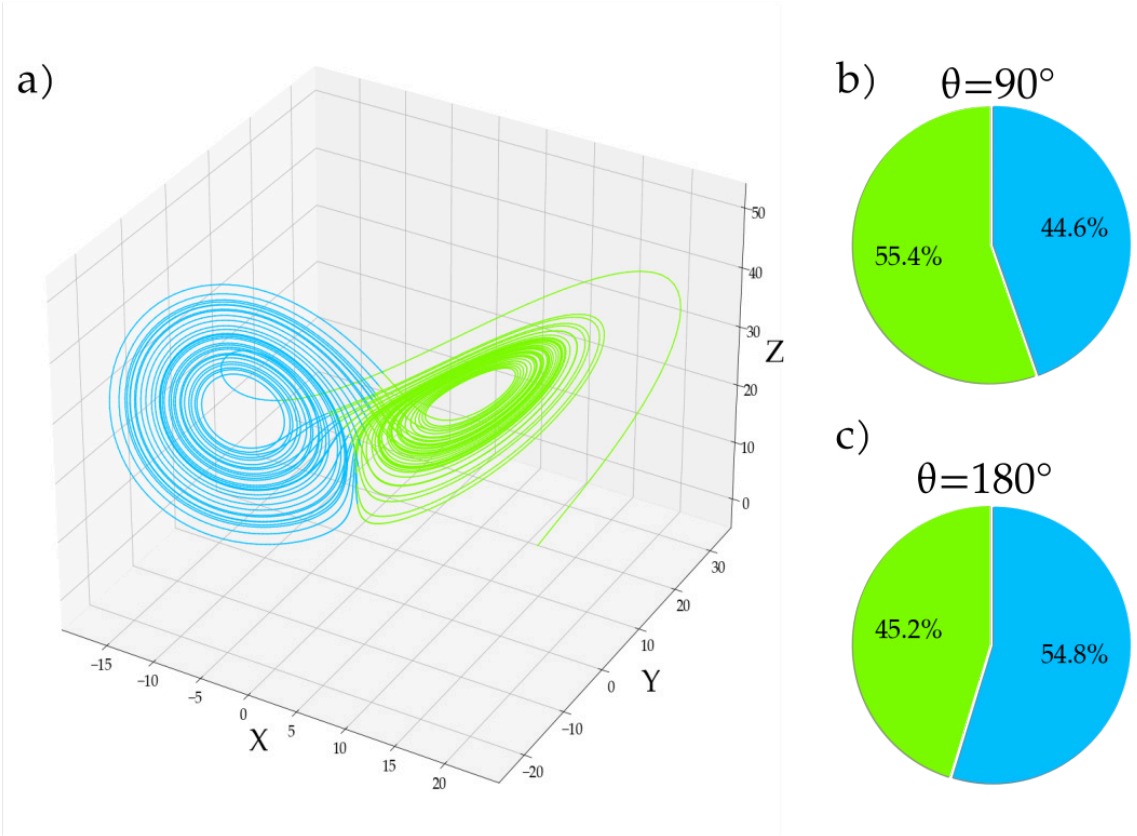

Figure 2.5: a) Chaotic attractor of the Lorentz system (Eqs. 2.10-2.12) with $a = 10, b = 28$ and $c = \frac{8}{3}$ exhibiting two regime states (green and blue). b,c) Pie charts of regime occupation probabilities for the forced Lorentz System ($f = 2.5$) with b) $\theta = 90°$ and c) $\theta = 180°$.

investigate the origin and the dynamical mechanisms of atmospheric regime behavior. By changing surface and dissipative forcing parameters they proposed a potential bifurcation route for the emergence of the Arctic Oscillation. In particular, they related the regime behavior within the chaotic attractor to transitions between the ruins of formerly coexisting attractors.

The potential analogy between atmospheric regime behavior and dynamics of nonlinear chaotic systems can also be conceptually demonstrated when considering low-order dynamical systems with regime structures (Corti et al., 1999). In one of the most fundamental studies on the topic of nonlinear and complex systems, Lorenz (1963) described a simplified model for fluid convection in a two-dimensional layer, called the *Lorentz system*

$$\dot{x} = a(y - x) + f \cdot \cos\theta \tag{2.10}$$

$$\dot{y} = x(b - z) - y + f \cdot \sin\theta \tag{2.11}$$

$$\dot{z} = xy - cz \tag{2.12}$$

Here, an additional imposed forcing of amplitude f with direction parameter θ has been added.

This nonlinear coupled differential equation system exhibits chaotic behavior and solutions for certain parameter values a, b and c. Its iconic chaotic attractor is shown in Fig. 2.5a

and exhibits two dominant regimes corresponding to each wing of the butterfly structure. Irregular transitions between both regimes characterize the system's low frequency variability. The unforced Lorenz system is characterized by an equal occurrence probability of both regimes; however, an imposed external forcing applied to the system is able to significantly effect the occurrence probability of both regime states (see Figs. 2.5b and c; and Palmer, 1999).

Based on these qualitative concepts the question arose to what extent external forcings, such as changes in sea surface temperatures SSTs (Straus et al., 2007; Palmer, 1993) or sea ice concentrations SIC (Crasemann et al., 2017), may affect the occurrence probability of regime states in the atmospheric dynamical system. In this respect, it has been noted that an imposed forcing may not necessarily be spatially correlated with a respective regime in order to induce frequency changes (Corti et al., 1999). Palmer (1999) studied the impact of a weak imposed forcing on a non-linear dynamical system in a theoretical linearized framework. He concluded that weak forcings primarily manifest in a change of occurrence frequencies, while barely affecting the spatial structure or the phase space position of the associated regime. Nevertheless, stronger imposed forcings may be able to alter the number or even the geographical structure of regimes (Handorf et al., 2009; Kageyama et al., 1999).

2.2.2 *Regime computation*

Circulation regimes are usually computed on variables such as SLP (Crasemann et al., 2017; Rust et al., 2010) or gph500 (Horton et al., 2015; Casado et al., 2009; Strommen et al., 2019). Typical regimes that are usually found when analyzing the Euro-Atlantic domain in winter include a positive and a negative state of the NAO, an Atlantic ridge or a pattern with an anticyclonic center over Scandinavia.The concept of circulation regimes has also been considered in terms of jet stream states by analyzing zonal wind fields. In this respect, Madonna et al. (2017) and Dorrington et al. (2020) tried to reconcile the different perspectives and assigned a northern, southern, central, tilted and splitted jet configuration to pressure-based regimes. Although in this thesis circulation regimes are only calculated over the Euro-Atlantic domain, it should be noted that the framework has also found applications in other regions of the world, such as over the SH (Pohl et al., 2012), the Pacific-North American Sector (Straus et al., 2007) or more limited geographical regions such as South Africa (Lennard et al., 2015).

A variety of statistical approaches have been employed in order to compute atmospheric circulation regimes (Hannachi et al., 2017). One main category of utilized statistical approaches are probabilistic models that try to estimate the probability density function of data points in phase space. Local maxima of a resulting multimodal distribution may than be interpreted as preferred states of atmospheric circulation. Approaches include kernel density estimates (Corti et al., 1999; Handorf et al., 2009) in low dimensional phases spaces (e.g. spanned by the first two leading PCs, see Sec. A.1) or Gaussian mixture models (Rust et al., 2010; Smyth et al., 1999). The latter assume that the probability density function can be described as a superposition of multiple multivariate Gaussian distributions.

A different class of approaches aims for a distant-based partition of the state space into different clusters and categorizes each data point to a specific cluster. The k-Means al-

gorithm (see Section A.2) aims to minimize the intracluster variance by in an iterative allocation and exchange procedure of cluster members (MacQueen, 1967). As the most frequently used approach it was applied in a variety of atmospheric studies (e.g. Michelangeli et al., 1995; Crasemann et al., 2017; Straus et al., 2007). The basic algorithm has been extended by e.g. introducing additional persistence constrain parameters (Falkena et al., 2020). Further algorithms include hierarchical clustering approaches (Casola et al., 2007; Cheng et al., 1993), as well as Self Organizing Maps (Kohonen, 2001; Horton et al., 2015; Rousi et al., 2020), that is, an unsupervised machine learning approach that employs an artificial neural network in order represent the original input data with a topology-preserving low dimensional map.

Furthermore, approaches aiming to incorporate temporal information from the underlying atmospheric time series have been suggested. In this respect, Franzke et al. (2008) outlined how metastable regime states can be identified by fitting a Hidden Markov Model to atmospheric time series. Horenko (2010) formulated a finite element clustering procedure (FEM-VARX), where the temporal dynamics within each regime are represented by a multivariate autoregressive VARX process that includes external forcing parameters.
Although atmospheric circulation regimes are computed from a variety of purely statistical methods, evidence has been reported that regimes are indeed physically meaningful and not just useful statistical categorizations of atmospheric dynamics (Hochman et al., 2021).

2.2.3 *Regime number*

Although an overall agreement on the existence of preferred states of atmospheric circulation was established over recent decades, the essential question regarding the exact number of Northern Hemispheric winter regimes remains highly debated. This question is of additional importance as the majority of frequently used clustering algorithms (e.g. k-Means, SOMs) require a distinct regime number defined a priori. Several earlier studies investigated this topic by using a variety of statistical approaches. Indeed, most studies suggest an optimal cluster number of three (Smyth et al., 1999; Dorrington et al., 2020), four (Straus et al., 2007; Dawson et al., 2012; Falkena et al., 2020), five (Crasemann et al., 2017; Dorrington et al., 2020) or even six (Falkena et al., 2020; Robertson et al., 2000) regimes, generally depending on different aspects such as the distinct spatial domain over which the regimes are computed.

Common methods in this respect include model selection procedures using information criteria (e.g. AIC or BIC, see Falkena et al., 2020; Dorrington et al., 2020) or cross-validation approaches within the framework of Gaussian mixture models (Smyth et al., 1999). Furthermore, Monte Carlo simulations that construct synthetic time series with similar statistical properties as the original data have been utilized for testing against the null hypothesis of a unimodal multivariate normal distribution (Dawson et al., 2012; Crasemann et al., 2017; Straus et al., 2007). Nevertheless, skepticism emerged whether such approaches are actually able to provide meaningful results, as the suggested optimal number of clusters may depend on the sample size, clustering algorithm, time period and prefiltering; sometimes, even multiple regimes can be erroneously reported in case of unimodal, skewed distributions (Christiansen, 2007). In this respect, subjective selection

criteria based on the actual application or judgment by experts may be used to complement aforementioned objective methods.

In this thesis, five circulation regimes are considered as it was shown by Crasemann et al. (2017) to be the optimal regime number over the distinct Euro-Atlantic domain (90°W-90°E,20°N-88°N) that is used for the presented analysis.

2.3 ARCTIC CLIMATE CHANGE

It has been recognized quite early that anthropogenic induced global warming is spatially non-uniform and shows considerable differences between different parts of the planet. In one of the first studies aiming to quantify carbon dioxides' contribution to the greenhouse effect, the Swedish scientist Svante Arrhenius already noted that, driven by feedbacks related to snow cover changes, temperature trends and variability in polar regions might be stronger compared to the rest of the world (Arrhenius, 1896). Starting in the mid of the 20th century, the idea of enhanced Arctic warming has been more and more supported by observational data (e.g. Mitchell, 1961), as well as by first Energy balance models (Sellers, 1969). Accompanied by a significant loss of Arctic Sea Ice SI over recent years, the phenomenon termed Arctic Amplification AA, became well-established and supported by observational data. In addition, it was found as a robust feature in simplified (Wetherald et al., 1975) and state-of-the-art general circulation climate models (Meredith et al., 2019).

This Section first reports on the latest SI and temperature developments over the Arctic domain. Before Sec. 2.3.3 discusses the most relevant feedback mechanisms that contribute to the phenomenon of AA, Sec. 2.3.2 provides an overview on surfaces fluxes and the surface energy budget at the atmosphere-ocean-sea ice interface in Arctic regions. This will allow for a better understanding of the consequences of prescribed Arctic SI loss in the analyzed model simulations on the lower atmosphere (see also Sec. B.6.3). Finally, Sec. 2.3.4 provides a review on the current state of knowledge on potential linkages between Arctic climate change and weather over mid-latitudes.

2.3.1 *Recent trends in Arctic sea ice and temperatures*

As indicated in Fig. 2.6c recent-past enhanced Arctic warming has first been recorded for the period 1920-1940. This period of early Arctic warming was predominately confined to high latitudes in winter and autumn. It was argued to be most likely a result of natural variability (Johannessen et al., 2004), but may possibly also be linked to positive feedback mechanisms that amplify atmospheric forcings (Yamanouchi, 2011). In the upcoming years, a period also termed mid-twentieth-century cooling (e.g. Haustein et al., 2019) was especially characterized by decreasing temperatures over Arctic regions till the 1980s.

Since the mid 1990s, a period of recent Arctic warming is present with a significant warming trend in Arctic regions, especially in autumn and winter. Depending on the methodology and dataset contemporary studies indicate that the Arctic has warmed up to four times faster than the global average (Rantanen et al., 2022). Arctic change over the last decades is also accompanied by a dramatic loss of Arctic SI, as shown in Fig. 2.6b. Around 50 % of this latest negative SI trend might be attributed to increased greenhouse

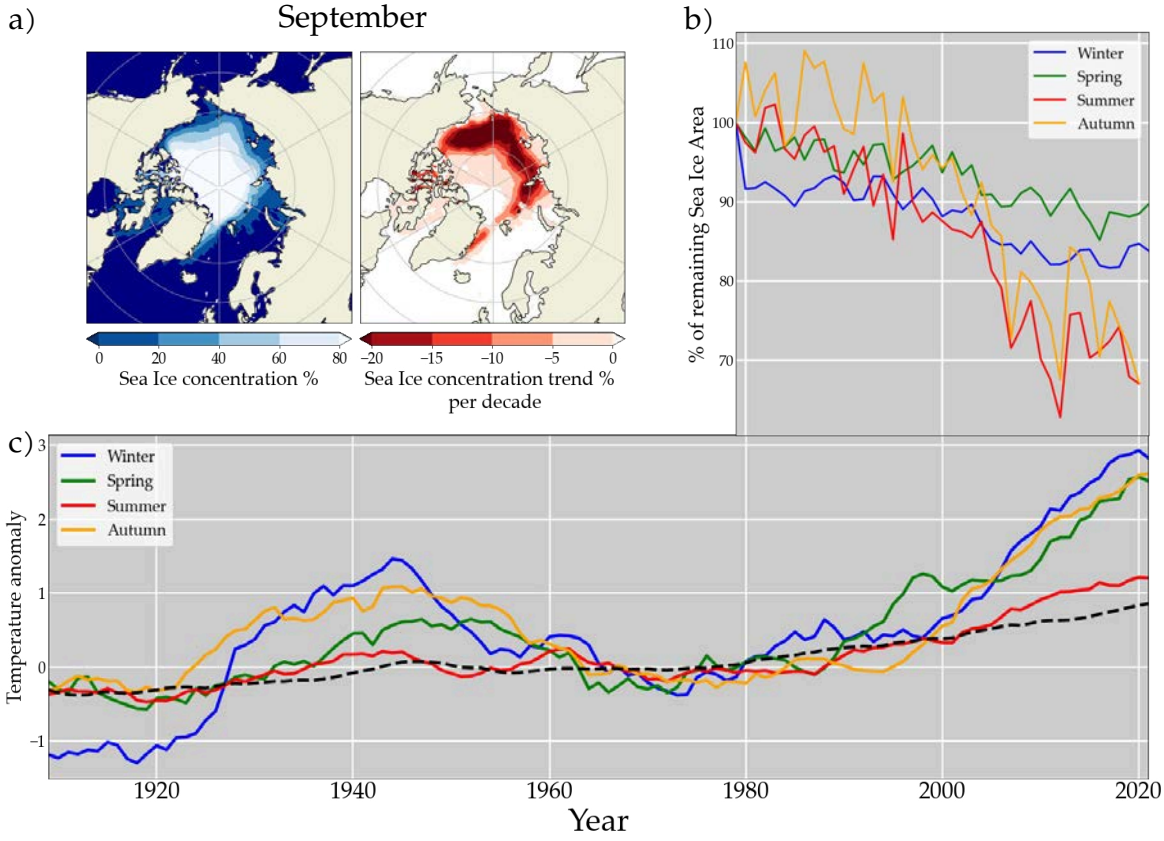

Figure 2.6: Recent Arctic SI and SSTs developments: a) Left: mean state of September sea ice concentration averaged over 1979–2018. Right: linear trend of monthly averaged ERA5 September sea ice concentration over the period 1979–2018. b) Change in Arctic sea ice area relative to 1979. Sea ice data are taken from ERA5. c) Arctic surface temperature anomalies calculated as the spatial average north of 65°N for different seasons. Anomalies are defined with respect to the base period 1951–1980. A 10-year running mean has been applied to the time series and the black dashed line indicates the global average for all seasons. Surface temperature data are provided by the *Goddard Institute for Space Studies Surface Temperature product version 4* (GISTEMP v4, see Lenssen et al., 2019).

gas concentrations (Meredith et al., 2019). Recent Arctic warming is most pronounced in winter and autumn season, but SI decline is strongest in summer with a relative September loss of more than 40 % over the last four decades (e.g. Stroeve et al., 2018). Figures 2.6a and b illustrate that for instance the contemporary spatial loss pattern during the annual SI minimum in September is most prominent in the Beaufort, East Siberian, and Laptev Sea, as well as parts of the Kara Sea. In late autumn, centers of SI loss are located in Chukchi, Kara and the Northern Barents Sea, whereas in mid and late winter (and spring) SI loss is strongest in the Sea of Okhotsk, the Barents and parts of the Greenland Sea (see also Fig. B.13). Model projections forced under different greenhouse gas scenarios show clear evidence that Arctic SI decline will persist over upcoming decades (Meredith et al., 2019), and some models even project a seasonally ice-free Arctic till the mid of the century (Notz et al., 2020).

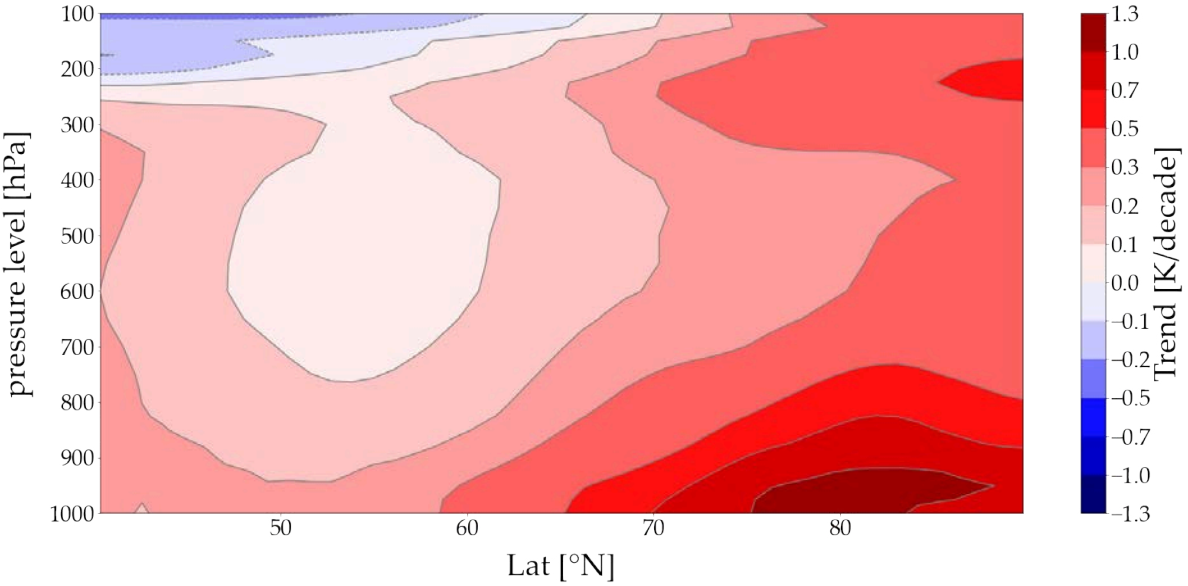

Figure 2.7: Vertical profile of linear trends of zonally monthly averaged ERA5 temperature data (1979-2018) for the extended winter season.

Figure 2.7 depicts observed linear trends of zonally averaged temperatures at different altitudes for DJFM. Although strongest at the surface level, the warming signal in high latitudes extents throughout the troposphere with a second apparent warming maximum near the tropopause. Nevertheless, climate models show evident deficiencies in simulating the structure of this vertical temperature response; in particular, they tend to exhibit large intermodel spreads (Ye et al., 2021) and produce mostly shallow and southward shifted warming signals (Cohen et al., 2020) . In contrast to high northern regions, the effect of Polar Amplification is only weakly present over Antarctica (see also Sec. 2.3.3). Largest warming signals have been detected in austral spring over regional warming hotspots such as the Antarctic Peninsula (Wang et al., 2021).

2.3.2 *Surface fluxes and energy balance in Arctic regions*

As already briefly mentioned in Sec. 2.1.1, fluxes between ocean/sea ice and the lower atmosphere are an important contribution to the overall atmospheric energy, momentum and water vapor budget—especially in Arctic regions (see also Taylor et al., 2018).

The energy exchange R_{tot} between the oceans, the cryosphere, land and the atmosphere in Arctic regions is governed by the surface energy budget that can be expressed as

$$R_{\text{tot}} = \underbrace{R_{\text{SW}\uparrow} + R_{\text{SW}\downarrow}}_{\text{shortwave flux}} + \underbrace{R_{\text{LW}\uparrow} + R_{\text{LW}\downarrow}}_{\text{longwave flux}} + \underbrace{\text{SH}}_{\text{sensible heat flux}} + \underbrace{\text{LH}}_{\text{latent heat flux}} \tag{2.13}$$

Thus, the overall surface energy budget can be additively decomposed into contributions from (upward ↑ and downward ↓) fluxes of shortwave and longwave radiation (R_{SW} and R_{LW}), as well as into contributions from turbulent sensible (SH) and latent (LH) heat fluxes.

In contrast to incoming shortwave radiation, incoming longwave radiation $R_{\mathrm{LW}\downarrow}$ is typically completely absorbed by the Earth's surface. The surface albedo α determines the fraction of reflected (contributing to $R_{\mathrm{SW}\uparrow}$), as well as the fraction 1-α of absorbed incoming shortwave radiation (contributing to $R_{\mathrm{SW}\downarrow}$). Whereas open ocean areas with an albedo of around 0.06 strongly absorb incoming shortwave radiation, snow covered and bare SI provide very reflective surfaces with high albedos up to 0.9 (Brandt et al., 2005). However, albedo over snow and ice surfaces depends on a variety of factors. For instance, very short visible wavelengths ($\lambda < 700\,\mathrm{nm}$) have higher albedo values compared to longer near-infrared wavelengths ($\lambda > 700\,\mathrm{nm}$). In addition, new ice has a relatively low albedo, which steadily increases as the ice gets thicker, but then rapidly jumps to very high values when even just a very thin snow layer covers the ice (Brandt et al., 2005).

The outgoing emitted thermal radiation from Earth's surfaces (that determines $R_{\mathrm{LW}\uparrow}$) can be approximated by the *Stefan–Boltzmann law*:

$$\Phi = \epsilon \sigma T^4 \tag{2.14}$$

where Φ is the emitted thermal energy per unit area and unit time, σ is the Stefan-Boltzmann constant ($5.67051 \cdot 10^{-8}\,\mathrm{Wm^{-2}K^{-4}}$), ϵ is emissivity ($\epsilon = 1$ for an ideal black radiator), and T is surface temperature.

Sensible heat fluxes (SH) refer to the turbulent fluxes of heat due to temperature differences between the surface and the lowermost atmospheric layer, whereas latent heat fluxes (LH) account for enthalpy gains/losses during the phase transition of water. When aiming to parameterize the turbulent sensible and latent heat fluxes at the atmosphere-ocean-sea ice interface, both fluxes are commonly treated in analogy to molecular diffusion. Thus, they are respectively assumed to be proportional to the temperature T and moisture q gradients between the surface ("surf") and the lowermost atmospheric layer ("air"). The respective bulk formulas are (e.g. Taylor et al., 2018)

$$\mathrm{SH} = \rho\, c_\mathrm{p}\, |\vec{v}_\mathrm{surf}|\, C_{\mathrm{H,k}} \cdot (T_\mathrm{surf,k} - T_\mathrm{air}) \tag{2.15}$$

$$\mathrm{LH} = \rho\, |\vec{v}_\mathrm{surf}|\, C_{\mathrm{E,k}}\, L_\mathrm{k} \cdot (q_\mathrm{surf,k} - q_\mathrm{air}), \tag{2.16}$$

where the index k represents water and SI surfaces. Here, ρ is air density, c_p is specific heat of air at constant pressure, $|\vec{v}_\mathrm{surf}|$ is the effective mean near-surface wind speed and L_k is the latent heat of evaporation over water (or of sublimation over ice). $C_{\mathrm{H,k}}$ ($C_{\mathrm{E,k}}$) describe the transfer coefficients of heat (moisture) over water and ice surfaces. They generally depend on surface properties and boundary layer conditions, and are therefore parameterized by a variety of existing turbulence parametrization schemes (e.g. Lüpkes et al., 2015).

Although Eqs. 2.15 and 2.16 imply that stronger near-surface winds strengthen turbulent surface fluxes, the sign and magnitude of the fluxes is usually governed by the respective near-surface temperature and humidity gradients (Taylor et al., 2018). In contrast to ice-covered areas, open-ocean surfaces are associated with stronger near-surface humidity gradients and therefore result in strong upward latent heat fluxes (see e.g. Taylor et al., 2018, Fig. 4). Strong upward-directed sensible heat fluxes are common over open-ocean in winter due to colder air temperatures and oceanic heat release, whereas in summer downward sensible heat fluxes with smaller magnitude occur when air temperatures tend to be warmer than the ocean. Sensible heat fluxes over ice are predominantly downward di-

rected, related to stable stratification, and have smaller magnitudes (see e.g. Taylor et al., 2018, Fig. 4).

In addition to surface-air heat exchanges in Arctic regions, the deposition of atmospheric momentum (Eq. 2.1) into the surface results in a slow down of near surface winds and is an important driver of Arctic SI drift. The momentum flux can be parameterized similar to 2.15 and 2.16, but depends on the near-surface wind speeds instead of humidity and temperature gradients. The transfer coefficients for momentum are determined by the general surface roughness, including the SI topography such as leads and ridges.

2.3.3 *Polar amplification mechanisms*

The phenomenon of AA is not exclusively observed in recent times. Analyses of historical and paleo data of the last three million years indicate enhanced Arctic warming relative to the global average even in such distant past periods (Miller et al., 2010). Nowadays, several local and remote feedback mechanisms that contribute to AA have been identified and studied extensively (e.g. Hahn et al., 2021; Pithan et al., 2014; Goosse et al., 2018). Nevertheless, quantifying and disentangling the individual contributions from different feedbacks to overall AA remains challenging. This issue mainly arises due to non-linear interactions between different feedback mechanisms and a lack of process understanding. Some local feedback mechanisms that are probably most relevant for AA are described and summarized below:

- Maybe the most prominent and one of the first-studied feedbacks is the positive *ice and snow albedo feedback*. Arctic SI retreat creates more open water areas with higher albedo values (see Sec. 2.3.2). This results in a stronger absorption of incoming radiation and consequently in an enhanced emission of longwave radiation. However, this mechanism is not working in winter due to the absence of incoming solar radiation.

- The negative *Planck feedback* is a consequence of the nonlinear Stefan Boltzmann law in 2.14 that relates the Earth surface temperature T to its emitted radiative energy Φ. Additional radiative forcing, e.g., induced by an enhanced greenhouse effect is balanced by a stronger temperature increase in polar regions[4], where background temperatures are colder compared to tropical regions.

- The *Lapse rate feedback* is related to the fact that Arctic regions are rather characterized by stable stratifications that suppress vertical mixing and trap surface warming in the lowermost atmosphere (positive feedback). As stable stratifications of the lower Arctic atmosphere are typically observed in winter, this feedback mechanism mostly operates in winter season. Contrary, tropical regions exhibit stronger vertical mixing induced by deep convective clouds. This leads to a relatively strong warming of the upper atmosphere and therefore increased outgoing longwave radiation to space (negative feedback).

- The positive *water vapor feedback* is associated with the enhanced moisture absorption of warmer air masses. Larger amounts of water vapor in a warmer atmosphere enhance the greenhouse effect and result in additional warming.

4 and consequently enhanced emitted longwave radiation

The sign and strength of cloud-related contributions from shortwave cooling and longwave warming feedback mechanisms still remain very uncertain, especially due to a lack of process understanding. Remote mechanisms such as changes in atmospheric heat and moisture transport convergences over Arctic regions have also been suggested to significantly contribute to AA (Hahn et al., 2021). Such changes in the atmospheric transport are directly related to different characteristics of the atmospheric large-scale circulation (see e.g. Secs. 2.1.3 and 2.1.4). Furthermore, changes in ocean heat uptake, but also altered oceanic currents and heat transport (Hahn et al., 2021; Pithan et al., 2014) may also contribute to AA.

A non-radiative feedback mechanism is e.g. given by the ice growth-thickness feedback (Goosse et al., 2018). As thinner ice tends to grow faster in thickness than thicker ice, SI melt is especially in summer season counteracted by increased SI growing rates in the upcoming winter months. Due to its insulating properties, snow is supposed to play an essential role in this respect, but a detailed understanding of the rather complex interplay between SI and snow properties is still lacking.

An assessment of the relative contributions from each of these feedback mechanisms to AA remains challenging. Year-round AA mostly arises from albedo, lapse rate and Planck feedbacks (Hahn et al., 2021; Stuecker et al., 2018; Pithan et al., 2014), whereas the water vapor feedback operates more effectively in tropical regions and therefore suppresses AA. The relatively weak Arctic summer warming compared to winter season might be a consequence of opposing mechanisms. In this respect, summer Arctic atmospheric warming caused by water vapor and albedo feedbacks is to a large extent offsetted by oceanic heat storage. The latter includes the latent heat of SI melt and the stronger oceanic absorption of incoming solar radiation due to more exposed open water areas. Subsequent oceanic heat release and an enhanced lapse rate feedback due to more stable Arctic stratification might be the main contributors to AA in winter (Hahn et al., 2021; Pithan et al., 2014). Although a study by e.g. Stuecker et al. (2018) argued that remote forcing mechanisms are probably of secondary importance for overall amplified Arctic warming, Hahn et al. (2021) showed that increased poleward moisture transports are an essential driver of AA. In addition, they found that such changes in the poleward moist atmospheric heat transport are probably the main contributor to projected warming over Antarctica.

The hemispherical asymmetry of Polar Amplification to e.g. recent greenhouse gas forcing has been attributed to a variety of factors. Especially the ice-albedo and lapse rate feedbacks have been shown to operate much weaker over Antarctica compared to Arctic regions (Hahn et al., 2021). Moreover, several studies highlighted the essential role of Antarctic surface elevation. Model experiments with a flat Antarctic orography showed indeed significant reductions of hemispherical differences in polar warming (Salzmann, 2017; Hahn et al., 2020). This was most likely a consequence of increased poleward atmospheric and oceanic heat transports, but also of a stronger operating lapse rate feedback for a flattened Antarctic orography.

It should be finally mentioned that recent Arctic climate change does not only have significant impacts on the local Arctic ecosystem. Moreover, it can also affect social-ecological systems in the Arctic, e.g., in terms of increased shipping activity (Meredith et al., 2019).

2.3.4 *Arctic-mid-latitude linkages*

The question if and to what extend recent Arctic climate change is able to affect weather and climate extremes over densely populated mid-latitudes became a growing and popular research topic over recent decades. Indeed, a variety of physical linkage mechanisms on how Arctic climate change and SI loss can effect atmospheric dynamics over mid-latitudes have been proposed (e.g. Cohen et al., 2018). Probably the most established mechanism in winter is associated with an intensification and northwestward shift of the Siberian high in response to SI loss over the Barents-Kara Sea BKS. This may lead to anomalously strong advection of cold Arctic air masses towards central Eurasia (Cohen et al., 2018). Some of the most widely discussed additional aspects and pathways will be summarized below; however, it should be noted that until now no overall consensus about the relevance and existence of specific mechanisms has been reached (Cohen et al., 2020).

Jet stream changes

A potential physical linkage can be derived from the geostrophic and the thermal wind equations (Eqs. 2.6 and 2.7). As enhanced Arctic warming decreases the meridional temperature gradient, it has been argued that such a decrease of atmospheric baroclinicity results in a weakening, stronger-meandering and an equatorward shift of the jet stream (Francis et al., 2012). A weakened and therefore less stable jet stream may tend to favor the formation of longwave Rossby waves with increased wave amplitudes. According to Equation 2.8 this may lead to a reduced phase speed of planetary waves and an increased probability of stationary weather patterns that may be linked to more frequent occurrences of extreme events. Although AA is surely able to impact certain jet stream characteristics (Barnes et al., 2015), it has been argued that such linkages can not statistically robust be detected in observational data. This is due to the fact that results are highly sensitive to the employed methodology and wave metric (Barnes, 2013; Screen et al., 2013). Even contradicting studies exist that provide evidence for a decrease of wave amplitude in response to a weaker meridional temperature gradient (Hassanzadeh et al., 2014).

Nevertheless, it should be noted that the decrease of baroclinicity and meridional temperature gradients associated with AA is predominantly confined to lower altitudes. Due to tropical upper tropospheric warming over recent decades (Allen et al., 2008) the meridional temperature gradient may even increase in higher altitudes. When arguing about mid-latitude circulation changes, this leads to a rather controversial situation (also termed "tug of war") that has been addressed in several previous studies (see e.g. Peings et al., 2019).

Time-delayed mechanisms

It has been suggested that the atmospheric autumn and winter circulation is affected by SI loss of the preceding summer/early autumn months in terms of a destabilized boundary layer, increased cloudiness, a weakened meridional pressure gradient and consequently a weakening of the polar jet stream (Francis et al., 2009). An atmospheric winter circulation response frequently found in reanalysis and model data resembles the negative NAO phase (e.g. Jaiser et al., 2012; Screen, 2017b; Nakamura et al., 2015; Deser et al., 2010). Such a negative NAO response may be associated with the aforementioned jet stream slowdown.

Nevertheless, detected signals generally vary between different models and some model analyses even suggest a positive NAO response (Screen et al., 2014).

When trying to understand the dynamical mechanisms that may contribute to such time-delayed circulation responses, pathways proceeding via the stratosphere might provide a potential explanation (Nakamura et al., 2015; Jaiser et al., 2016; Sun et al., 2015). In this respect, Nakamura et al. (2016) showed how the mid-latitudinal winter response is absent when suppressing stratospheric mean flow interactions in model simulations. The starting point of a physically consistent explanation for a stratospheric pathway can be found in studies that relate the additional diabatic heat source due to SI loss in late summer to a strengthened Scandinavian/Ural high, and an enhanced upward propagation of planetary waves in late fall/early winter (Honda et al., 2009; Kim et al., 2014; Jaiser et al., 2013). Evidence has been provided that especially the BKS and parts around the Beaufort and East Siberian sea play an essential role in this respect (Jaiser et al., 2016). This enhanced vertical wave propagation into the stratosphere subsequently might be able to weaken the stratospheric polar vortex in early winter, resulting in an overall temperature increase and a slowdown of zonal winds within the vortex. These induced stratospheric circulation changes afterwards propagate downward into the troposphere (Baldwin et al., 1999) and can lead to a negative NAO response in late winter.

Tailored model sensitivity experiments that isolated the impact of late summer SI loss in order to draw more causal inferences yielded conflicting results (e.g. Blackport et al., 2019; Sun et al., 2015). On the one hand, studies by e.g. Sun et al. (2015) compared early autumn versus year-round SI loss in model simulations and reported the existence of a negative NAO response in late winter via a stratospheric pathway. On the other hand, Blackport et al. (2019) employed a similar approach and suggested that correlations between late summer/autumn SI anomalies and the winter circulation merely arise due to persistence of these anomalies into winter time. In order to overcome the issue of common drivers and indirect links between different variables in observational data Kretschmer et al. (2016) utilized a causal effect network. They provided additional evidence about the existence of a stratospheric pathway and emphasized the essential role of SI in the BKS. Consistent with the usually weak signal-to-noise ratio of atmospheric responses to SI loss, Siew et al. (2020) recently highlighted the potential intermittent and state-dependent character of such a stratospheric pathway.

Additional latent heat and oceanic moisture releases during low SI phases have shown to be linked to increased snowfall over mid-latitudes (Liu et al., 2012). Especially SI loss in the BKS has been proposed to act as an important moisture source that enhances autumn snow depth over Russia (Wegmann et al., 2015). In this context, Cohen et al. (2007) and several ensuing studies (e.g. Handorf et al., 2015; Wegmann et al., 2020; Gastineau et al., 2017) reported a linkage between Eurasian snow cover in October/November and a negative NAO circulation response in winter. Above average Eurasian snow cover in autumn was supposed to strengthen the development of the Siberian High. This subsequently results in anomalously high time-delayed wave activity and heat fluxes into the stratosphere and therefore engages into the aforementioned stratospheric pathway (Cohen et al., 2014a; Cohen et al., 2007). However, the existence of such a snow cover induced causality chain is still under debate, as model experiments struggle to reproduce the signals found in observational data (Henderson et al., 2018).

Potential reasons for discrepancies

Studies about the topic of Arctic-mid-latitude linkages frequently report divergent results that are in general argued to be a consequence of high internal atmospheric variability and therefore low signal-to-noise ratios (Ye et al., 2021). As briefly addressed above, investigations of observational data usually lack distinct causal inferences due to correlation-related issues with indirect links or common drivers (Kretschmer et al., 2016).

Furthermore, even specifically designed model sensitivity experiments may suffer from a variety of issues. Such model experiments are usually performed in an atmosphere-only setup with different prescribed SI loss patterns, SI thicknesses as well as for instance different Sea Surface Temperature SST background states (e.g. Smith et al., 2017). Although some models have shown to reproduce vertical planetary wave propagation responses to SI loss that were found when comparing recent periods of low and high Arctic SI conditions (Jaiser et al., 2016), other studies revealed discrepancies in this regard. Therefore, it was suggested that lacking SI-induced atmospheric responses in model simulations are at least partly a consequence of deficits in simulating planetary wave propagation characteristics (Handorf et al., 2015).

Furthermore, several contemporary studies (He et al., 2020; Labe et al., 2020; Xu et al., 2019; Sellevold et al., 2016) showed that despite an absence of mid-latitudinal responses to Arctic surface warming or SI retreat, deep Arctic warming may be a key feature of AA that potentially triggers responses in mid-latitudes . Characterized by temperature anomalies that extend into the upper troposphere, deep Arctic warming has been linked to an intensification of the Siberian high (Labe et al., 2020; Xu et al., 2019) and a stationary wave response (Sellevold et al., 2016). As models tend to show deficiencies in simulating AA's vertical structure (Ye et al., 2021) this may provide a potential explanation for divergent research results.

Such shortcomings might stem from a variety of different issues (Screen et al., 2018): oversimplified parameterizations of relevant model physics, including for instance processes related to clouds (Taylor et al., 2019), boundary layer turbulence parameterizations (e.g. Lüpkes et al., 2015) or gravity waves (Köhler et al., 2021), as well as insufficient representations of stratospheric processes (Sun et al., 2015) and stratospheric ozone chemistry (Romanowsky et al., 2019). In addition, inconsistencies between different modeling studies can arise due to different experimental setups and boundary forcings. Hence, coordinated experimental protocols such as the Polar Amplification Intercomparison Project protocol (Smith et al., 2019) were created in order to overcome this issue.

As many modeling studies utilize atmosphere-only experiments, the importance of a coupled interactive ocean model has also been stressed (Screen et al., 2018). Full ocean-atmosphere coupling may allow for representing additional oceanic pathways, such as altered ocean currents, and have shown to amplify circulation responses to Arctic SI loss (Deser et al., 2015). However, a recent study by England et al. (2022) shows that different approaches that impose SI perturbations in a coupled model setup add artificial heat to the Arctic region. This causes a spurious warming signal that is added to the warming expected from SI loss alone, and therefore finally results in an overestimation of the climate response to SI retreat in coupled model setups.

Summer season

The overwhelming majority of studies that address linkages between Arctic and the mid-latitudes focuses on winter season. Only a relatively small number of studies investigates the Arctic's impact on the mid-latitudinal summer circulation, where the polar vortex is quasi non-existent and circulation is generally weaker compared to winter. Some plausible hypothetical pathways for boreal summer season have been summarized by e.g. Coumou et al. (2018). Although located at different latitudes compared to winter season, it can be argued that decreased meridional temperature gradients in summer can, on the one hand, lead to a slowdown of zonal winds. On the other hand, the reduced baroclinicity may result in weakened storm tracks. Indeed, studies reported a recent decrease in summer eddy kinetic energy over the NH that could be linked to AA (Coumou et al., 2015).

In addition, AA might be able to favor the occurrence of double jet configurations (Coumou et al., 2014; Hoskins et al., 2015). Such double jet configurations have shown to be closely tied to quasi-resonant amplification events (Petoukhov et al., 2013; Coumou et al., 2014; Kornhuber et al., 2017). Such events are associated with more persistent weather patterns and consequently may promote the occurrence of extreme events (see also Sec. 2.4.2).

2.4 WEATHER AND CLIMATE EXTREMES

Climate extremes pose a great danger to modern-day society. For instance, the Russian heat wave in 2010 did not only cause more than 50000 additional deaths, but was also accompanied by crop failure of around 25% relative to previous years and large numbers of wildfires and burnt areas (Barriopedro et al., 2011). The 2003 heat wave over Central Europe resulted in 15000 excess deaths only in France (Fouillet et al., 2006). In 2018, around 22% of densely populated and cultivated areas in Scandinavia and Central Europe experienced concurrent heat waves from May to July (Vogel et al., 2019). In combination with exceptional drought conditions this did not only result in a 50% reduction of crop yields (Toreti et al., 2019), but also in unprecedented forest mortality events (Senf et al., 2021). Winter cold spells like over Europe in 2010 or the more recent cold outbreak over North America in 2021 (Bolinger et al., 2022) can also result in higher mortality rates (Díaz et al., 2005), and are able to significantly stress the energy sector (Savić et al., 2014; Añel et al., 2017). In this respect, winter warm spells can also have a significant impact on agriculture, soil biochemistry and on ecosystems via changed freeze-thaw cycles (e.g. Grimm et al., 2013).

Aside from extreme events that are related to unprecedented temperature anomalies, wind storms and heavy precipitation events can also result in severe impacts. For instance, the recent flood event in July 2021 in western Germany and parts of Belgium and the Netherlands was a consequence of locally heavy rainfall events. River catchments like the Ahr catchment in the Eifel recorded around 115 mm of precipitation within 3 days (Junghänel et al., 2021). In combination with already saturated water storage capacities of the local soils and narrow river valleys, the resulting torrents caused severe devastations of local towns and killed more than 100 people. In January 2007, storm Kyrill raged over Europe and led to massive destructions of transport infrastructure, blew down around 75 million trees and caused only in German insured losses of 2.4 billion Euros (Deutsche-Rück, 2008).

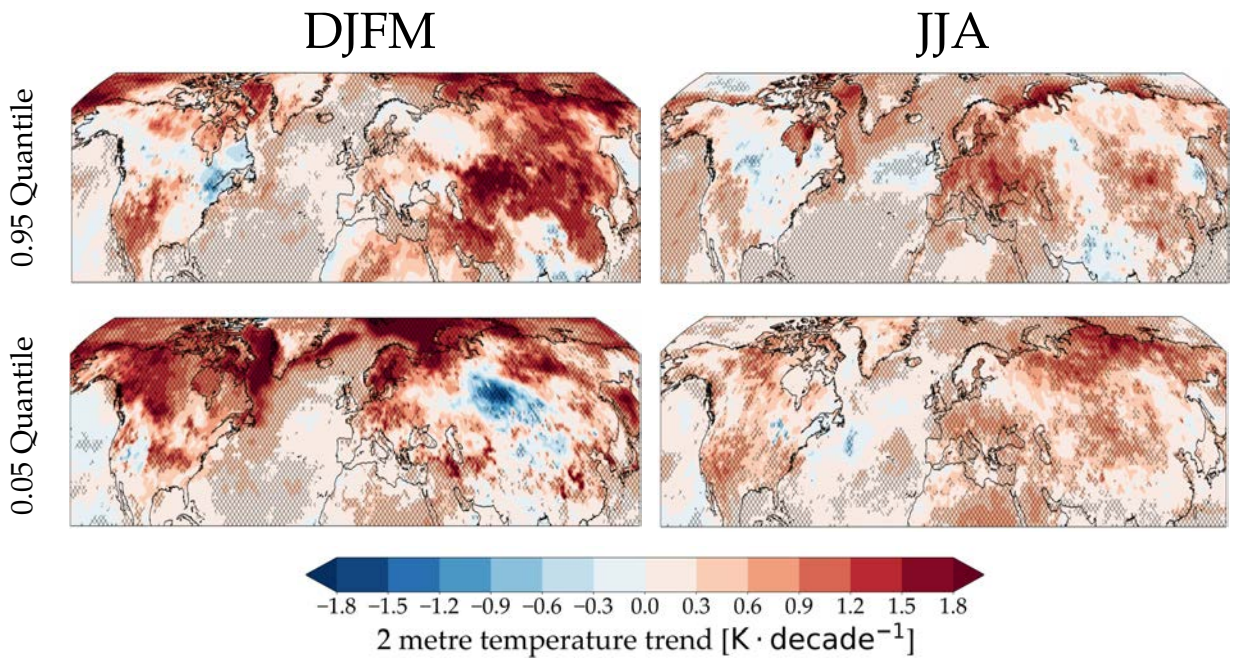

Figure 2.8: Linear time trends of the 0.95 (0.05) quantiles of weekly-averaged ERA5 daily maximum (minimum) 2-meter temperatures over the period 1979–2018. The plots show the extended winter, as well as summer season and trends of the quantiles were calculated with quantile regression (Koenker et al., 1978). Trends in the 0.95 temperature quantile are associated with recent trends in the intensity of heat/warm extremes, while trends in the 0.05 temperature quantile are associated with trends in the intensity of cold extremes. Hatchings indicate regions where the 95% confidence interval of the regressed trends do not include a zero trend.

Indeed, several of the aforementioned examples included a variety factors (e.g. concurrent heat wave and drought conditions or storm and heavy precipitation) that resulted in severe impacts. In this respect, the term compound event considers the multivariate character of extreme events and was defined by e.g. Zscheischler et al. (2018) as "the combination of multiple drivers and/or hazards that contributes to societal or environmental risk". Thus, the dependence structure of the different contributing components has to be taken into account (e.g. negative correlation between warm temperatures and precipitation), as an independent perspective would highly underestimate the risk of high impacts. The upcoming Section starts to review recent trends in temperature (winter and summer) and wind extremes. As the present thesis focuses on temperature extremes, the most relevant dynamical drivers of temperature extremes in summer and winter season are subsequently described.

2.4.1 *Recent trends*

Temperature extremes

The latest sixth assessment report of the IPCC (Arias et al., 2021) assessed that over mostly all parts of the world there is at least medium confidence that the overall frequency and severity of hot extremes increased since the 1950s. For most of these regions there is

medium to high confidence that human activities significantly contributed to the respective regional trends. Exceptions are the Central and Eastern US, were no agreement on the type of change was found. For cold extremes it has been reported as virtually certain that due to human activities the frequency and severity of cold spells over most land areas decreased since 1950. In addition, this trend will most likely continue until the end of the century.

However, the detailed picture typically appears to be more complicated and can depend on a variety of factors, such as season, time period and spatial scales. This is also apparent in Fig. 2.8, which shows recent linear time trends of the 0.95 (0.05) quantiles of weekly averaged ERA5 maximum (minimum) 2-meter temperatures for summer and the extended winter season. The overall trend towards more (less) severe warm (cold) weeks is observed over most parts of the NH, but is especially pronounced in winter season and over higher latitudes (see Sec. 2.3.1). The magnitudes of more regional warming trends depend on the type of extreme (warm or cold), season (summer or winter) and vary between different regions. An outstanding feature is the recent trend towards more severe cold spells over Central Eurasia (see also Horton et al., 2015; Cohen et al., 2014b), which may be considered as a contradiction to the aforementioned general warming trend.

When focusing on the European region, Fig. 2.8 suggests an overall warming of heat extremes in summer, as well as a warming of winter cold spells especially over Central and Northern Europe. In this context, a study by Lorenz et al. (2019) demonstrated that on average the number of days with extreme heat has more than tripled across Europe over the last 70 years. This was accompanied by an average warming of such heat days by more than 2°C. Indeed, they showed that this increase in heat extreme occurrences was consistent across different European subregions. Another recent study by Sulikowska et al. (2021) also found overall increasing trends in the occurrence frequency, severity and spatial range of extreme warm temperature events over different European regions. They noticed the most pronounced changes over Central and Eastern Europe in summer. However, they additionally highlighted the regional and seasonal differences in the rate of these changes in warm extremes. Consistent with the increased number of warm days, Lorenz et al. (2019) showed that across Europe the averaged number of cold days has decreased from 1950–2018 by a factor of 2–3. At the same time, European cold extremes warmed on average by more than 3°C, and especially over Northern and Central Europe this warming trend was considerably larger than the local mean temperature warming.

Wind extremes

Changes in the occurrence frequency and severity of wind extremes over continental regions have for sure not received similar attention as temperature extremes. Nevertheless, a study by Kumar et al. (2015) evaluated the performance of CMIP5 models in simulating observed trends in extreme continental surface winds over the period 1979–2005. Around the globe they found a spatially heterogeneous trend pattern in the magnitude of annual wind maxima and observed significant trends only over some few regions. Another study by Vautard et al. (2010) analyzed station data and reported a decrease in the magnitude of the mean, but especially of strong near-surface wind speeds over most parts of the continental NH. They showed that reanalysis data explain only between 10–50% of the observed surface wind slowdown. They argued that this fraction is related to a recent weakening

of the general atmospheric circulation, captured by the reanalysis (e.g. due to AA, see Sec. 2.3.4). By analyzing additional model simulations they suggested that the remaining fraction of wind slowdown, which is not captured by the reanalysis, is a result of the recent increase in surface roughness, e.g. due to increases in biomass and land-use.

2.4.2 *Dynamical driver of temperature extremes*

The underlying physical and dynamical mechanisms that lead to the occurrence of temperature extremes generally differ between warm and cold extremes, but also depend on whether they occur in summer or winter season.

Summer heat waves

Pfahl et al. (2012) showed that in contrast to winter cold extremes the majority of summer heat extremes north of 45°N co-occur with atmospheric blocking (see Section 2.1.3). Especially over Scandinavia such blocking situations are commonly associated with omega-like blocking structures, whereas heatwaves over Southern Europe typically co-occur with flat subtropical ridges (see e.g. Zschenderlein et al., 2019, Fig. 5). For a recent comprehensive review about blocking and extremes over the Euro-Atlantic region see Kautz et al. (2022).

Lagrangian backward trajectory analysis by e.g. Zschenderlein et al. (2019) and Bieli et al. (2015) showed that horizontal temperature advection plays a minor role for the formation of heatwaves. Actually, the local subsidence of air masses and the associated adiabatic heating, as well as diabatic heating by upward surface sensible heat fluxes are the dominant processes for creating high surface temperatures in summer. Surface sensible heat fluxes are typically raised as a consequence of increased incoming solar radiation under clear-sky conditions, but also when surface cooling via evapotranspiration is lacking due to depleted soil moisture (Alexander, 2010).

In addition, heat extremes might be potentially linked to a weakening of the jet stream and the associated slowdown and increased persistence of Rossby waves (e.g. Francis et al., 2012). However, their occurrence has also been hypothesized to be a result of a mechanism termed quasi-resonant amplification (Petoukhov et al., 2013; Coumou et al., 2014; Kornhuber et al., 2017). When the energy of quasi-stationary free Rossby waves is trapped in a mid-latitude waveguide and when the external forcing pattern is close to that of the free Rossby wave, then, the forced quasi-stationary component of waves 6–8 may be amplified due to resonance. It has been shown that wave guide conditions can be associated with double jet configurations (e.g. Kornhuber et al., 2017). Such double jet structures are usually characterized by two distinct peaks in the zonally averaged zonal wind profile at around 40°N and 70°N, respectively.

Over many continental regions that are affected by stormtracks (e.g. Europe or North America), studies by Lehmann et al. (2015) or Coumou et al. (2015) showed that summer heat extremes over these regions are usually linked to reduced synoptic-scale or baroclinic activity. Weakened synoptic-scale activity is typically related to low atmospheric variability on 2–6 day timescales; therefore, it can be linked to preferred occurrences of persistent weather patterns that may promote the occurrence of heat extremes.

Winter temperature extremes

In contrast to heat extremes in summer, cold and warm events in winter are typically not co-located with atmospheric blocking. For Europe, several studies indeed showed that cold extremes are associated with advective processes of cold air masses from remote northern or eastern-continental regions. Indeed, a lagrangian backward trajectory analysis by Bieli et al. (2015) demonstrated that cold extremes over Central Europe and the Balkans are typically a result of cold air advection from Scandinavia, the Barents Sea and Western Russia. This anomalous northeasterly and easterly advection of cold air masses has been linked to a blocking anticyclone over Scandinavia and Ural regions (e.g. Vihma et al., 2020; Andrade et al., 2012; Petoukhov et al., 2010). Cold events over the United Kingdom are also commonly a consequence of cold air advection from Western Russia, but also from Fram Strait regions. The transport the target regions is typically accompanied by a steady and mostly adiabatic descent of air masses. However, the maritime advection branch of UK colds spells that originates in the Fram Strait is also characterized by diabatic heating. This diabatic heating is a consequence of ocean-to-atmosphere sensible heat fluxes during the last days prior to the event.

Pronounced positive states of the NAO in winter are typically associated with a stronger westerly transport of relatively warm and moist Atlantic air masses. The resulting convergence of latent heat transport over Northern Europe (Vihma et al., 2020) favors anomalously warm temperatures over the same region. As a consequence of the weakened zonal flow, anomalously strong negative winter NAO events frequently result in cold spells or negative temperature anomalies over Mid-to Northern Europe (e.g. Vihma et al., 2020; Rust et al., 2015; Andrade et al., 2012; Cattiaux et al., 2010). Sillmann et al. (2011) also found a statistical relationship between blocking over the North Atlantic and more extreme 2 meter temperatures over large parts of Europe in winter.

3 DATA AND METHODS

The upcoming Chapter describes the datasets that are used for the analyses in this thesis. Section 3.1 first introduces the *ERA5* reanalysis. ERA5 is an assimilation product that combines observational with forecast data and represents a "real-world" dataset over the last four decades. Afterwards, Section 3.2 describes the atmospheric model ECHAM6 and the respective experimental setups that are analyzed in this thesis .

3.1 ERA5 REANALYSIS

For several parts of the analyses data from the ERA5 reanalysis project are used (Hersbach et al., 2020). ERA5 is a global atmospheric reanalysis dataset provided by the ECMWF and is the successor of the ERA-Interim product. The time period of the ERA5 dataset starts in 1979 and is updated to real time (a back extension starting in 1950 has recently become available). The reanalysis is produced based on a 2016 release (Cy41r2) of the ECMWF Integrated Forecasting System IFS. The IFS includes a forecast model with fully coupled components for the atmosphere, land surface and ocean waves. Compared to the IFS version used for the ERA-Interim product, several improvements in representing physical processes have been incorporated. Such improvements range from modifications in the radiation and cloud parametrization schemes to the introduction of a new soil texture map and an updated model bathymetry. As an additional core element the ERA5 IFS version uses a 4D-Var (4-Dimensional Variational analysis) assimilation scheme with a 12 hourly analysis cycle. During each cycle, available *in-situ* observations and measurements are combined with a previously generated first-guess of the atmospheric state from the forecast model. This assimilation procedure finally provides an estimate of the actual global atmospheric state with an hourly output frequency for all variables. For the first time uncertainty estimates are provided for the final output fields based on the spread among nine perturbed ensemble members. A huge amount of observational data are assimilated each day, ranging from 0.75 million in 1979 to around 24 million in 2019. These observation originate for instance from a large variety of over 200 satellite instruments like polar-orbiting and geostationary imagers and sounders, many ground-based *in-situ* measurements of near-surface variables such as wind, humidity and pressure, as well as radiosonde and aircraft measurements of upper-air wind, temperature and humidity.

The ERA5 IFS version operates on 137 vertical levels from the surface up to 1 Pa with a spectral resolution of T639 (see also Sec. 3.2.1). This results in a final horizontal resolution of around 31 km on the corresponding N320 reduced Gaussian grid.

Variables

For the analyses in this thesis a variety of daily ERA5 variables over the time period 1979–2018 are used: sea level pressure SLP, geopotential height of the 500 Pa pressure level gph500, 2 meter temperature T2m, daily minimum/maximum 2 meter temperature T2min/T2max, near-surface wind speed and zonal wind speed at 850 hPa. All variables were initially regridded to a regular lat-lon grid with 1.125° resolution. SLP and gph500 fields for

the regime and analogue computation in Secs. 4.2 and 4.6 were finally regridded to a 100×100 km Equal-Area Scalable Earth Grid *EASE-Grid 2.0* (see Brodzik et al., 2012).

Furthermore, the SI fields used in the ERA5 product are used. The SI (but also SST) fields in ERA5 are externally provided and prescribed as lower boundary conditions. They are consequently not directly calculated by the IFS. For the time period 1979–2018, SI data from the EUMETSAT Ocean and Sea Ice Satellite Applications Facility (OSI-SAF) are used in ERA5.

3.2 MODEL EXPERIMENTS

For the analysis in this thesis data from the Atmospheric General Circulation Model (AGCM) ECHAM6 are investigated. In order to isolate the impact of Arctic SI changes on atmospheric dynamics and extreme events, atmosphere-only sea ice sensitivity experiments from the Polar Amplification Intercomparison Project (PAMIP) are used. These sensitivity experiments basically follow the protocol of the Atmospheric Model Intercomparison Project AMIP and are forced under different SI and SST boundary conditions, representing present day and future SST and Arctic SI states. Nevertheless, other forcings like greenhouse gas or ozone concentrations are kept constant for all experiments.

Section 3.2.1 initially highlights some essential features of the ECHAM6 model. In Sec. 3.2.2, the simulation setup and the prescribed forcing conditions of the analyzed sensitivity experiments from PAMIP are finally explained.

3.2.1 *The atmospheric general circulation model ECHAM6*

ECHAM6 is the latest version of a global AGCM that was developed at the Max-Planck-Institute for meteorology in Hamburg and whose dynamical core is based on a global forecast model from ECMWF (Stevens et al., 2013). Since the late 1980s, the original model version was continuously improved, mostly by incorporating a huge variety of more sophisticated parameterization schemes. As an atmospheric component ECHAM6 is nowadays integrated into fully coupled Earth System Models, such as the AWI Climate Model *AWI-CM* and the *MPI-ESM* from the Max-Planck-Institute for meteorology.

The dynamical core of ECHAM6 is, as usual for AGCMs, governed by the primitive equations already outlined in Section 2.1.1. However, ECHAM6 transforms these basic equation into a spectral representation (Machenhauer, 1979). This is done by expressing the global fields of the basic prognostic variables as a truncated time series of spherical harmonics. This is typically achieved by a Fast Fourier Transformation in zonal direction followed by a Legendre transform in meridional direction. Although these forward and the respective backward transforms require additional computational costs at each time step, a main advantage of the spectral representation is that the spatial derivatives of variables can be calculated analytically and do not have to be discretized. The vertical discretization scheme is specified by a hybrid σ-pressure coordinate system reaching up to 0.01 hPa or roughly 80 km altitude. This ensures a terrain-following vertical coordinate system in lower tropospheric regions that smoothly transitions into pure pressure levels at higher altitudes.

Different configuration setups in terms of model resolution are generally available for ECHAM6. The model simulations used in this thesis have been conducted with the latest

release ECHAM6.3 in a high resolution setup T127/L95. Here, T127 represents the spectral truncation number, which corresponds to a horizontal resolution of around 0.94°. This results in a zonal spacing of grid points of around 100 km in the tropics, and a higher resolution in zonal direction toward the poles—for instance about 25 km at 75°N. L95 denotes a vertical resolution of 95 unevenly spaced model levels with a finer vertical resolution in the atmospheric boundary layer near the surface. The model's integration time step is set to 200 s. For more details on e.g. specific parameterizations or the implementation of the governing equations see Giorgetta et al. (2013).

3.2.2 *Polar Amplification Intercomparison Project data*

In this thesis different ECHAM6 experiments from the PAMIP are analyzed (Smith et al., 2019). The PAMIP protocol seeks to advance the understanding of the impact and relative roles of Arctic SI and SST changes on the global climate system. For this reason, each respective sensitivity experiment includes 100 ensemble members of one-year-long atmosphere-only time slice simulations that are forced under different annual cycles of SIC, but also SST boundary conditions. For a brief outline on how fluxes and surface temperatures over SI and ocean surfaces are computed in an ECHAM6 atmosphere-only setup see Sec. B.6.3.

Initial conditions of each ensemble member are based on AMIP simulations for 1st April 2000. Each ensemble member was run for 14 months, but the first two months were finally excluded for model spin up reasons. Greenhouse gas forcings for all experiments are constantly set to present day conditions of the year 2000. In order to study the impact of future SI changes on the large-scale atmospheric circulation and extremes the following experiments are considered:

- present day SST and present day SI conditions (pdSST/pdSI, PAMIP setup 1.1)
- present day SST and future/reduced Arctic-wide SI conditions (futArcSI, PAMIP setup 1.6)
- present day SST and future/reduced SI in the BKS region 65-85°N, 10-110°E (futBKSI, PAMIP setup 3.2).

In order to contrast the importance of future changes in global SSTs to future Arctic SI changes a sensitivity simulation forced under

- present day SI and globally raised future SST conditions (futSST, PAMIP setup 1.4)

is also considered. The pdSST/pdSI simulation serves in a first place as a reference simulation to which the sensitivity simulations futArcSI, futBKSI and futSST are compared to.

Present day forcing fields are obtained from the climatologies of observations from the Hadley Centre sea ice and Sea Surface Temperature dataset over the period 1979–2008 (Rayner et al., 2003). Future conditions are derived from RCP8.5 multimodel simulations for a 1.43 (2)°C warming scenario over present day (preindustrial) conditions. At grid points where SI has been removed under future conditions, the present day SSTs are replaced by future SSTs if the difference in SIC between future and present day is greater than 10 %. Comparisons of JJA, DJFM and September SI and SST forcing fields of present day and the sea ice sensitivity simulations are shown in Fig. 3.1. In winter, future SI conditions are predominantly reduced over the BKS, the Sea of Okhotsk, the Bering Sea, east of

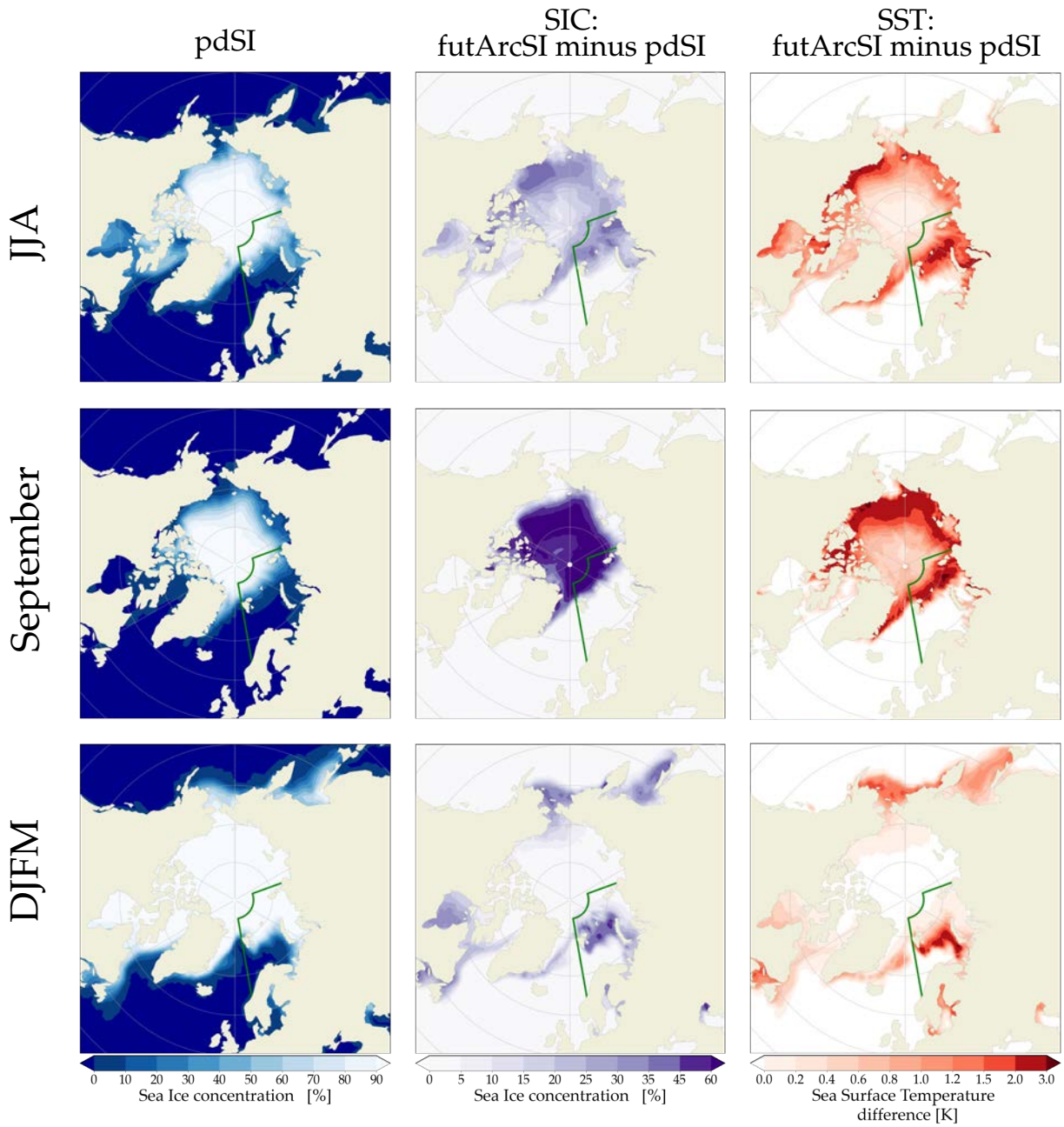

Figure 3.1: Illustration of PAMIP present day SIC mean fields (left), as well as differences in SIC (middle) and SST (right) between the futArcSI and pdSST/pdSI experiments. Upper row for JJA, middle row for September and bottom row for DJFM. The area confined by the green line indicates the region where SIC and SST fields are adapted in the futBKSI experiment.

Greenland and along the east coast of North America. The respective substituted SST forcing fields are increased by less than 1°C over most areas where SIC was lowered more than 10%, but by also more than 2°C over parts of the BKS. Summer conditions are characterized by SI reductions and ice-free areas over central Arctic regions. Here, SSTs especially over marginal SI areas are increased by more than 1.5°C. Strongest SI reductions and SST substitutions can be found in September. The globally increased SSTs in the futSST experiment are illustrated in Fig. B.14.

Variables

For the analysis presented in this thesis nearly the same daily variables from the model simulations are used as for ERA5: SLP, gph500, T2m, T2min, T2max, near-surface wind speed, and zonal and meridional wind speed at 850 hPa. All variables were provided on a regular lat-lon grid of 0.9375° resolution. SLP and gph500 fields were again regridded to a 100×100 km equal-area grid for the regime and analogue computation in Secs. 4.2 and 4.6.

3.3 METHODS

The employed methods are briefly motivated in the beginning of each result section and are more extensively described in the respective sections in Appendix A. Here, the general bootstrapping approach is described, that is used to report statistical significance for the majority of the presented results. Additionally, the definition of temperature and wind extreme event occurrences in the PAMIP experiments is explained.

3.3.1 *Statistical significance*

In this thesis, uncertainty and significance estimates are mostly reported with 90 percent confidence intervals based on the 0.05 and 0.95 quantiles of bootstrapped distributions of the statistic of interest. If the computed confidence intervals do not include unity (for ratios) or a zero value (for differences), the signal is termed significant. Daily temperature, wind and SI times series, but also daily nominal time series of circulation regime allocations are used throughout the analysis. These time series typically exhibit significant temporal dependencies over several days. In order to preserve the temporal structure of the original daily time series during the resampling procedure a moving block bootstrap is used (Kunsch, 1989).

An original time series x_n of length n is therefore divided into overlapping blocks of size k, where the first block contains $x_1, ..., x_k$ and the second block $x_2, ..., x_{k+1}$ etc. . Afterwards, a bootstrapped sample time series is created by concatenating randomly picked blocks to a new time series of original length n. Afterwards, the statistic of interest (e.g. cluster frequency, extreme occurrence ratios etc.) is computed for this generated bootstrapped sample time series. When employing this procedure for statistics that are computed from multiple variables (Secs. 4.2.2, 4.5 and 4.6), the different time series[1] are blocked and resampled pairwise. This procedure is repeated M times, yielding a bootstrapped prob-

1 of e.g. daily temperature and cluster allocations

ability distribution for the respective statistic of interest. The block length k is always set to 5 days in order to account for the typical persistence time of atmospheric circulation regimes and analogues, but also for the autocorrelation of temperatures, wind and SI time series.

3.3.2 *Extreme definition*

In this thesis warm and cold extreme events are defined as exceedances (or drops below) of a threshold temperature T_{ref}. Thus, if a daily T2max (T2min) value exceeds (falls below) the temperature threshold T_{ref}, the respective day represents a warm (cold) extreme event. In the same way, wind extremes are defined as exceedances of a near-surface wind speed threshold $|\vec{v}_{\text{ref}}|$.

The threshold temperature T_{ref} of warm (cold) extreme events at some grid point is computed for each month separately as the 0.95 (0.05) quantile of the respective underlying daily T2max (T2min) distribution in pdSST/pdSI. Similar, the wind speed threshold $|\vec{v}_{\text{ref}}|$ at each grid point is calculated for each month separately as the 0.95 quantile of the underlying daily near-surface wind speed distribution in pdSST/pdSI.

4 RESULTS AND DISCUSSION

This Chapter presents and discusses results that aim to answer the different **RQ**s stated in the introduction. Section 4.1 initially assesses what biases in near-surface variables can be found in the pdSST/pdSI reference simulation with respect to ERA5. In addition, the climatological mean states of near-surface fields in the different PAMIP sensitivity experiments are compared with the pdSST/pdSI reference simulation. Afterwards, Sec. 4.2 will start to address **RQ1**. Therefore, winter and summer circulation regimes computed from ERA5 reanalysis and ECHAM6 PAMIP experiments are presented and compared. Subsequently, recent changes in ERA5 regime occurrence frequencies are studied with a focus on the impact of recent SI decline. It is afterwards analyzed how regime occurrence frequencies are affected by future SI loss prescribed in the different PAMIP sensitivity experiments. Section 4.3 will then study what overall frequency changes in temperature extreme occurrences can be expected under future Arctic SI loss in the sea ice sensitivity experiments. This analysis aims to address **RQ2** and will be extended by an investigation of changes in temperature return levels computed from different sensitivity experiments, allowing to assess the sea ice-related impact on very rare temperature extreme events. Afterwards, Sec. 4.4 will identify suitable regime storylines for summer and winter temperature extremes over the European domain. For this reason, it is investigated which of the computed circulation regimes can be linked to preferred occurrences of temperature extremes over Europe. Based on the detected regime frequency changes in Sec. 4.2 and the previously identified storylines, Sec. 4.5 will address **RQ3** and will decompose the detected changes in winter extreme occurrence frequencies into thermodynamically and dynamically induced contributions. As the summer circulation regimes are less suitable storylines for the occurrence of summer heat extremes, Sec. 4.6 employs an approach that identifies circulation analogues of distinct blocking structures over Europe. Based on changes in analogue occurrence frequencies this finally allows to decompose changes in summer heat extreme occurrences into thermodynamically and dynamically induced contributions. Therefore, Sec. 4.6 will contribute to address in particular **RQ1** and **RQ3**.

In order to assess the importance of future Arctic SI loss relative to more global facets of future warming, the analysis is for the most part complemented by an investigation of the futSST experiment. Parts of the upcoming results[1] are also published and discussed in Riebold et al. (2023).

4.1 MEAN CIRCULATION IN ERA5 AND ECHAM6 EXPERIMENTS

This Section initially compares the climatological mean states of the extended winter and summer season between the pdSST/pdSI reference simulation and ERA5. In this way, it can be initially assessed to what extent the pdSST/pdSI reference simulation represents present day conditions over the last decades. In particular, SLP, T2m and zonal wind speed at 850 hPa u850 are considered, as such "near-surface" variables are used for large parts of the upcoming analysis. Afterwards, the mean response of these variables in the differ-

1 including Figs. 4.5, 4.6 and 4.12; Fig. 4.15; Fig. 4.23; Figs. 4.25–4.29; Figs. B.7 and B.8

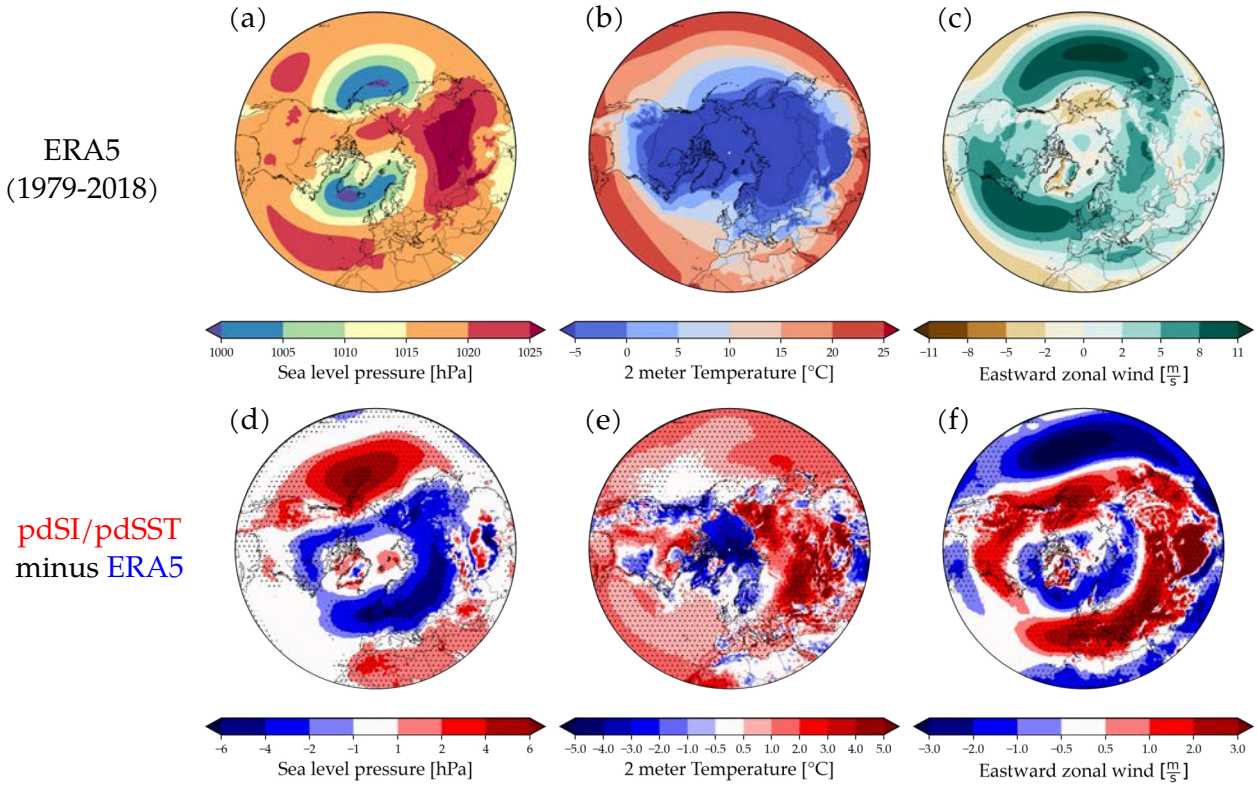

Figure 4.1: Upper row: ERA5 climatological means of monthly-averaged daily a) SLP, b) T2m and c) u850 fields for the extended winter season (DJFM) over the period 1979–2018. Bottom row: Climatological differences of monthly-averaged d) SLP, e) T2m and f) u850 between the pdSST/pdSI reference experiment and ERA5. ERA5 data were regridded to the model resolution. Stippling indicates statistical significance at the 99% level according to a two-sided student's t-test.

ent PAMIP sensitivity experiments with respect to pdSST/pdSI are evaluated, again for the extended winter and summer season.

4.1.1 *Climatological mean states in ERA5 and the reference simulation*

Winter

Figures 4.1a–c show the ERA5 climatological winter means of SLP, T2m and u850 over the period 1979–2018. Familiar structures can be noted such as the Aleutian low, the North Atlantic storm track, the Siberian high or the North Pacific and North Atlantic jet stream. Compared to ERA5, the ECHAM6 pdSST/pdSI experiment exhibits significant biases in winter (see Figs. 4.1d–f). Consistent with the comparison of ECHAM6 AMIP style experiments and ERA-Interim by Stevens et al. (2013), a weakening of the Aleutian low and decreased SLPs over Mid-to Northern Eurasia can be detected in pdSST/pdSI (Fig. 4.1d). Compared to ERA5, near-surface temperatures in the model simulations are highly underestimated over Arctic Ocean areas, while they are mostly overestimated over mid-latitudinal and continental regions (Fig. 4.1e). Nevertheless, as ERA5 overestimates near-surface temperatures over Arctic SI in winter (e.g. Graham et al., 2019), the model simulation should be

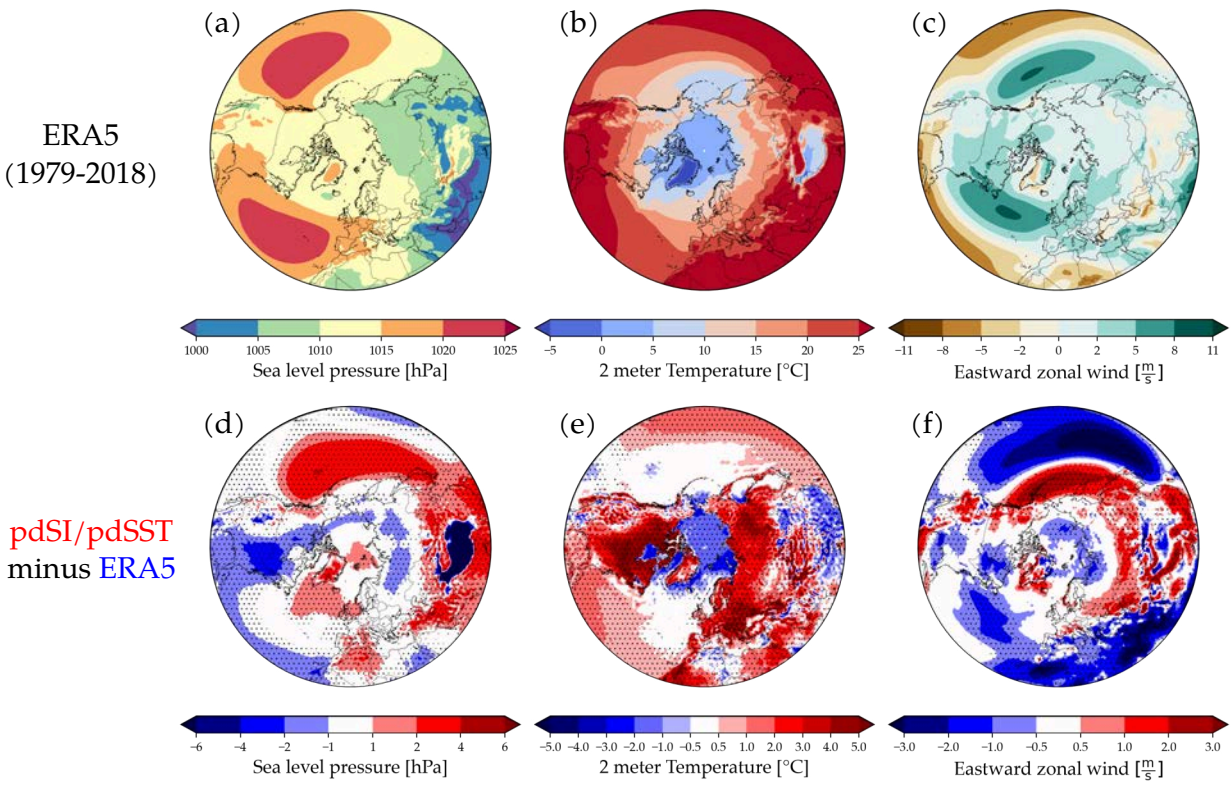

Figure 4.2: Same as in Fig. 4.1 but for summer season (JJA).

actually closer to reality than the reanalysis. Consistent with the observed SLP response, Fig. 4.1f furthermore indicates a strengthening of low-tropospheric zonal winds over mid-latitudes when contrasted to ERA5.

Summer

Figure 4.2 illustrates summer mean states in ERA5 (Figs. 4.2a–c), as well as summer biases of the pdSST/pdSI experiment with respect to ERA5 (Figs. 4.2d–f). As in winter season the ECHAM6 simulation reveals significantly increased SLPs over the North Pacific region (see again Stevens et al., 2013), resulting in an intensification and northwestward shift of the North Pacific High. Fixed SSTs in the model simulation do not allow for a representation of natural SST variability patterns over the Pacific region, such as ENSO or the Pacific Decadal Oscillation. This also leads to a reduced atmospheric variability over Pacific regions that may contribute to the SLP model bias pattern over the North Pacific. Also in summer season the pdSST/pdSI experiment appears to amplify the land-sea contrast over northern latitudes (Fig. 4.2e). The negative near-surface temperature bias over the Arctic Ocean is not as strong as in winter, but the summer mean surface temperatures over Europe are highly overestimated by several degree. Besides a poleward shift of the North Pacific jet, changes in low-tropospheric zonal winds over mid-latitudes are less pronounced compared to winter season (Fig. 4.2f). This observation is consistent with the relatively small SLP bias over these regions in summer.

4.1.2 *Climatological responses in ECHAM6 sensitivity experiments*

Winter differences

Figure 4.3 compares the climatological DJFM mean states of SLP, T2m and u850 between the different PAMIP sensitivity experiments and the pdSST/pdSI reference simulation. futArcSI indicates a general tendency towards lower SLPs over northern latitudes (Fig. 4.3a), while futBKSI exhibits slight decreases over some mid-latitude regions in form of a (non-significant) wave-3 pattern (Fig. 4.3d). In accordance, especially the zonal wind response in futBKSI indicates a westward extension of the eddy-driven jet over mid-latitudes (Fig. 4.3f); however, as for the SLP response significance differences can barely be detected at the 95% significance level according to a two-sided student's t-test. Arctic regions directly affected by the thermodynamical forcing experience a strong warming of mean near-surface temperatures in the sea ice sensitivity experiments (Figs. 4.3b and e). Horizontal advection also leads to a mean warming over nearby continental regions.

In contrast to the sea ice sensitivity experiments, futSST reveals more striking differences when compared to pdSST/pdSI. SLPs significantly increase in mid-latitudinal regions over the Euro-Atlantic domain and parts of North America. A strengthening of the Aleutian low can be observed as well (Fig. 4.3g). Over the Euro-Atlantic region the SLP response even projects onto the positive phase of the NAO. Consistent with Fig. 4.3g, the lower tropospheric eddy-driven jet over the North Pacific experiences a significant strengthening, while the North Atlantic jet is additionally extended westwards (Fig 4.3i). As expected, the global SST forcing leads to pronounced near-surface temperature increases over the entire NH, with a maximum warming over the Arctic Ocean (Fig. 4.3h).

Summer differences

Compared to winter season, the summer climatological responses in the sea ice sensitivity experiments are even smaller and mostly insignificant (Fig. 4.4a-f). Less dynamical activity over Arctic regions in summer compared to winter season confines the SST response to local areas (Figs. 4.4b and e). The slight cooling over central Arctic SI areas in summer (Fig. 4.4b) might be related to differences in the amount of simulated clouds, as warmer and more open-water surfaces in the sea ice sensitivity experiments favor cloud formation.

As in winter, summer responses for the futSST experiment are much stronger as for the sea ice sensitivity simulations. Figure 4.4g indicates a pronounced weakening of the North Pacific and Azores High, while surface pressures are increased over large parts of Eurasia. In addition, a southward shift of the low-level jet stream can be detected over the Atlantic and Pacific Oceans. As in winter, strong increases of near-surface temperatures are observed in response to the global SST forcing.

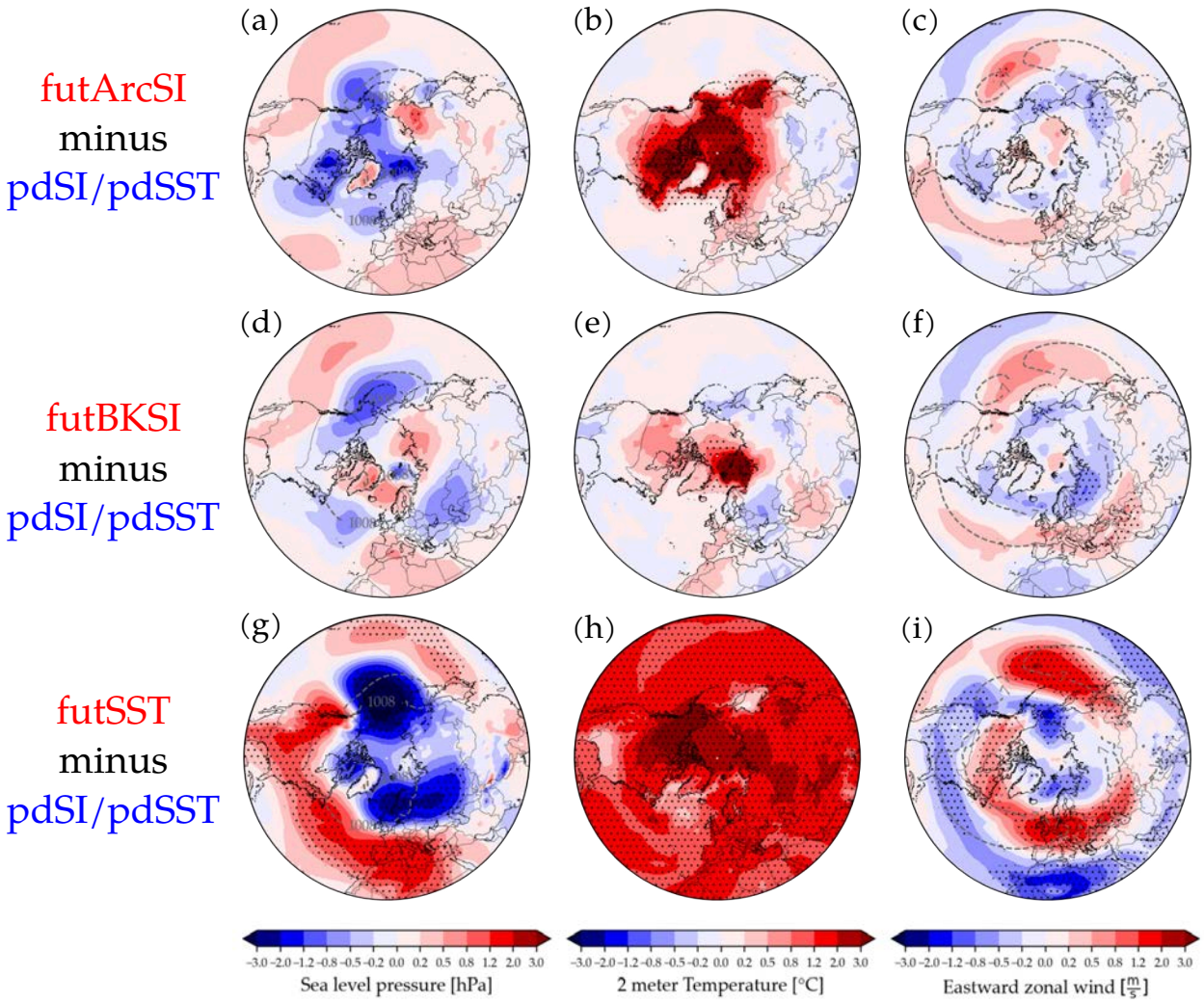

Figure 4.3: ECHAM6 PAMIP differences in mean states of monthly-averaged SLP (a,d,g), T2m (b,e,h) and u850 (d,f,i) for the DJFM. Compared are the futArcSI (a–c), futBKSI (d–f) and the futSST (g–i) experiments with the pdSST/pdSI reference simulation. Stippling indicates statistical significance at the 95% level according to a two-sided student's t-test. Dashed gray contours signify 1008 hPa and 7 m s^{-1} isolines in pdSST/pdSI, providing a rough visual guidance for the position of the Aleutian low and North Atlantic stormtrack, as well as of the North Atlantic and North Pacific jets.

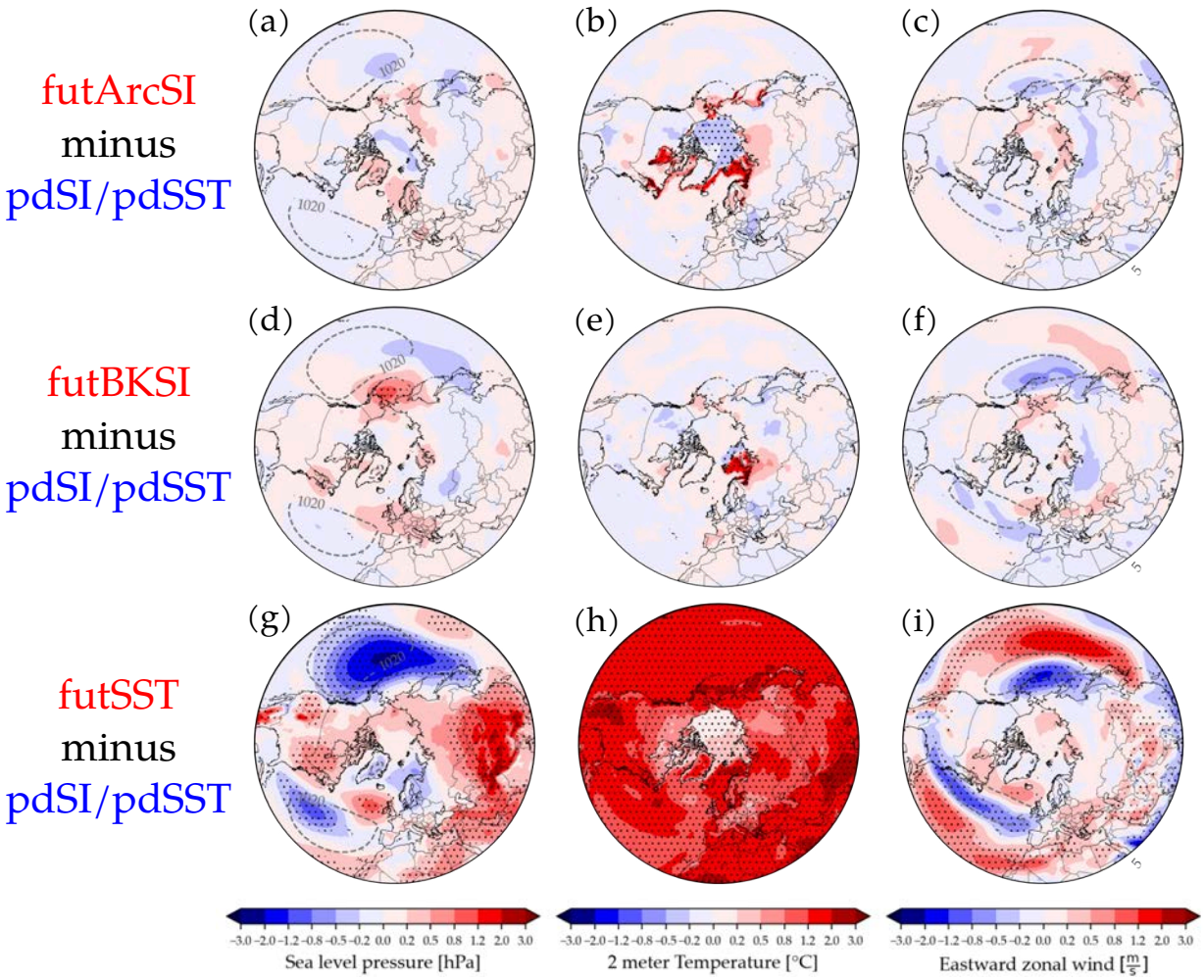

Figure 4.4: Same as in Fig. 4.3 but for JJA. Dashed gray contours signify 1020 hPa and 5 m s^{-1} isolines in pdSST/pdSI, providing a rough visual guidance for the position of the North Pacific High and the Azores high, as well as of the jet stream positions in summer.

4.2 CIRCULATION REGIMES AND SEA ICE-INDUCED FREQUENCY CHANGES

This Section discusses how future Arctic SI retreat impacts large-scale atmospheric dynamics in terms of occurrence frequency changes of atmospheric circulation regimes (see also Sec. 2.2). Section 4.2.1 initially presents and discusses the regimes structures for winter and summer season found in ERA5. Furthermore, it is investigated how well the ECHAM6 PAMIP simulations (see Sec. 3.2.2) are able to reproduce the spatial structures of the ERA5 regimes. Afterwards, it is studied to what extent changes in regime occurrence frequencies can be related to future Arctic SI reductions. Therefore, in Sec. 4.2.2 recent trends in regime occurrence frequencies in the ERA5 reanalysis are initially presented. This specifically aims to identify links between ERA5 regime occurrence frequencies and recent Arctic SI changes. In order to better isolate the impact of Arctic SI loss it is subsequently investigated how regime occurrence frequencies change when the different PAMIP sea ice sensitivity are compared with the pdSST/pdSI reference simulation. The frequency changes found in the simulations are then contrasted with the previously detected ERA5 tendencies for low and high Arctic SI conditions. This allows to finally support the robustness of the identified impacts of future Arctic SI retreat on the occurrence frequencies of atmospheric circulation regimes in ECHAM6.

4.2.1 *Regime structures in ERA5 and ECHAM6 experiments*

To start with, winter and summer circulation regimes computed from ERA5 and from different combinations of ECHAM6 PAMIP experiments[2] are initially presented. Different combinations of ECHAM6 PAMIP model experiments were considered here instead of single experiments, as the joint regime patterns will be used in upcoming analysis steps (Secs. 4.2.3 and 4.5). Circulation regimes were computed with the *k*-Means clustering algorithm applied to SLP anomaly data. For more details on the algorithm itself, its application and the definition of the respective SLP anomalies see Sec. A.2. The ability of the ECHAM6 PAMIP simulations to reproduce the ERA5 regimes is quantified in Taylor diagrams (see Sec. A.3).

Winter regimes

The upper row in Fig. 4.5 shows five circulation regimes computed from daily ERA5 SLP anomalies (1979–2018) for DJFM over the Euro-Atlantic domain (-90°W–90°W, 20°N–88°N). The overall structure of the individual regimes is relatively unaffected by the exact definition of winter season (e.g. by excluding March) and by modifications of the spatial domain (using e.g. -80°W–80°W, 30°N–88°N).

The computed winter regimes closely resemble regimes found in previous studies (e.g. Crasemann et al., 2017), and include a frequently detected Scandinavian Blocking regime (Dorrington et al., 2020; Falkena et al., 2020; Yiou et al., 2017), termed SCAN, with an anticyclonic blocking structure over Scandinavia and parts of the Ural mountains. Studies by for instance Jung et al. (2017) and Sato et al. (2014) suggested that such an anticyclonic anomaly over Northeastern Europe might be part of a wave train structure that originates

2 that is, the reference pdSST/pdSI dataset merged with one of the sensitivity experiments futArcSI, futBKSI or futSST

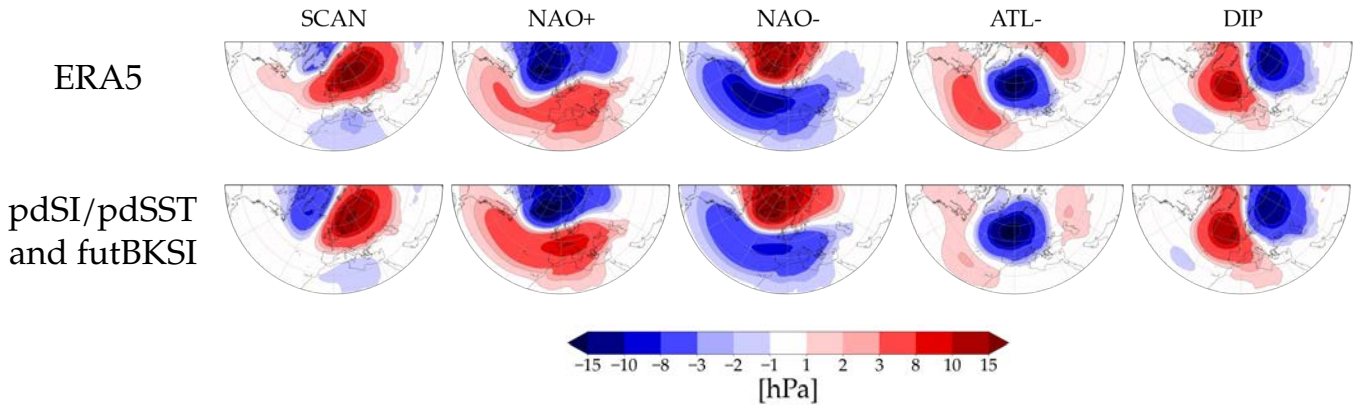

Figure 4.5: Five circulation regimes over the Euro-Atlantic domain computed from daily ERA5 (upper row) and ECHAM6 PAMIP (bottom row) SLP anomaly data for DJFM. For the displayed PAMIP model regimes, data from the pdSST/pdSI and futBKSI simulations have been merged before applying the *k*-Means algorithm.

from the east coast of North America and is forced by warming anomalies over this remote region. Another regime is characterized by a cyclonic structure over the Atlantic and parts of Western Europe (ATL-) and has previously been named negative Atlantic ridge (Falkena et al., 2020) or Scandinavian trough (Dorrington et al., 2020). A dipole pattern (DIP) is found with positive pressure anomalies over the North Atlantic and negative pressure anomalies over Northeastern Europe. This dipole pattern has also been frequently termed Atlantic Ridge (Dorrington et al., 2020; Falkena et al., 2020; Yiou et al., 2017). Finally, two of the computed regimes resemble the positive and negative phase of the North Atlantic Oscillation, termed NAO+ and NAO- respectively.

Upcoming analyses in Secs. 4.2.3 and 4.5 are based on circulation regimes computed for different combinations of the pdSST/pdSI reference simulation merged with one of the sensitivity simulations. Therefore, the bottom row of Fig. 4.5 exemplary shows the five winter regimes computed for the merged pdSST/pdSI+futBKSI dataset. By visual inspection it is evident that the ECHAM6 PAMIP simulations are apparently able to realistically simulate the ERA5 winter regime patterns. This will allow for a reasonable comparison between ERA5 and PAMIP in the upcoming analyses (Secs. 4.2.3, 4.4 and 4.5). In addition, Taylor diagram 4.6a (see also Sec. A.3) quantifies different statistics that allow to compare the ERA5 winter regime patterns with regime patterns computed for different combinations of PAMIP experiments. It appears that all PAMIP winter regime patterns show high pattern correlation coefficients (generally greater than 0.9) with the ERA5 regimes, as well as similar pattern amplitudes compared to ERA5. However, especially the pattern amplitude for the NAO+ and DIP are slightly overestimated compared to ERA5. It is also obvious from Fig. 4.6a that the resulting winter pattern structures are relatively insensitive to the combination of reference and sensitivity datasets. Thus, the different SI and SST forcings in the sensitivity experiments can be considered as weak forcings that do not significantly affect the overall regime structure (Palmer, 1999).

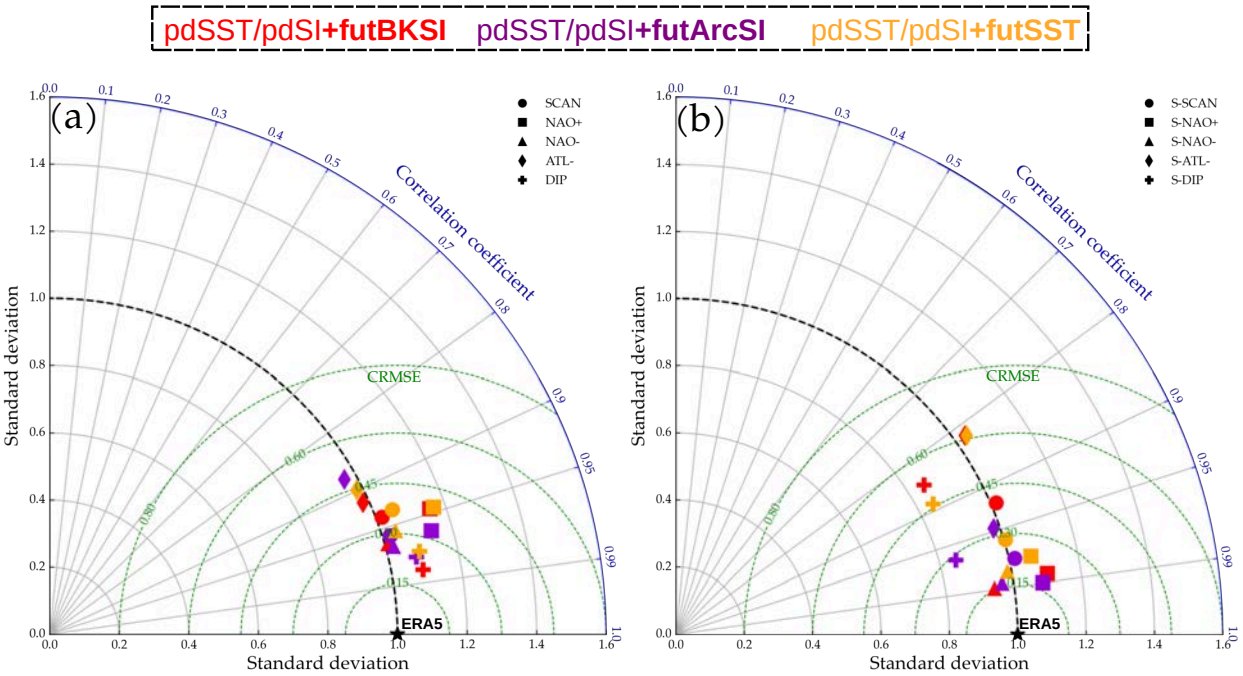

Figure 4.6: Taylor diagram (see Taylor, 2001) that quantifies different statistics in order to compare the regime patterns obtained from ERA5 with model patterns computed for different combinations of merged PAMIP datasets: a) for winter patterns, b) for summer patterns. Different symbols indicate different regimes and different colors stand for different combinations of model simulations for which regimes are computed in this thesis. The black star symbolically indicates the ERA5 reference pattern. The concentric quadrants centered around the origin show the pattern standard deviation of the different model patterns relative to the standard deviation of the ERA5 reference patterns. The blue polar axis depicts the pattern correlation coefficient between the respective model patterns and the reanalysis pattern. The green concentric semicircles centered around the black reference point indicate the centered root mean square error CRMSE when comparing model and reanalysis patterns. Thus, model symbols close the reference star mean high resemblance between model and reanalysis pattern. For definitions of the aforementioned statistics see Sec. A.3

Summer regimes

As done for the extended winter season five circulation regimes for JJA were computed over the Euro-Atlantic region. The resulting ERA5 summer regimes are shown in the upper row in Fig. 4.7. It shows that each summer regime can be roughly assigned as a counterpart to one of the previously discussed winter regimes (prefix "S" denotes the respective summer regimes). However, the summer patterns' amplitudes are significantly reduced when contrasted to the winter patterns. This reflects the weaker atmospheric circulation in the summer months. Additionally, the centers of action within the respective summer patterns appear to be spatially more confined and are shifted polewards. The summer parallels to the different winter NAO states, termed S-NAO+ and S-NAO- (see e.g. Folland et al., 2009), are in addition characterized by a more zonally symmetric structure over mid-to subpolar latitudes when contrasted to the winter regimes.

Summer regimes calculated from PAMIP model simulations (see bottom row in Fig. 4.7) again strongly resemble the ERA5 regime patterns. The Taylor diagram 4.6b illustrates

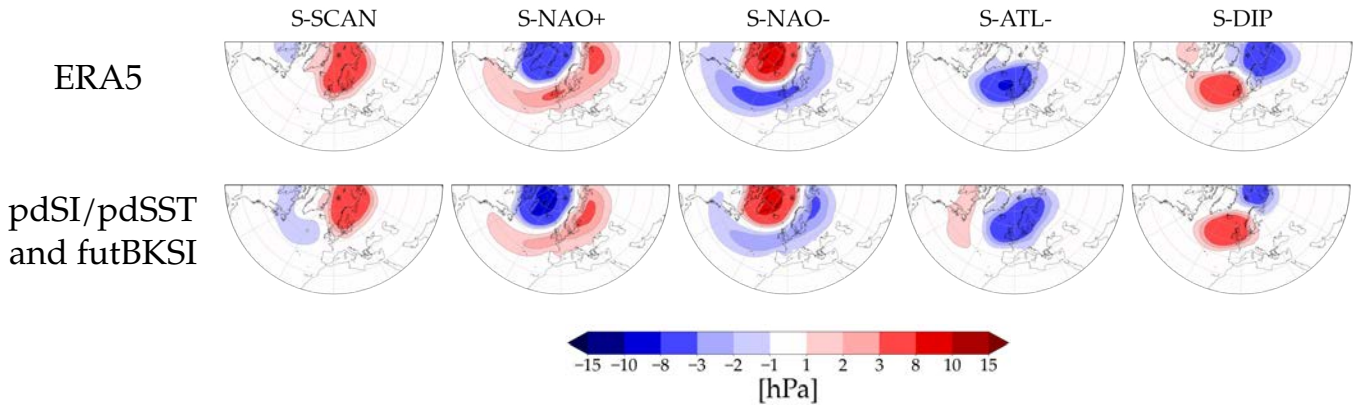

Figure 4.7: Same as in Fig. 4.5, but for JJA.

that especially the S-NAO+ and S-NAO- patterns are excellently and robustly reproduced by the different combinations of PAMIP simulations. Also the summer Scandinavian blocking pattern S-SCAN shows pattern correlation coefficients larger than 0.9 for all dataset combinations when compared with the ERA5 regime. In contrast, the summer dipole S-DIP and summer Atlantic cyclone S-ATL- patterns reveal more striking differences in terms of pattern correlation and/or pattern amplitude compared to ERA5. In addition, the structures of these model patterns seem to be less robustly reproduced by the different sensitivity experiments.

In Fig. B.1 it is additionally shown how well ECHAM6 reproduces the observed ERA5 winter and summer regime structures compared to some other PAMIP models[3]. It shows that ECHAM6 simulates the respective regimes equally well or even better than the other models.

4.2.2 *Regime frequency changes in ERA5*

Now, it will be discussed how the occurrence frequencies of the previously presented ERA5 winter and summer circulation regimes have changed over the recent period of Arctic SI retreat (1979–2018).

Therefore, a Multinomial Logistic Regression (MNLR) model approach is employed with a linear predictor containing the covariates *month*, *time* and *Arctic Sea Ice Area* anomaly. For more details on the MNLR approach, the definition of the linear predictor and the calculation of confidence bands see Sec. A.4. To briefly summarize, the essence of this regression approach is to describe the log-odds[4] as a linear combination of the different covariates (also termed linear predictor, see Equation A.15). This allows to finally quantify the relationship between the occurrence probabilities of circulation regimes and the different covariates.

3 Models were chosen based on data availability at the *Earth System Grid Federation* (ESGF) at the time the analysis was conducted

4 defined as the logarithm of the chance of observing some circulation regime with respect to some predefined baseline regime

As mentioned above, the following covariates are considered:

- *time*: this covariate is frequently used as a proxy for recent global climate change. However, studies by Crasemann et al. (2017) or Jaiser et al. (2016) also considered time as a proxy for recent Arctic SI retreat. As a part of their analysis they detected changes in ERA-Interim regime occurrence frequencies by dividing the recent time period into "high ice" (1979–2000) and "low ice" (2000–2014) phases. For sure, the covariate *time* does also include the effect of the linear trend component of recent Arctic SI decline[5], but also contains the effects of all other facets of recent global climate change.

- *Arctic Sea Ice Area* anomaly: aiming to better isolate the influence of recent Arctic SI variations on regime occurrence frequencies, Arctic sea ice area SIA anomaly is also considered as a covariate. Here, instantaneous and linearly detrended daily-averaged Arctic SIA anomalies from ERA5 over the period 1979–2018 are used. Anomalies were calculated as deviations from the annual cycle, which is defined as the average of each day of a year over all years. Detrending the SI times series allows to account for changes in regime occurrence frequencies due to variations in Arctic SIA, that are not explained by the recent linear trend in time.

- *month*: this allows to account for differences in regime occurrence frequency changes between different months of a season. This is motivated by Arctic-mid-latitude linkage pathways, such as the stratospheric pathway that is commonly associated with a negative NAO response in late winter. Consequently, individual investigation of each winter month is required to detect such intraseasonal signals. Indeed, Crasemann et al. (2017) found that recent changes in winter regime occurrence frequencies can show pronounced intraseasonal variability. A study by Detring et al. (2021) also demonstrated that recent changes in Northern Hemispheric blocking activity exhibit strong differences between individual months. Technically, interaction effects between the covariates time/SIA anomalies with the covariate month are considered (see Sec. A.4.3). This makes it possible not only to describe for instance the seasonal mean effect of the covariates time and SIA anomalies, but also resolve these effects for the different months of a season.

A similar MNLR setup was recently also implemented by Detring et al. (2021), who studied recent temporal trends in blocking probabilities and in transition probabilities between different blocking states over the NH.

It should be noted beforehand that the identified links between regime occurrences and Arctic SI do not provide any direction of causality. Thus, it can not be inferred whether SI changes actually impact the occurrence frequency of circulation regimes, or whether changed regime occurrence frequencies influence Arctic SIA. This issue will be addressed in the upcoming Sec. 4.2.3, where the impact of future Arctic SI retreat on regime occurrence frequencies in the PAMIP experiments is assessed. For this reason, this Section especially aims to identify links between regime occurrences and SI changes in "real-world" data, that can be used to support the plausibility of detected regime changes in the PAMIP sea ice sensitivity experiments.

5 correlation coefficient of around 0.85 between time and Sea Ice Area time series

Table 4.1: Occurrence frequencies of ERA5 winter circulation regimes over the period 1979–2018. Upper row: occurrence frequencies averaged over all months of the extended winter season. Lower rows: occurrence frequencies calculated for the different winter months separately. Bold numbers indicate that the respective occurrence frequency significantly differs from 20% (based on a moving block bootstrap with $M = 3000$).

	SCAN	NAO+	NAO-	ATL-	DIP
DJFM	**0.222**	0.204	**0.176**	0.200	0.198
Dec	0.221	0.190	0.173	0.214	0.202
Jan	0.216	0.198	0.165	0.211	0.209
Feb	**0.25**	0.202	0.168	0.191	0.189
Mar	0.203	0.223	0.196	0.180	0.198

Winter

Before presenting results of the MNLR approach for the extended winter season, a coarse overview about the total regime occurrence frequencies over the ERA5 time period is initially provided. Therefore, the upper row in Table 4.1 shows the seasonally-averaged occurrence probabilities of the five ERA5 winter circulation regimes over the period 1979–2018. It appears that on a seasonal average the SCAN regime occurs significantly more frequent (22.2%) when compared to a uniform distribution of regime occurrences (20%). In contrast, the NAO- regime occurs significantly less frequent (17.6%). Regime occurrence frequencies in Table 4.1 for the individual winter months indicate that especially in February the SCAN regime occurs anomalously more often (25%). Although not significantly different from 20% for the different winter months, the NAO- indicates anomalously low occurrence frequencies from December to February (around 17%).

Figure 4.8 shows MNLR results for the recent temporal trends of regime occurrence frequencies for the individual winter months. As mentioned above, this temporal trend also includes the effect of the linear trend component of recent Arctic SI decline, but does not allow to separate this effect from other aspects of recent global climate change. Consistent with the ERA-Interim analysis by Crasemann et al. (2017), over recent decades one can detect a pronounced increase (decrease) of SCAN (DIP) regime occurrences in January (Fig. 4.8b), a decrease of NAO+ occurrences in February (Fig. 4.8c), as well as a decrease of SCAN occurrences in March (Fig. 4.8d). In addition, a distinct upward trend of the ATL- regime is found in midwinter (Figs. 4.8b and c), as well as a recent tendency towards decreased NAO- occurrences in December (Fig. 4.8a) and increased DIP occurrences in March (Fig. 4.8d). Compared to Crasemann et al. (2017), we can however not detect a recent increased occurrence of the SCAN regime in December (only in January), as well as no late winter NAO- decrease over recent times.

It has been suggested by Crasemann et al. (2017) that this early winter SCAN and late winter negative NAO response might indicate a strengthening of the stratospheric pathway under recent low Arctic SI conditions (see Sec. 2.3.4). The reason why the recent late winter NAO- increase can not be detected here is related to the fact that compared to Crasemann et al. (2017) the present analysis additionally includes the years 2014–2018.

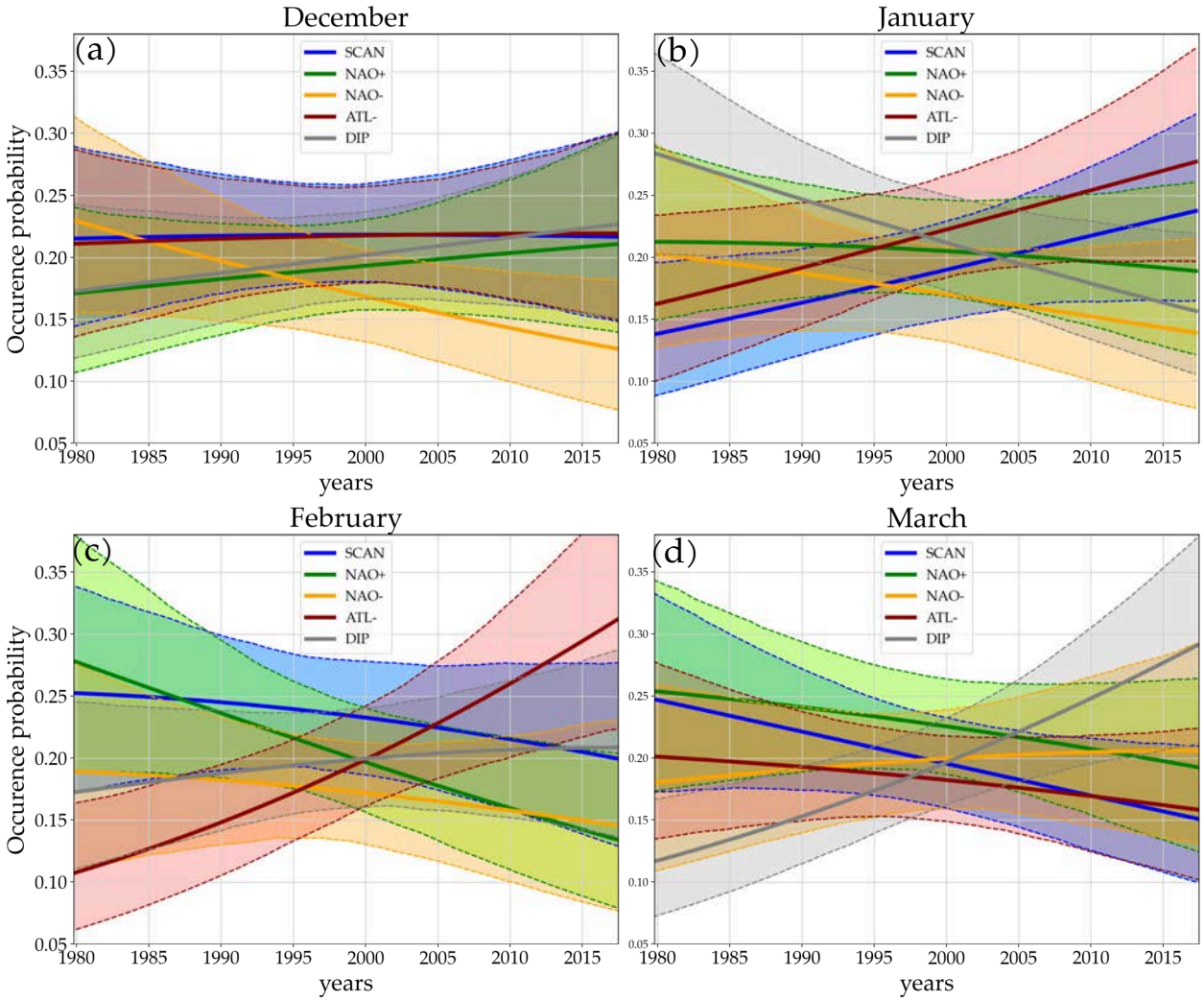

Figure 4.8: Recent temporal trends of ERA5 winter regime occurrence frequencies computed with the MNLR model described in Sec. A.4. Shading around the mean probabilities (thick lines) represent 90 percent confidence bands, computed based on a moving block bootstrap with $M = 3000$.

Furthermore, the employed MNLR approach is based on a linear predictor which makes the resulting curves relatively sensitive to the cluster assignments near the endpoints of the considered time range. Thus, low occurrence frequencies of the NAO- regime from 2014–2018 lead to no recent upward trend of NAO- occurrences when employing the present regression approach.

In order to better isolate and describe the impact of recent Arctic SIA variations (excluding the effect of the linear trend component of recent Arctic SI retreat), Fig. 4.9 depicts ERA5 regime occurrence probabilities in dependence on instantaneous linearly detrended Arctic SIA anomalies. For these plots the covariate time in the MNLR model was fixed to the year 1999, which may be interpreted as some form of mean SI-regime relationship over the ERA5 period (see Sec. A.4.3).

Figures 4.9a–d show that throughout all winter months negative Arctic SIA anomalies are associated with increased occurrence frequencies of the SCAN regime. This link is most

pronounced in January and February (Figs. 4.9b and c). Furthermore, a tendency towards more frequent NAO+ and ATL- occurrences under high Arctic SI conditions can be observed in January (Fig. 4.9b), but for NAO+ also in February (4.9c). Finally, a tendency towards more frequent DIP occurrences in December and March is indicated in Figs. 4.9a and d.

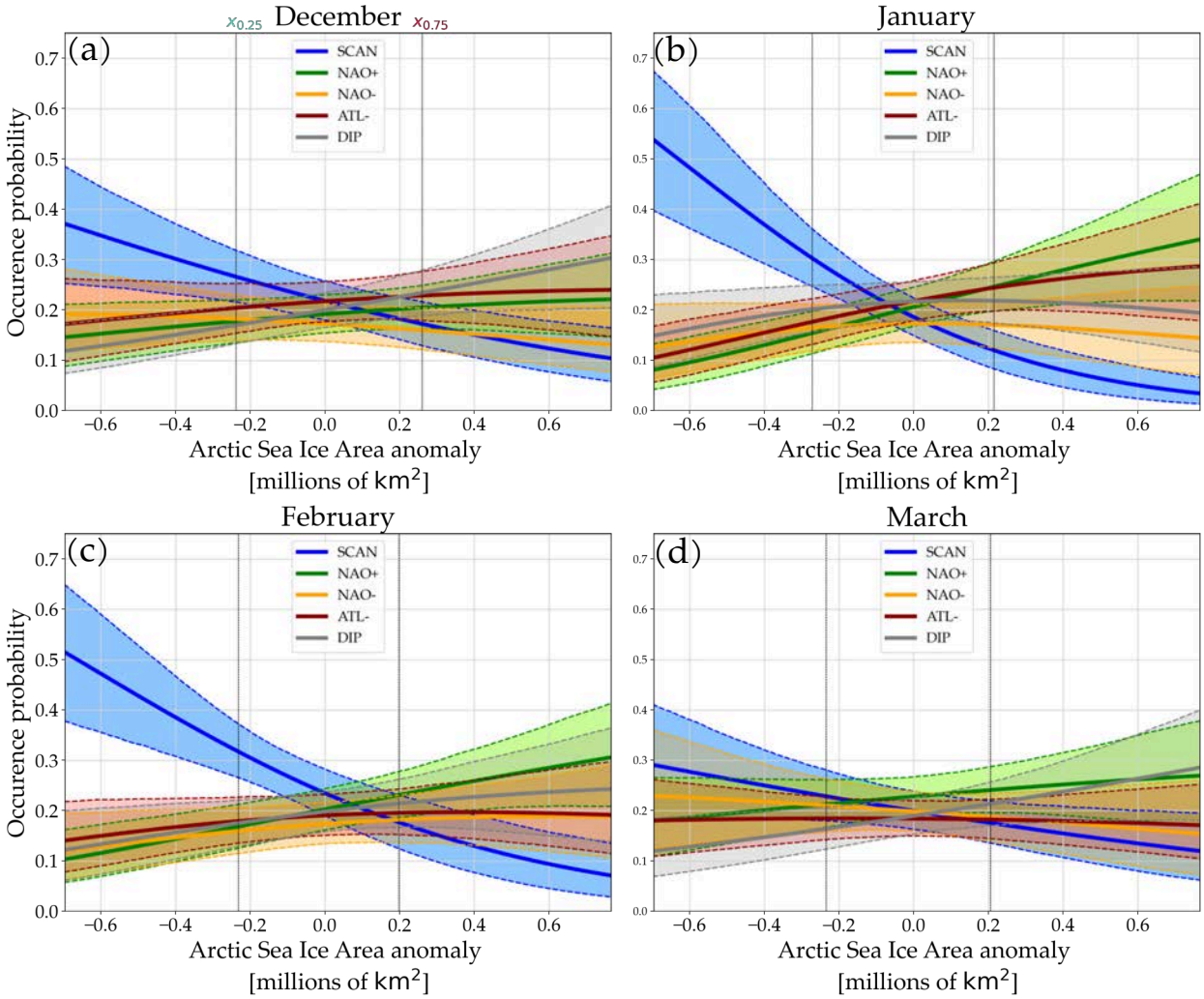

Figure 4.9: ERA5 winter regime occurrence frequencies in dependence on instantaneous linearly detrended Arctic SIA anomalies. For these plots, the covariate time in the MNLR model was fixed to the midpoint of the ERA5 period (see Sec. A.4.3). The dashed vertical lines indicate for each month the respective 0.25 and 0.75 quantiles of the SIA covariate ($x_{0.25}$ and $x_{0.75}$). Shading around the mean probabilities (thick lines) represent 90 percent confidence bands, computed based on a moving block bootstrap with $M = 3000$.

Table 4.2: Same as in 4.1, but for JJA and the respective summer regimes.

	S-SCAN	S-NAO+	S-NAO-	S-ATL-	S-DIP
JJA	0.205	0.216	0.191	0.202	0.185
Jun	0.181	0.211	0.213	0.216	0.179
Jul	0.208	0.218	0.191	0.202	0.181
Aug	0.226	0.22	0.171	0.190	0.193

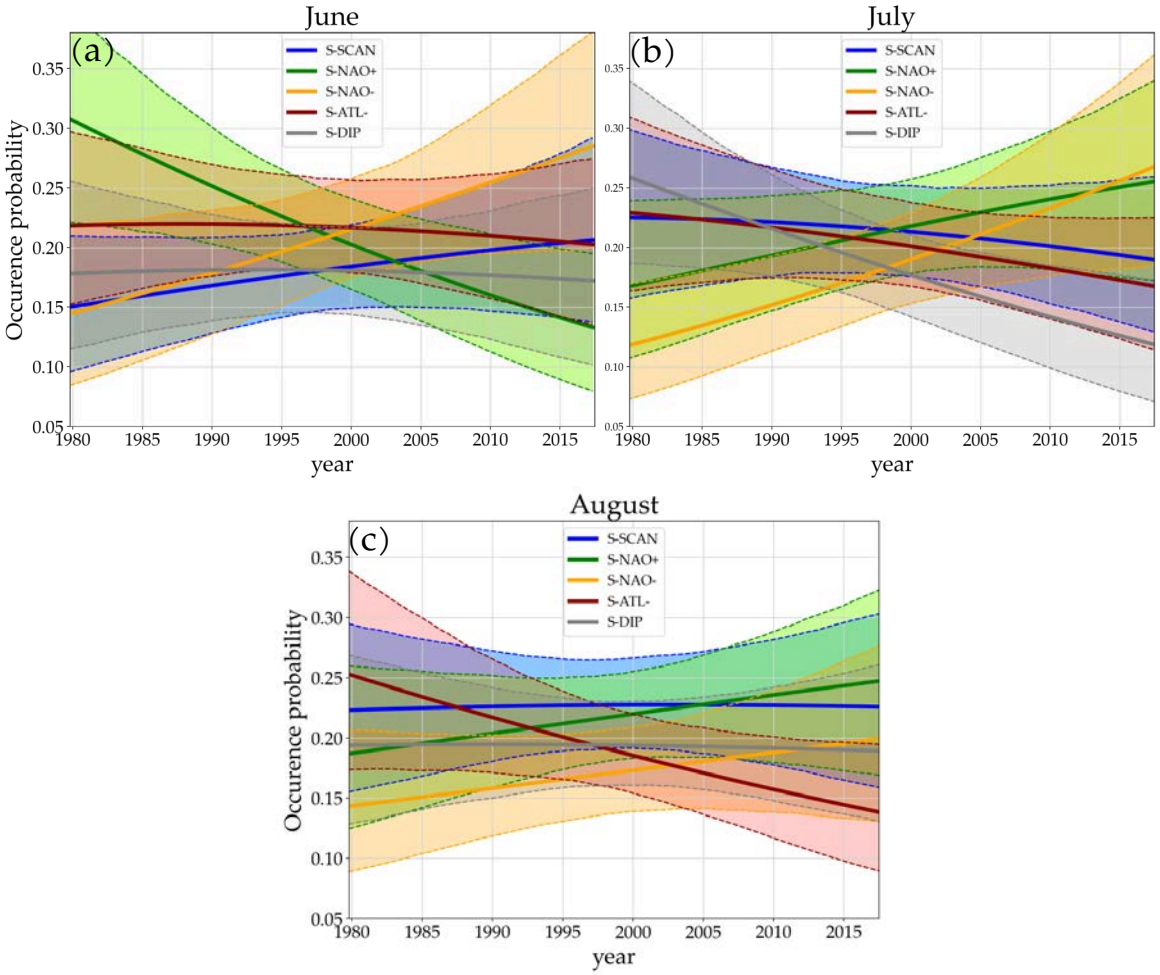

Figure 4.10: Same as in Fig. 4.8, but for JJA and the respective summer regimes (see Fig. 4.5).

Summer

Now, the same analysis is presented, but for the ERA5 summer regimes (see Fig. 4.7). Table 4.2 shows that none of the total occurrence frequencies of ERA5 summer regimes significantly differs from 20%, neither for the entire summer season nor for individual summer months.

Figure 4.10 displays recent temporal trends of summer regime occurrences. In June and July, a clear increase of S-NAO- occurrences over recent decades (Fig. 4.10a and b) can be reported. In June, a distinct decrease of S-NAO+ occurrences (Fig. 4.10a) can also be detected. This suggests an overall recent negative shift of the summer NAO, which can be for instance associated with a southward shift of the North Atlantic stormtrack (Folland et al., 2009). In addition, a tendency towards less frequent S-DIP occurrences is evident in July (Fig. 4.10b), as well as decrease of S-ATL- in August (Fig. 4.10c).

Interestingly, Figs. 4.11a and b suggest increasing S-NAO- occurrence frequencies in June and July, as well as a decrease of S-NAO+ occurrences in all summer months under low Arctic SI conditions. These are similar tendencies as in Fig. 4.10, when assuming that the temporal trends in Fig. 4.10 are related to the recent negative trend of Arctic SIA. This may supports that the detected recent shift towards more frequent S-NAO- occurrences in Fig. 4.10 is actually caused by recent Arctic SI decline.

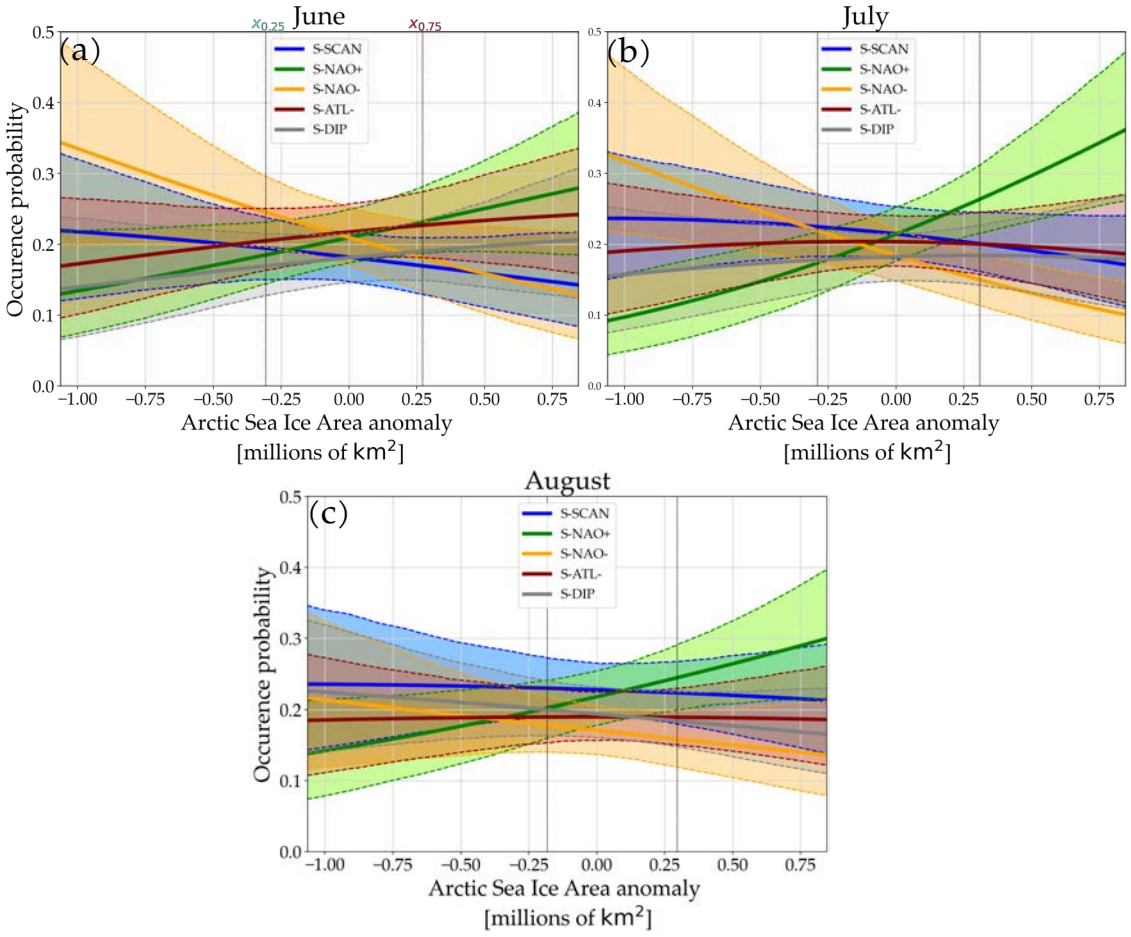

Figure 4.11: Same as in Fig. 4.9, but for JJA and the respective summer regimes (see Fig. 4.7).

4.2.3 *Regime frequency changes in ECHAM6 experiments*

It will now be discussed what changes in regime occurrence frequencies can be expected under future Arctic SI loss in the ECHAM6 PAMIP simulations.

Winter

Figure 4.12 shows monthly-splitted histograms that compare the relative occurrence frequencies of the computed PAMIP winter regimes between the pdSST/pdSI reference simulation and the futArcSI (Figs. 4.12a-e), as well as the futBKSI (Figs. 4.12f-j) sea ice sensitivity experiment. As already described in Sec. 4.2.1, circulation regimes were computed based on the joint datasets of the pdSST/pdSI reference and the respective sensitivity experiment. The paired dark blueish/redish bars in Fig. 4.12 indicate significant differences in occurrence frequencies.

In order to support the robustness of the found regime frequency changes in the model experiments, the triangles in Fig. 4.12 indicate the previously detected ERA5 tendencies of regime frequencies for anomalously high and low Arctic SI conditions (see Fig. 4.9). Anomalously low Arctic SI conditions (red triangles) were defined as the 0.25 quantile of detrended ERA5 Arctic SIA anomalies for the respective month. For high Arctic SI conditions (blue triangles) the 0.75 quantile was chosen (see vertical lines in Fig. 4.9). The ERA5 tendencies/values were finally read off from Fig. 4.9 at the respective values for a low and high Arctic SIA anomaly. ERA5 tendencies are only shown in Fig. 4.12, if the occurrence probabilities for low and high SI conditions significantly differ from each other[6]. The choices of the high and low SI conditions in ERA5 are debatable and might be not representative for the different SI forcings in the PAMIP reference and sensitivity experiments. It could be argued that for low ERA5 SI conditions more extreme quantiles might be more suitable. Nevertheless, the defined ERA5 tendencies are considered here as additional evidence for the reliability of the model results, as choosing more extreme quantiles would actually result in even more distinct and significant ERA5 signals .

Overall, it can be observed that the winter regime frequency changes in Fig. 4.12 associated with the futArcSI and futBKSI sensitivity simulations share many similar features. Consistent with previous studies this again emphasizes the potential key role of SI loss in the BKS region when trying to identify and understand linkages between the Arctic and mid-latitudes.

In agreement with ERA5 tendencies, an overall midwinter increase of SCAN occurrences by several percent is detected in both sea ice sensitivity simulations (Figs. 4.12a and f). For futBKSI this frequency change is significantly pronounced in January and February, whereas for futArcSI the signal is only detectable in January. Such an overall midwinter SCAN response is consistent with previous studies, such as by Luo et al. (2016) who related a strengthening of the Scandinavian or Ural Blocking in winter season to instantaneous SI loss in the BKS. Petoukhov et al. (2010) analyzed sea ice sensitivity model experiments and showed that for moderate winter SI reductions over the BKS an anticyclonic anomaly centered over the same region can be observed in February. However, they emphasized that such an anticyclonic circulation response depends on the actual prescribed magnitude of SI loss over the BKS in a highly nonlinear way.

6 this was done along with the moving block bootstrap in Figs. 4.9 and 4.11.

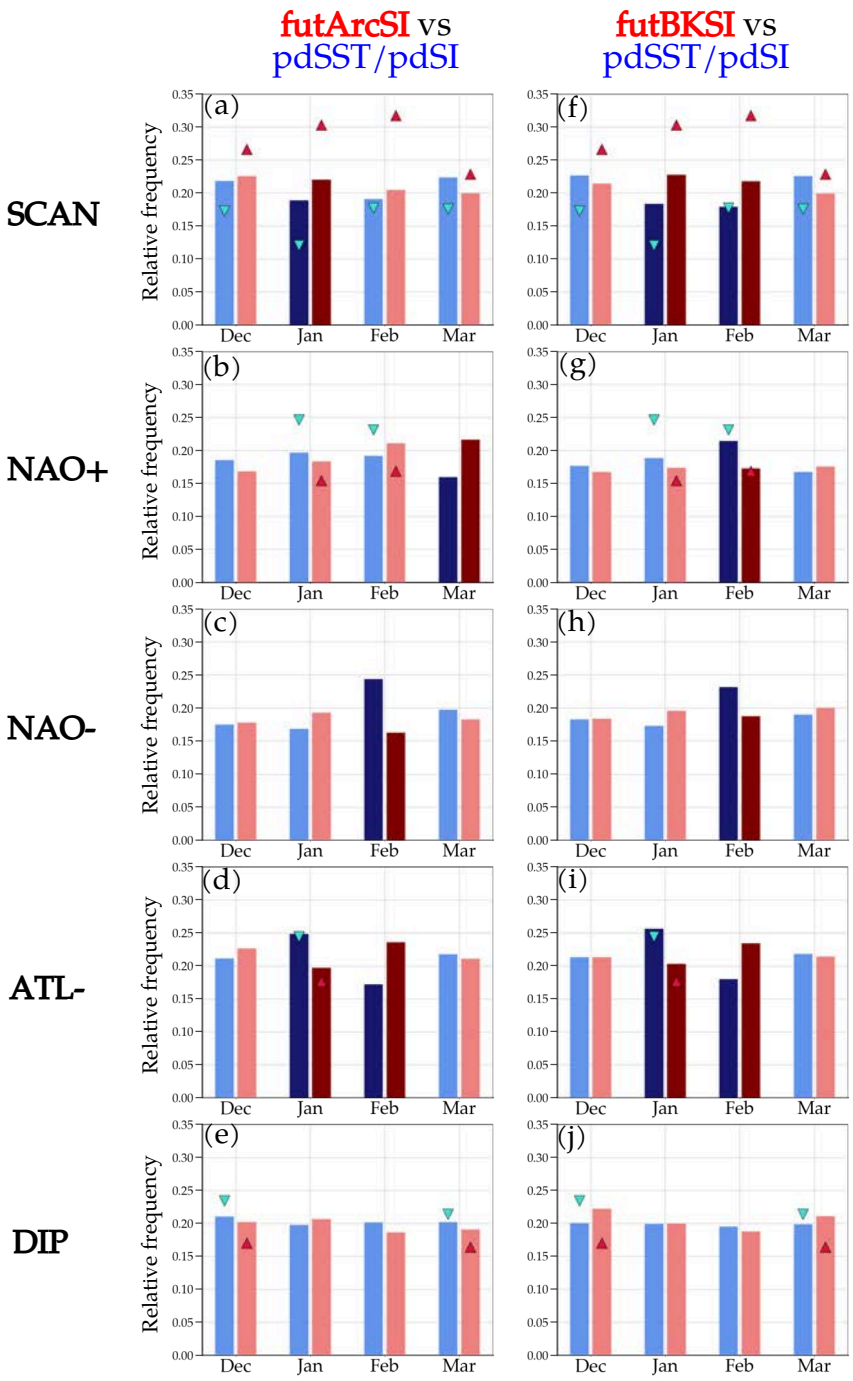

Figure 4.12: Relative regime occurrence frequencies for different winter months compared between the pdSST/pdSI reference simulation (blueish bars) and the futArcSI (first column, redish bars), as well as the futBKSI sensitivity simulation (second column, redish bars). Light redish and blueish bars indicate non-significant frequency differences between reference and sensitivity simulations, whereas the paired dark blueish/redish bars indicate significant differences in occurrence frequencies. Note, that by definition the sum over all clusters for a specific month in a given simulation is one. The triangles indicate the tendencies of ERA5 regime occurrence frequencies for low (upright redish triangles, curves in Fig. 4.9 at $x_{0.25}$) and high (inverted bright-blueish triangles, curves in Fig. 4.9 at $x_{0.75}$) Arctic SI conditions. Only ERA5 occurrence frequencies for months where significant differences between low ($x_{0.25}$)and high ($x_{0.75}$) SI conditions were found are shown here. Significant differences in model and reanalysis are derived from a moving block bootstrap with M=3000.

Within the framework of circulation regimes Crasemann et al. (2017) detected an increased December SCAN occurrence frequency—however only in response to recent Arctic SI loss. It should be mentioned that a variety of recent modeling studies (Kim et al., 2022; Peings, 2019) did not find any intensifications of Ural blockings in response to SI loss over the BKS region.

In addition to the previously discussed changes in SCAN occurrences, especially the futBKSI sensitivity simulation exhibits a reduced occurrence frequency of the NAO+ and NAO- pattern in February (Figs. 4.12g and h). This might be interpreted as a weakened dominance of NAO variability under future conditions. However, only the tendency towards a diminished occurrence frequency of the NAO+ regime can be observed in ERA5 as well. This reduction of positive NAO events is consistent with the commonly reported negative NAO response to SI loss (Jaiser et al., 2012; Screen, 2017b; Nakamura et al., 2015; Deser et al., 2010).

Another significant signal found in both sensitivity experiments (and in ERA5), is a less frequent occurrence of the ATL- pattern in January (Figs. 4.12d and i). It appears plausible that the reduced meridional temperature gradient under future SI conditions is related to reduced baroclinic activity over the North Atlantic, which consequently may lead to less frequent formations of cyclonic systems over this region. In contrast, both simulations indicate significantly more frequent ATL- occurrences in February; however, similar tendencies are not reported in ERA5.

Summer

Figure 4.13 shows the same analysis, but for summer season and the respective PAMIP summer regimes. Here, significant changes in summer regime occurrences can be barely detected when comparing the sea ice sensitivity experiments with the reference simulation. Consistent with ERA5 tendencies, only a decreased occurrence probability of the S-NAO+ regime can be observed in both sea ice sensitivity experiments in July. In addition, increased July occurrence frequencies of the S-SCAN regime are found in both sea ice sensitivity experiments; however, no similar tendencies are detected in ERA5.

futSST experiment

Figure 4.14 shows summer and winter results for the futSST experiment. In contrast to the previously analyzed sea ice sensitivity experiments, significant signals can rarely be detected, neither in winter season nor in summer. Section 4.1 actually showed that the relatively strong global forcing in the futSST experiment significantly impacts the mean atmospheric background state (see Figs. 4.3 and 4.4). However, when accounting for this different background state prior to applying the clustering algorithm, the globally raised SSTs in futSST do apparently not significantly impact the occurrence frequency of circulation regimes. This may suggest that not the absolute magnitude and spatial scale of an applied forcing (e.g. global SSTs increases) is of primary importance for changes in regime occurrence frequencies. Rather, more localized forcings, such as Arctic SI reductions, can apparently have a more pronounced impact on regime occurrence frequencies.

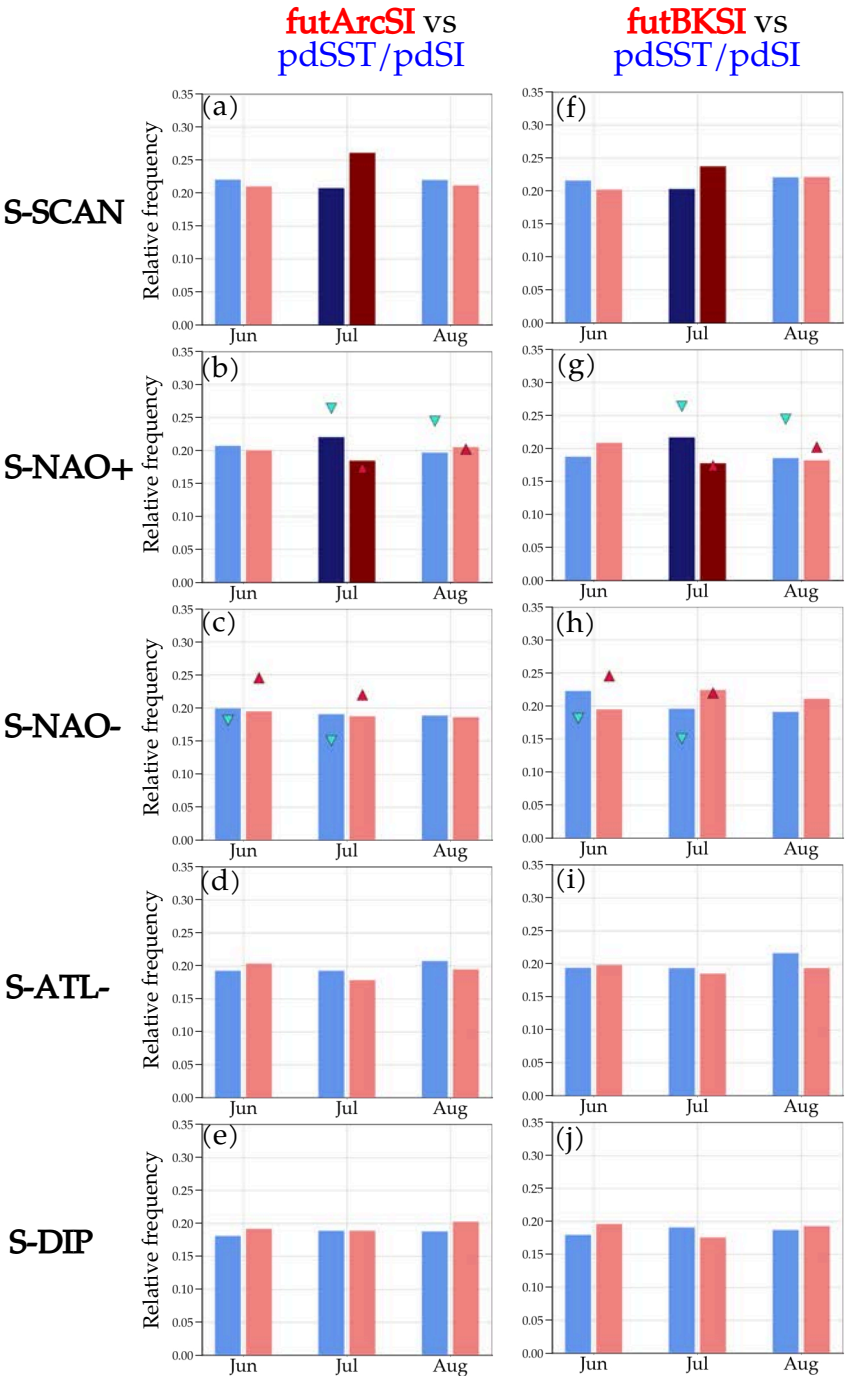

Figure 4.13: Same as in Fig. 4.12, but for summer season and the respective summer regimes.

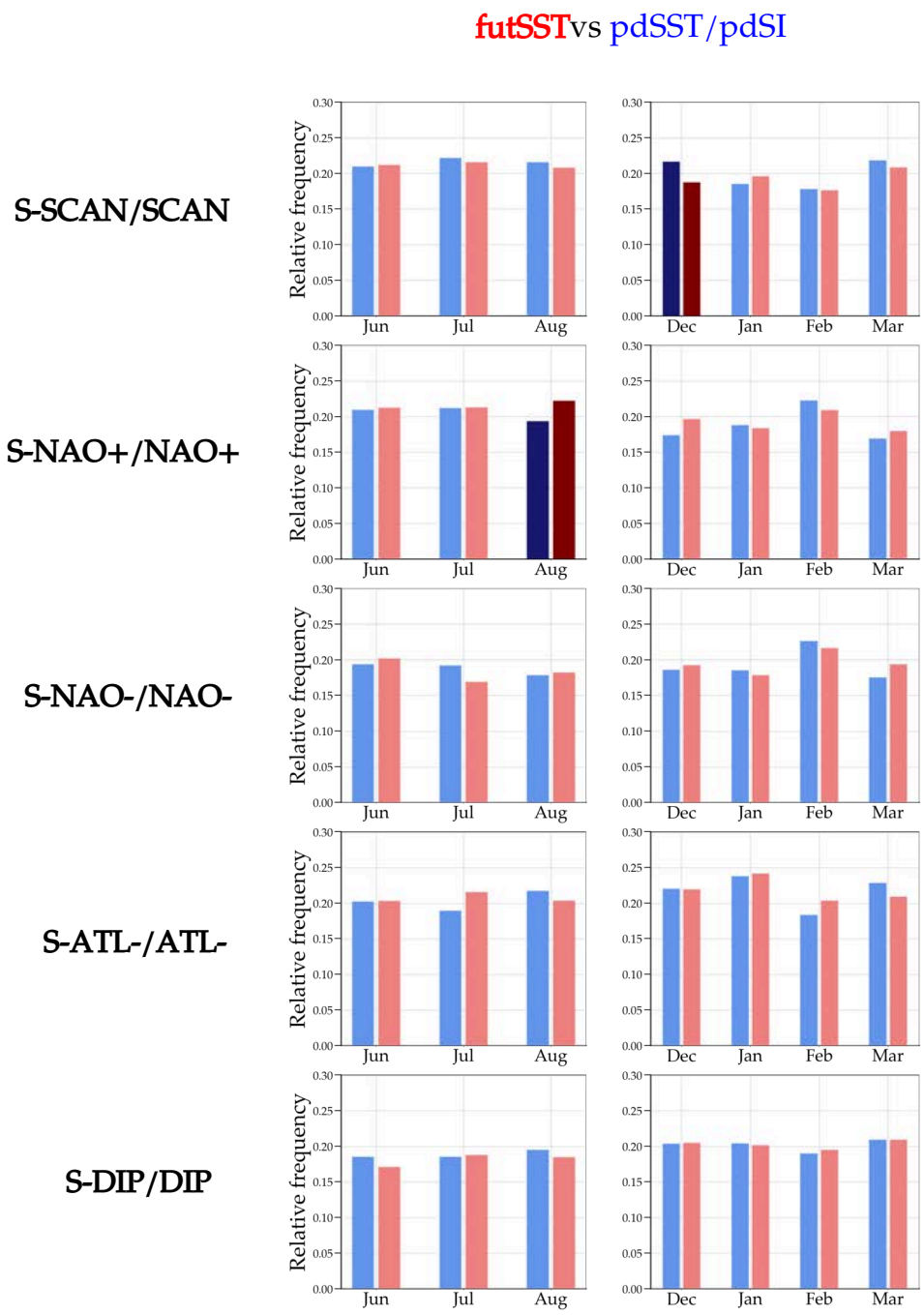

Figure 4.14: Similar to Fig. 4.12, but for winter and summer season and comparing the pdSST/pdSI reference experiment with the futSST simulation. Here, no ERA5 tendencies are shown.

4.3 CHANGES IN NORTHERN HEMISPHERIC TEMPERATURE EXTREMES INDUCED BY SEA ICE LOSS

This Section investigates how occurrence frequencies of temperature extreme events over the NH are affected in the ECHAM6 PAMIP sensitivity experiments. Subsection 4.3.1 therefore starts to investigate how the occurrence frequencies of temperature extremes over continental parts of the NH change in the PAMIP sensitivity simulations with respect to the reference pdSST/pdSI experiment. In particular, changes in occurrence frequencies of winter cold extremes, as well as warm extremes in summer and winter are discussed. Results for wind extremes are shown in the appended Sec. B.2. After presenting these changes in occurrence frequencies based on exceedances of moderately high thresholds, Sec. 4.3.2 discusses how the magnitude of very rare extreme temperature events is affected in the sensitivity simulations when compared to the reference experiment. Based on a fit of a *Generalized Extreme value* distribution to annual temperature maxima and minima, 10, 20 and 50-year temperature return levels are computed for the different PAMIP experiments over Northern Hemispheric continental regions. This allows to finally compare return levels computed from the PAMIP sensitivity experiments with the ones calculated for the pdSST/pdSI reference simulation.

4.3.1 *Extreme occurrence frequency changes*

As already explained in Section 3.3.2, temperature (and wind) extreme occurrences are defined as exceedances (or drops below) of a threshold value, e.g. termed T_{ref}. The threshold values are defined for each month separately and are computed based on 0.95/0.05 distribution quantiles in the pdSST/pdSI reference simulation.

In order to investigate changes in extreme occurrence probabilities Pr between the different PAMIP simulations, the extreme occurrence ratio for e.g warm extremes is defined as

$$\rho = \frac{\Pr\left(\mathrm{T_o} > \mathrm{T_{ref}}\right)}{\Pr\left(\mathrm{T_1} > \mathrm{T_{ref}}\right)}, \tag{4.1}$$

where T_0 denotes daily T2max values in some sensitivity experiment and T_1 in the pdSST/pdSI reference simulation. Note, that as the definition of extremes is based on 0.95/0.05 quantiles in pdSST/pdSI, the denominator's value in 4.1 is constantly 0.05 for each month.

Winter cold extremes

Figure 4.15 depicts the overall occurrence ratio ρ of cold extremes over continental parts of the NH, comparing the extreme occurrence probabilities in the futArcSI and futBKSI experiments with the reference simulation. Figure 4.15 indicates a general tendency towards less frequent cold extreme occurrences in the sea ice sensitivity experiments over mid-latitude to subpolar regions. From a thermodynamical perspective this observation is consistent with the fact that more open water areas and the associated increased surface temperatures in the sensitivity runs provide an additional energy source to the atmosphere.

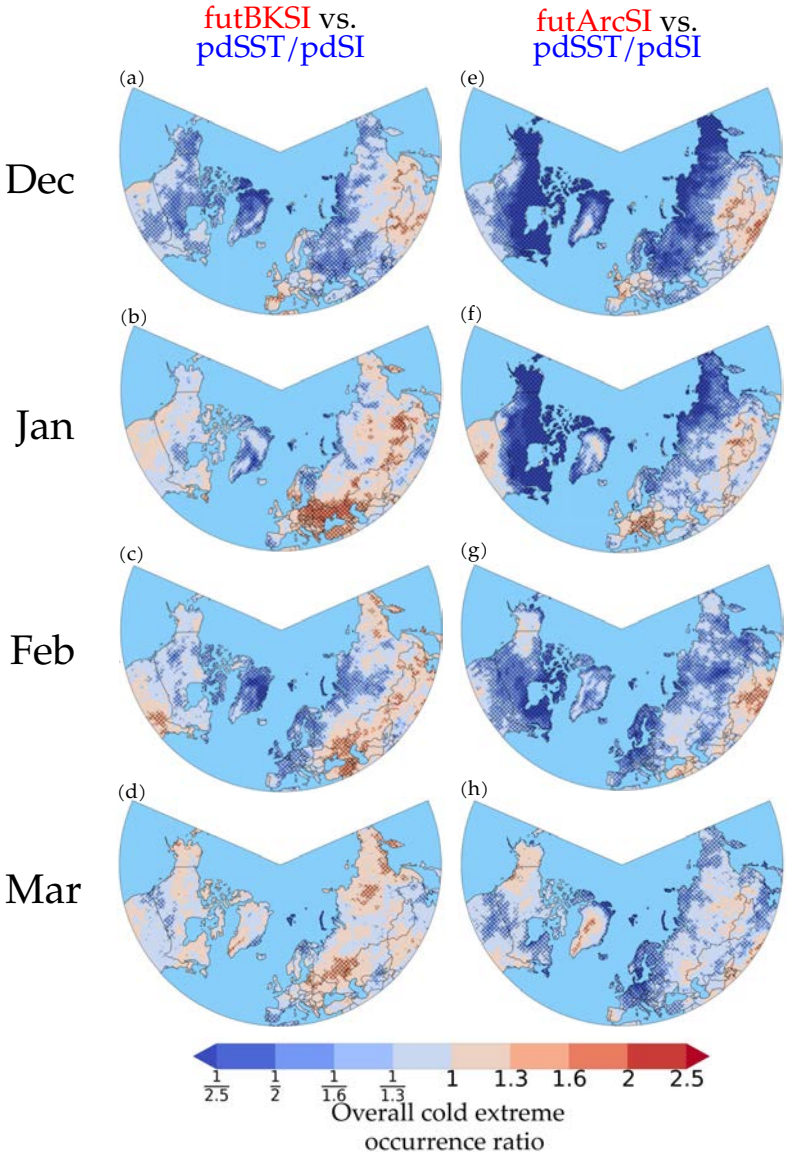

Figure 4.15: Cold extreme occurrence ratio for December, January, February and March. The occurrence probabilities of Northern Hemispheric continental cold extremes are compared between the sea ice sensitivity experiments (more frequent occurrences red) and the pdSST/pdSI reference simulation (more frequent occurrences blue). Left column (a)–(d): futBKSI sensitivity simulation. Right column (e)–(h): futArcSI sensitivity experiment. Hatching indicates regions where the ratio differs significantly from unity based on a moving block bootstrap with $M = 1000$.

However, the spatial pattern and the signals' magnitude strongly depend on the specific month and whether SI is reduced over the entire Arctic (see Fig. 4.15e-h) or just over the BKS (see Fig. 4.15a-d). Although spatial tendencies show to some extent relatively similar patterns in both sensitivity simulations, futArcSI exhibits much more pronounced reductions in cold extremes by a factor of more than 2.5 over high northern latitudes. Contrary, some parts over Mid-and Northern Eurasia show more frequent cold extreme occurrences in futBKSI from January to March. This observation is consistent with the frequently reported Eurasian cooling response to sea ice loss in the BKS (Cohen et al., 2018), that has

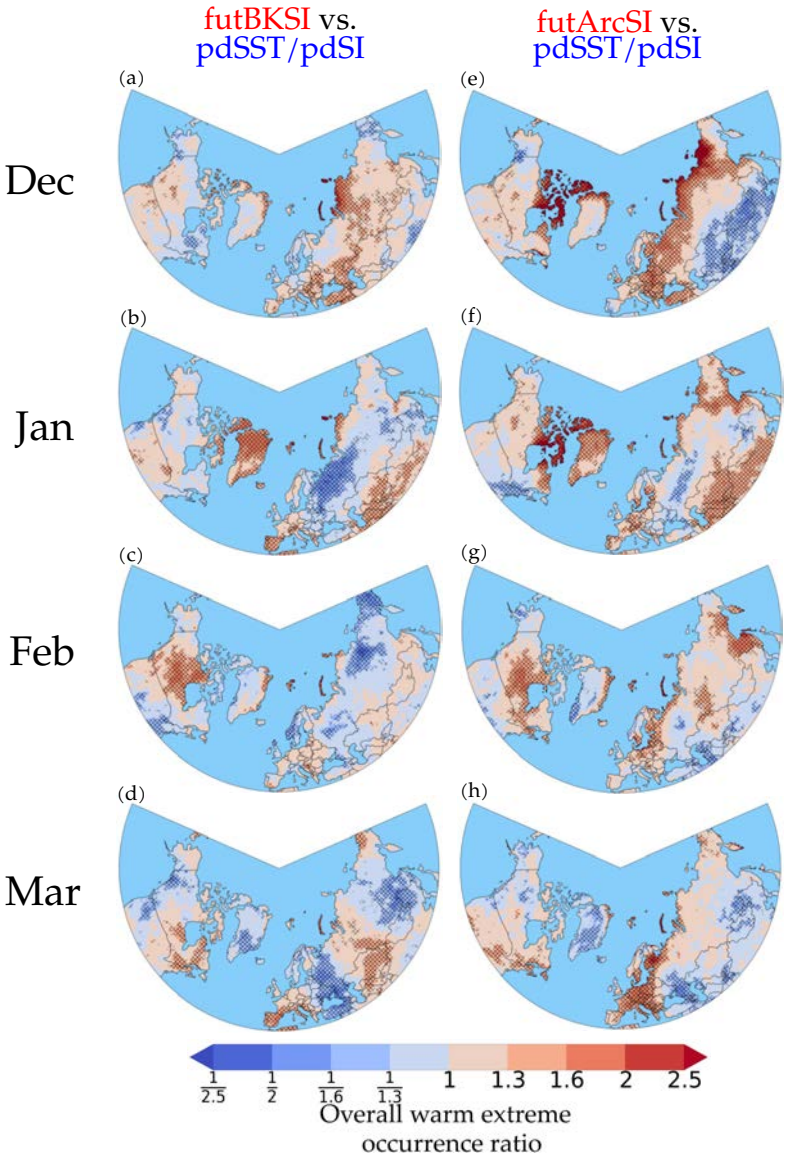

Figure 4.16: Same as in Fig. 4.15, but for winter warm extremes.

been associated with a strengthening of the Siberian high. Over Europe significant reductions of cold extreme occurrences can be observed in futBKSI in February (Fig. 4.15c), as well as in the futArcSI simulation in February and March (Figs. 4.15g and h). Interestingly, January tends to exhibit slightly more cold extremes over Central and Eastern Europe in both sensitivity simulations (Figs. 4.15b and f).

Winter warm extremes

As illustrated in Fig. 4.16 significant changes in the occurrence of warm extremes are generally less pronounced compared to cold extremes. This observation is consistent with Screen (2014) who argued that Arctic amplification leads to reduced subseasonal temperature variability over the mid-to high latitude NH. In particular, he showed that this variability decrease can be partly explained by a stronger warming of northerly winds (less

frequent/severe cold days) compared to a weaker warming of southerly winds (more frequent/severe warm days).

Over Europe an overall tendency towards more frequent occurrences of warm extremes can be reported, especially under diminished Arctic sea ice conditions in the futArcSI simulation (Figs. 4.16e-h). In many regions and month reductions in cold extreme occurrences are accompanied by increased probabilities of warm extremes. This might be associated with an overall thermodynamical shift of the underlying temperature distribution due to reduced sea ice concentrations and warmer surface temperatures in the sensitivity experiments. For futArcSI this is e.g. the case over northern Siberia in December (Figs. 4.15e and 4.16e), or over Europe in March (Figs. 4.15h and 4.16h). However, several regions such as Central Europe in February show for instance in futBKSI reductions in cold extreme occurrences, but no significant complementary changes in warm extremes (Figs. 4.15c and 4.16c). Such asymmetric responses in the tails of the temperature distributions could be thermodynamically explained by a stronger warming of northerly polar winds compared to southerly winds as argued by Screen (2014). Nevertheless, such responses could also be a result of other contributing factors, such as changes in the dynamical situations leading to certain extremes. In rare cases, such as over Central and Eastern Europe in January, the futArcSI experiment even shows an increased occurrence probability in both, cold and warm extremes (Figs. 4.15f and 4.16f). This might be also interpreted as an overall increase of temperature variability over the respective regions.

Summer heat extremes

Similar to Figs. 4.15 and 4.16, Fig. 4.17 illustrates summer heat extreme occurrence ratios. Compared to winter season, an overall tendency towards more frequent warm extreme occurrences in the sea ice sensitivity experiments is less clear. However, for instance in July both sensitivity simulations show significantly more frequent occurrences of summer heat extremes over Central and Northeastern Europe (Figs 4.17b and f). In futBKSI increased warm extreme occurrences over Central Europe can also be detected in June (Fig. 4.17a). Even less frequent occurrences can be e.g. observed in futArcSI over Southeastern Europe in August (Fig.4.17g), or in futBKSI over parts of Eastern Siberia in July (Fig. 4.17b). Nevertheless, when contrasted to the signals in winter season, the responses of summer heat extreme occurrences appear to be weaker and more noisy. Assuming that changes in extreme occurrences are predominantly driven by changes in atmospheric dynamics, this observation is consistent with the relatively small and mostly insignificant impact of SI loss on summer regime occurrence frequencies (see Fig. 4.13).

Occurrence frequency changes in futSST

Figure 4.18 illustrates the same analysis of temperature extremes, but for the futSST sensitivity experiment. In contrast to the sea ice sensitivity simulations, futSST exhibits pronounced and significant increases (decreases) of warm (cold) extreme occurrences over the vast majority of Northern Hemispheric continental regions. Again, winter responses appear to be more pronounced compared to summer. Over many regions the occurrence frequency of warm (cold) extremes increases (decreases) by a factor of 2–3.

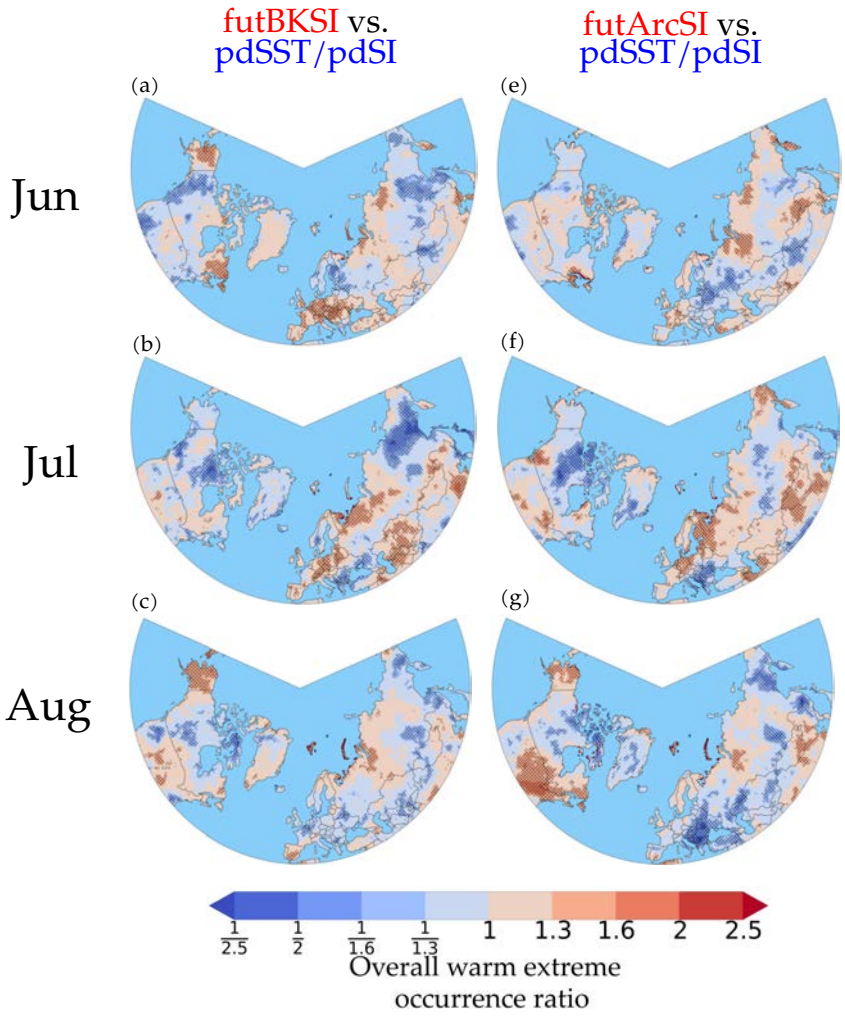

Figure 4.17: Same as in Fig. 4.15, but for heat extremes in different summer months.

The order of magnitude of theses changes is comparable to changes in occurrence frequencies of European temperature extremes over the last 70 years (e.g. Lorenz et al., 2019). Nevertheless, such an overall strong and large-scale response to globally increased SSTs may intuitively suggest that the changes are primarily thermodynamically driven. Indeed, it was already observed that at least within the framework of circulation regimes changes in atmospheric dynamics are mostly absent in futSST (see Fig. 4.14). This may support the notion that the striking changes in extreme occurrence frequencies can be solely explained by thermodynamical arguments. However, this topic will be addressed in more detail in Sec. 4.5.

Winter wind extremes

Results for winter wind extremes are shown in the appended Fig. B.2. In both sea ice sensitivity experiments changes in winter wind extreme occurrence frequencies are absent over the overwhelming majority of Northern Hemispheric continental regions. Consistent with the mean strengthening of mean zonal winds in Fig. 4.3i, futSST shows especially in

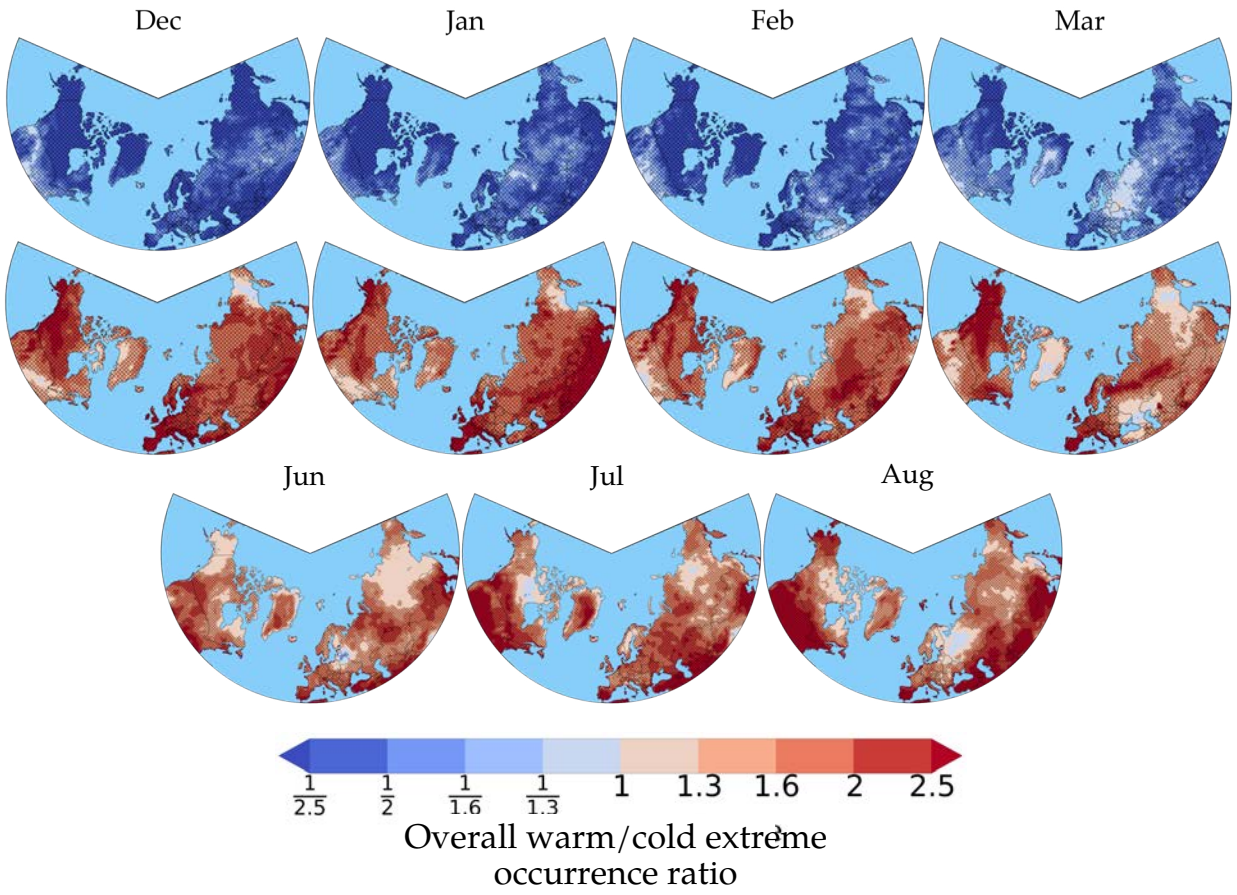

Figure 4.18: Same as in Figs. 4.15–4.17, but for the futSST experiment. Shown are occurrence ratios for winter cold extremes (upper row), winter warm extremes (middle row) and summer heat extremes (bottom row).

December and January more frequent wind extreme occurrences over mid- to subpolar latitudes.

4.3.2 *Temperature return level changes*

Until now, changes in extreme occurrence frequencies were solely based on exceedances (or drops below) of threshold values that were defined as 0.95 (0.05) distribution quantiles in pdSST/pdSI. The choice of these relatively high (low) quantiles ensured a decent compromise between characterizing changes in the tail behavior of the probability distributions while still having a sufficiently large number of extreme events defined. If one would be interested in more rare extreme events, more extreme quantiles may be chosen for the threshold definitions (e.g. 0.99 or 0.999). However, this would dramatically reduce the number of extreme events in the respective simulations, making it even more difficult to detect significant extreme frequency changes—especially in the sea ice sensitivity experiments. In this respect, Naveau et al. (2020) stressed that when using such a non-parametric binomial counting approach the return period of interest should always

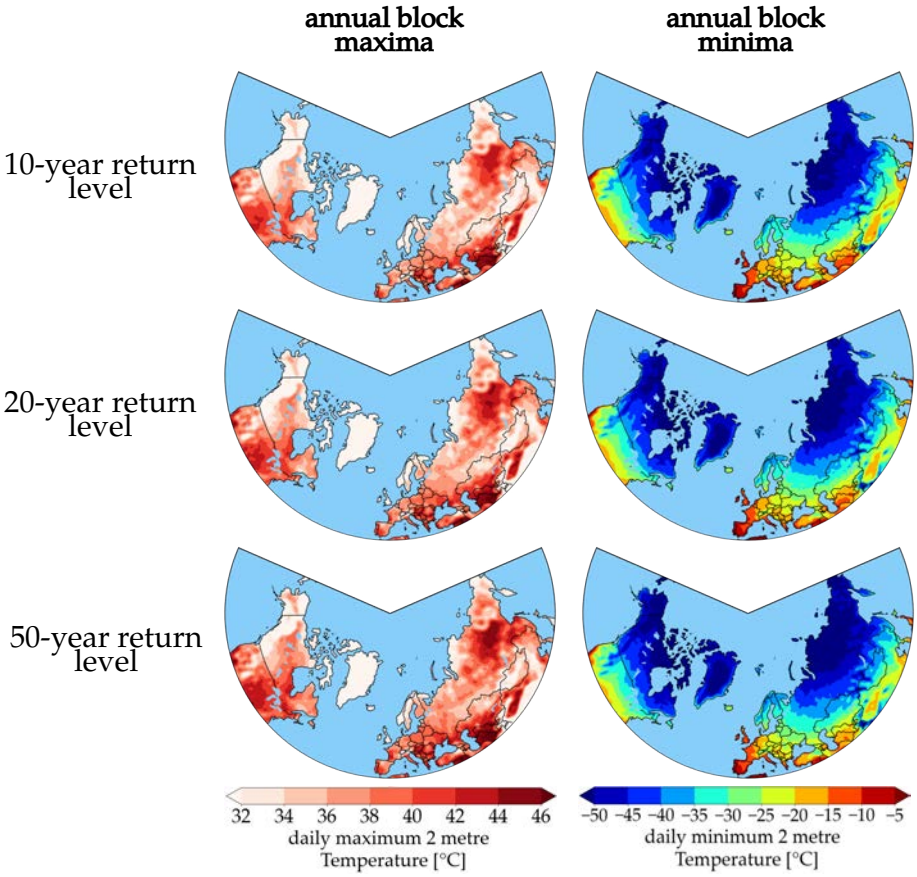

Figure 4.19: 10, 20 and 50-year temperature return levels based on a GEV fit to annual T2max maxima (left column) and T2min minima (right column) of the pdSST/pdSI reference simulation.

be much smaller than the available sample size[7]; otherwise, confidence intervals of frequency changes explode and become useless.

In order to study such very rare extremes (or sometimes even to extrapolate beyond the length of the available data set), *Extreme Value Theory* offers an attractive and well–established alternative to the non-parametric counting approach. For instance, the probability $Pr(X > x|X > v)$ that some variable X exceeding a sufficiently large threshold v is greater than x can be parameterized by a *Generalized Pareto Distribution* (see e.g. Coles, 2001). However, the upcoming analysis complements the previous investigations by employing the probably most basic concept of classical extreme value theory—the so-called block maxima approach (e.g. Coles, 2001).

The essence of this approach can be summarized as follows: at each grid point and for each PAMIP experiment the annual maxima (minima) of the 100-year long daily T2max (T2min) time series are respectively extracted. Afterwards, a *Generalized Extreme Value* (GEV) distribution is fitted to the resulting 100 annual maxima/minima. Based on the fitted GEV parameters estimates and confidence intervals for return levels—a widely used measure of extreme events—are subsequently computed. For instance, a 10-year return level computed from annual block maxima of T2max refers to the temperature that is on average exceeded by an annual maximum of daily T2max once every 10 years.

7 choosing e.g. the 0.99 (0.999) quantile for a sample size of 100 simulated winters would result in threshold that corresponds to a 1 (10)-year return period in the pdSST/pdSI simulation

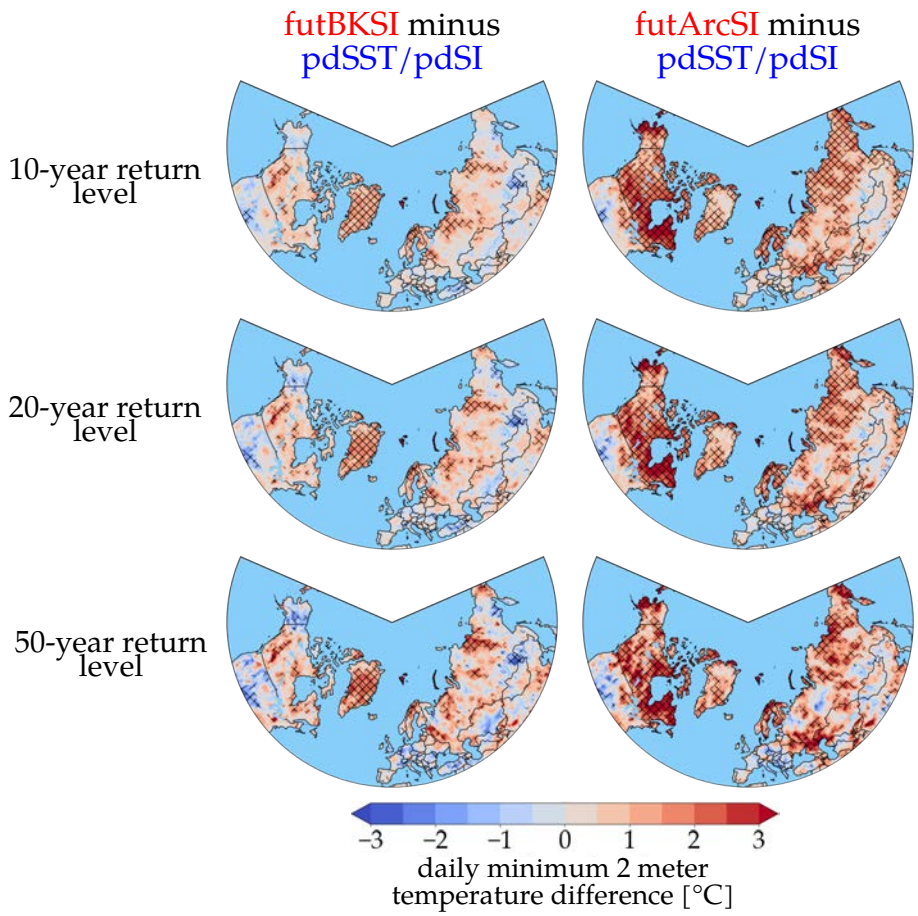

Figure 4.20: Differences in 10, 20, 50-year return levels calculated from annual minima of daily T2min. Left column: futBKSI minus pdSST/pdSI. Right column: futArcSI minus pdSST/pdSI. Hatching indicates that differences significantly differ from zero, as described in Section A.5.2.

Similarly, an annual block minima of daily T2min falls below the 10-year return level on average once every 10 years. For more details on the foundations of the block maxima approach, the calculation of return levels and their confidence intervals see Sec. A.5.

Annual minima

The right column in Fig. 4.19 displays the 10, 20 and 50-years return levels derived from annual minima of daily T2min in pdSST/pdSI. It can be for instance observed that over Central Europe an annual minimum T2min of -20°C can be expected on average once every 10 years, while the 50-year return level is associated with temperatures reaching down to -25°C.

Northern Siberia and Canada, as well as Central Greenland exhibit temperatures down to -50°C for all illustrated return periods. In order to assess how future Arctic SI loss may affect such very rare cold extremes over the NH, Fig. 4.20 depicts return level differences for annual minima of T2min between the sea ice sensitivity experiments and the pdSST/pdSI reference simulation. It appears that especially in futArcSI temperature return levels of annual minima experience a significant warming by up to 3°C. This result is consistent with

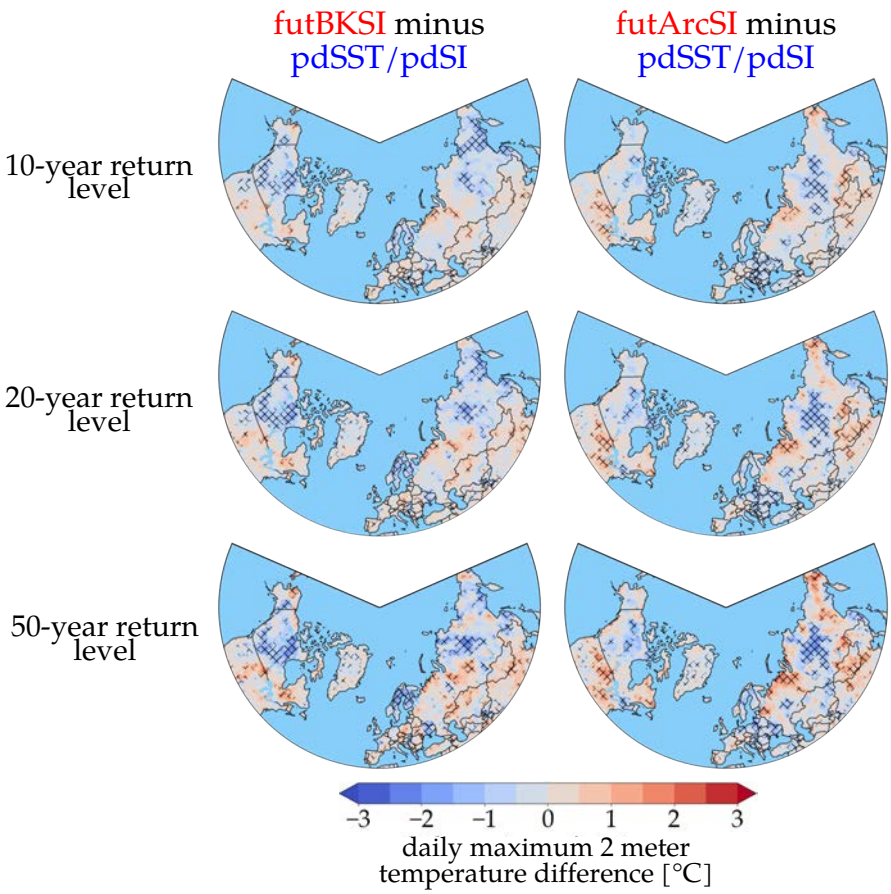

Figure 4.21: Differences in 10, 20, 50-year return levels calculated from annual maxima of daily T2max. Left column: futBKSI minus pdSST/pdSI. Right column: futArcSI minus pdSST/pdSI. Hatching indicates that differences significantly differ from zero, as described in Section A.5.2.

Fig. 4.15, where strong reductions of cold extreme occurrences were detected over the same regions. In contrast, return level increases in futBKSI are much less pronounced compared to futArcSI.

Overall, the return level differences show similar spatial patterns for the illustrated return periods. Some regional differences in this respect between the illustrated return periods can be related to changes the tail behavior[8] of the fitted GEV distribution. Uncertainties for return level estimates generally increase for longer return periods; hence, especially for futArcSI less significant differences can be found for return levels corresponding to longer return periods.

Annual maxima

The left column in Fig. 4.19 displays the 10, 20 and 50-years return levels derived from annual maxima of daily T2max in pdSST/pdSI. Figure 4.21 shows return level differences for annual maxima of T2max between the sea ice sensitivity experiments and the pdSST/pdSI ref-

8 that is determined by the shape parameter ξ. Fitted temperature GEV distributions over the NH were on average Weibull-like, with $\xi < 0$.

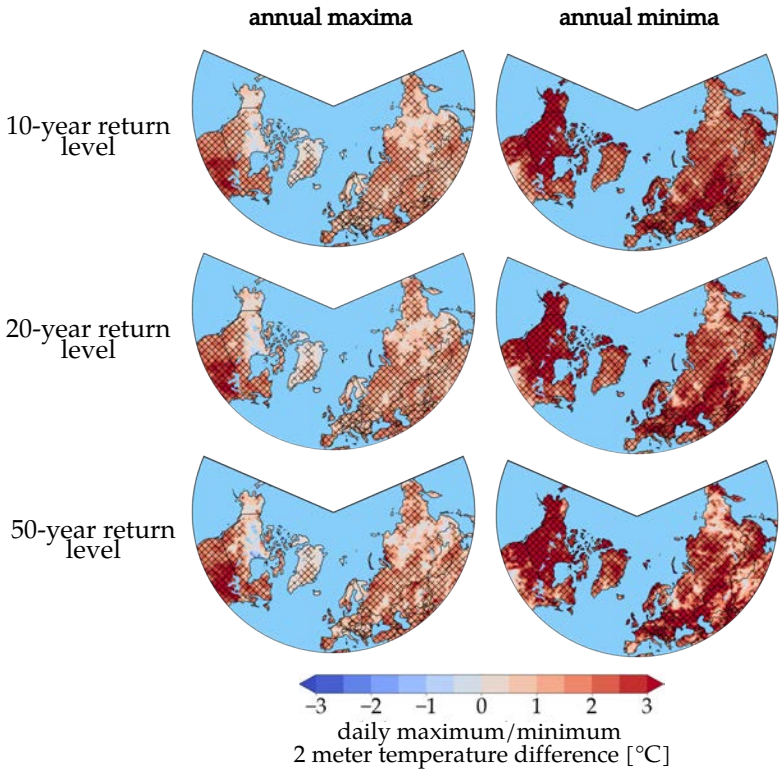

Figure 4.22: Temperature return level differences as in Figs. 4.20 and 4.21, but for futSST minus pdSST/pdSI. Left column: return level differences computed from annual T2max maxima. Right column: return level differences computed from annual T2min minima.

erence simulation. Consistent with frequency changes of summer warm extremes shown in Fig. 4.17, the return level changes in Fig. 4.21 are rather weak and noisy. In both sea ice sensitivity experiments, a cooling over Central Siberia and Canada can be reported for all return periods. In futBKSI, e.g. a cooling of return levels over Scandinavia is also detected.

Return level changes in futSST

Return level differences computed from annual minima and maxima of the daily temperature time series in the futSST experiment are shown in Fig. 4.22. Similar to the previous Subsection, the globally increased SSTs lead to a strong hemispheric–wide warming of the 10, 20 and 50-year return levels. Especially return levels associated with annual minima reveal temperatures increases by more than 3°C over e.g. Canada or Europe. Consistent with Fig. 4.18, return levels computed from annual maxima show more moderate temperature increases of around 1—2°C over most regions.

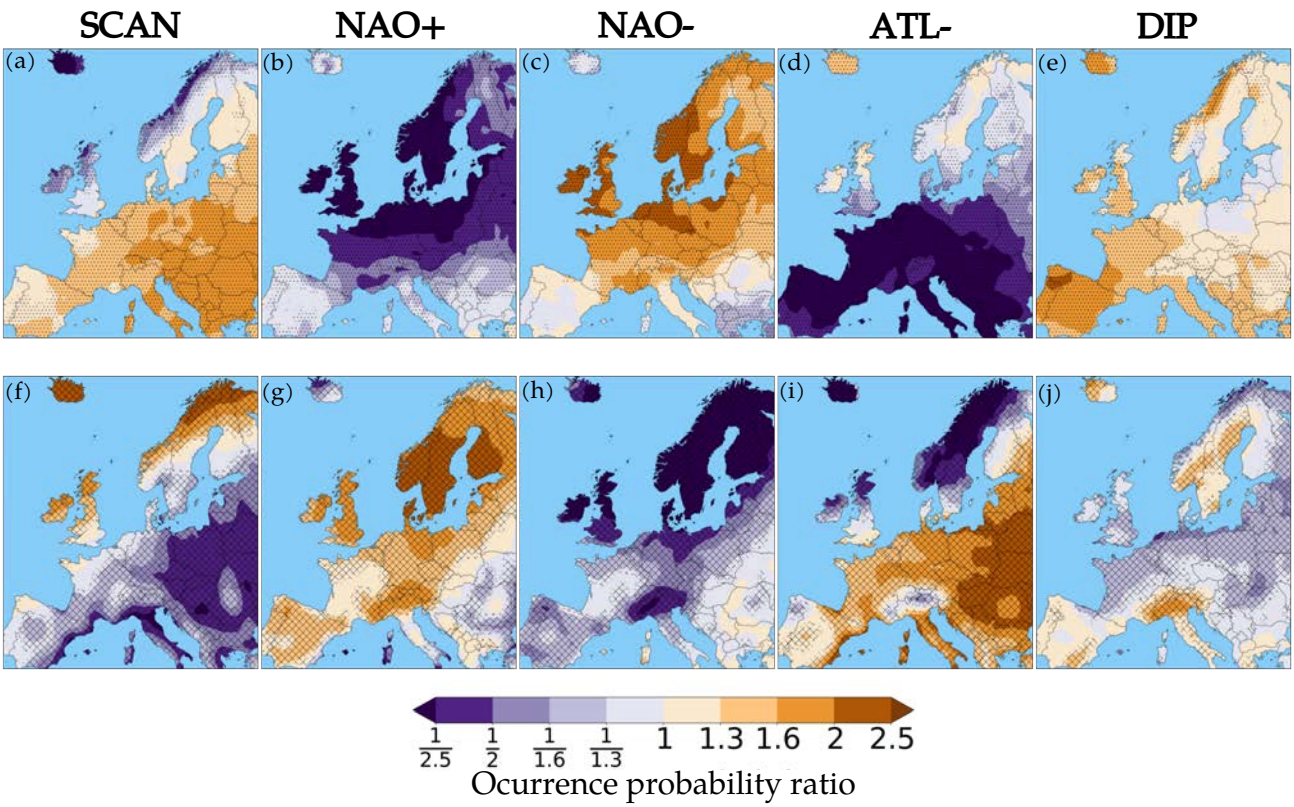

Figure 4.23: Temperature extreme occurrence probability ratios (DJFM) for different winter circulation regimes plotted over the European domain using the ECHAM6 PAMIP pdSST/pdSI simulation. Upper row (a–e): cold extremes, bottom row (f–j): warm extremes. The plotted ratio compares the occurrence probability of an extreme day given a certain circulation regime to the unconditioned probability of extreme occurrence. Thus, values greater than one at a specific grid point indicate a preferred extreme occurrence during the presence of a certain regime compared to the overall extreme occurrence. Hatchings indicate ratios that are significantly different from unity based on a moving bootstrap with $M = 1000$.

4.4 LINKS BETWEEN CIRCULATION REGIMES AND EXTREMES OVER EUROPE

This Section investigates which of the computed circulation regimes already presented and analyzed in Sec. 4.2 can be linked to preferred occurrences of temperature extremes over Europe. This will help to identify suitable regime storylines for the upcoming Sec. 4.5, where extreme frequency changes are decomposed into dynamically and thermodynamically induced contributions.

4.4.1 *Winter temperature extremes*

Figure 4.23 compares the occurrence probability of DJFM temperature extremes given a specific winter circulation regime to the unconditioned probability of extreme occurrence. Thus, a ratio of e.g. two at some grid point means that, given the presence of a circulation regime at some day, an extreme occurs twice as likely compared to some arbitrary day. The results in this Section are based on data from the pdSST/pdSI reference simulation. Re-

sults for the different sensitivity model experiments are however qualitatively extremely similar.

Overall, it can be summarized in advance that the findings from Fig. 4.23 are highly consistent with the dynamical drivers of winter temperature extremes already outlined in Sec. 2.4.2. Figure 4.23c shows that the presence of the NAO- regime is associated with an up to more than doubled probability than usual of cold extreme days over large parts of Mid- to Northern Europe (see e.g. Cattiaux et al., 2010; Andrade et al., 2012; Screen, 2017b). Indeed, Fig. B.7c shows that NAO- events are related to easterly/northeasterly wind anomalies which consequently lead to favored cold air advection of continental air masses towards Northern Europe. These easterly anomalies can generally also be related to a suppressed advection of warmer maritime air masses, favoring colder conditions over Europe. As shown in Riebold et al. (2023), up to 40% of NAO- regime days are associated with atmospheric blocking activity over Greenland and the North Atlantic. As already outlined in Sec. 2.4.2, blocking conditions over North Atlantic regions have previously been linked to European winter cold spells as well (Sillmann et al., 2011).

In addition to the NAO- regime, preferred occurrences of cold extremes over Central and Eastern Europe are reported during SCAN days (see Fig. 4.23a). Links between anticyclonic systems over Scandinavian/Ural regions and cold days over large parts of Europe have been detected previously (Petoukhov et al., 2010; Andrade et al., 2012). As shown in Fig. B.7a, Scandinavian high pressure systems are typically associated with easterly/northeasterly wind anomalies over Eastern and Central Europe. This results in anomalously strong advection of cold continental air masses towards Central Europe during SCAN regime days (Bieli et al., 2015).

Additionally, Fig. 4.23e indicates preferred cold extreme occurrences over most parts of Western Europe during the presence of the DIP regime. This link is related to a favored southward advection (see also Fig. B.7e) of cold air masses from the Fram Strait region during DIP days (see also Bieli et al., 2015).

Warm days in winter over large parts of Central, Eastern and Southern Europe occur preferably during the presence of the ATL- regime (see Fig. 4.23i). As shown in Fig. B.8a, around and westwards of the British Isles the ATL- regime is associated with enhanced baroclinic activity. This consequently results in an eastward extension of the North Atlantic storm track towards Western Europe. Therefore, more storm systems than usual may advect warm and moist Atlantic air masses towards Mid-and Southern Europe. This can also be related to the westerly/southwesterly wind anomalies towards Southern and Central Europe shown in Fig. B.7d.

Complementary, as shown in Fig. 4.23g warm days over Scandinavia are linked to the presence of the NAO+ regime. As already outlined in Sec. 2.4.2 warm extremes over Northern Europe are linked to a strengthened westerly transport of moist Atlantic air masses during NAO+ events, resulting in enhanced latent energy transport towards Scandinavia (see e.g. Vihma et al., 2020, and Fig. B.7b). As shown in Fig. B.8b this is also related to a northward tilt of the North Atlantic stormtrack towards Northern Europe and the Arctic.

The same analysis but done for ERA5 data over the period 1979–2018 is shown in Fig. B.3. Indeed, results for ERA5 are qualitatively extremely similar to the PAMIP results discussed above. Only the link between NAO+ days and preferred occurrences of warm winter days extends more towards Mid-and Southern Europe in the reanalysis.

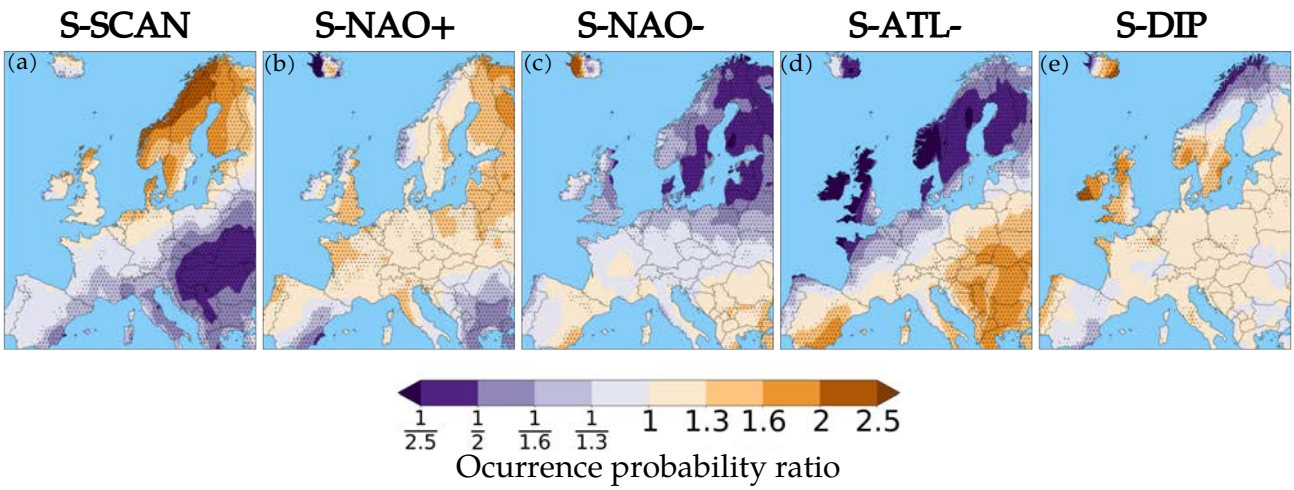

Figure 4.24: Same as in Fig. 4.23, but for heat extremes in summer (JJA). Stippling indicates ratios that significantly differ from unity based on a moving block bootstrap ($M = 1000$).

4.4.2 *Summer heat extremes*

Similar to Fig. 4.23, Fig. 4.24 compares the occurrence probability of JJA heat extremes given a specific summer circulation regime to the unconditioned probability of extreme occurrence. Overall, it appears that compared to winter season the respective summer regimes do not show similar large-area associations with preferred extreme occurrences over Europe.

As mentioned in Sec. 2.4.2, heat extremes in summer are typically co-located with quasi-stationary barotropic high pressure systems (termed blocking). Indeed, the S-SCAN regime with its anticyclonic center over Scandinavia is linked to preferred occurrences of heat extremes over Northern Europe (see Fig. 4.24a). This link can also be observed in ERA5 (see Fig. B.4), where even heat days over Western Europe occur more often during S-SCAN regime occurrences. Daily flows that show blocking structures over other European regions are allocated among the different summer regimes. In this respect, Fig. 4.24d for instance suggests that heat days over the Balkans occur more frequently during the presence of the S-ATL- regime; however, this link is barely found when conducting the same analysis for ERA5 (see Fig. B.4).

A potential solution within the employed methodological framework would be to increase the number of computed circulation regimes until some more distinct regional blocking structures over some European region can be identified in some regime pattern. However, this issue will be addressed in Sec. 4.6 with a circulation analogue-based approach.

4.4.3 *Winter wind extremes*

Wind extremes are mostly associated with intense cyclones. The appended Fig. B.5 (and B.6 for ERA5) indicates that extreme winter wind speeds over Southern, Central and Western Europe occur anomalously often during ATL- days. This is related to the aforementioned eastward extension of the North Atlantic stormtrack associated with ATL-.

In addition, especially the model experiment (Fig. B.5) shows that winter wind extremes over Northern Europe are predominantly associated with the NAO+ regime. Here, the poleward tilt of the stormtrack results in more frequent cyclones traveling towards Northern Europe.

4.5 DECOMPOSITION OF SEA ICE-INDUCED FREQUENCY CHANGES IN EUROPEAN WINTER EXTREMES

This Section aims to identify dynamically and thermodynamically induced contributions to changes in European temperature extreme occurrence frequencies found in the sea ice sensitivity experiments. Dynamically induced changes in the occurrence frequencies of certain local extreme events are related to changes in the relevant dynamical conditions, e.g., in terms of more frequent occurrences of some atmospheric flow pattern that promotes the occurrence of an extreme. In contrast, thermodynamical contributions are typically associated with changes of extreme probabilities that would also occur in the absence of any relevant dynamical changes (e.g. due to overall global warming). From a methodological point of view it is however challenging to clearly separate dynamical and thermodynamical components. This issue is related to the fact that there is generally no unique way to define and detect changes in all contributing dynamical and non-dynamical factors that impact a certain class of extreme event. Nevertheless, a variety of approaches have been outlined over the years that aim to decompose atmospheric responses into thermodynamical and dynamical contributions (e.g. Yiou et al., 2017; Deser et al., 2016; Vautard et al., 2016; Cassano et al., 2007).

In this thesis a framework for conditional extreme event attribution is utilized (Yiou et al., 2017). This method provides a suitable approach for decomposing changes in extreme event occurrence frequencies when employing the framework of circulation regimes. For a more detailed mathematical description of the decomposition see Appendix A.6. The general philosophy of this methodology is to assume that an extreme event at some grid point does occur during the presence of some reference regime C_{ref}. Following the storyline approach (Trenberth et al., 2015; Shepherd, 2016), one may also say that the storyline of C_{ref} can explain the occurrence of the extreme event.

By employing Bayes' formula, the overall extreme occurrence ratio ρ between sensitivity and reference experiment (see Eq. 4.1) can be decomposed into

$$\rho = \rho_{\text{FR}} \cdot \rho_{\text{CR}} \tag{4.2}$$

The first term ρ_{FR} ("Fixed-Regime") considers changes in extreme occurrences between sensitivity and reference simulation for fixed atmospheric dynamics. Therefore, the probability of extreme occurrence during the presence of a reference regime C_{ref} is computed and compared between the sensitivity and reference experiment. This terms has previously been named "thermodynamical" contribution (Yiou et al., 2017), as the atmospheric circulation is fixed in terms of circulation regimes. Nevertheless, caution is needed when using such names as this term to a certain extent assumes that the regime pattern structures do not change between both experiments. As already discussed in Fig. 4.6, for weak forcings this might be a reasonable assumption (see also Palmer, 1999). In addition to this, the individual daily SLP patterns that are associated with the reference regime C_{ref} may also differ between both simulations.

The term ρ_{CR} ("Changed-Regime") in 4.2 relates changes in extreme occurrences to changes in regime occurrence frequencies. It has therefore previously also been termed "dynamical" contribution (Yiou et al., 2017).

Based on the previously detected regime frequency changes in the ECHAM6 PAMIP sensitivity experiments (Secs. 4.2.2 and 4.2.3), but also on the identified links between circulation regimes and extreme occurrences (Sec. 4.4), the following decompositions are considered:

- *Midwinter cold extremes along a SCAN storyline*: in Figs. 4.12a and f, a significant increase of January SCAN occurrences was detected in both sea ice sensitivity experiments, for futBKSI also in February. Furthermore, Fig. 4.23a shows that cold extremes over of Eastern and Central Europe occur anomalously often during SCAN days.
- *January warm extremes along a ATl- storyline*: Figs. 4.12d and i illustrate decreased ATL-occurrences in January for futArcSI and futBKSI. In addition, Fig. 4.23i indicates that warm extremes over of Eastern and Central Europe are frequently linked to ATL-regime occurrences.
- *February warm extremes along a NAO+ storyline*: Fig. 4.12g depicts that the NAO+ regime occurs more frequently in futBKSI in February. Furthermore, Fig. 4.23g shows that warm extremes over Mid-and Northern Europe occur anomalously often during NAO+ days

The employed decomposition method assumes that the presence of the respective reference regime C_{ref} is necessary for an extreme to occur; hence, ρ_{CR} and ρ_{FR} are only plotted for regions where Fig. 4.23 shows statistically significant more frequent extreme occurrences during C_{ref}. Although Fig. 4.23 may indicate a statistical link between regime and extreme occurrence, one should bear in mind that some of the atmospheric SLP patterns allocated to the reference regime C_{ref} are just closer to the regime centroid than others. They do not necessarily have to be close to the actual circulation that typically prevails during an extreme event at some grid point.

4.5.1 *Midwinter cold extremes along a SCAN storyline*

Figure 4.25 shows the decomposition for the January cold extreme occurrence ratio ρ for futArcSI and futBKSI. It appears that Eastern and parts over Central Europe are associated with significantly more frequent cold extremes in the futBKSI simulation (Fig. 4.25a). The decomposition reveals that these signals can, especially over Central Europe, be associated with a significant contribution of the Changed-Regime term ρ_{CR} (Fig. 4.25c). This contribution is related to a 26% increase of SCAN regime occurrences in the futBKSI simulation in January. Such a dynamical contribution is however absent in more eastern parts of Europe, where the Fixed-Regime term ρ_{FR} significantly contributes to more frequent cold extreme occurrences (Fig. 4.25b). If ρ_{FR} was interpreted as a purely thermodynamical contribution, warmer surface temperatures over additional ice-free areas and the ensuing advection of these warmer air masses towards Eastern Europe (see Fig. B.7a) would be actually associated with less cold extreme occurrences. ρ_{FR} only compares the extreme occurrence probability during SCAN days, and as mentioned in the beginning of this Section the individual daily flow patterns allocated to the SCAN regime can differ between different experiments.

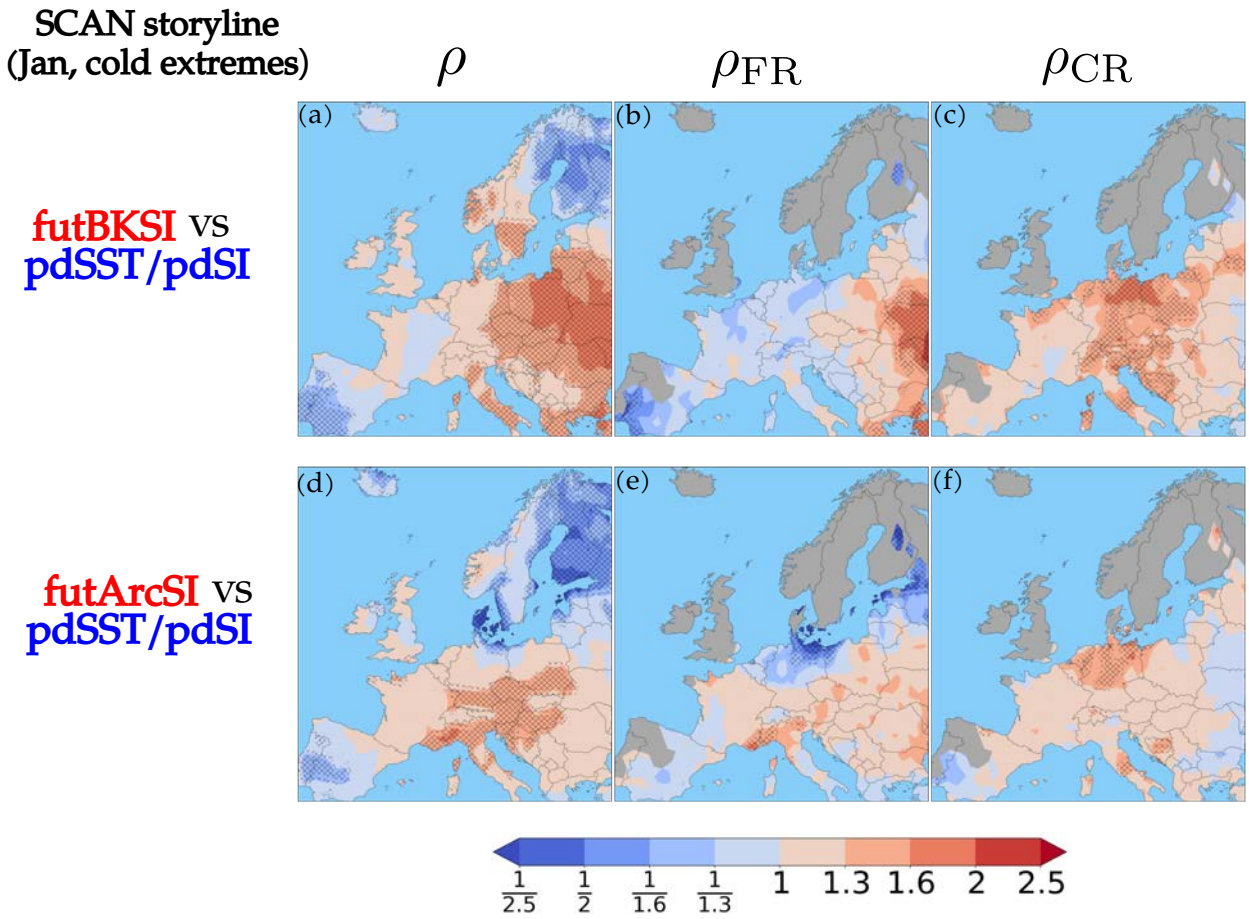

Figure 4.25: Conditional extreme event attribution framework applied for European cold extremes in January assuming a SCAN-storyline. Compared are the pdSST/pdSI reference simulation (blue indicates favored occurrence) with the futArcSI and futBKSI sensitivity simulation (red indicates favored occurrence). Upper row: futBKSI with a 26% increase of January SCAN occurrences. Bottom row: futArcSI with a 17% increase of SCAN occurrences in January. The first column shows the overall cold extreme occurrence ratio $\rho = \rho_{FR} \cdot \rho_{CR}$ between both simulations, the second column shows the Fixed-Regime contribution ρ_{FR}, the third one shows the Changed-Regime contribution ρ_{CR}. Hatching indicates regions where the ratios significantly differ from unity based on a moving block bootstrap (M=1000). ρ_{FR} and ρ_{CR} are only plotted for regions where preferred winter cold extreme occurrences during SCAN days were identified (see Fig. 4.23a).

Therefore, it can not be ruled out that the individual SCAN flow patterns in futBKSI could change in way that, instead of relatively warm maritime air masses from the BKS, more colder continental air masses are advected from the east. For such a scenario ρ_{FR} could actually indicate more frequent cold extreme occurrences over Eastern Europe in futBKSI.

The overall cold extreme response in futArcSI (Fig. 4.25d) shows a significantly increased probability of January cold extreme occurrences over some parts of Central-to Southern Europe. The increased cold extreme occurrence probability over central Europe shows how two non-significant contributions (Figs. 4.25e and f) can finally yield a significant overall response. In addition, decreased January cold extreme frequencies are detected over Northeastern Europe. However, as the SCAN storyline is not well-justified for cold

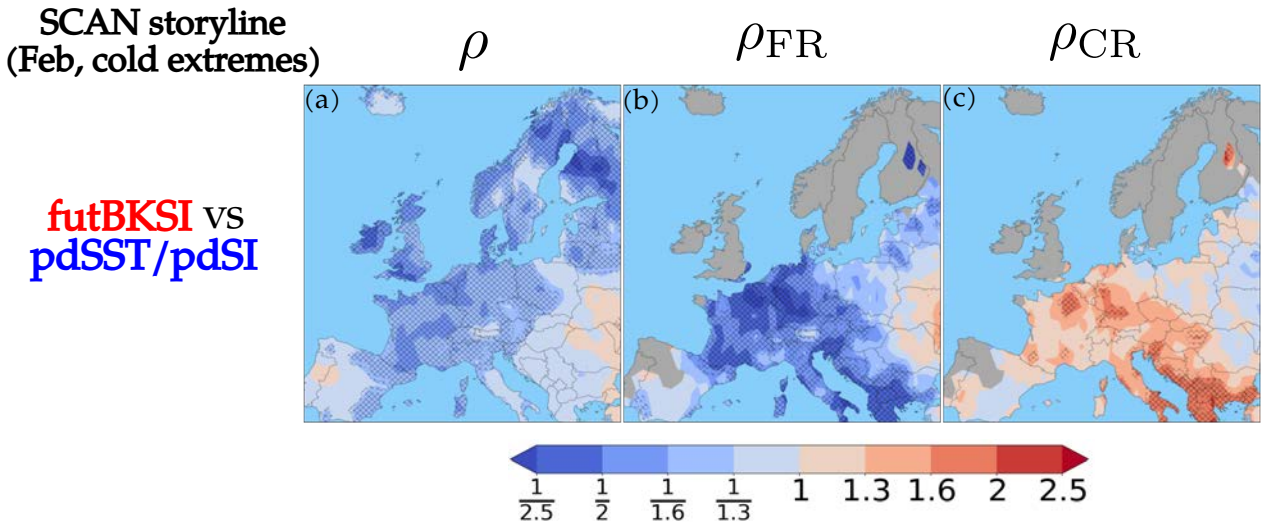

Figure 4.26: Same as in Fig. 4.25, but only for February cold extremes in futBKSI. Again, a SCAN storyline is assumed. February SCAN occurrences increase by 23% in futBKSI.

extremes over Northern Europe, the decomposition can not be reasonably interpreted for cold extreme frequency changes over these regions.

In February, strong frequency decreases of cold extremes over large parts of Western, Central and Northern Europe can be reported in the futBKSI simulation (Fig. 4.26a). In contrast to January, the predominant part of these changes is explained by the Fixed-Regime term ρ_{FR} (Fig. 4.26b). This might be indeed interpreted as an overall thermodynamical warming effect since more ice-free areas in the model simulations are typically associated with overall stronger ocean–to–atmosphere heat fluxes and consequently with warmer surface temperatures. As air masses from Northeastern Europe and the BKS frequently serve as source regions for advective processes that lead to cold spells over Central Europe (see Fig. B.7a or Bieli et al., 2015), an average warming of these reservoir regions may suppress the occurrence of cold extremes over Europe in futBKSI. As it can be seen for the Changed-Regime term ρ_{CR} in Fig. 4.26c, February frequency changes in SCAN occurrences basically tend to favor cold extremes over most parts of Europe. However, compared to the Fixed-Regime term ρ_{FR} these signals are relatively small and non-significant over most regions.

4.5.2 *January warm extremes along a ATl- storyline*

Figure 4.27 shows the decomposition for European warm extremes in January. Here, the ATL- regime was considered as the reference pattern C_{ref}. For futBKSI, the absence of significant signals in the overall warm extreme occurrence ratio over most parts of Europe (Fig. 4.27a) is especially over Mid- and parts of Eastern Europe a result of opposing ρ_{FR} (Fig. 4.27b) and ρ_{CR} (Fig. 4.27c) contributions. On the one hand, the reduced ATL- occurrence in the futBKSI simulation can be associated with less frequent advections of warm air masses by Atlantic storm systems (see Sec. 4.4.1). On the other hand, the aforementioned thermodynamical warming effect due to more open water areas and the subsequent advection towards Europe tend to favor the occurrence of warm extremes (see Fig. B.7d).

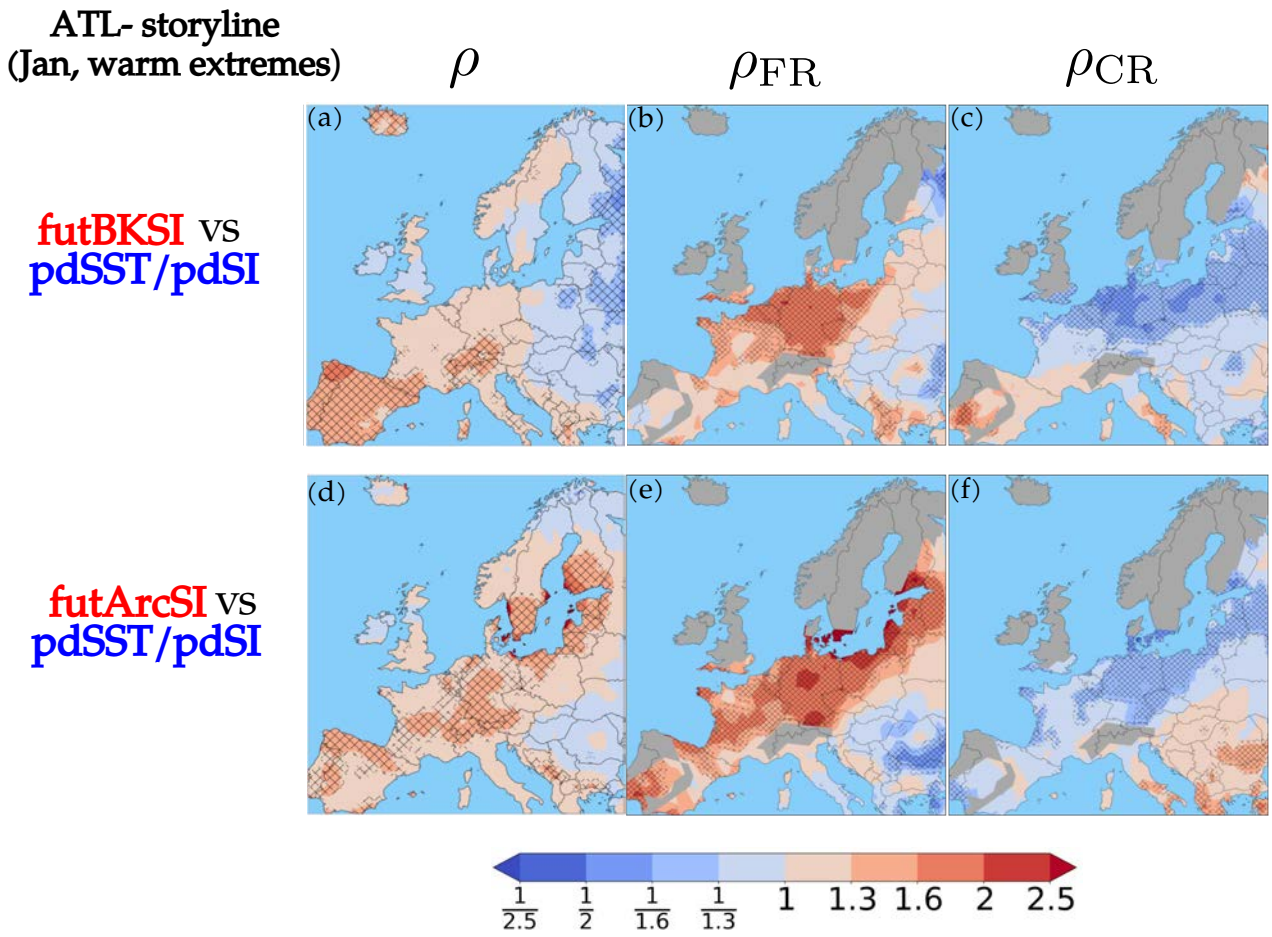

Figure 4.27: Same as in Fig. 4.25, but for January warm extremes and assuming a ATL- storyline. Upper row: futBKSI with a 20% decrease of January ATL- occurrences. Bottom row: futArcSI with a 21% decrease of ATL- occurrences in January. ρ_{FR} and ρ_{CR} are only plotted for regions, where statistically significant preferred winter warm extreme occurrences were identified during ATL- days (see Fig. 4.23i).

A similar line of reasoning for January warm extremes along a ATL- storyline can be used in Figs. 4.27d–f, where the futArcSI simulation is considered and both contributions also appear to counteract each other. Compared to futBKSI, an overall tendency towards more warm extremes can be observed over several parts of Europe. This stems from a stronger dominance of the Fixed-Regime term ρ_{FR} (Fig. 4.27d), probably due to the more pronounced thermodynamical forcing for Arctic-wide SI loss compared to SI loss over the BKS only.

4.5.3 *February warm extremes along a NAO+ storyline*

Figure 4.28 shows the decomposition for European warm extremes in February. The NAO+ regime is considered as the reference pattern C_{ref} , since, on the one hand it can be associated with warm extremes especially over more northern parts of Europe. On the other hand, the NAO+ regime showed significantly less frequent occurrences in the futBKSI simulation in February. The overall warm extreme occurrence ratio ρ shows some significantly

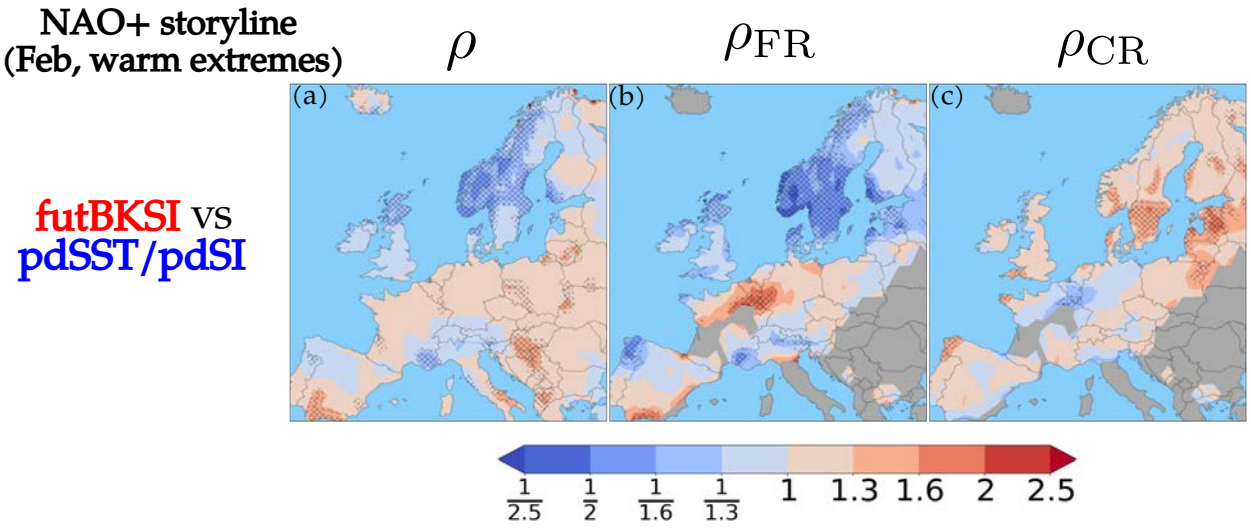

Figure 4.28: Same as in Fig. 4.25, but for February warm extremes in futBKSI and assuming a NAO+ storyline. February NAO+ occurrences decrease by 20% in futBKSI. ρ_{FR} and ρ_{CR} are only plotted for regions, where preferred winter warm extreme occurrences during NAO+ days were identified (see Fig. 4.23g).

less frequent extreme occurrences in the futBKSI simulation only over parts of Scandinavia (Fig. 4.28a). These signals are mostly explained by the Fixed-Regime contribution ρ_{FR} in Fig. 4.28b. The term ρ_{CR} shows basically no significant contribution (Fig. 4.28c).

4.5.4 *Comparison with futSST*

Finally, the previous results are contrasted to results for the futSST experiment. This allows to assess the relative importance of Arctic SI loss compared to a future increase of global SSTs. Therefore, Fig. 4.29 compares the futSST with the reference simulations and shows the overall response and the two contributions ρ_{FR} and ρ_{CR} for midwinter cold extremes. Here, the NAO- regime was set as the reference regime, but results for other storylines reveal the same qualitative picture. First, it shows that cold extremes occur massively and significantly less frequent in the futSST simulation over all plotted regions (Fig. 4.29a). Secondly, these overall changes are almost completely explained by the fixed-circulation term ρ_{FR} (Fig. 4.29b). Although the NAO- regime only shows non-significant changes between both simulation in midwinter (4% decrease), even significant and more distinct changes in regime occurrences could not contribute in the same way as the Fixed-Regime contribution. This illustrates how the overall thermodynamical warming effect induced by warmer global SSTs clearly dominates any circulation induced changes in extreme occurrences. A complementary picture is found for warm extremes.

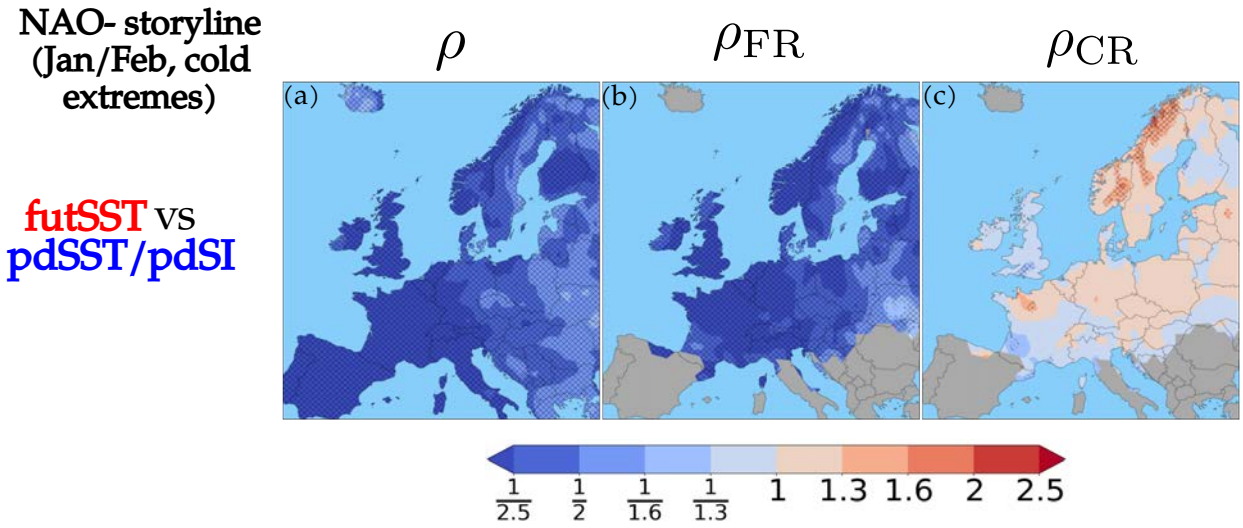

Figure 4.29: Similar to Fig. 4.25, but comparing the pdSST/pdSI reference simulation and the futSST sensitivity simulation. Analyzed are cold extremes in January/February and a NAO- storyline is assumed here. ρ_{FR} and ρ_{CR} are only plotted for regions, where preferred winter cold extreme occurrences during NAO- days were identified (see Fig. 4.23c).

4.5.5 *January wind extremes along a ATL- storyline*

The appended Fig. B.9 shows the decomposition for European January wind extremes for both sea ice sensitivity experiments. The ATL- regime is again considered as the reference pattern C_{ref} , since based on Figs. B.5 and B.8a it was argued that this regime is associated with an eastward extensions of the North Atlantic stormtrack and consequently more passing cyclones over Western-to Central Europe. For the futArcSI experiment, the decreased January occurrence frequency of ATL- can be dynamically related to decreased occurrence frequencies of January wind extremes (Fig. B.5f). This contribution is however offsetted by ρ_{FR} (Fig. B.5e), which might be related to regional changes in the meridional temperature gradient and the resulting strength of westerly winds during ATL- days.

4.6 CIRCULATION ANALOGUE-BASED APPROACH FOR SUMMER SEASON

The previous Section only addressed the decomposition of changes in the occurrence frequencies of winter extremes. Indeed, no any analysis was conducted for heat extremes in summer. The reason for this was twofold: on the one hand, Fig. 4.13 barely showed any significant summer regime occurrence frequency changes in the sensitivity experiments. Such changes in regime occurrence frequencies were however necessary in order to relate the Changed-Regime term ρ_{CR} to changes in atmospheric dynamics. On the other hand, in Fig. 4.24 physically consistent links between regime and heat extreme occurrences in summer could only scarcely be identified. As explained in Sec. 2.4.2, heat extremes over Europe are typically co-located with blockings. Indeed, apart from the S-SCAN regime none of the other summer regimes could be plausibly linked to a blocking structure over Europe. Daily flows that show blockings over other European regions than Scandinavia were consequently allocated among the different summer regimes. Compared to winter season, the assumption that the storyline of some summer regime explains the occurrence of a summer heat extreme is therefore in general less justified (except for the S-SCAN regime and Scandinavian heat extremes). This assumption was however the basis for a reasonable interpretation of the decomposition in Eq. 4.2. A potential solution for this issue would be to increase the number of prescribed regimes until more distinct blocking structures can be identified in the regime patterns.

However, in order to study European summer heat extremes in this Section the previous decomposition procedure is employed but based on circulation analogues (Yiou et al., 2017). This allows to quantify thermodynamically and dynamically induced contributions to summer heat extreme frequency changes in the sensitivity experiments, while avoiding the aforementioned issue when trying to identify suitable regime storylines in summer season. Circulation analogues are generally defined as atmospheric circulations that are similar to some specified atmospheric flow pattern of interest. From early on, the methodology of circulation analogues was used in a variety of contexts to study atmospheric dynamics (e.g. Lorenz, 1969), including nowadays for instance the implementation of stochastic weather generators (Yiou, 2014), or the detection of changes in the atmospheric circulation patterns that are associated with extreme events (Faranda et al., 2020; Yiou et al., 2017).

Basic procedure

Inspired by previous studies (e.g. Yiou et al., 2017; Jézéquel et al., 2018), the basic idea is first to specify start and end dates for selected heat waves over different European regions that occurred in the recent past. Based on the specified date ranges, temperature thresholds for different European regions are defined as the average linearly detrended ERA5 T2max anomaly[9] during a respective heat wave. Afterwards, the flow patterns of individual heat wave days are extracted from linearly detrended ERA5 gph500 anomalies. The selected reference flow patterns can be considered as atmospheric situations that typically prevail during the occurrence of heat waves over the respective European regions. Subsequently, for each flow pattern the 30 best-matching analogues in the ERA5 time se-

9 Anomalies are here again defined as deviations from the annual cycle, which is obtained by averaging each day of the season overall all years.

Table 4.3: Summary of start and end dates of the different heat waves in ERA5, as well as of the spatial domains for temperature averaging and analogue computation. Threshold temperatures identified for each heat wave are also shown. Bold temperatures indicate the thresholds that were actually used for the final decomposition.

	start date	end date	Temperature domain	Analogue domain	threshold temperature
Russian heat wave	2010-07-05	2010-08-17	28–48°E, 48–64°N	-10–80°E, 35–75°N	**6.8**°C
Scandinavian heat wave	2018-07-15	2018-08-02	10–35°E, 57–70°N	-15–65°E, 45–80°N	**4.5**°C
WC-European heat wave	2003-08-01	2003-08-14	-2–12°E, 43–53°N	-40–50°E, 35–75°N	7.5/**5.5** °C

ries are determined. This allows to define threshold values as the Euclidean distance of the 30th best-matching analogue to the respective reference flow patterns. By means of these thresholds, circulation analogues are subsequently identified in the different PAMIP simulations. Based on the selected analogues and the threshold temperatures derived from the corresponding heat waves, the same decomposition as in Sec. 4.5 is applied. This eventually allows to separate dynamically and thermodynamically induced contributions to summer heat extreme frequency changes in the different PAMIP sensitivity experiments.

4.6.1 *ERA5 event definitions*

For the upcoming analysis, the following three European heat wave are considered (see also beginning of Sec. 2.4): the Russian heat wave in 2010, the Scandinavian heat wave in 2018, and the Western/Central European heat wave in 2003.

The first task is to define start and end dates for the different heat waves, as well as spatial domains over which surface temperatures are strongly increased during the occurrence of the respective heat wave. On the one hand, it is worthwhile to consider time frames and domains as long and as large as possible. This ensures that the event is temporally persistent and impacts a large area. Furthermore, a longer period ensures that the upcoming analogue selection for each heatwave is based on a larger variety of reference flows. On the other hand, temperatures over the selected time frames and spatial domains still have to be somehow extreme, which might be problematic for larger domains and longer time periods. The choices for the spatial domains (afterwards termed Russian, Scandinavian and WC-European sector), and the time frames of the heat waves are summarized in the first three columns of Tab. 4.3. It should be mentioned beforehand that choosing slightly different periods and spatial domains does no alter upcoming results.

Figures 4.30a–c depict linearly detrended ERA5 T2max anomalies averaged over the chosen heat wave time periods. In particular, the two-week-long 2003 heat wave was associated with temperature anomalies of more than 10°C over central France. Figures 4.30d–f show detrended ERA5 T2max anomalies for the respective summer seasons averaged over the respective spatial domains (black boxes in Figs. 4.30a–c). Only grid points over land were considered. Nearly all defined heat wave days exhibit temperature anomalies at least greater than 4°C. Based on the temperature time series in Figs. 4.30d–f, representative threshold temperatures are now defined for each spatial domain.

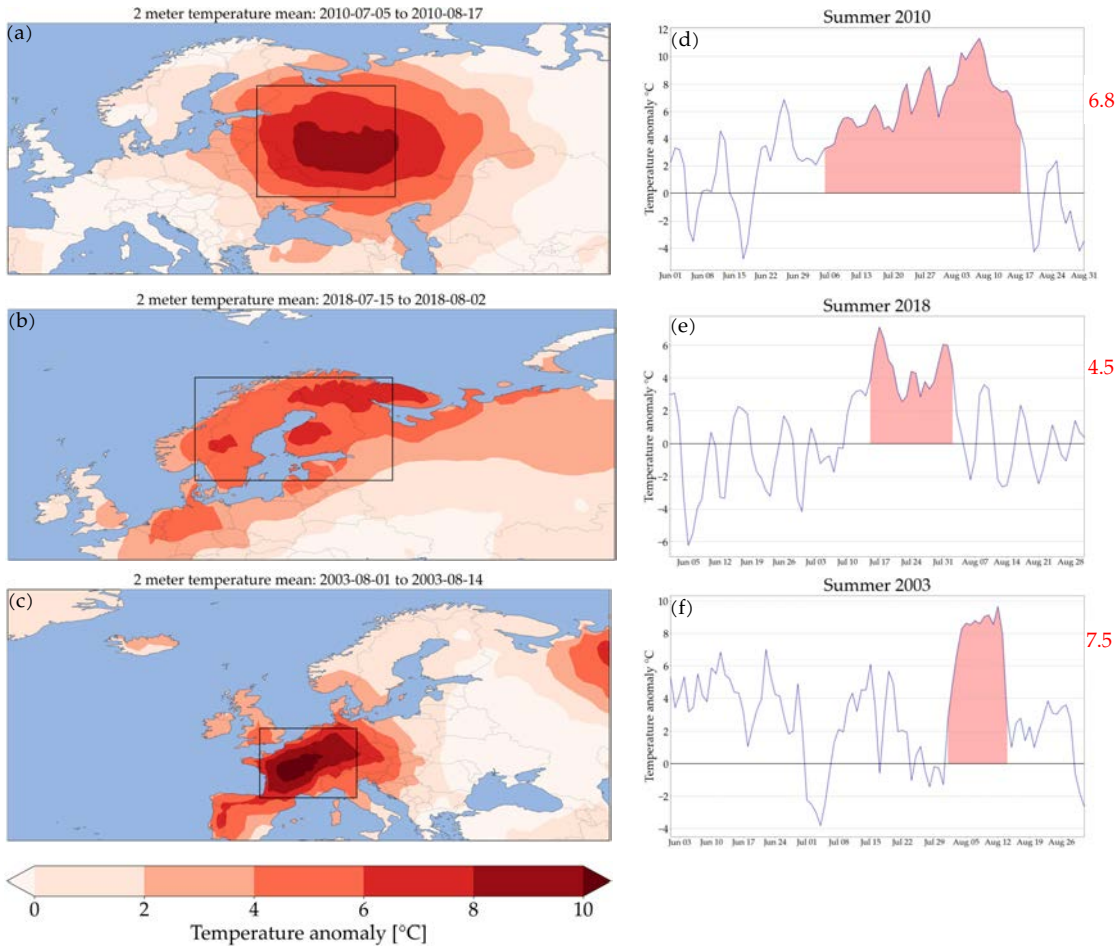

Figure 4.30: Left column: mean plots of linearly detrended ERA5 T2max anomalies over the time periods of the three heat waves: a) Russian heat wave in 2010, b) Scandinavian heat wave in 2018 and c) European heat wave in 2003. Black boxes indicate the respective domains over which temperature time series in the right columns were spatially-averaged. Right column: time series of detrended ERA5 T2max anomalies plotted over the respective summer seasons. The temperature time series was computed as a spatial average over the black boxes in the left plots. Only grid points over land were considered. Red-shaded areas indicate the defined heat wave periods. The red numbers on the right side of the plots denote the respective threshold temperature, computed as the average T2max anomaly over the respective heat wave time period.

The threshold temperatures are calculated as the average detrended T2max anomaly over the respective heat wave time period. For the Russian heat wave this results in a threshold temperature anomaly of 6.8°C, for the Scandinavian heat wave in 4.5°C, and for the heat wave over the WC-European sector even in 7.5°C.

4.6.2 *Reference flows and analogues in ERA5*

Based on the defined date ranges, the individual daily reference flow patterns can now be extracted for each heat wave day in ERA5. Figure 4.31 shows the mean of linearly detrended ERA5 gph500 anomalies averaged over the respective heat wave time periods. The

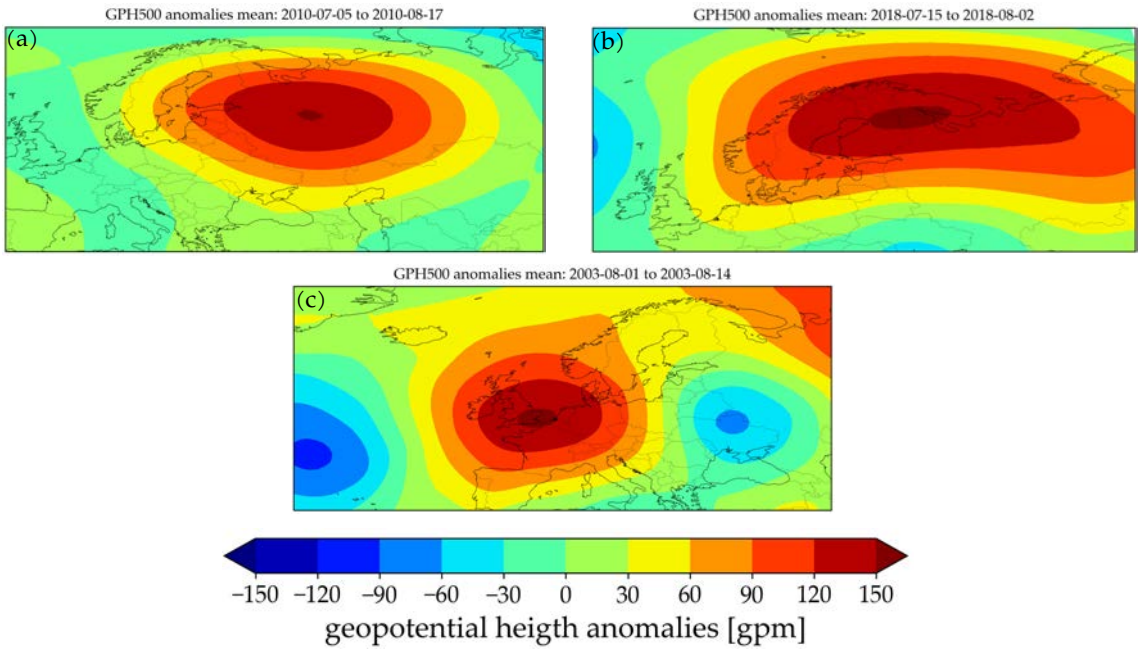

Figure 4.31: Linearly detrended ERA5 gph500 anomaly mean plots for the respective heat wave time periods: a) Russian heat wave in 2010, b) Scandinavian heat wave in 2018 and c) European heat wave in 2003.

individual daily gph500 anomaly patterns during the different heat waves can be found in the appended Figs. B.10–B.12.

As expected, all heat waves are co-located with pronounced blocking structures. Whereas the Russian and Scandinavian heat waves were accompanied by persistent anticyclonic systems over Ural and Scandinavian regions (Figs. 4.31a and b), the European heat wave in 2003 was co-located with an extended ridge or omega blocking (Fig. 4.31c). Especially the Russian heat wave in 2010 was accompanied by a stationary Ural blocking that persisted over nearly all 44 heat wave days (see Fig. B.10).

With the selected daily reference flows it is now possible to search for the best matching analogues for each heat wave day in ERA5. Therefore, for all daily flows[10] in JJA over the period 1979–2018 the Euclidean distance is calculated with respect to each daily heat wave pattern shown in Figs. B.10–B.12. This procedure requires the specification of a spatial domain, over which the similarity of summer flows and the reference patterns is assessed. On the one hand, the chosen domain should be large enough in order to capture the relevant synoptic and large-scale features of the prevailing circulation during heat wave days. If on the other hand the domain is too large, circulation features that are not relevant for a heat extreme occurrence may have too much influence on the resulting Euclidean distances. Choices for the domain sizes are also summarized in Tab. 4.3. Again, slight modifications ($\pm$ 10° longitude or latitude) of the domains do not significantly impact the final results.

Finally, for each heat wave day the 30 best-matching analogues are selected, that are, the daily summer flows over 1979–2018 with the smallest Euclidean distance to some reference flow pattern. E.g., for the 44 days of the Russian heatwave this results in 1320 circulation analogues found in ERA5. Daily flows are allowed to be selected as analogues

10 days within the respective heat wave are excluded

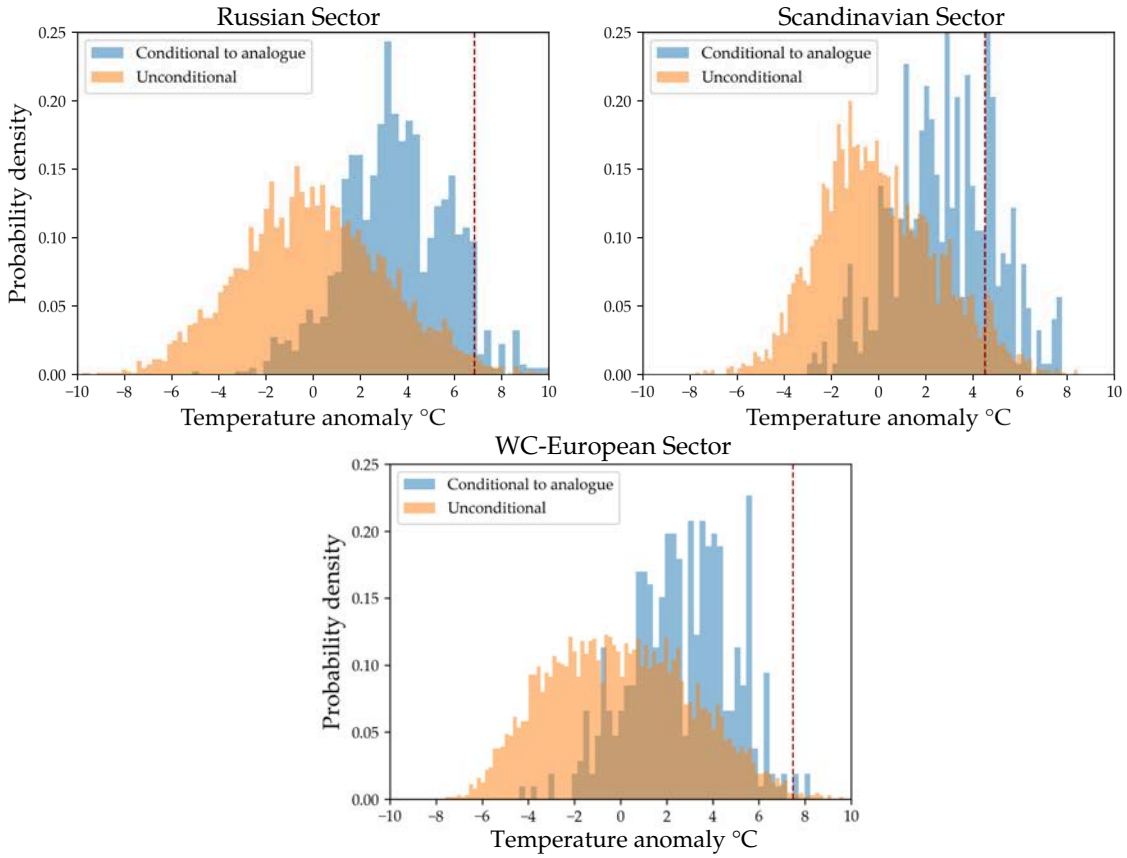

Figure 4.32: Histograms of detrended ERA5 T2max anomalies for JJA averaged over the different spatial domains (black boxes in Figs. 4.30a–c, only land grid points). Orange bars indicate the unconditioned temperature probability distributions, that is, all JJA T2max anomalies over the period 1979–2018. Blue bars indicate temperature probability distributions conditioned on the prevailing circulation during the different heat waves. The conditioned distribution only considers temperatures at days that were selected as analogues for the respective heat wave[11]. The dashed red vertical lines indicate the temperature thresholds that were derived from each respective heat wave event.

more than once, which happens frequently as the reference flows of the individual heat wave days are mostly quite similar to each other. For each heat wave day, the Euclidean distance of the 30th-best matching analogue finally defines a threshold value. This value is later on used to extract analogues from the PAMIP simulations.

Figure 4.32 eventually shows different distributions of T2max averaged over the Russian, Scandinavian and WC-European sectors: one unconditioned T2max distribution for all ERA5 JJA days over the period 1979–2018, and another conditioned distribution where only days were considered that have been identified as analogues of the respective heat wave[11]. It can be reported that temperature thresholds derived from the Russian, but especially from the heat wave over WC-Europe are barely reached within the ERA5 period. In contrast, the temperature threshold of the Scandinavian heat wave appears to be less extreme and is exceeded by around 95% of summer days in ERA5. As expected, conditioning the temperature distribution on the prevailing circulation during heat extremes

11 note that the same day can be selected multiple times as an analogue

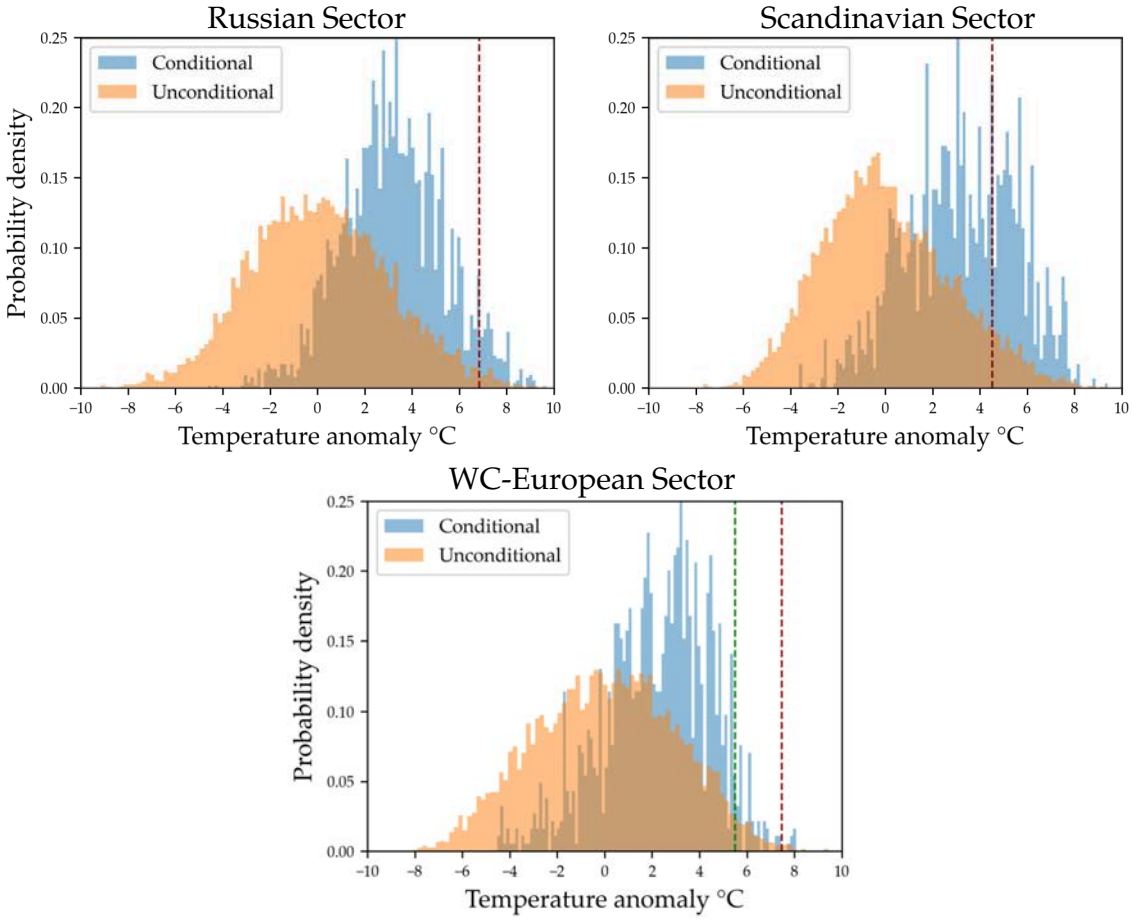

Figure 4.33: Same as in Fig. 4.32, but for T2max anomalies of the pdSST/pdSI simulation. Similar to Fig. 4.32, the conditioned probability distributions only consider temperatures at days in pdSST/pdSI that were selected as analogues for the associated heat wave. The dashed greenish vertical line in c) indicates the redefined threshold temperature (5.5°C) for the European 2003 heat wave.

leads to a narrowing and shift of the resulting distribution towards larger temperature anomalies.

4.6.3 *Circulation analogues in ECHAM6 experiments*

Now, circulation analogues can be extracted from the different PAMIP experiments. Based on detrended ERA5 gph500 anomalies, for each heat wave day a threshold value was defined as the Euclidean distance of the 30th-best-matching circulation analogue found in ERA5 summer seasons over the period 1979–2018. The Euclidean distances of all daily JJA flows in the different 100-year-long PAMIP experiments are now computed with respect to each ERA5 reference pattern (Figs. B.10–B.12). PAMIP flows are provided by gph500 anomaly fields and anomalies are calculated based on the individual seasonal cycle of each experiment. PAMIP analogues are subsequently defined as all JJA flows in a PAMIP experiment for which the Euclidean distance to a respective reference flow pattern is smaller than the threshold value derived from ERA5.

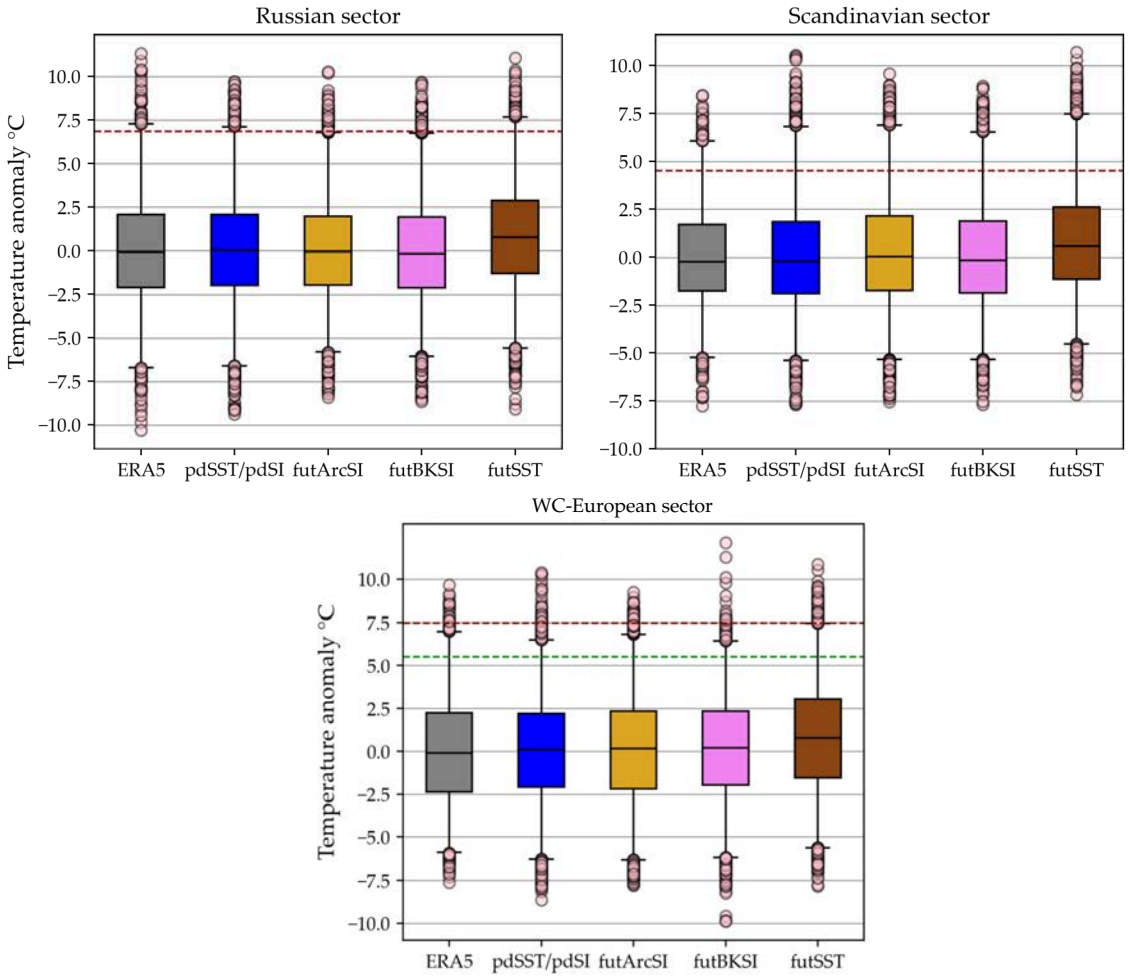

Figure 4.34: Boxplots of JJA T2max anomalies averaged over the different spatial domains (black boxes in Figs. 4.30a–c, only land points). Shown are detrended ERA5 T2max anomalies, but also T2max anomalies for the different PAMIP experiments. T2max anomalies for the different PAMIP simulations were calculated with respect to the annual cycle of the pdSST/pdSI reference experiment. The central line in each box indicate the median, the upper and lower borders of the boxes signify the quartiles, and the upper (lower) whiskers indicate the 0.99 (0.01) quantiles of the respective temperature distribution. The dashed horizontal lines indicate the temperatures thresholds as in Fig. 4.33.

Choosing the 30th-best-matching analogue in ERA5 ensures that the PAMIP analogues are still very similar to the reference flows, while still having a sufficiently large number of analogues available in the model data. It should be mentioned that upcoming results are relatively insensitive to the exact number of best-matching ERA5 analogues. Indeed, when considering the 20th- and 40th-best matching ERA5 analogues final results were found to be very similar.

Like in Fig. 4.32, Fig. 4.33 displays unconditioned and conditioned T2max probability distributions, but for the pdSST/pdSI reference simulation. A similar picture emerges as for the ERA5 histograms: conditioning on the circulation analogues shifts the temperature distributions towards more extreme temperatures. Again, the threshold temperature derived from the European 2003 heat wave in ERA5 is barely reached over the European sector. As the temperature during the 2003 heat wave was apparently that extraordinarily

high that it can be hardly observed in the 100-year long PAMIP simulation, the temperature threshold for the WC-European sector is redefined to 5.5°C. This ensures that a sufficiently large number of temperature extremes are defined for the upcoming decomposition analysis.

4.6.4 *Decomposition of sea ice-induced changes in European heat extremes*

Eventually, frequency changes of heat extreme occurrences over the Russian, Scandinavian and WC-European sectors can be decomposed into dynamically and thermodynamically induced contributions.

In this respect, the boxplots in Fig. 4.34 initially display unconditioned T2max anomaly distributions of ERA5 and the different ECHAM6 PAMIP experiments over the different sectors. Overall, it appears that the spread in the modeled distributions of temperature anomalies is very similar to ERA5 and among different experimental setups. From Fig. 4.34 it can be concluded that a sufficiently large number of heat extremes over the different sectors can be identified in each experiment. Consistent with previous results, distributions from futSST experiment show a 1°C shift of the median towards higher temperatures.

Based on the identified PAMIP circulation analogues, the conditional framework for extreme event attribution already applied in Sec. 4.5 can be utilized. Like in Sec. 4.5, this allows to decompose the occurrence ratio of heat extremes over the different regions into

$$\rho = \rho_{\mathrm{FA}} \cdot \rho_{\mathrm{CA}}, \tag{4.3}$$

where the individual terms are defined as follows:

- Heat extreme occurrence ratio ρ: as in Sec. 4.5 this ratio compares the overall heat extreme occurrence ratio between a sensitivity and the pdSST/pdSI reference simulation. However, as temperatures thresholds T_{ref} for each sector the previously defined threshold values derived from the respective ERA5 heat waves are used (see e.g. Tab. 4.3).

- "Fixed-analogue" term ρ_{FA}: Similar to the "Fixed-regime" term ρ_{FR} in Sec. 4.5, this term compares heat extreme occurrence frequencies between sensitivity and reference experiment for fixed atmospheric dynamics in terms of circulation analogues. Hence, the probability of a heat extreme occurrence given a circulation analogue is computed and compared between the experiments.

- "Changed-analogue" term ρ_{CA}: Similar to the "Changed-Regime" term ρ_{CR} in Sec. 4.5, this term relates heat extreme occurrence frequency changes to changes in analogue occurrence frequencies (denoted as ρ_{ana})

- Analogue occurrence ratio ρ_{ana}: this term is additionally shown in Fig.4.35 and compares the number of analogues found in a sensitivity experiment versus the number of analogues found in the pdSST/pdSI reference experiment. This term actually corresponds to ρ_{circ} in Sec. A.6.

In the following, decomposition results for the different European sectors will be presented and discussed.

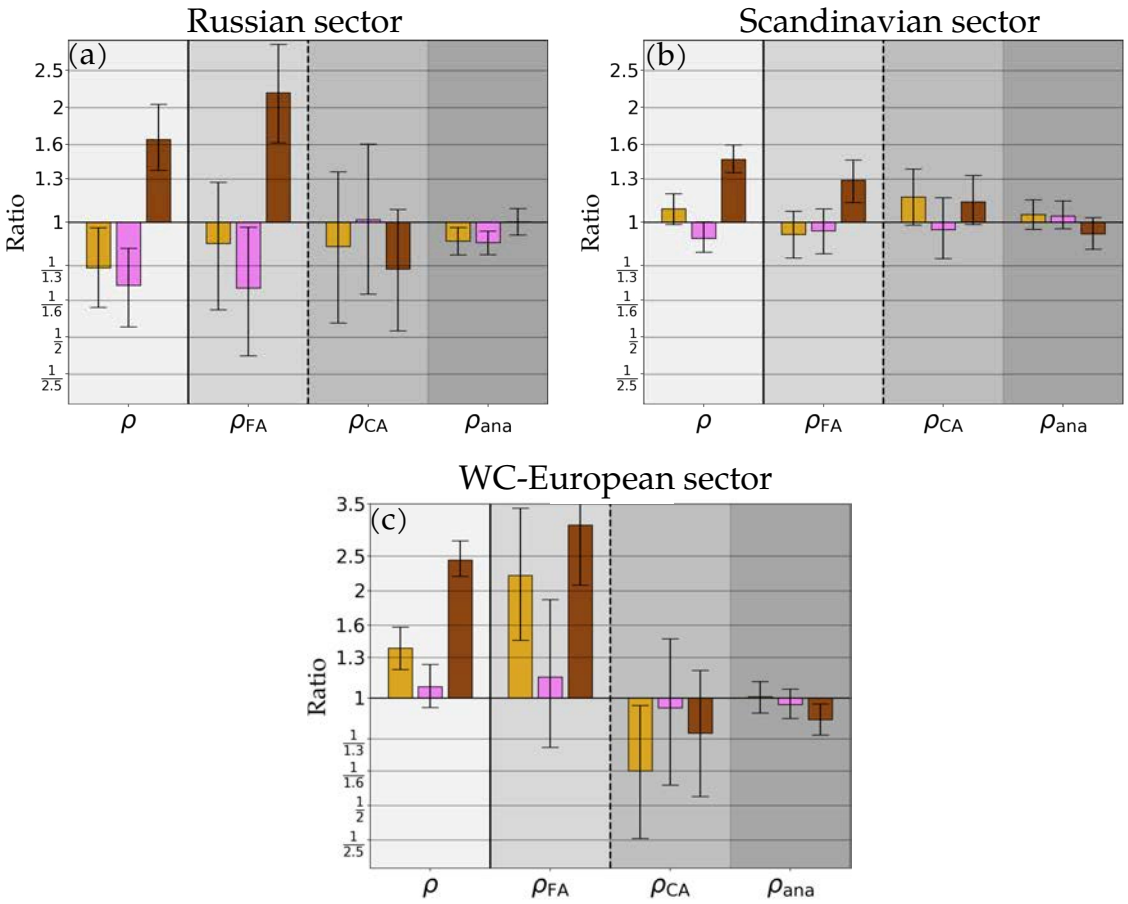

Figure 4.35: Same conditional decomposition procedure as already applied and explained in Secs. A.6 and 4.5, but based on circulation analogues. For each sector, the overall JJA heat extreme occurrence ratio between sensitivity and reference simulation is shown, as well as the "Fixed-analogue" term ρ_{FA}, the "Changed-analogue" term ρ_{CA}, and the occurrence ratio of analogues ρ_{ana} (see also main text). Different colors indicate results for the futArcSI (gold), futBKSI (pink) and futSST (brown) experiments. The illustrated 90-percent confidence intervals are based on a moving block bootstrap (M=1000).

Russian sector

The extreme occurrence ratio ρ in Fig. 4.35a shows that days with temperatures comparable to the Russian heat wave in 2010 occur less frequent in both sea ice sensitivity experiments. Especially the reduced occurrence frequency in futBKSI is completely explained by ρ_{FA}. Increased BKS surface temperatures in futBKSI are, from a thermodynamical perspective, however supposed to actually promote the occurrence of heat extremes. If it is assumed that the prevailing circulation during the Russian heat wave in 2010 is indeed representative for all heat extremes over the Russian sector, the analogues should by design replicate the atmospheric circulation during Russian heat extremes very well. Hence, in contrast to the circulation regime approach, it can hardly be argued that the selected analogues comprise a too large variety of flows that might not be related to the actual extreme.

The employed methodology does however only consider heat extremes in terms of single days with extraordinary high temperature anomalies. The typical persistence

of heat waves and their associated atmospheric conditions is not considered. However, progressive heat accumulation over several days or weeks in combination with soil moisture depletion is typically required to reach extremely high temperatures (Miralles et al., 2014). If for instance the selected analogues in futBKSI form on average less persistent heat extremes compared to pdSST/pdSI, this could explain why ρ_{FA} in Fig. 4.35a promotes less frequent heat extreme occurrences in futBKSI.

Consistent with the decreased occurrence frequency of heat extremes over Russia, a significantly smaller number of circulation analogues in futBKSI and futArcSI is found ($\sim$ 10% decrease in ρ_{ana}). However, despite these changes in the atmospheric circulation the related changed-analogue terms ρ_{CA} do not show any significant contributions. This is probably related to the aforementioned shortcomings of the employed methodology, that is, not accounting for the persistence of blocking-like circulations. Consistent with earlier results in this thesis, futSST exhibits significantly more frequent ($\sim$ 60%) heat extreme occurrences over the Russian region that are mostly explained by ρ_{FA}. Changes in the number of analogues are not reported for futSST.

Scandinavian sector

Figure 4.35b indicates a slight increase (decrease) of heat extreme occurrence frequencies over the Scandinavian sector in futArcSI (futBKSI) by around 10%. In contrast to the Russian sector, significant changes in the number of circulation analogues found in the sea ice sensitivity experiments can however not be detected. Consequently, dynamical changes in terms of altered frequencies of blocking patterns over Scandinavia can not explain the slight changes in heat extreme occurrences over the Scandinavian sector. In this respect, the different contributions ρ_{FA} and ρ_{CA} for the sea ice sensitivity experiments do not show any significant and interpretable signals.

Similar to the Russian sector, heat extremes over Scandinavia occur nearly 50% more frequent in futSST. Again, these changes are mostly explained by ρ_{FA}, that is related to the overall thermodynamical warming effect of global SST increases.

Western/Central-European sector

Heat extremes over the WC-European sector show more than doubled occurrence frequencies in futSST, but also an increased occurrence probability in futArcSI by around 40% (see Fig. 4.35c) . In both cases these change can be related to the overall thermodynamical warming effect, indicated by a significant contribution of ρ_{FA}. In addition, for futArcSI (futSST) a significant (insignificant) contribution of ρ_{CA} can be reported that counteracts the thermodynamical warming associated with ρ_{FA}. Nevertheless, only for futSST the contribution from the "Changed-Analogue" term ρ_{CA} can be linked to a decreased analogue occurrence frequency by around 15% (see ρ_{ana} in Fig. 4.35c). As however already noted in Sec. 4.5.4, such relatively weak changes in the atmospheric circulation are completely outweighed by the thermodynamical warming effect in futSST.

Overall, it can be summarized that the presented analysis based on circulation analogues extends the analysis of the previous Sections in a reasonable way. Compared to the summer circulation regimes, the occurrences of distinct blocking structures over different European regions were considered as more suitable storylines of summer heat extremes. This

allowed to apply the framework of conditional extreme event attribution to summer heat extremes, and finally to assess the relevance of thermodynamically and dynamically induced contributions to changes in such extreme events. As however noted in the end, relating in particular the detected changes in heat extreme occurrences in the sea ice sensitivity experiments to such contributions remained rather challenging within the employed decomposition framework.

5 CONCLUSION

5.1 SUMMARY

Extreme climate events are among the greatest dangers for today's human society (World Economic Forum, 2021; Future Earth, 2020). Along with global climate change, an increasing number of such events over the NH was observed over recent decades (e.g. Coumou et al., 2012). Due to the significant economical, ecological and societal impacts of such extreme events there is a high demand for reliable statements on future developments in extreme event occurrences. From a purely thermodynamical perspective it can be expected that recent and future global warming lead to more frequent and severe hot extremes (and vice versa for cold extremes). However, climate extremes are usually dynamically driven by specific atmospheric circulation patterns. Hence, future changes of these dynamical drivers could potentially either reinforce or counteract the expected thermodynamical response to future global warming.

In addition to changes in extreme event occurrences, recent global warming includes a phenomenon termed Arctic Amplification that is characterized by an up to four times faster warming of Arctic regions compared to global average (Rantanen et al., 2022). This amplified Arctic warming is accompanied by a tremendous loss of Arctic SI over recent decades (Stroeve et al., 2018), and model projections suggest that a seasonally ice-free Arctic might be possible in the mid of the 21st century (Notz et al., 2020). The question if and to what extent Arctic SI loss is able to affect large-scale atmospheric dynamics and weather and climate extremes over mid-latitudes remains a widely studied and highly debated topic (Cohen et al., 2020). In this respect, several previous studies reported links between recent Arctic SI retreat and the atmospheric circulation, e.g. in terms of a weakening and stronger meandering of the jet stream (Francis et al., 2012), a negative NAO response in winter (e.g. Screen, 2017b; Nakamura et al., 2015; Jaiser et al., 2012), or an intensification of the Scandinavian and Ural highs (e.g. Cohen et al., 2018).

Thus, the overreaching objective of this thesis was to contribute to a better understanding of the impact of future Arctic SI retreat on mid-latitude atmospheric dynamics and extreme events.

The results of this thesis overall support that future Arctic SI loss is indeed able to impact climate extremes over mid-latitudes and the related large-scale atmospheric dynamics. The outcomes of this thesis are largely based on data from ECHAM6 sea ice sensitivity model experiments that are part of the PAMIP data pool. In particular, simulations forced under future SI reductions over the entire Arctic, as well as only over the BKS were considered and compared to a reference simulation forced under present day conditions. In addition to the sea ice sensitivity experiments, a sensitivity experiment forced under future globally increased SSTs was analyzed.

Along with the guiding research questions (**RQ**s) stated in the introduction, the following conclusions can be drawn:

RQ1: *What changes in the atmospheric large-scale circulation over the Euro-Atlantic sector can be expected under future Arctic sea ice retreat in ECHAM6?*

As mentioned before, several earlier studies have proven that Arctic SI decline can impact large-scale atmospheric dynamics in the NH (e.g. Francis et al., 2012; Crasemann et al., 2017; Screen, 2017b). Similar to Crasemann et al. (2017) the present thesis predominately employed the framework of atmospheric circulation regimes and studied how the occurrence frequencies of five large-scale circulation regimes over the Euro-Atlantic domain are affected by future Arctic SI changes. In Sec. 4.2, five well-known winter circulation regimes were computed from ECHAM6 PAMIP SLP anomalies: a Scandinavian blocking regime SCAN, a Dipole or Atlantic ridge pattern DIP, an Atlantic trough pattern ATL-, and two patterns that respectively resemble the positive and negative states of the North Atlantic Oscillation, termed NAO+ and NAO-. Similar regime structures were computed for the summer season, however with weaker amplitude and a northward shift of the centers of action. When comparing the model regimes with regimes computed from ERA5 data it appears that ECHAM6 is able to realistically simulate the regime structures.

A variety of significant changes in the occurrence frequencies of winter regimes was detected when contrasting the idealized atmosphere-only model simulations forced under present day and future Arctic SI conditions. In concert with previous studies (e.g. Crasemann et al., 2017; Detring et al., 2021), the sign and significance of the signals are, however, highly dependent on the respective month. Furthermore, SI reductions that are only locally prescribed over the BKS already explain most of the frequency changes found for Arctic-wide SI loss. In particular in winter, this highlights the potential key role of SI loss in the BKS when aiming to understand links between Arctic SI retreat and mid-latitude weather and atmospheric dynamics (Screen, 2017a; Jaiser et al., 2016; Kretschmer et al., 2016). In agreement with recent ERA5 tendencies derived from a Multinomial Logistic regression approach, a significant increase of midwinter SCAN occurrences is detected in both sea ice sensitivity experiments. Although this winter response is consistent with several previous studies (e.g. Luo et al., 2016; Petoukhov et al., 2010), recent studies did not report a Scandinavian/Ural blocking response to SI loss over the BKS (e.g. Kim et al., 2022; Peings, 2019). Consistent with the frequently observed negative NAO response to Arctic SI loss, less frequent occurrences of the NAO+ regime are detected in February under future SI reductions over the BKS (in agreement with ERA5 tendencies). Furthermore, in accordance with ERA5 a decreased occurrence of the ATL- pattern is observed in January in both sea ice sensitivity simulations. In summer, however, the regime frequency changes in the sea ice sensitivity experiments are only minor. In agreement with recent ERA5 tendencies, only in July a decrease of Summer-NAO+ occurrences was detected in both sea ice sensitivity experiments. Additionally, both experiments also show an increased frequency of the Summer-SCAN pattern in July.

The experiment with globally increased SSTs exhibits much stronger changes in the future SLP background state compared to the sea ice sensitivity experiments. Over

the Euro-Atlantic domain, this mean response even projects onto the positive phase of the NAO. However, when accounting for this background pattern significant changes in regime occurrences are mostly absent—in winter and in summer.

In Sec. 4.6 the circulation regime analysis was extended by an approach based on circulation analogues. It is found that blocking-like circulation patterns that prevailed during the Russian heat wave in 2010 occur less frequent in the sea ice sensitivity experiments. In addition, a summer decrease in the occurrence frequency of an omega-block structure over central Europe is detected in the experiment with globally increased SSTs.

RQ2: *What overall changes in temperature extremes over the continental Northern Hemisphere can be expected in response to future Arctic sea ice loss in ECHAM6?*

Motivated by previous studies (e.g. Screen, 2017b; Cohen et al., 2014b; Francis et al., 2012), Sec. 4.3 investigated what changes in temperature extremes can be expected in response to future Arctic SI loss in the ECHAM6 PAMIP sea ice sensitivity experiments.

The initial analysis of extreme event occurrences is based on exceedances (drops below) of the 0.95 (0.05) near-surface temperature distribution quantile in the present day reference simulation. It is found that prescribed SI reductions in the model simulations result in an overall tendency towards less cold extreme days in winter, especially over mid-latitude to subpolar Northern Hemispheric continental regions. A general tendency towards more winter warm extremes is however less clear. This overall asymmetric response in winter cold and warm extremes is consistent with Screen (2014), who showed that Arctic amplification results in reduced subseasonal temperature variability over the mid- to high latitude NH, mostly due to fewer (or less severe) cold days compared to a smaller increase in the number (or severity) of warm days. Nevertheless, it can be summarized that the winter extreme responses detected in mid-latitudes, their signs as well as their significances highly depend on the specific region and month. Indeed, over some Northern Hemispheric regions significant reductions in cold extreme occurrences are not accompanied by more frequent occurrences of winter warm extremes, and vice versa. This can be interpreted as an increase of temperature variability for the respective regions and month. In contrast to the relatively strong winter signals in temperature extreme occurrence frequencies, responses in summer heat extremes to future SI loss in the sea ice sensitivity experiments are very weak.

The initial analysis based on threshold exceedances was furthermore extended by an investigation of sea ice-induced changes of 10, 20 and 50 year return levels derived from annual temperature maxima and minima. Consistent with the aforementioned observations a warming by more than 3°C of very rare cold extremes is detected over some mid-latitude to subpolar regions for future Arctic-wide SI loss. Changes in very rare summer heat extremes are again mostly absent.

A future increase of global SSTs results in strong hemispheric-wide increases (decreases) of warm (cold) extreme occurrences in winter and summer season. Contrasting the sea ice-induced changes to the impacts of future increased SSTs suggests: aside from more northern and Arctic latitudes, the impact of future Arctic SI loss is

probably of secondary importance compared to more global facets of future warming.

RQ3: *What are dynamically and thermodynamically induced contributions to frequency changes of European temperature extremes that are related to future Arctic sea ice loss in ECHAM6?*

Previous studies investigated how changes in mid-latitude weather in response to Arctic SI loss can be explained by dynamically and thermodynamically contributing factors (e.g. Screen, 2017b; Deser et al., 2016; Chripko et al., 2021). In this thesis, a framework for conditional extreme event attribution (Yiou et al., 2017) was employed in order to decompose sea ice-related frequency changes of European temperature extremes into dynamically and thermodynamically induced contributions. For this reason, Sec. 4.4 identified suitable circulation regime storylines for European temperature extremes in winter and summer season. In combination with the identified regime frequency changes in **RQ1**, changes in European temperature extremes were decomposed into two different contributions: one contribution that is related to dynamical changes in regime occurrence frequencies, and another more thermodynamically driven contribution that assumes fixed atmospheric dynamics in terms of circulation regimes.

Section 4.5 demonstrated that sea ice-induced changes in occurrences of European winter extremes can linked to significant contributions related to changes in winter regime frequencies. This is especially the case for increased January cold extreme frequencies over Central Europe that are related to increased SCAN occurrences. In addition, decreased January warm extreme occurrences over central- and parts of Eastern Europe are linked to a reduced frequency of the ATL- regime. Furthermore, it was observed that the contribution related to fixed circulation regimes yielded, from a thermodynamical point of view, intuitively expected decreased (increased) occurrence frequencies of cold (warm) extremes. This is especially pronounced for European cold extremes in February along a SCAN storyline, or for January warm extremes along a ATL- storyline. Finally, different scenarios for the resulting European temperature extreme frequency response are detected: first, one contribution may dominate and results in a significant overall response, and secondly, both contributions may counteract each other resulting in no detectable overall change in extreme occurrences.

When analyzing changes in midwinter cold extremes induced by future increased global SSTs, a strong and significant decrease of cold extreme occurrences is reported over entire Europe. Furthermore, this decrease can be nearly completely explained by the contribution that assumes fixed atmospheric dynamics in terms of circulation regimes. This suggests a dominance of overall thermodynamical warming over changes in atmospheric dynamics.

Compared to winter season, circulation regimes in summer are less suitable storylines for the occurrence of summer heat extremes. Therefore, in Sec. 4.6 the framework for conditional extreme event attribution was applied to summer heat extremes, but based on circulation analogues of distinct blocking structures that prevailed during different European heat waves of the recent past. Compared to summer circulation regimes, these blocking structures can be considered as more suitable storylines of summer heat extremes. Over Western/Central Europe, an increased heat extreme

occurrence frequency under Arctic-wide SI reductions can be explained by a thermodynamically induced contribution. Consistent with the previous findings, global SST increases result in considerably more frequent heat extreme occurrences over different European sectors. This response in extreme occurrences is again mostly explained by thermodynamical warming contributions that outweigh any potential dynamically induced changes. The changes in analogue frequencies mentioned in **RQ1** can however barely be related to changes in summer heat extreme occurrences—at least within the employed decomposition framework.

5.2 FINAL DISCUSSION AND OUTLOOK

In the following, some final remarks on the presented analysis and perspectives for future research directions are provided:

- The analysis of this thesis was only based on PAMIP data from the ECHAM6 model. Hence, it can not be ruled out that results for other models from the PAMIP data pool differ from the present ones. On the one hand, the ECHAM6 model was chosen as the different experiments were conducted at the DKRZ in Hamburg and all required output variables were consequently stored and directly available at the DKRZ as well. On the other hand, it was demonstrated that ECHAM6 is able to reproduce the ERA5 circulation regimes very well, especially when compared to some few other models that participated in PAMIP, and for which SLP data were available at the time the analysis was conducted (see Fig. B.1). Repeating the entire analysis for other PAMIP models was beyond the scope of this thesis, but would be an interesting perspective for future investigations.

- The presented analysis was conducted based on 100 ensemble members of one-year-long time slice simulations for each respective experimental setup. In this respect, recent studies by Streffing et al. (2021) and Peings et al. (2021) suggested that 100 ensemble members may not be sufficient in order to isolate the forced mean response from internal atmospheric variability in PAMIP sea ice sensitivity experiments. Hence, a larger ensemble size, if available, could be analyzed in order to assess the reliability and robustness of the results—especially of the detected dynamical responses.

- The question to what extent the detected winter changes in extremes and the atmospheric circulation are a result of time-delayed stratospheric pathways triggered by SI loss in autumn cannot be answered with the presented methodology and experimental design.

  From the experimental side this would require more tailored model experiments as for instance done by Blackport et al. (2019). They used coupled model experiments with modified albedo parameters and compared the delayed effect of autumn SI loss with the effect of year-round SI loss on the atmospheric winter circulation. Similarly designed model experiments could also be analyzed with the presented methodological framework. This could help for better understanding on the underlying dynamical pathways that lead to the detected sea ice-induced atmospheric responses.

When studying model experiments with prescribed year-round sea ice loss, more dynamically based analyses (e.g. Jaiser et al., 2016) are required in order to assess the role of dynamical pathways. This was however not the focus of the present thesis.

- The analysis within this thesis mainly considered changes in the occurrence probability of extremes, defined by a fixed threshold temperature in a present day simulation. Similarly, changes in circulation regimes were only considered in terms of frequency changes. When aiming to draw conclusions about changes in the intensity and severity of extremes, other factors have to be taken into account such as the actual strength of advection processes in winter. Therefore, it might be helpful to distinguish between days that strongly (weakly) project onto a relevant pattern (e.g. NAO- for cold extremes), and are therefore connected to stronger (weaker) advective processes. This could provide improvement possibilities of the employed approach for upcoming investigations.

- As stated during the discussion of the decomposition results in Secs. 4.5 and 4.6, an interpretation of the different terms as "thermodynamical" and "dynamical" contributions (as originally termed by Yiou et al. (2017)) is not always straightforward. Hence, the employed decomposition framework would benefit from further elaborations in this respect. As motivated in Sec. 4.5, it would be helpful to investigate in more detail how individual flow patterns that are allocated to a circulation regime change between different simulations. This could probably provide a clearer picture on the interpretation of some of the detected signals.

- In addition, the presented analysis did mostly consider extreme events in terms of single days with exceptionally high or low temperatures. However, heatwaves and winter cold/warm spells are characterized by persistent temperature anomalies over several days or weeks and might be more interesting from an impact-related perspective. As for instance already discussed in Sec. 4.6, a persistent atmospheric circulation and progressive heat accumulation over several days is indeed usually required to reach extremely high temperatures during heat waves (Miralles et al., 2014). In this respect, accounting for the persistence of atmospheric circulation regimes/analogues (and changes therein) would definitely elaborate the presented analysis.

- In this thesis the impact of future Arctic SI loss was contrasted to the influence of globally increased SSTs, that were prescribed in one of the simulation setups (futSST). Considering future SSTs as a proxy for overall global warming, this allowed to assess the relative importance of future SI retreat in the sea ice sensitivity runs to future global warming. Indeed, the future SST forcing fields were derived from RCP8.5 model projections that are based on fully coupled model experiments and include all aspects of future climate change. Hence, the future SSTs account to a large extent for the overall thermodynamical impact of future global warming. As for instance greenhouse gas concentrations were kept constant for all PAMIP experiments, changes in radiative interaction effects within the atmosphere were not taken into account. Therefore, it appears plausible that the overall thermodynamical effect of future global warming tends to be underestimated in the futSST experiment. Setting both, SSTs and greenhouse gas forcings to future levels may provide a perspective for upcoming model experiments in order to additionally account for the effect of

increased greenhouse gas concentrations. Nevertheless, it can be argued that this would potentially overestimate the impact of future global warming, as future SSTs to a large extent already comprise the effects of future greenhouse gas concentrations.

In summary, the present thesis provides an additional and useful perspective on the question how future Arctic sea ice retreat can impact large-scale atmospheric dynamics, to what extent European temperature extremes will be affected by future Arctic sea ice loss, and how these changes can be separated into dynamically and thermodynamically induced contributions. Nevertheless, the topic of Arctic-mid-latitude linkages will still remain a highly debated research area in future times. Further progress towards a consensus on this societally and scientifically important research topic will require model improvements in the representation of Arctic climate processes, but also in the underlying tropospheric and stratospheric processes that are involved in potential Arctic-mid-latitude linkage pathways.

METHODS

A.1 PRINCIPAL COMPONENT ANALYSIS

Depending on the resolution climate data usually span a high-dimensional phase space with the respective dimension corresponding to the number of grid points. Principal Component analysis PCA is a common and widely used multivariate statistical tool for analyzing high-dimensional climate data (see e.g. Wilks, 2006). The intention of PCA in atmospheric science is generally twofold: on the one hand, it can be used for dimensionality reduction when dealing with high-dimensional atmospheric data sets. On the other hand, it can be used to extract dominant modes of variability from atmospheric variables (as done in Section 2.1.4). The general aim of PCA is to find a new set of orthogonal axes or Empirical Orthogonal Functions EOFs in a way, that the first EOF explains the maximum possible amount of variance within the dataset. The subsequent second EOF should explain the maximum possible amount of remaining residual variance conditioned to the orthogonality constraint to the first axis (and so forth for the remaining axes).

To be more precise, suppose that some climate variable y is defined on N grid points measured at T different time steps t_k. The variable at grid point $i = 1, ..., N$ at time t_k ($k = 1, 2, ...T$) is denoted by $y_i(t_k)$. The objective is to transform the original data vector

$$\mathrm{y}(t_k) = (y_0(t_k), y_1(t_k), ..., y_N(t_k)) = \sum_{i=1}^{N} \mathrm{e}_i^u u_i(t_k) \tag{A.1}$$

into a new reference system with basis vectors e_i^u. Here, e_i^u is also referred to the i-th EOF and $u_i(t_k)$ denotes the corresponding Principal component PC, that is, the projection of the original data vector $\mathrm{y}(t_k)$ onto the respective EOF

$$u_i(t_k) = \mathrm{e}_i^u \mathrm{y}^T(t_k) = \sum_{j=1}^{N} e_{ij}^u y_j(t_k) \tag{A.2}$$

In order to find the leading EOF e_1^u the corresponding projected variance

$$\sigma_1^2 = \frac{\mathrm{e}_1^u \underline{\underline{S}}^y \mathrm{e}_1^{u^T}}{\mathrm{e}_1^u \mathrm{e}_1^{u^T}} \tag{A.3}$$

has to be maximized. Here, $\underline{\underline{S}}^y$ is the covariance matrix of size $N \times N$, which components are defined as

$$S_{ij}^y = \mathrm{E}[(y_i(t_k) - \mu_i)(y_j(t_k) - \mu_j)] \tag{A.4}$$

where $\mu_{i,j}$ denotes the expectation value in time at grid point i, j; E[...] is the temporal expectation operator and the y-index signifies that the matrix is given in the original grid-point-based coordinate system.

It appears that the leading EOF e_i^u is given by the *eigenvector* of the covariance matrix $\underline{S}^y$ corresponding to its largest *eigenvalue*. The subsequent EOFs e_i^u are given by the subsequent eigenvectors of $\underline{S}^y$.

The covariance matrix $\underline{S}^u$, that is the representation of $\underline{S}^y$ in its *eigenbasis*, is by definition a diagonal matrix

$$\underline{S}^u = \begin{pmatrix} \lambda_1 & 0 & \dots & 0 \\ 0 & \lambda_2 & \dots & 0 \\ \vdots & \vdots & \ddots & \vdots \\ 0 & 0 & \dots & \lambda_N \end{pmatrix},$$

where the respective diagonal entries are given by the eigenvalues λ_i of $\underline{S}^y$. As all off-diagonal elements or covariances in $\underline{S}^u$ are zero, the new variables $u_i(t_k)$ are uncorrelated. The fraction of explained overall variance R_i^2 by EOF e_i^u is given by the ratio of the respective eigenvalue λ_i to the total variance as

$$R_i^2 = \frac{\lambda_i}{\sum_{j=1}^{N} \lambda_j} \tag{A.5}$$

Different scaling conventions for EOFs and the corresponding PCs can be used. In this thesis, EOFs are always scaled in a way that the respective PC time series has unit variance. Original input data were regridded to a 100× 100km Equal-Area Scalable Earth Grid *EASE-Grid 2.0* (see Brodzik et al., 2012) in order to avoid grid point convergence at higher latitudes.

A.2 *k*-MEANS CLUSTERING

K-Means clustering, first introduced by MacQueen (1967), is the most frequently used clustering algorithm in atmospheric science for the computation of atmospheric circulation regimes (e.g. Michelangeli et al., 1995; Crasemann et al., 2017; Straus et al., 2007).

A.2.1 *Algorithm*

Given a dataset that consists of N-dimensional data vectors $y(t_k)$ observed at different time steps t_k, k-Means aims to partition the dataset into M different cluster sets $\mathcal{C} = \{C_1, C_2, ..., C_M\}$ in a way that minimizes the intracluster variance over all clusters. This can be formally written as

$$\arg\min_{\mathcal{C}} \sum_{i=1}^{M} \sum_{y(t_k) \in C_i} \|y(t_k) - C_i\|^2 \tag{A.6}$$

where $\|\cdot\|^2$ denotes the L^2-norm and C_i are the N-dimensional cluster centroids calculated as the average

$$C_i = \frac{1}{|C_i|} \sum_{y(t_k) \in C_i} y(t_k) \tag{A.7}$$

over all elements $y(t_k)$ allocated to a respective set C_i.

For the present thesis, the k-Means package of the Python machine learning library `Scikit-learn` was used. By default, the most frequently used algorithm by *Lloyd* was employed in order find the optimal cluster sets C_i. The algorithm can be divided into different steps:

1. Initialize the cluster centroids C_i randomly
2. Allocate each data vector $y(t_k)$ to cluster set C_i with the closest centroid C_i, such that the intracluster variance for the given centroids C_i is minimized
3. Calculate the new cluster centroids C_i^{new} according to Equation A.7

Steps 2 and 3 are repeated until a convergence criterion is met and the intracluster variance can not be optimized anymore. However, this procedure does not ensure to find the global minimum of overall intracluster variance.

A.2.2 *Computation of circulation regimes*

Centroids C_i of five atmospheric circulation regimes over the Euro-Atlantic domain (90°W–90°E,20°N–88°N) in model and reanalysis data were computed by applying the k-means algorithm to daily SLP anomaly data of the respective season.

In order to reduce computational demands a dimensionality reduction via PCA has been applied prior to the clustering algorithm. Here, the first 20 PCs were used that roughly explain around 90% of winter and 81% of total summer variance of the respective daily SLP anomaly fields. Further increasing the number of PCs did not effect the final outcome of the clustering algorithm. Before applying the initial dimensionality reduction via PCA, SLP anomaly data were regridded to a 100×100 km Equal-Area Scalable Earth Grid *EASE-Grid 2.0* (see Brodzik et al., 2012). The final allocation of some daily SLP anomaly field to the best-matching regime centroid was based on the Euclidean distance in the reduced phase space. The k-means algorithm has been initialized 1000 times and the best result in terms of minimizing the intracluster variance was finally chosen.

Anomaly definition

For the computation of ERA5 circulation regimes SLP anomalies were calculated as deviations from the annual cycle, that is, the average of each day of a year over all years.

For several parts of the PAMIP analysis in this thesis one joint set $\{C_0, ..., C_5\}$ of cluster centroids for two experimental setups was computed (typically the PAMIP pdSST/pdSI reference experiment and one of the sensitivity experiments). For the merged pdSST/pdSI+futBKSI and pdSST/pdSI+futArcSI datasets a joint annual cycle of both simulations was computed. It shows that the resulting cluster allocations are not considerably affected by whether the

SLP anomalies have been calculated as deviations from the joint annual cycle as described above, or by removing the annual cycles for each experiment individually (as done by e.g. Crasemann et al., 2017). This is also related to the fact that when contrasting the reference with both sea ice sensitivity experiments the respective winter and summer SLP background states (see e.g. Figs. 4.3 and 4.4) show mostly negligible and non-significant differences, neither did they project on any mode of variability. In contrast to the sea ice sensitivity simulations, the relatively strong forcing in the futSST experiment leads to an evident change of the SLP background state, which in winter even projects on a positive NAO pattern (see Fig. 4.3g). This background difference pattern significantly affects the final cluster allocations when subtracting a joint annual cycle. Therefore, the annual cycle was computed for both simulations individually when merging data from the futSST and the pdSST/pdSI experiments to take into account the different background states.

When regimes were computed for one single model experiment SLP anomalies were calculated as deviations from the annual cycle.

A.3 TAYLOR DIAGRAM

Taylor diagrams (Taylor, 2001) are useful tools in order to graphically compare a spatial model pattern $\mathrm{f} = (f_1, ..., f_N)$ with a reference pattern $\mathrm{r} = (r_1, ..., r_N)$, both defined on N grid points with respective components f_i and r_i at grid point i. In this thesis, 'r' and 'f' are respectively given by the different ERA5 and PAMIP regime patterns/centroids in the original non-reduced phase space. The relative skill of the model simulations in reproducing a reference regime pattern 'r' is characterized by different statistics:

- The amplitude of the model pattern is given by the spatial standard deviation

$$\sigma_f = \sqrt{\frac{1}{N-1} \sum_{i=1}^{N} \left(f_i - \bar{f}\right)^2}, \tag{A.8}$$

  where $\bar{f}$ denotes the mean over all grid points. The standard deviation σ_r of the reanalysis pattern 'r' is defined in a similar way.

- The centered root-mean-square error (CRMSE) between model and reanalysis pattern

$$E' = \sqrt{\frac{1}{N} \sum_{i=1}^{N} [(f_i - \bar{f}) - (r_i - \bar{r})]^2} \tag{A.9}$$

- And the pattern correlation coefficient between both patterns

$$R = \frac{\frac{1}{N} \sum^{N} (f_i - \bar{f}) \cdot (r_i - \bar{r})}{\sigma_f \sigma_r} \tag{A.10}$$

The relationship between these four different statistics may be written as

$$E'^2 = \sigma_f^2 + \sigma_r^2 - 2\sigma_f \sigma_r \cos(R), \tag{A.11}$$

allowing in combination with the law of cosine for a convenient simultaneous representation of all four statistics in a 2-D Taylor diagram by a single dot.

A.4 REGRESSION MODEL FOR DESCRIBING ERA5 REGIME FREQUENCY CHANGES

Section 4.2.2 investigates how the occurrence probabilities of ERA5 winter and summer regimes depend on the covariates *month*, *time* and *Arctic Sea Ice Area* anomaly. In order to describe the regime occurrence frequencies in dependence on the different covariates a suitable approach that is utilized in the presented analysis is termed *Multinomial Logistic Regression* (MNLR, for an application to atmospheric blocking see Detring et al., 2021). MNLR can be considered as an generalization of ordinary logistic regression (e.g. Wilks, 2006) for multiclass problems and can also be formulated within the framework of Vector Generalized Linear Models (VGLM, Yee, 2015).

A.4.1 *General setup*

Suppose that N daily observations of a nominal categorical variable Z_k (time step or day $k = 1, ..., N$) are simultaneously observed with L different independent variables $x_{l,k}$ ($l = 1, ..., L$), also termed *covariates*. For the application in this thesis, the M categories of the categorical variable Z are associated with the five different possibilities of allocating some observed daily averaged SLP pattern y_k to one of the cluster sets C_i, where $i \in \{1, 2, 3, 4, 5\}$. An allocation of y_k to some cluster set C_i at day k is denoted by $Z_k = i$. The order of the cluster sets does not matter; thus, the integers i can be arbitrarily assigned to the cluster sets. The random variable Z_k at day k follows a Multinomial distribution with $n = 1$ trials, which is completely determined when given the occurrence probabilities $\Pr(Z_k = i)$ for four of the five cluster sets.

The overall objective is to describe the occurrence probability $\Pr(Z_k = i)$ in dependence on the covariates $x_{l,k}$, which can be formally written as $\Pr(Z_k = i \,|\, x_{1,k}, ..., x_{L,k})$. In the following, $\Pr(Z_k = i \,|\, x_{1,k}, ..., x_{L,k})$ is abbreviated by p_i.

A.4.2 *Multinomial Logistic Regression*

A suitable approach for the aforementioned multi-class problem of describing p_i in dependence on some covariates is MNLR. Probably the simplest approach to MNLR is to declare one of the five categories as a baseline category (here category "1"), define the *log-odds* as $\ln\left(\frac{p_i}{p_1}\right)$ for the remaining four categories with respect to the baseline category, and then let the log-odds be a linear combination of the covariates:

$$\ln\left(\frac{p_i}{p_1}\right) = \beta_0^i + \beta_1^i x_{1,k} + ... + \beta_L^i x_{L,k} \quad \text{for} \quad i \in \{2, 3, 4, 5\}, \tag{A.12}$$

where the right-hand side is also termed *linear predictor*. Thus, four separate sets of regression coefficients $\{\beta_0^i, ..., \beta_L^i\}$ were introduced, one set for each of the four categories except the baseline category. The intuition behind describing the log-odds by a linear predictor of covariates is that the log-odds are defined on $[-\infty, \infty]$, whereas the respective probabilities should finally stay between zero and one.

When accounting for the constraint $\sum_{i=1}^{5} p_i = 1$, the probability of the baseline category can finally be expressed as a function of the covariates $x_{l,k}$:

$$p_1 = \frac{1}{1 + \sum_{j=2}^{5} e^{\beta_0^j + \beta_1^j x_{1,k} + \ldots + \beta_L^j x_{L,k}}} \tag{A.13}$$

and the probabilities of the other categories are given as

$$p_i = \frac{e^{\beta_0^i + \beta_1^i x_{1,k} + \ldots + \beta_L^i x_{L,k}}}{1 + \sum_{j=2}^{5} e^{\beta_0^j + \beta_1^j x_{1,k} + \ldots + \beta_L^j x_{L,k}}}, \quad \text{for} \quad i \in \{2,3,4,5\} \tag{A.14}$$

In this thesis, the `statsmodels.discrete.discrete_model.MNLogit` class from the python library `statsmodels` is used for fitting the regression parameters to the observations and for calculating the final probabilities. Maximum likelihood estimation is employed in order to obtain the final estimates for the regression parameters β_l^i.

A.4.3 *Linear predictor*

As mentioned before the objective is to model the occurrence probabilities of regime occurrences in dependence on the covariates *month* $x_{m,k}$, *time* $x_{t,k}$ and instantaneous linearly detrended daily-averaged *Arctic Sea Ice Area* anomaly $x_{SIA,k}$. In addition to the continuous covariates $x_{t,k}$ and $x_{SI,k}$, a binary categorical variable $x_{m,k}$ is introduced, which is one if month m is present at some day k and zero if not. From now on, the subscript k will be dropped when denoting the covariates.

The Figures in Sec. 4.2.2 are based on a MNLR model with a linear predictor specified for e.g. winter as

$$\log\left(\frac{p_i}{p_1}\right) = \beta_0^i + \beta_t^i x_t + \beta_{SIA}^i x_{SIA} + \sum_{m \in \{Dec,Jan,Feb\}} \beta_m^i x_m + \beta_{t,m}^i x_m \cdot x_t + \beta_{SIA,m}^i x_m \cdot x_{SIA} \tag{A.15}$$

where β_0^i is an intercept parameter. A set of parameters for March is not necessary due to redundancy reasons. Relation A.15 does not only consider the main effects ($\beta_t^i x_t$ and $\beta_{SIA}^i x_{SIA}$) of the covariates time and detrended Arctic Sea Ice Area anomaly, but also accounts for an interaction of both covariates with the covariate month ($\beta_{t,m}^i x_m \cdot x_t$ and $\beta_{SIA,m}^i x_m \cdot x_{SIA}$). This allows not only to describe the averaged seasonal influence of time and Arctic Sea Ice Area on regime occurrence frequencies, but also to account for differences of these effects within individual months of a season.

After fitting the regression parameters to the observed regime and covariate time series, the occurrence probability of the baseline regime p_1 and of the remaining regimes p_i are respectively given by Equations A.13 and A.14.

Evaluating Equation A.13 for e.g. December yields

$$p_1 = \frac{1}{1 + \sum_{j=2}^{5} e^{\beta_0^j + \beta_{Dec}^j + \beta_t^j x_t + \beta_{SIA}^j x_{SIA} + \beta_{t,Dec}^j x_t + \beta_{SIA,Dec}^j x_{SIA}}}, \tag{A.16}$$

for the occurrence probability of the baseline regime.

For the Figures in Sec. 4.2.2 two different cases were distinguished:

- Figs. 4.8 and 4.10: the regime occurrence probabilities were plotted as a function of time for different months. Therefore, detrended sea ice area anomaly x_{SIA} in the linear predictor term (e.g. in Eq. A.16) was set to zero, which can be associated with neutral Arctic SI conditions. This allows to describe the recent temporal trends in regime occurrence frequencies in the absence of any detrended Arctic sea ice anomalies.

- Figs. 4.9 and 4.11: here, the regime occurrence probabilities were plotted as a function of detrended Arctic sea ice anomalies for different months. Therefore, time x_t was set to the year 1999 in the linear predictor term, which corresponds to the midpoint of the ERA5 time period. This allows to relate regime occurrence frequency changes that are not captured by the recent trend in time to variations in detrended Arctic sea ice area anomalies.

Confidence bands

Confidence bands around the mean responses were constructed based on the moving block bootstrap in order to account for regime persistence (see Sec. 3.3.1). For each bootstrapped time series the parameters of the MNLR model were fitted and the occurrence probabilities for the respective values of covariates were calculated. The 90 percent confidence bands are finally determined by computing the 0.95 and 0.05 quantiles of the resulting bootstrapped distributions of occurrence probabilities.

A.5 DEFINITION AND CALCULATION OF RETURN LEVELS

Section 4.3.2 showed how extreme temperature return levels change when contrasting the PAMIP sensitivity experiments with the reference run. The presented return levels were based on a fit of a generalized extreme value distribution to yearly block-maxima (minima) of daily maximum (minimum) 2 meter temperature data. Here, a brief review of the basic theory of classical extreme value theory is provided, followed by a description of the definition and estimation of return levels. Finally, it is outlined how significant differences in estimated return levels are defined when different PAMIP sensitivity experiments are compared with the reference simulation.

A.5.1 *Block maxima approach and Generalized Extreme Value distribution*

Probably the most fundamental concept of classical extreme value theory is the so-called *block maxima approach* (see e.g. Coles, 2001). A time series x_i of i.i.d. observations or random variables that share a common Probability Distribution Function PDF is divided into non-overlapping blocks $\{x_1^k, ..., x_n^k\}$, where n is the block size and k signifies the k-th block. The objective is to find a probability function $\Pr(M_n < z)$ that describes the distribution of block maxima

$$M_n^k = \max\{x_1^k, ..., x_n^k\}. \tag{A.17}$$

Indeed, the *Fisher-Tippett Theorem* (Fisher et al., 1928; Gnedenko, 1943) motivates a family of probability distributions as models for block maxima M_n. In its generalized form it states (Coles, 2001):

Theorem. *If there exist sequences of constants* $\{a_n > 0\}$ *and* $\{b_n\}$ *such that*

$$\Pr\left(\frac{M_n - b_n}{a_n} < z\right) \to G(z) \text{ as } n \to \infty \tag{A.18}$$

for a non-degenerate function G, then G is a member of the generalized extreme value family

$$G(z) = \exp\left\{-\left[1 + \xi\left(\frac{z-\mu}{\sigma}\right)\right]^{-\frac{1}{\xi}}\right\}, \tag{A.19}$$

defined on $\{z : 1 + \xi(z-\mu)/\sigma > 0\}$ *, where* $-\infty < \mu < \infty$, $\sigma > 0$ *and* $-\infty < \xi < \infty$.

Thus, independent of the original distribution function of observations x_i and for large block sizes n, the *Generalized Extreme Value* GEV distribution is an adequate parametric model for describing the probability function of block maxima. In practical settings knowledge of the normalization constants is not required.

Generally speaking, the location parameter μ characterized the location and the scale parameter σ the spread of the respective GEV distribution. The shape parameter ξ determines the tail behavior, where $\xi > 0$ results in a heavy-tailed Type II (*Fréchet*) distribution, and $\xi < 0$ yields a Type III (*Weibull*) distribution with a fixed upper end point (see Fig. A.1 for the respective PDFs). For the limit case $\xi = 0$, the GEV distribution A.19 leads to the Type I (*Gumbel*) distribution

$$G(z) = \exp\left[-\exp\left\{-\left(\frac{z-\mu}{\sigma}\right)\right\}\right] \quad -\infty < z < \infty, \tag{A.20}$$

that is characterized by an exponentially decaying upper tail (light tail).

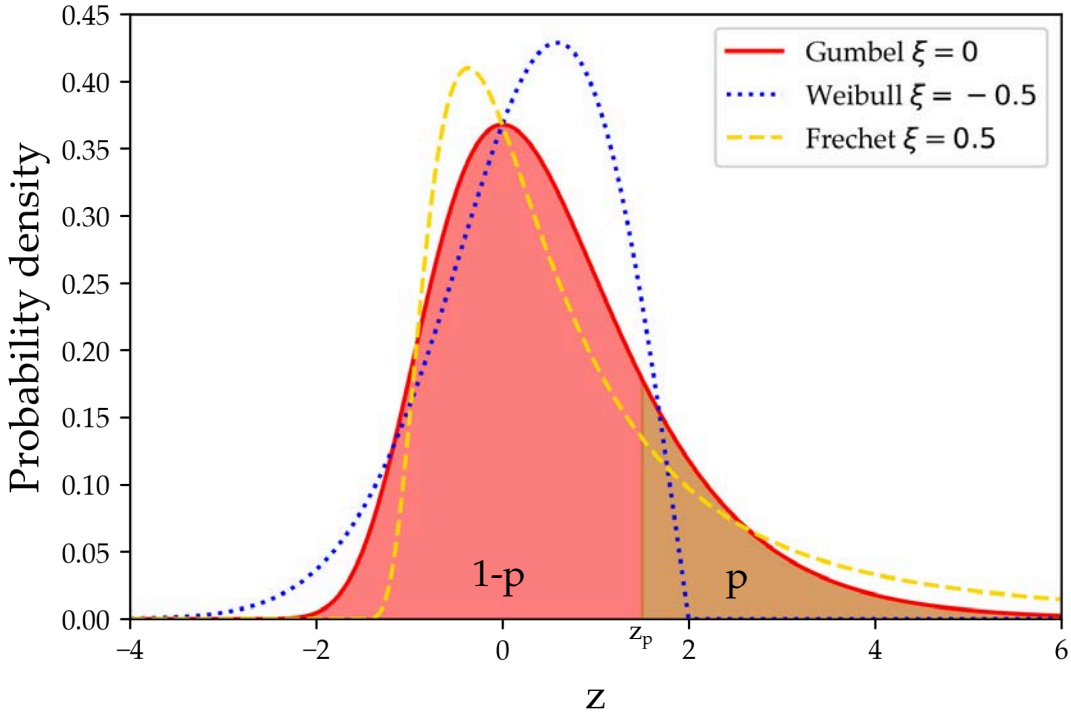

Figure A.1: Illustration of different GEV probability density functions for block maxima (Gumbel, Weibull, Fréchet) with location parameter $\mu = 0$ and scale parameter $\sigma = 1$. The Gumbel distribution exemplifies the principle of return levels: here, z_p corresponds to a threshold that is exceeded by a block maximum with probability $p = 1 - G\left(z_p\right) = 0.2$ (brown area). Complementary, the red area signifies the probability $1 - p$ of non-exceedance. If the illustrated GEV distribution was obtained by a fit to annual block maxima, z_p would correspond to the 5-year return level.

Return level

The probability p of e.g. a yearly maximum exceeding a certain value z_p is given as $1 - G\left(z_p\right)$ (see also the area fraction under the respective PDFs in Fig. A.1). z_p is also termed *return level* and can be obtained by inverting Equation A.19:

$$z_p = \begin{cases} \mu - \frac{\sigma}{\xi}\left\{1 - y_p^{-\xi}\right\} & \text{for} \quad \xi \neq 0 \\ \mu - \sigma \log y_p & \text{for} \quad \xi = 0 \end{cases} \tag{A.21}$$

where $y_p = -\log(1 - p)$. A return level can be associated with a *return period* $T = \frac{1}{p}$, such that z_p is in case of annual block maxima on average exceeded once every T years.

Block minima

Based on the GEV distribution for maxima in A.19, a GEV distribution for block minima $\tilde{M}_n^k = \min\{x_1^k, ..., x_n^k\}$ can be derived as (Coles, 2001)

$$\tilde{G}(z) = 1 - \exp\left\{-\left[1 - \tilde{\xi}\left(\frac{z-\tilde{\mu}}{\tilde{\sigma}}\right)\right]^{-\frac{1}{\tilde{\xi}}}\right\}, \tag{A.22}$$

defined on $\{z : 1 - \tilde{\xi}(z-\tilde{\mu})/\tilde{\sigma} > 0\}$, where $-\infty < \tilde{\mu} < \infty$, $\tilde{\sigma} > 0$ and $-\infty < \tilde{\xi} < \infty$.

Similar to block maxima, a return level $\tilde{z}_p$ for minima can be defined as

$$\tilde{z}_p = \begin{cases} \tilde{\mu} + \frac{\tilde{\sigma}}{\tilde{\xi}}\left\{1 - y_p^{-\tilde{\xi}}\right\} & \text{for} \quad \tilde{\xi} \neq 0 \\ \tilde{\mu} + \tilde{\sigma}\log y_p & \text{for} \quad \tilde{\xi} = 0 \end{cases} \tag{A.23}$$

where e.g. an annual block minima falls below $\tilde{z}_p$ on average once every $T = \frac{1}{p}$ years.

A.5.2 *Return level estimation*

In this thesis temperature return levels were computed for the different ECHAM6 PAMIP experiments at grid points over the continental NH. At each grid point annual block maxima (minima) of the respective 100-year long daily T2max (T2min) time series were extracted. In climates sciences, blocks of 1 year are frequently used (e.g. Zwiers et al., 1998; Huang et al., 2016). The extracted annual maxima and minima temperatures can then be respectively used to estimate the GEV parameters.

Block maxima

Estimates $\hat{\mu}, \hat{\sigma}, \hat{\xi}$ of the true GEV parameter values can be obtained by minimizing the log-likelihood for the different parameters (Coles, 2001). Under suitable regularity conditions and in the limit of large block sizes ($n \to \infty$), the estimated parameter vector $\hat{\theta} = (\hat{\mu}, \hat{\sigma}, \hat{\xi})$ is actually multivariate normal distributed

$$\hat{\theta} \sim \mathcal{N}_{MV}(\theta^\star, V) \tag{A.24}$$

where $\theta^\star$ denotes the true parameter vector and V is an approximated covariance matrix.

Maximum likelihood estimation of the GEV parameters and calculation of the covariance matrix V is carried out using the function `vglm()` from the `R` package `VGAM` (see Yee, 2015, Chapter 16). As recommended by Yee (2015) the possible values for the estimated shape parameter are restricted to $\hat{\xi} > -0.5$. Maximum likelihood estimates of return levels $\hat{z}_p$ are finally derived from the estimated parameters $\hat{\mu}, \hat{\sigma}, \hat{\eta}$ and Equation A.21.

Block minima

Estimates for GEV parameters $\hat{\tilde{\mu}}, \hat{\tilde{\sigma}}, \hat{\tilde{\xi}}$ and return levels $\hat{\tilde{z}}_p$ of annual block minima can be obtained when exploiting the duality between the GEV distributions for maxima and

minima (Coles, 2001). Indeed, the maximum likelihood estimates $\hat{\mu}$, $\hat{\sigma}$, $\hat{\xi}$ for the negated values of annual block minima correspond exactly to the required GEV parameters for minima, apart from the sign correction $\hat{\tilde{\mu}} = -\hat{\mu}$. Consequently, the respective off-diagonal entries of the computed covariance matrix V have to be negated as well.

Return level uncertainty estimates

The variance of the sampling distributions of the return level estimates $\hat{z}_p$ can be for instance approximated with the *delta method* (Coles, 2001):

$$\mathrm{Var}\left(\hat{z}_p\right) \approx \nabla z_p^T \, V \, \nabla z_p, \tag{A.25}$$

where e.g. for block maxima and for $\xi \neq 0$ we have

$$\nabla z_p^T = \left[\frac{\partial z_p}{\partial \mu}, \frac{\partial z_p}{\partial \sigma}, \frac{\partial z_p}{\partial \xi} \right] \tag{A.26}$$

$$= \left[1, -\xi^{-1}\left(1 - y_p^{-\xi}\right), \sigma\xi^{-2}\left(1 - y_p^{-\xi}\right) - \sigma\xi^{-1} y_p^{-\xi} \log y_p \right] \tag{A.27}$$

evaluated at $(\hat{\mu}, \hat{\sigma}, \hat{\xi})$.

In order to define significance difference between estimated return levels $\hat{z}_{p,1}$ and $\hat{z}_{p,2}$ that were calculated from two different PAMIP simulations we proceed as follows:
The sampling distributions of return level estimates are approximately normal:

$$\hat{z}_{p,1/2} \sim \mathcal{N}\left(z^\star_{p,1/2}, \mathrm{Var}(z_{p,1/2})\right), \tag{A.28}$$

where $z^\star_{p,1/2}$ are the true return level values.

The sampling distribution of return level differences can then also be approximated by a normal distribution

$$\hat{z}_{p,2} - \hat{z}_{p,1} \sim \mathcal{N}\left(z^\star_{p,2} - z^\star_{p,1}, \mathrm{Var}(\hat{z}_{p,2}) + \mathrm{Var}(\hat{z}_{p,1})\right) \tag{A.29}$$

Finally, a 90 percent confidence interval for the true return level difference is given as

$$\hat{z}_{p,2} - \hat{z}_{p,1} \pm 1.645\sqrt{\mathrm{Var}(\hat{z}_{p,2}) + \mathrm{Var}(\hat{z}_{p,1})} \tag{A.30}$$

Both return levels are reported to significantly differ from each other, if the computed 90 percent confidence interval does not include a zero return level difference.

A.6 FRAMEWORK FOR CONDITIONAL EXTREME EVENT ATTRIBUTION

In Section 4.5 a framework of conditional extreme event attribution proposed by Yiou et al. (2017) was employed. This allowed to decompose frequency changes of European temperature extremes into two different contributions: one term that is related to dynamical changes in regime occurrence frequencies, and another more thermodynamically driven contribution that assumes fixed atmospheric dynamics in terms of circulation regimes.

As already explained in the beginning of Section 4.3.1, extreme events are defined as exceedances (or falls below) of a threshold value, for temperature extremes termed T_{ref}. The threshold value at a given grid point is computed for each month separately based on the 0.95 or 0.05 distribution quantiles in pdSST/pdSI.

Based on the respective threshold one can define the probabilities p_0 and p_1 in a counterfactual and factual world , respectively, of an extreme occurrence at a certain grid point as

$$p_{0/1} = \Pr(T_{0/1} \lesseqgtr T_{\text{ref}}) \tag{A.31}$$

where T_0 is the temperature in the counterfactual world and T_1 in the factual world. In this thesis, the factual world (the world as it is) is defined as the pdSST/pdSI reference simulation. The counterfactual world (a world that might occur) is given by the different ECHAM6 PAMIP sensitivity experiments.

By employing Bayes' formula the extreme occurrence probabilities can be expressed with conditional probabilities as

$$p_{0/1} = \Pr(T_{0/1} \lesseqgtr T_{\text{ref}} | \mathrm{y}_{0/1} \in C_{\text{ref}}) \cdot \frac{\Pr(\mathrm{y}_{0/1} \in C_{\text{ref}})}{\Pr(\mathrm{y}_{0/1} \in C_{\text{ref}} | T_{0/1} \lesseqgtr T_{\text{ref}})} \tag{A.32}$$

As introduced in Section A.2, C_{ref} describes the set of all daily SLP anomaly fields $\mathrm{y}_{0/1}$ in the respective world that are allocated to a certain reference regime centroid C_{ref}. When applying this decomposition it is assumed that the occurrence of an extreme at some grid point can be explained by the presence of a specific reference regime C_{ref}. Otherwise, a reasonable interpretation is not possible.

The probability (or risk ratio) ρ was already introduced in Eq. 4.1 and compares the extreme occurrence probabilities in the counterfactual (p_0) and in the factual world (p_1). When using Eq. A.32 this ratio can be multiplicatively decomposed into

$$\rho = \frac{p_0}{p_1} = \rho_{FR} \cdot \rho_{CR}, \tag{A.33}$$

that is, a "Changed-Regime" term ρ_{CR} relating changes in extremes to changes in regime occurrences, and a "Fixed-Regime" term ρ_{FR} that considers such changes in extremes for a fixed circulation regime.
The Fixed-Regime contribution term is given by

$$\rho_{\text{FR}} = \frac{\Pr(T_0 \lesseqgtr T_{\text{ref}} | \mathrm{y}_0 \in C_{\text{ref}})}{\Pr(T_1 \lesseqgtr T_{\text{ref}} | \mathrm{y}_1 \in C_{\text{ref}})} \tag{A.34}$$

This term describes the extreme occurrence probability ratio between both worlds given a regime allocation $y_{0/1} \in C_{ref}$ to a reference regime set C_{ref}. This terms has previously been named thermodynamical contribution (Yiou et al., 2017), as the atmospheric circulation is fixed in terms of circulation regimes. Nevertheless, in the beginning of Section 4.5 it was already stressed that caution is needed when using such names as this term assumes that the regime pattern structures do not change between simulation scenarios. In addition to this, the individual flows allocated to a respective set C_{ref} may also differ between different simulations.

The second contribution related to regime changes is defined as

$$\rho_{CR} = \rho_{reci} \cdot \rho_{circ} = \frac{\Pr(y_1 \in C_{ref} | T_1 \lessgtr T_{ref})}{\Pr(y_0 \in C_{ref} | T_0 \lessgtr T_{ref})} \cdot \frac{\Pr(y_0 \in C_{ref})}{\Pr(y_1 \in C_{ref})}. \tag{A.35}$$

The latter term ρ_{circ} is related to changes in the occurrence probability of the reference regime C_{ref} between both simulations. Therefore, this term has previously also been termed dynamical contribution (Yiou et al., 2017), as ρ_{circ} can be directly associated with dynamical changes within the framework of circulation regimes. The term ρ_{reci} evaluates changes in the probability of a circulation such as C_{ref} when given an extreme. ρ_{reci} allows for connecting the more meaningful and interpretable terms ρ, ρ_{FR} and ρ_{circ}. Furthermore, it was also suggested by Yiou et al. (2017) that ρ_{reci} helps to reconcile the risk-based approach (estimation of ρ only) with the storyline approach of extreme event attribution.

B ADDITIONAL FIGURES

B.1 CIRCULATION REGIMES AND SEA ICE-INDUCED FREQUENCY CHANGES

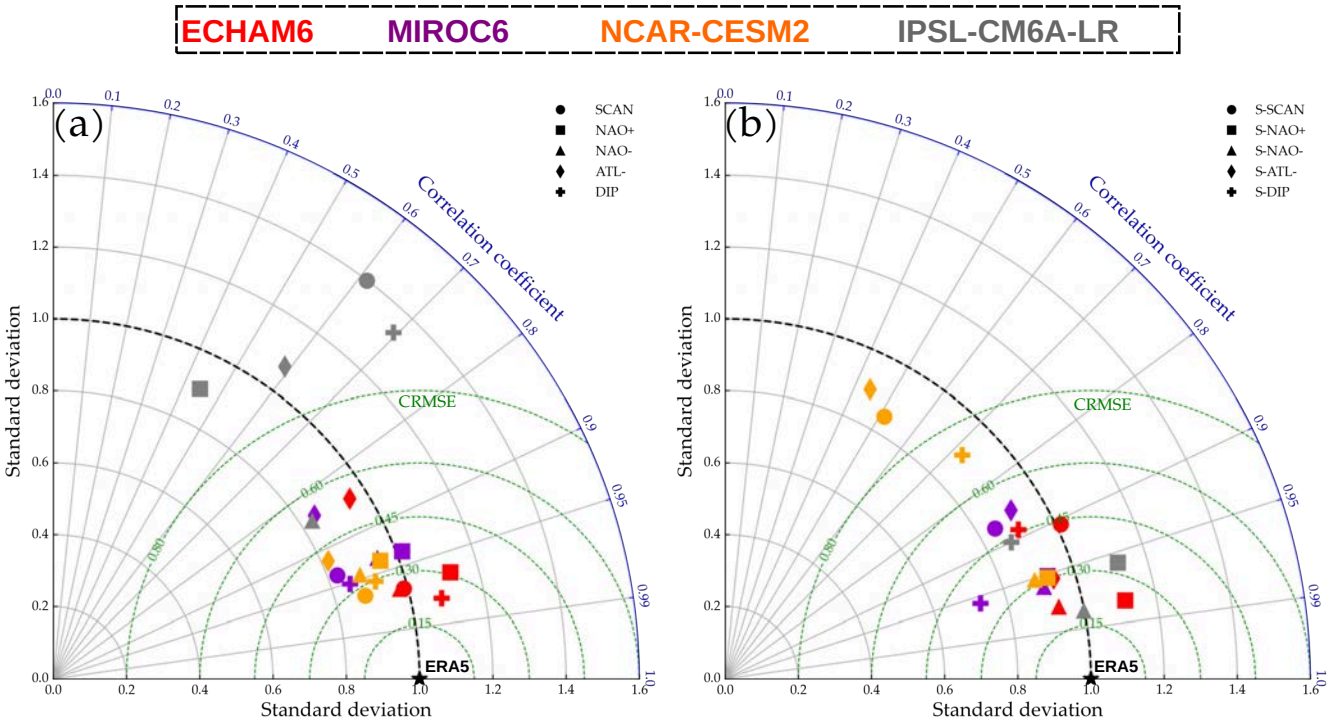

Figure B.1: Taylor diagram as in Figure 4.6 but comparing the ERA5 winter (a) and summer (b) regimes with regimes from ECHAM6 PAMIP data, but also for pdSST/pdSI atmosphere-only experiments from other models within the PAMIP data pool: the Japanese climate Model for Interdisciplinary Research on Climate *MIROC6*, the Community Earth System Model Version 2 *CESM2* from the National Center for Atmospheric Research (NCAR) and *CM6A-LR*, the latest version of the climate model from the Institut Pierre-Simon Laplace (IPSL). Models were chosen based on data availability at the *Earth System Grid Federation* (ESGF) at the time the analysis was conducted.

B.2 CHANGES IN NORTHERN HEMISPHERIC TEMPERATURE EXTREMES INDUCED BY SEA ICE LOSS

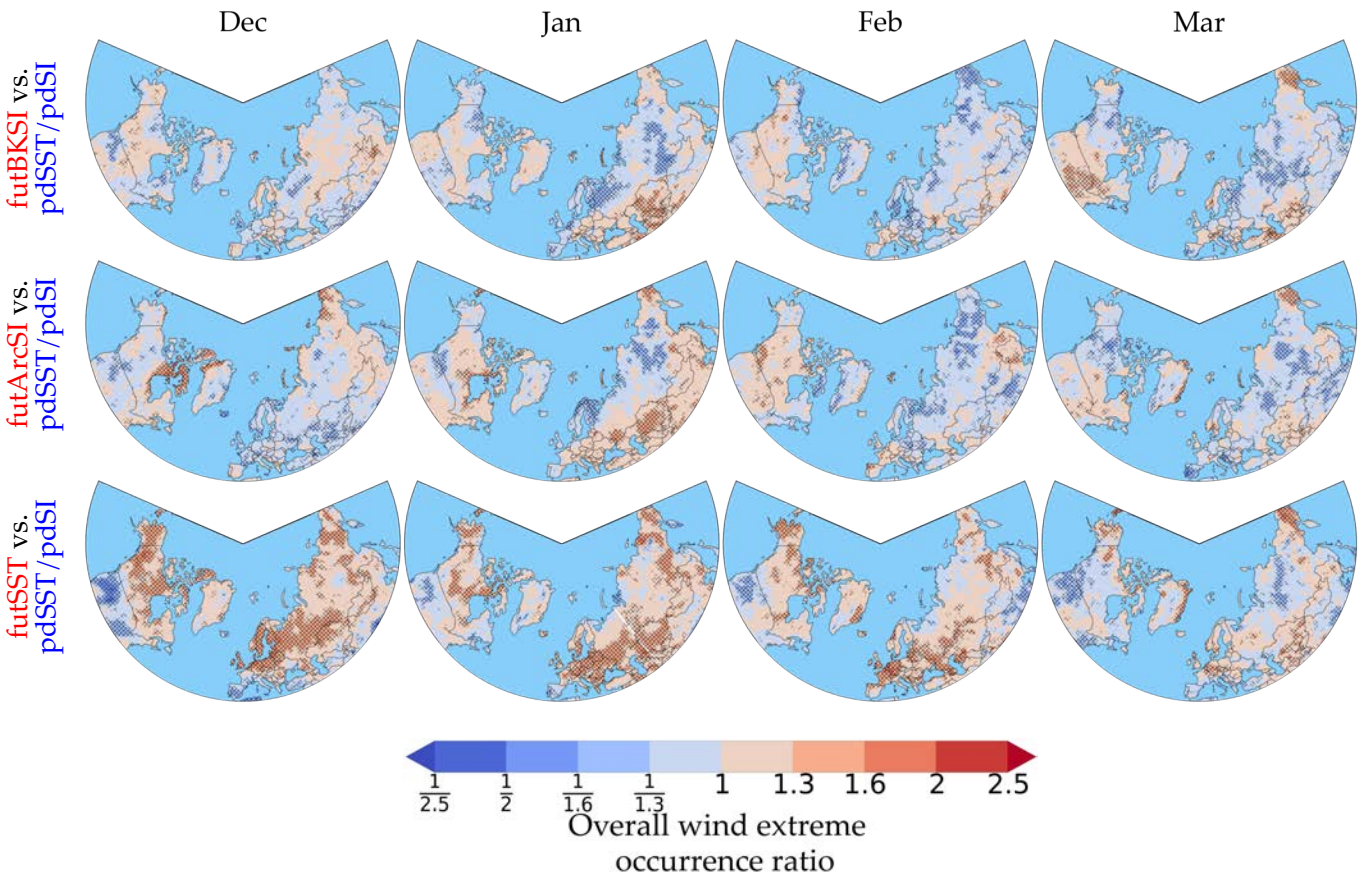

Figure B.2: Similar to Fig. 4.15, but for winter wind extremes. Upper row: futBKSI vs. pdSST/pdSI, Middle row: futArcSI vs. pdSST/pdSI, Bottom row: futSST vs. pdSST/pdSI.

B.3 LINKS BETWEEN CIRCULATION REGIMES AND EXTREMES OVER EUROPE

B.3.1 *Conditioned vs. unconditioned ERA5 and wind extreme probabilities*

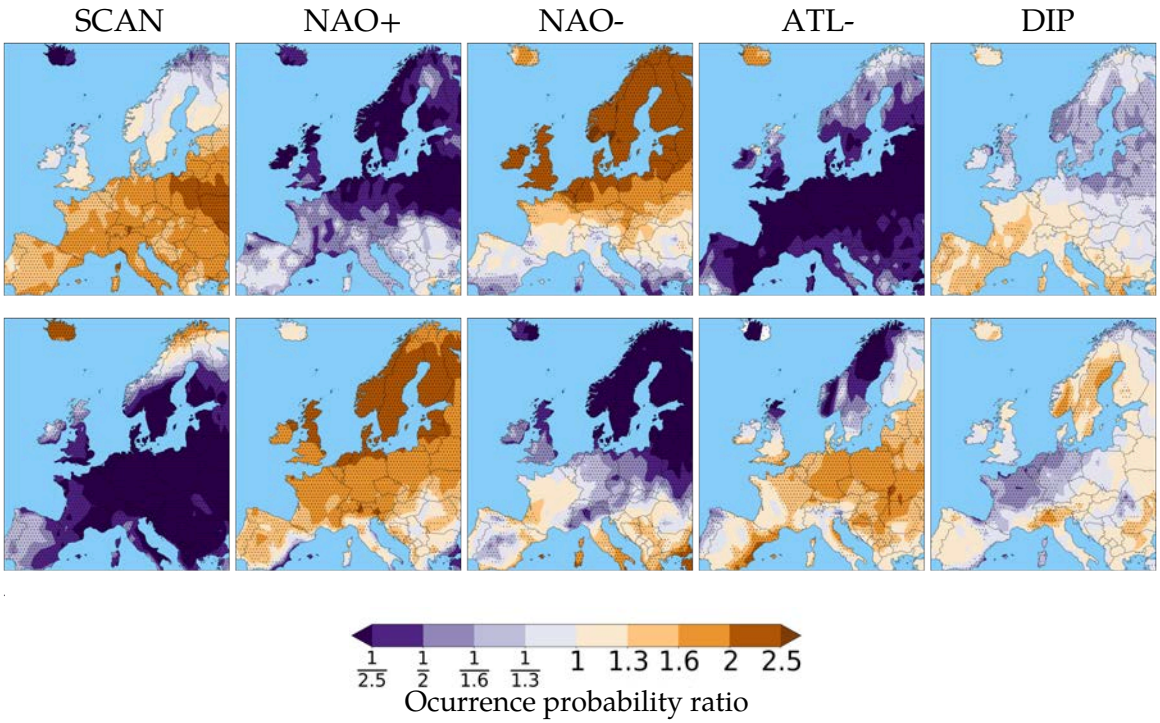

Figure B.3: Same analysis for winter cold and warm extremes as in Fig. 4.23, but for ERA5 over the period 1979–2018. Thus, regime patterns computed from ERA5 were used for computing these plots. ERA5 T2max/T2min times series at each grid point were linearly detrended beforehand. Stippling indicates ratios that significantly differ from unity based on a moving block bootstrap ($M = 1000$).

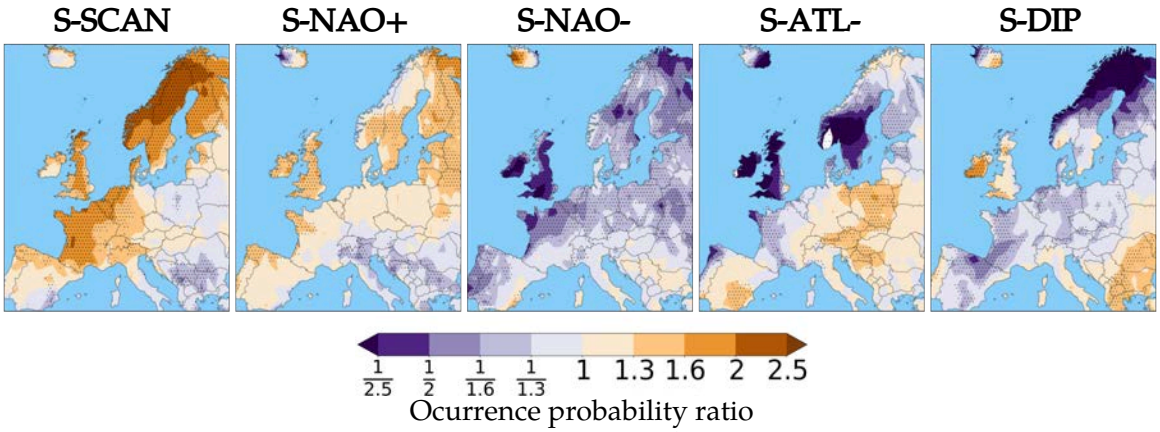

Figure B.4: Same analysis for summer heat extremes as in Fig. 4.24, but for ERA5 over the period 1979–2018. Thus, summer regime patterns computed from ERA5 were used for computing these plots. ERA5 T2max/T2min times series at each grid point were linearly detrended beforehand. Stippling indicates ratios that significantly differ from unity.

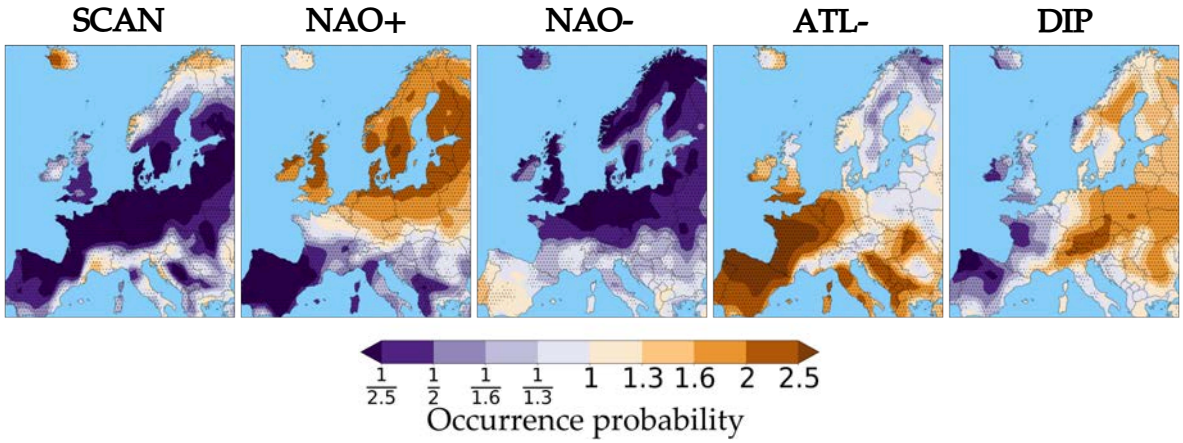

Figure B.5: Same analysis of the PAMIP pdSST/pdSI experiment as in Fig. 4.23, but for winter wind extremes. Stippling indicates ratios that significantly differ from unity based on a moving block bootstrap ($M = 1000$).

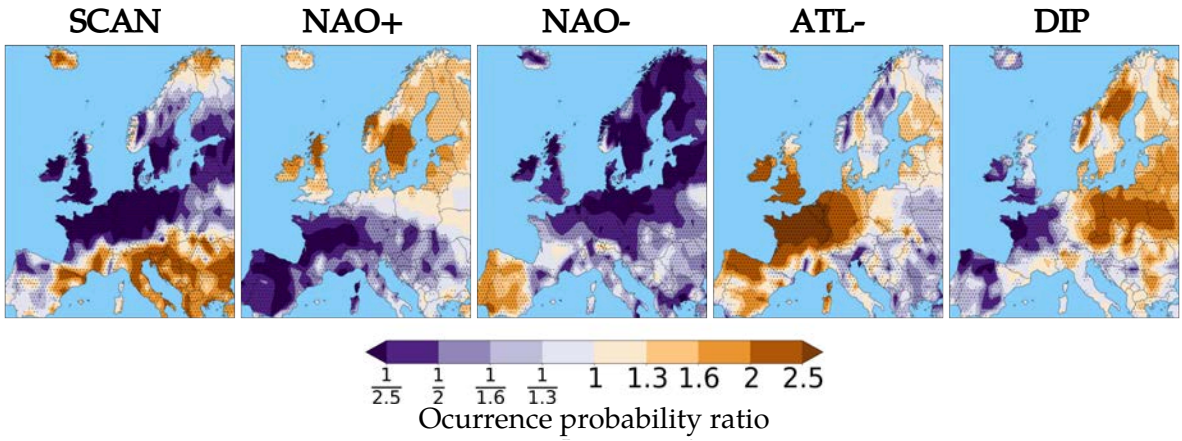

Figure B.6: Same as in Fig. B.5, but for ERA5 over the period 1979–2018. Thus, regime patterns computed from ERA5 were used for computing these plots. ERA5 near-surface wind times series at each grid point were linearly detrended beforehand. Stippling indicates ratios that significantly differ from unity based on a moving block bootstrap ($M = 1000$).

B.3.2 *Wind and synoptic-scale activity anomalies*

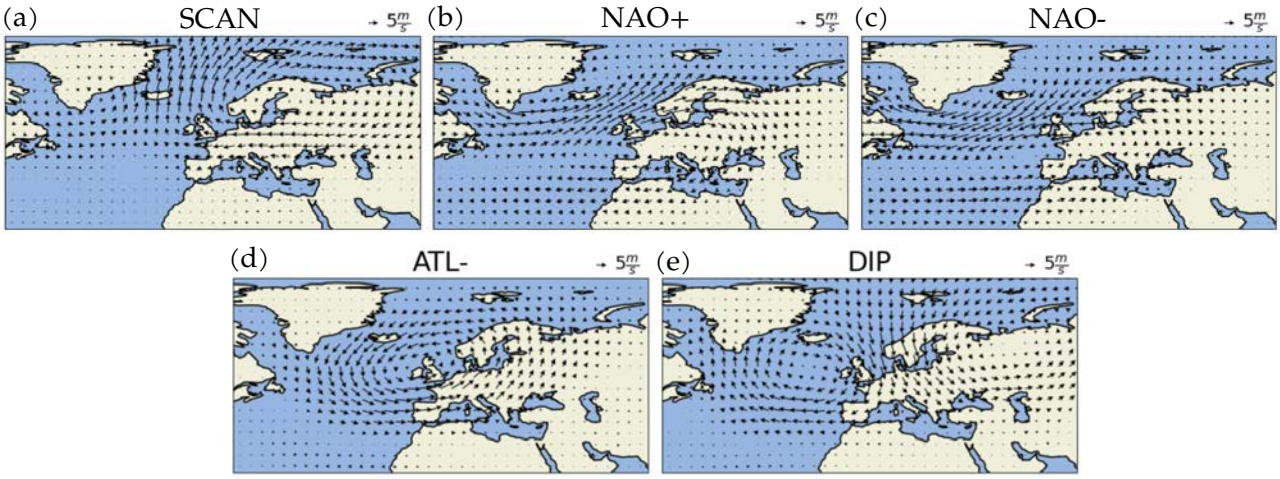

Figure B.7: Wind anomalies at 850 hPa in DJFM for the five circulation regimes. The plots are based on data from the PAMIP pdSST/pdSI reference simulation. Surface wind fields were regridded to a regular lat-lon grid with 3.75° resolution.

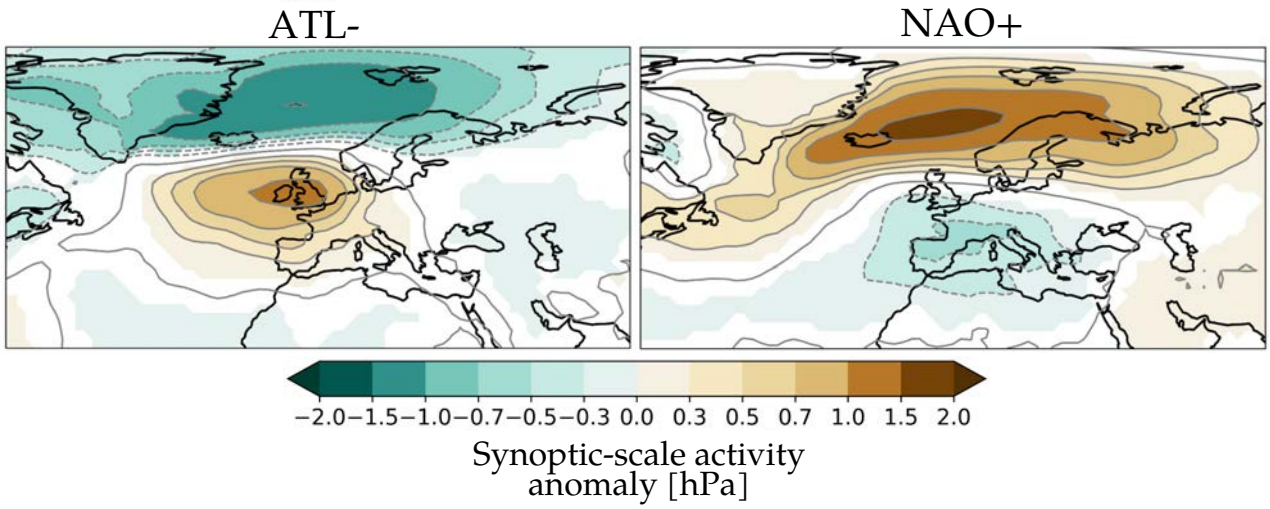

Figure B.8: DJFM synoptic-scale activity anomalies for the ATL- and NAO+ regimes computed from PAMIP pdSST/pdSI model data. Synoptic-scale activity is computed here as the 2–6 day bandpass filtered standard deviation of SLP data (Blackmon, 1976). It provides a measure for baroclinic activity and characterizes stormtrack locations. Only anomalies that significantly differ from zero according to a moving block bootstrap ($M = 1000$) are shown in colors.

B.4 DECOMPOSITION OF SEA ICE-INDUCED FREQUENCY CHANGES IN EUROPEAN WINTER EXTREMES

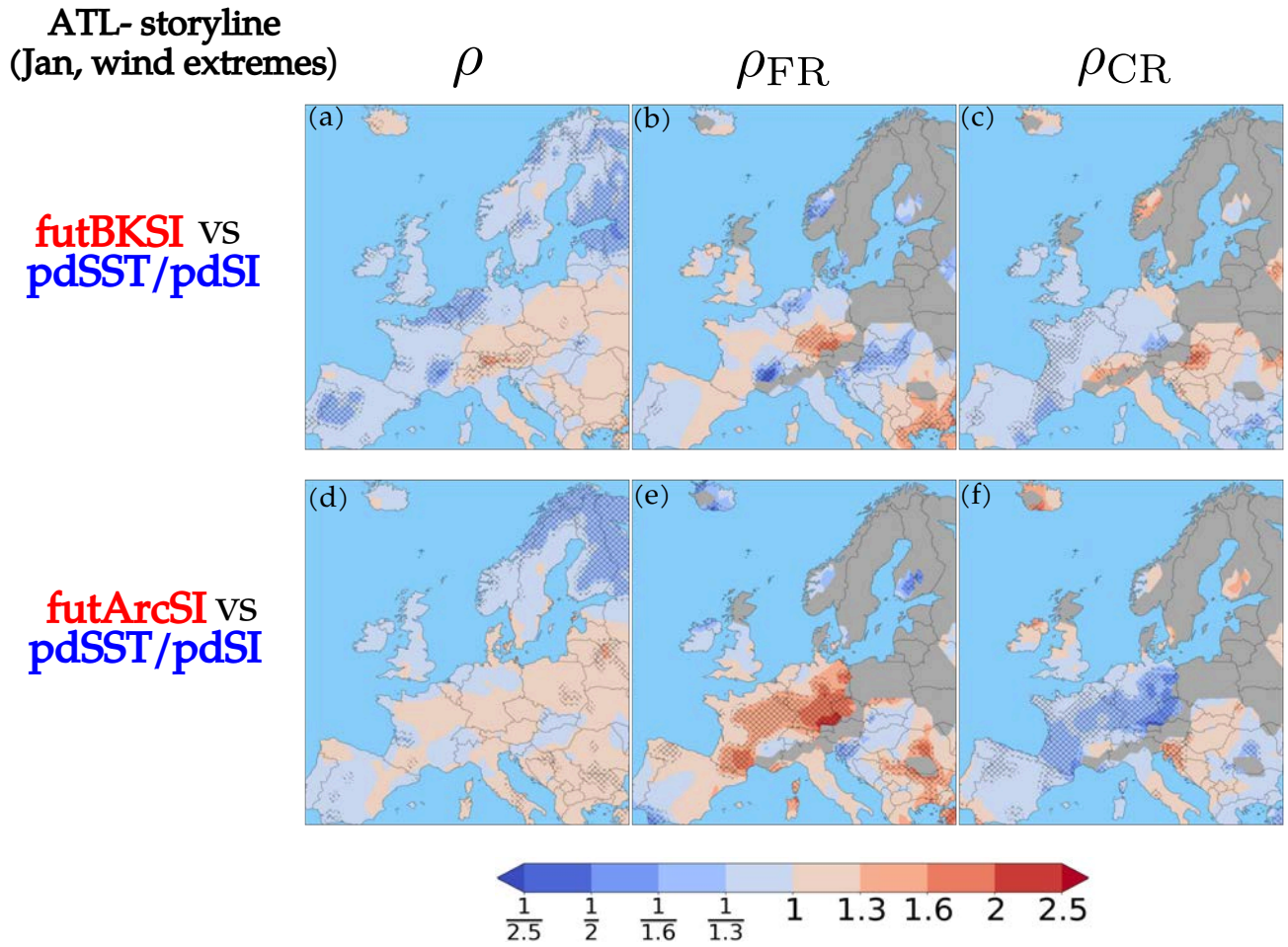

Figure B.9: Same as in Fig. 4.25, but for January wind extremes and assuming a ATL- storyline. Upper row: futBKSI with a 20% decrease of January ATL- occurrences. Bottom row: futArcSI with a 21% decrease of ATL- occurrences in January. ρ_{FR} and ρ_{CR} are only plotted for regions, where statistically significant preferred winter wind extreme occurrences were identified during ATL- days (see Fig. B.5).

B.5 CIRCULATION ANALOGUE-BASED APPROACH FOR SUMMER SEASON

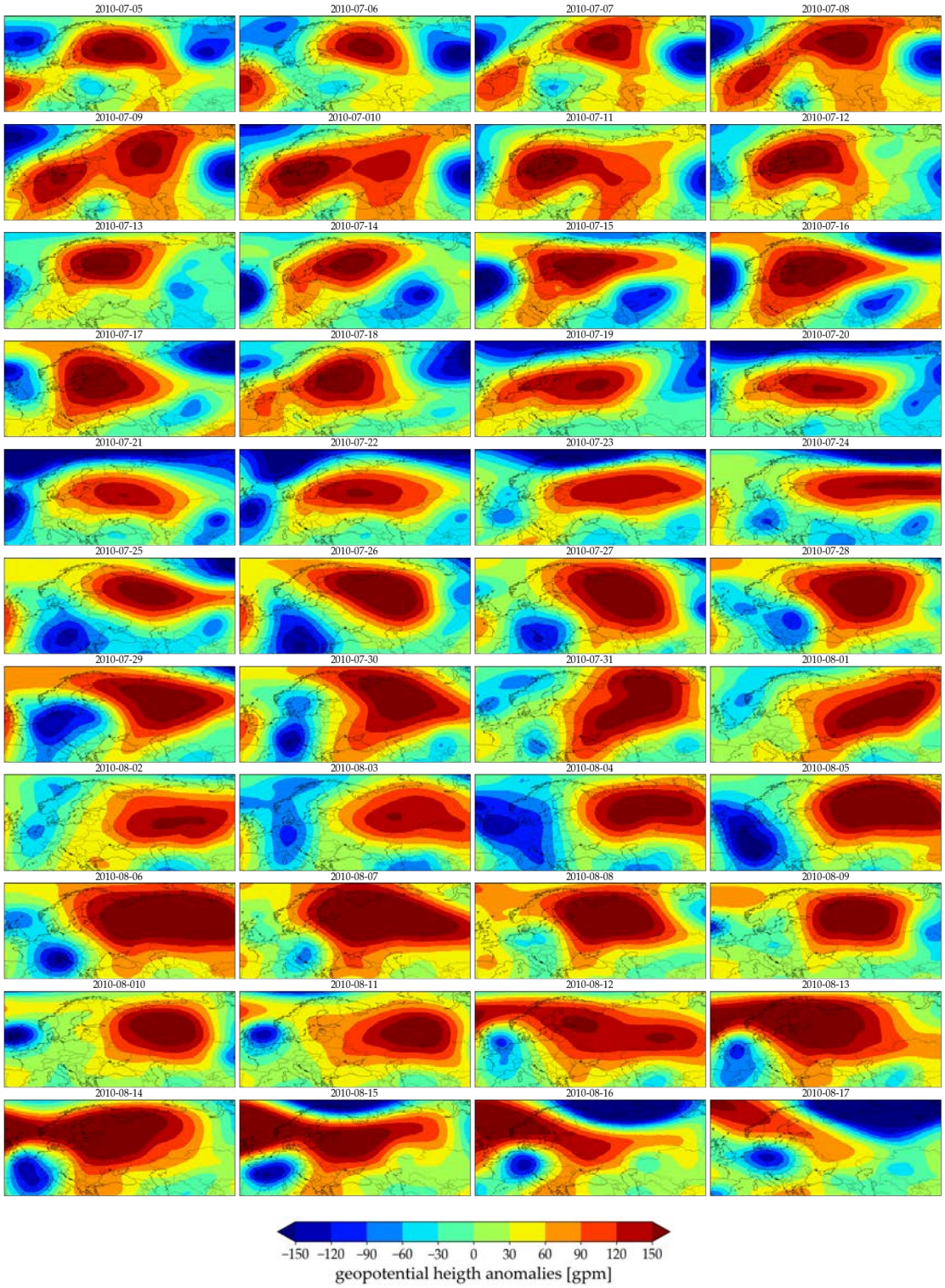

Figure B.10: Individual detrended daily ERA5 gph500 anomaly pattern during the Russian heat wave in 2010.

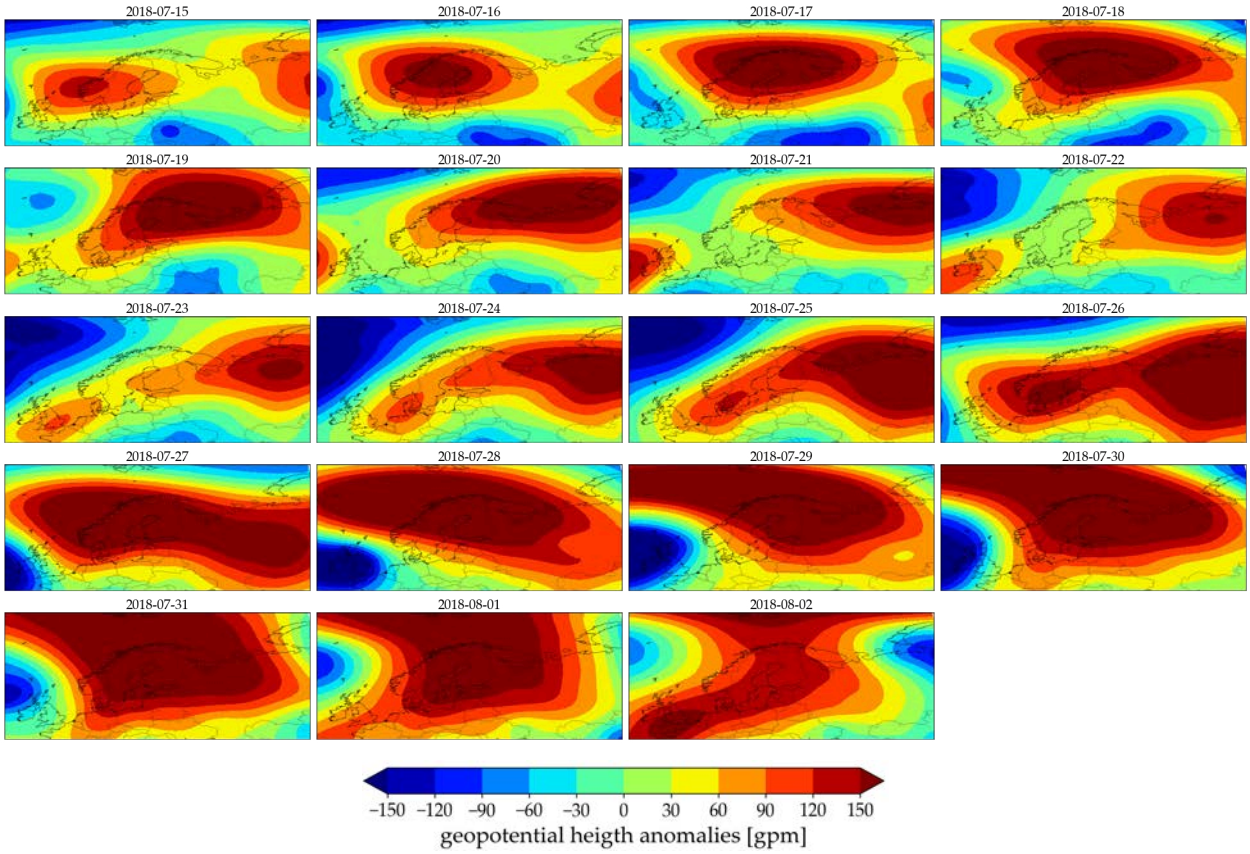

Figure B.11: Individual detrended daily ERA5 gph500 anomaly pattern during the Scandinavian heat wave in 2018.

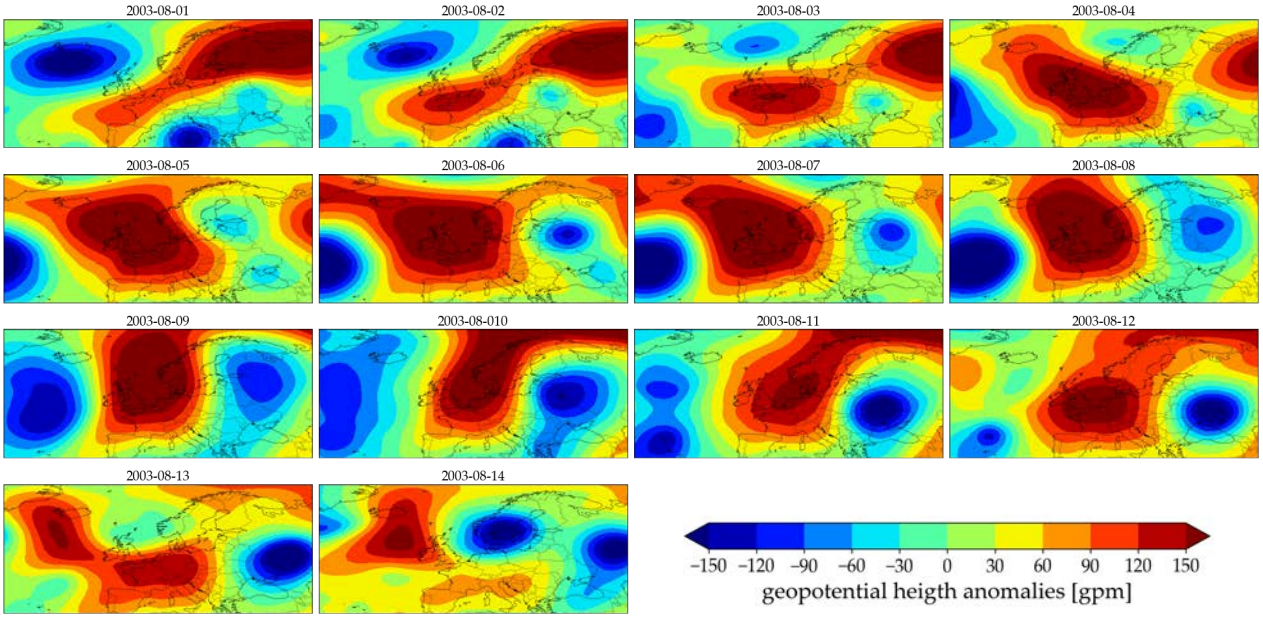

Figure B.12: Individual detrended daily ERA5 gph500 anomaly pattern during the European heat wave in 2003.

B.6 MISCELLANEOUS

B.6.1 *Recent Arctic sea ice trends*

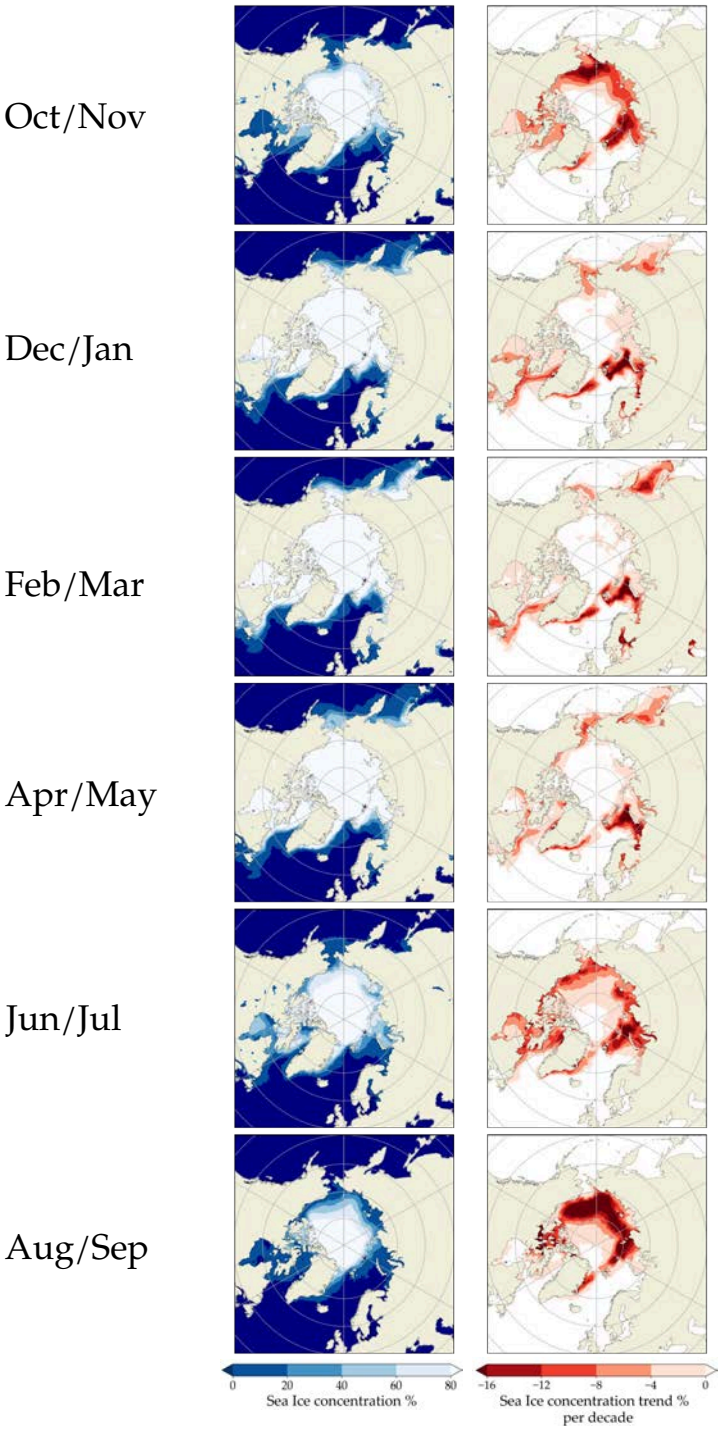

Figure B.13: Same as in Fig. 2.6a, but for different pairs of months of the year. Left: mean state of ERA5 SIC averaged over 1979–2018. Right: linear trend of monthly averaged ERA5 SIC over the period 1979–2018.

B.6.2 *futSST forcing field*

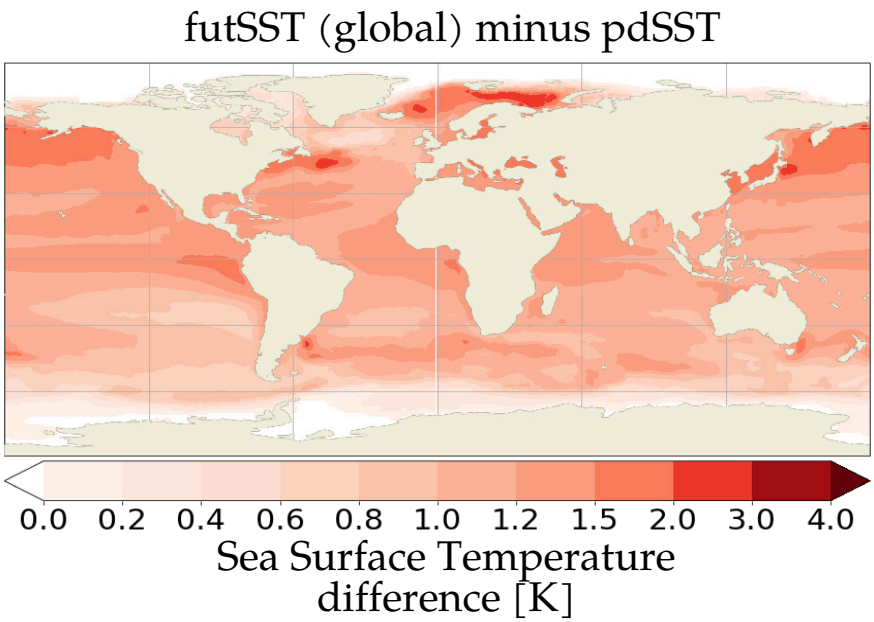

Figure B.14: Global SST forcing differences between the futSST experiment and the pdSST/pdSI reference simulation averaged over all months.

B.6.3 *Fluxes over sea ice and ocean surfaces in ECHAM6*

Atmosphere-only experiments following the AMIP protocol require a variety of prescribed forcing fields or boundary conditions, such as prescribed ozone and greenhouse gas concentrations, as well as lower boundary conditions over land and ocean surfaces. However, only SI and SST conditions are modified between the different ECHAM6 PAMIP experiments that are analyzed in this thesis. Here, it is briefly outlined how the computation of fluxes and surface temperatures over SI and ocean surfaces is handled in an ECHAM6 atmosphere-only setup.

At each ocean grid point i, a SIC value f_i and a SST value are provided, where f_i defines the fraction of ice-covered areas within a model grid point. Sea ice thickness is set to a constant value h_i=2 m and snow cover on ice surfaces is consequently neglected.

The turbulent fluxes of sensible and latent heat, as well as the flux of momentum between the surface and the lowermost atmospheric layer are computed with the bulk exchange formulas (see Eqs. 2.15 and 2.16). The respective fluxes within a grid cell are initially calculated over ocean and ice surfaces separately. The total surface fluxes within a respective grid cell are afterwards computed as the weighted average with respect to the area fraction of open water (1-f_i) and SI (f_i).

In order to calculate sensible heat fluxes over SI, a sea ice surface temperature is required. The sea ice surface temperature T_i^{n+1} at time step $n+1$ is calculated from the heat budget of a thin slab of ice with thickness h_o=0.05 m

$$C_i \frac{(T_i^{n+1} - T_i^n)}{\Delta t} = R_{tot} + H_c, \tag{B.1}$$

where $C_i = \rho_i c_i h_o$ is the heat capacity of the ice slab, c_i the specific heat of ice, ρ_i is ice density and Δt is the integration time step. Thus, the ice surface temperature change is the sum of all net surface radiative and turbulent energy fluxes R_{tot} (see Eq. 2.13), plus, the conductive heat flux H_c through the ice with thickness h_i. The conductive heat flux through the ice is assumed to be proportional to the temperature difference between the ice surface and the ocean surface beneath

$$H_c = -\frac{\kappa_i}{h_i}(T_i^{n+1} - T_o), \tag{B.2}$$

where κ_i is the thermal conductivity of ice (e.g. around 2.23 $W\,m^{-1}\,K^{-1}$ at $T_o = -1.77°C$).

The radiative surface fluxes that contribute to the net surface flux R_{tot} depend on the ice albedo α. The albedo of bare SI surfaces thicker than 1 m is set to 0.76 for the visible spectrum ($\lambda < 689$ nm) and to 0.29 for the near infrared spectrum($\lambda > 689$ nm). For open water surfaces the albedo is set to 0.07. Emissivity (see Eq. 2.14) is set to 0.996 for all surfaces.

BIBLIOGRAPHY

Alexander, L. (2010). "Extreme heat rooted in dry soils." In: *Nature Geoscience 2010* 4.1, pp. 12–13. DOI: 10.1038/ngeo1045.

Allen, R. J. and S. C. Sherwood (2008). "Warming maximum in the tropical upper troposphere deduced from thermal winds." In: *Nature Geoscience* 1.6, pp. 399–403. DOI: 10.1038/ngeo208.

Almazroui, M. et al. (2021). "Projected Changes in Climate Extremes Using CMIP6 Simulations Over SREX Regions." In: *Earth Systems and Environment* 5.3, pp. 481–497. DOI: 10.1007/s41748-021-00250-5.

Andrade, C., S. M. Leite, and J. A. Santos (2012). "Temperature extremes in Europe: Overview of their driving atmospheric patterns." In: *Natural Hazards and Earth System Science* 12.5, pp. 1671–1691. DOI: 10.5194/nhess-12-1671-2012.

Añel, J. A. et al. (2017). "Impact of Cold Waves and Heat Waves on the Energy Production Sector." In: *Atmosphere* 8.11. DOI: 10.3390/ATMOS8110209.

Arias, P. et al. (2021). "Technical Summary. In Climate Change 2021: The Physical Science Basis. Contribution of Working Group I to the Sixth Assessment Report of the Intergovernmental Panel on Climate Change." In: *Cambridge University Press*, pp. 33–144. DOI: 10.1017/9781009157896.002.

Arrhenius, S. (1896). "On the Influence of Carbonic Acid in the Air upon the Temperature of the Ground." In: *The London, Edinburgh, and Dublin Philosophical Magazine and Journal of Science* 41.251, pp. 237–276.

Baldwin, M. P. and T. J. Dunkerton (1999). "Propagation of the Arctic Oscillation from the stratosphere to the troposphere." In: *Journal of Geophysical Research: Atmospheres* 104.D24, pp. 30937–30946. DOI: 10.1029/1999JD900445.

Barnes, E. A. (2013). "Revisiting the evidence linking Arctic amplification to extreme weather in midlatitudes." In: *Geophysical Research Letters* 40.17, pp. 4734–4739. DOI: 10.1002/grl.50880.

Barnes, E. A. and J. A. Screen (2015). "The impact of Arctic warming on the midlatitude jet-stream: Can it? Has it? Will it?" In: *Wiley Interdisciplinary Reviews: Climate Change* 6.3, pp. 277–286. DOI: 10.1002/wcc.337.

Barriopedro, D. et al. (2011). "The hot summer of 2010: Redrawing the temperature record map of Europe." In: *Science* 332.6026, pp. 220–224. DOI: 10.1126/SCIENCE.1201224/SUPPL_FILE/BARRIOPEDRO-SOM.PDF.

Baur, F., P. Hess, and H. Nagel (1944). "Kalender der grosswetterlagen Europas 1881–1939." In: *Bad Homburg*.

Bieli, M., S. Pfahl, and H. Wernli (2015). "A Lagrangian investigation of hot and cold temperature extremes in Europe." In: *Quarterly Journal of the Royal Meteorological Society* 141.686, pp. 98–108. DOI: 10.1002/qj.2339.

Blackmon, M. L. (1976). "A climatological spectral study of the 500 mb geopotential height of the Northern Hemisphere." In: *Journal of the Atmospheric Sciences* 33.8, pp. 1607–1623. DOI: 10.1175/1520-0469(1976)033<1607:ACSSOT>2.0.CO;2.

Blackport, R. and J. A. Screen (2019). "Influence of Arctic Sea Ice Loss in Autumn Compared to That in Winter on the Atmospheric Circulation." In: *Geophysical Research Letters* 46.4, pp. 2213–2221. DOI: 10.1029/2018GL081469.

Bolinger, R. A. et al. (2022). "An assessment of the extremes and impacts of the February 2021 South-Central U.S. Arctic outbreak, and how climate services can help." In: *Weather and Climate Extremes* 36. DOI: 10.1016/j.wace.2022.100461.

Brandt, R. E. et al. (2005). "Surface Albedo of the Antarctic Sea Ice Zone." In: *Journal of Climate* 18.17, pp. 3606–3622. DOI: 10.1175/JCLI3489.1.

Brodzik, M. J. et al. (2012). "EASE-Grid 2.0: Incremental but Significant Improvements for Earth-Gridded Data Sets." In: *ISPRS International Journal of Geo-Information* 1.1, pp. 32–45. DOI: 10.3390/ijgi1010032.

Butler, A. H. et al. (2017). "A sudden stratospheric warming compendium." In: *Earth System Science Data* 9.1, pp. 63–76. DOI: 10.5194/ESSD-9-63-2017.

Carvalho, D., S. Cardoso Pereira, and A. Rocha (2021). "Future surface temperatures over Europe according to CMIP6 climate projections: an analysis with original and bias-corrected data." In: *Climatic Change* 167.1, pp. 1–17. DOI: 10.1007/S10584-021-03159-0/FIGURES/5.

Casado, M. J., M. A. Pastor, and F. J. Doblas-Reyes (2009). "Euro-Atlantic circulation types and modes of variability in winter." In: *Theoretical and Applied Climatology*. Vol. 96. 1, pp. 17–29. DOI: 10.1007/s00704-008-0036-2.

Casola, J. H. and J. M. Wallace (2007). "Identifying Weather Regimes in the Wintertime 500-hPa Geopotential Height Field for the Pacific–North American Sector Using a Limited-Contour Clustering Technique." In: *Journal of Applied Meteorology and Climatology* 46.10, pp. 1619–1630. DOI: 10.1175/JAM2564.1.

Cassano, J. J. et al. (2007). "Predicted changes in synoptic forcing of net precipitation in large Arctic river basins during the 21st century." In: *Journal of Geophysical Research: Biogeosciences* 112.G4. DOI: 10.1029/2006JG000332.

Cattiaux, J. et al. (2010). "Winter 2010 in Europe: A cold extreme in a warming climate." In: *Geophysical Research Letters* 37.20. DOI: 10.1029/2010GL044613.

Charney, J. G. and P. G. Drazin (1961). "Propagation of planetary-scale disturbances from the lower into the upper atmosphere." In: *Journal of Geophysical Research* 66.1, pp. 83–109. DOI: 10.1029/JZ066i001p00083.

Charney, J. G. and D. M. Straus (1980). "Form-drag instability, multiple equilibria and propagating planetary waves in baroclinic, orographically forced, planetary wave systems." In: *Journal of Atmospheric Sciences* 37.6, pp. 1157–1176.

Charney, J. G. and J. G. DeVore (1979). "Multiple Flow Equilibria in the Atmosphere and Blocking." In: *Journal of the Atmospheric Sciences* 36.7, pp. 1205–1216. DOI: 10.1175/1520-0469(1979)036.

Cheng, X. and J. M. Wallace (1993). "Cluster analysis of the Northern Hemisphere wintertime 500-hPa height field: spatial patterns." In: *Journal of the Atmospheric Sciences* 50.16, pp. 2674–2696. DOI: 10.1175/1520-0469(1993)050<2674:caotnh>2.0.co;2.

Chripko, S. et al. (2021). "Impact of reduced arctic sea ice on northern hemisphere climate and weather in autumn and winter." In: *Journal of Climate* 34.14, pp. 5847–5867. DOI: 10.1175/JCLI-D-20-0515.1.

Christiansen, B. (2007). "Atmospheric Circulation Regimes: Can Cluster Analysis Provide the Number?" In: *Journal of Climate* 20.10, pp. 2229–2250. DOI: 10.1175/JCLI4107.1.

Cohen, J et al. (2018). "Arctic change and possible influence on mid-latitude climate and weather: a US CLIVAR White Paper." In: *US CLIVAR reports*. DOI: 10.5065/D6TH8KGW.

Cohen, J. et al. (2020). "Divergent consensuses on Arctic amplification influence on mid-latitude severe winter weather." In: *Nature Climate Change* 10.1, pp. 20–29. DOI: 10.1038/s41558-019-0662-y.

Cohen, J. et al. (2007). "Stratosphere–Troposphere Coupling and Links with Eurasian Land Surface Variability." In: *Journal of Climate* 20.21, pp. 5335–5343. DOI: 10.1175/2007JCLI1725.1.

Cohen, J. et al. (2014a). "Linking Siberian Snow Cover to Precursors of Stratospheric Variability." In: *Journal of Climate* 27.14, pp. 5422–5432. DOI: 10.1175/JCLI-D-13-00779.1.

Cohen, J. et al. (2014b). "Recent Arctic amplification and extreme mid-latitude weather." In: *Nature Geoscience* 7.9, pp. 627–637. DOI: 10.1038/ngeo2234.

Coles, S. (2001). *An Introduction to Statistical Modeling of Extreme Values*. London: Springer.

Corti, S., F. Molteni, and T. N. Palmer (1999). "Signature of recent climate change in frequencies of natural atmospheric circulation regimes." In: *Nature* 398.6730, pp. 799–802. DOI: 10.1038/19745.

Coumou, D. et al. (2018). "The influence of Arctic amplification on mid-latitude summer circulation." In: *Nature Communications* 9.1, pp. 1–12. DOI: 10.1038/s41467-018-05256-8.

Coumou, D., J. Lehmann, and J. Beckmann (2015). "The weakening summer circulation in the Northern Hemisphere mid-latitudes." In: *Science* 348.6232, pp. 324–327. DOI: 10.1126/science.1261768.

Coumou, D. and S. Rahmstorf (2012). "A decade of weather extremes." In: *Nature Climate Change* 2.7, pp. 491–496. DOI: 10.1038/nclimate1452.

Coumou, D. et al. (2014). "Quasi-resonant circulation regimes and hemispheric synchronization of extreme weather in boreal summer." In: *Proceedings of the National Academy of Sciences* 111.34, pp. 12331–12336. DOI: 10.1073/PNAS.1412797111.

Crasemann, B. et al. (2017). "Can preferred atmospheric circulation patterns over the North-Atlantic-Eurasian region be associated with arctic sea ice loss?" In: *Polar Science* 14, pp. 9–20. DOI: 10.1016/J.POLAR.2017.09.002.

Davini, P. and F. D'Andrea (2020). "From CMIP3 to CMIP6: Northern hemisphere atmospheric blocking simulation in present and future climate." In: *Journal of Climate* 33.23, pp. 10021–10038. DOI: 10.1175/JCLI-D-19-0862.1.

Dawson, A., T. N. Palmer, and S. Corti (2012). "Simulating regime structures in weather and climate prediction models." In: *Geophysical Research Letters* 39.21. DOI: 10.1029/2012GL053284.

De Bono, A. et al. (2004). "Impacts of Summer 2003 Heat Wave in Europe." In: *Environment Alert Bulletin* 2.

Deser, C., L. Terray, and A. S. Phillips (2016). "Forced and internal components of winter air temperature trends over North America during the past 50 years: Mechanisms and implications." In: *Journal of Climate* 29.6, pp. 2237–2258. DOI: 10.1175/JCLI-D-15-0304.1.

Deser, C., R. A. Tomas, and L. Sun (2015). "The role of ocean-atmosphere coupling in the zonal-mean atmospheric response to Arctic sea ice loss." In: *Journal of Climate* 28.6, pp. 2168–2186. DOI: 10.1175/JCLI-D-14-00325.1.

Deser, C. et al. (2010). "The seasonal atmospheric response to projected Arctic sea ice loss in the late twenty-first century." In: *Journal of Climate* 23.2, pp. 333–351. DOI: 10.1175/2009JCLI3053.1.

Detring, C. et al. (2021). "Occurrence and transition probabilities of omega and high-over-low blocking in the Euro-Atlantic region." In: *Weather and Climate Dynamics* 2.4, pp. 927–952. DOI: 10.5194/wcd-2-927-2021.

Deutsche-Rück (2008). *Sturmdokumentation 2007 Deutschland*. Tech. rep. Duesseldorf: Deutsche Rückversicherung.

Díaz, J. et al. (2005). "Mortality impact of extreme winter temperatures." In: *International Journal of Biometeorology* 49.3, pp. 179–183. DOI: 10.1007/S00484-004-0224-4/TABLES/1.

Dorrington, J. and K. J. Strommen (2020). "Jet Speed Variability Obscures Euro-Atlantic Regime Structure." In: *Geophysical Research Letters* 47.15. DOI: 10.1029/2020gl087907.

England, M. R., I. Eisenman, and T. J. W. Wagner (2022). "Spurious Climate Impacts in Coupled Sea Ice Loss Simulations." In: *Journal of Climate* 35.22, pp. 3801–3811. DOI: 10.1175/jcli-d-21-0647.1.

Falkena, S. K. J. et al. (2020). "Revisiting the Identification of Wintertime Atmospheric Circulation Regimes in the Euro-Atlantic Sector." In: *Quarterly Journal of the Royal Meteorological Society* 146.731, pp. 2801–2814. DOI: https://doi.org/10.1002/qj.3818. arXiv: 1912.10838.

Faranda, D. et al. (2020). "Changes in Future Synoptic Circulation Patterns: Consequences for Extreme Event Attribution." In: *Geophysical Research Letters* 47.15. DOI: 10.1029/2020GL088002.

Fisher, R. A. and L. H. Tippett (1928). "Limiting forms of the frequency distribution of the largest or smallest member of a sample." In: *Mathematical Proceedings of the Cambridge Philosophical Society* 24.2, pp. 180–190. DOI: 10.1017/S0305004100015681.

Folland, C. K. et al. (2009). "The summer North Atlantic oscillation: Past, present, and future." In: *Journal of Climate* 22.5, pp. 1082–1103. DOI: 10.1175/2008JCLI2459.1.

Fouillet, A. et al. (2006). "Excess mortality related to the August 2003 heat wave in France." In: *International Archives of Occupational and Environmental Health* 80.1, pp. 16–24. DOI: 10.1007/S00420-006-0089-4/FIGURES/2.

Francis, J. A. and S. J. Vavrus (2012). "Evidence linking Arctic amplification to extreme weather in mid-latitudes." In: *Geophysical Research Letters* 39.6. DOI: 10.1029/2012GL051000.

Francis, J. A. et al. (2009). "Winter Northern Hemisphere weather patterns remember summer Arctic sea-ice extent." In: *Geophysical Research Letters* 36.7. DOI: 10.1029/2009GL037274.

Franzke, C. et al. (2008). "A Hidden Markov Model Perspective on Regimes and Metastability in Atmospheric Flows." In: *Journal of Climate* 21.8, pp. 1740–1757. DOI: 10.1175/2007JCLI1751.1.

Future Earth (2020). *Risk Percepitions Report 2020*. Tech. rep.

Gastineau, G., J. García-Serrano, and C. Frankignoul (2017). "The Influence of Autumnal Eurasian Snow Cover on Climate and Its Link with Arctic Sea Ice Cover." In: *Journal of Climate* 30.19, pp. 7599–7619. DOI: 10.1175/JCLI-D-16-0623.1.

Giorgetta, M. A. et al. (2013). "The atmospheric general circulation model ECHAM6 - Model description." In: *Reports on Earth System Science/Max Planck Institute for Meteorology* 135. DOI: 10.17617/2.1810480.

Gnedenko, B. (1943). "Sur La Distribution Limite Du Terme Maximum D'Une Serie Aleatoire." In: *The Annals of Mathematics* 44.3, pp. 423–453. DOI: 10.2307/1968974.

Goosse, H. et al. (2018). "Quantifying climate feedbacks in polar regions." In: *Nature Communications* 9.1, pp. 1–13. DOI: 10.1038/s41467-018-04173-0.

Graham, R. M. et al. (2019). "Evaluation of six atmospheric reanalyses over Arctic sea ice from winter to early summer." In: *Journal of Climate* 32.14, pp. 4121–4143. DOI: 10.1175/JCLI-D-18-0643.1.

Grimm, N. B. et al. (2013). "The impacts of climate change on ecosystem structure and function." In: *Frontiers in Ecology and the Environment* 11.9, pp. 474–482. DOI: 10.1890/120282.

Hahn, L. C. et al. (2020). "Antarctic Elevation Drives Hemispheric Asymmetry in Polar Lapse Rate Climatology and Feedback." In: *Geophysical Research Letters* 47.16. DOI: 10.1029/2020GL088965.

Hahn, L. C. et al. (2021). "Contributions to Polar Amplification in CMIP5 and CMIP6 Models." In: *Frontiers in Earth Science* 9. DOI: 10.3389/FEART.2021.710036/BIBTEX.

Handorf, D. and K. Dethloff (2012). "How well do state-of-the-art atmosphere-ocean general circulation models reproduce atmospheric teleconnection patterns?" In: *Tellus A: Dynamic Meteorology and Oceanography* 64.1, pp. 1–27. DOI: 10.3402/tellusa.v64i0.19777.

Handorf, D. et al. (2009). "Climate regime variability for past and present time slices simulated by the fast ocean atmosphere model." In: *Journal of Climate* 22.1, pp. 58–70. DOI: 10.1175/2008JCLI2258.1.

Handorf, D. et al. (2015). "Impacts of Arctic sea ice and continental snow cover changes on atmospheric winter teleconnections." In: *Geophysical Research Letters* 42.7, pp. 2367–2377. DOI: 10.1002/2015GL063203.

Hannachi, A. et al. (2017). "Low-frequency nonlinearity and regime behavior in the Northern Hemisphere extratropical atmosphere." In: *Reviews of Geophysics* 55.1, pp. 199–234. DOI: 10.1002/2015RG000509.

Hassanzadeh, P., Z. Kuang, and B. F. Farrell (2014). "Responses of midlatitude blocks and wave amplitude to changes in the meridional temperature gradient in an idealized dry GCM." In: *Geophysical Research Letters* 41.14, pp. 5223–5232. DOI: 10.1002/2014GL060764.

Haustein, K. et al. (2019). "A limited role for unforced internal variability in twentieth-century warming." In: *Journal of Climate* 32.16, pp. 4893–4917. DOI: 10.1175/JCLI-D-18-0555.1.

He, S. et al. (2020). "Eurasian Cooling Linked to the Vertical Distribution of Arctic Warming." In: *Geophysical Research Letters* 47.10. DOI: 10.1029/2020GL087212.

Henderson, G. R. et al. (2018). "Snow–atmosphere coupling in the Northern Hemisphere." In: *Nature Climate Change* 8.11, pp. 954–963. DOI: 10.1038/s41558-018-0295-6.

Hersbach, H. et al. (2020). "The ERA5 global reanalysis." In: *Quarterly Journal of the Royal Meteorological Society* 146.730, pp. 1999–2049. DOI: 10.1002/qj.3803.

Hess, P. and H. Brezowsky (1952). *Katalog Der Großwetterlagen Europas*. Tech. rep. Bad Kissingen, Germany.

Hochman, A. et al. (2021). "Do Atlantic-European Weather Regimes Physically Exist?" In: *Geophysical Research Letters* 48.20. DOI: 10.1029/2021GL095574.

Honda, M., J. Inoue, and S. Yamane (2009). "Influence of low Arctic sea-ice minima on anomalously cold Eurasian winters." In: *Geophysical Research Letters* 36.8. DOI: 10.1029/2008GL037079.

Horenko, I. (2010). "On the Identification of Nonstationary Factor Models and Their Application to Atmospheric Data Analysis." In: *Journal of the Atmospheric Sciences* 67.5, pp. 1559–1574. DOI: 10.1175/2010JAS3271.1.

Horton, D. E. et al. (2015). "Contribution of changes in atmospheric circulation patterns to extreme temperature trends." In: *Nature* 522.7557, pp. 465–469. DOI: 10.1038/nature14550.

Hoskins, B. and T. Woollings (2015). "Persistent Extratropical Regimes and Climate Extremes." In: *Current Climate Change Reports* 1.3, pp. 115–124. DOI: 10.1007/s40641-015-0020-8.

Huang, W. K. et al. (2016). "Estimating changes in temperature extremes from millennial-scale climate simulations using generalized extreme value (GEV) distributions." In: *Advances in Statistical Climatology, Meteorology and Oceanography* 2.1, pp. 79–103. DOI: https://doi.org/10.5194/ascmo-2-79-2016.

Hurrell, J. W. et al. (2003). "An overview of the north atlantic oscillation." In: *AGU Geophysical Monograph* 134, pp. 1–36. DOI: 10.1029/134GM01.

Jaiser, R. et al. (2012). "Impact of sea ice cover changes on the Northern Hemisphere atmospheric winter circulation." In: *Tellus A: Dynamic Meteorology and Oceanography* 64.1. DOI: 10.3402/tellusa.v64i0.11595.

Jaiser, R., K. Dethloff, and D. Handorf (2013). "Stratospheric response to Arctic sea ice retreat and associated planetary wave propagation changes." In: *Tellus A: Dynamic Meteorology and Oceanography* 65.1. DOI: 10.3402/tellusa.v65i0.19375.

Jaiser, R. et al. (2016). "Atmospheric winter response to Arctic sea ice changes in reanalysis data and model simulations." In: *Journal of Geophysical Research: Atmospheres* 121.13, pp. 7564–7577. DOI: 10.1002/2015JD024679.

Jézéquel, A., P. Yiou, and S. Radanovics (2018). "Role of circulation in European heatwaves using flow analogues." In: *Climate Dynamics* 50.3-4, pp. 1145–1159. DOI: 10.1007/s00382-017-3667-0.

Johannessen, O. M. et al. (2004). "Arctic climate change: observed and modelled temperature and sea-ice variability." In: *Tellus A: Dynamic Meteorology and Oceanography* 56.4, pp. 328–341. DOI: 10.3402/tellusa.v56i4.14418.

Jung, O. et al. (2017). "How does the SST variability over the western North Atlantic Ocean control Arctic warming over the Barents-Kara Seas?" In: *Environmental Research Letters* 12.3. DOI: 10.1088/1748-9326/aa5f3b.

Junghänel, T et al. (2021). *Hydro-klimatologische Einordnung der Stark- und Dauerniederschläge in Teilen Deutschlands im Zusammenhang mit dem Tiefdruckgebiet „Bernd" vom 12. bis 19. Juli 2021.* Tech. rep. Deutscher Wetterdienst.

Kageyama, M. et al. (1999). "Weather regimes in past climate atmospheric general circulation model simulations." In: *Climate Dynamics* 15.10, pp. 773–793. DOI: 10.1007/s003820050315.

Kautz, L.-A. et al. (2022). "Atmospheric blocking and weather extremes over the Euro-Atlantic sector – a review." In: *Weather and Climate Dynamics* 3.1, pp. 305–336. DOI: 10.5194/wcd-3-305-2022.

Kim, B. M. et al. (2014). "Weakening of the stratospheric polar vortex by Arctic sea-ice loss." In: *Nature Communications* 5.1, pp. 1–8. DOI: 10.1038/ncomms5646.

Kim, S. H. et al. (2022). "Contribution of Ural and Kamchatka Blockings to the Amplified Warm Arctic–Cold Eurasia Pattern under Arctic Sea Ice Loss and Eurasian Cooling." In: *Journal of Climate* 35.13, pp. 4071–4083. DOI: 10.1175/JCLI-D-21-0635.1.

King, A. D. et al. (2019). "Observed Relationships Between Sudden Stratospheric Warmings and European Climate Extremes." In: *Journal of Geophysical Research: Atmospheres* 124.24, pp. 13943–13961. DOI: 10.1029/2019JD030480.

Koenker, R. and G. Bassett (1978). "Regression Quantiles." In: *Econometrica: journal of the Econometric Society* 46.1, pp. 33–50. DOI: 10.2307/1913643.

Köhler, R. et al. (2021). "Improved Circulation in the Northern Hemisphere by Adjusting Gravity Wave Drag Parameterizations in Seasonal Experiments With ICON-NWP." In: *Earth and Space Science* 8.3. DOI: 10.1029/2021EA001676.

Kohonen, T. (2001). *Self-Organizing Maps*. 3rd ed. Springer Berlin Heidelberg. DOI: https://doi.org/10.1007/978-3-642-56927-2.

Kornhuber, K. et al. (2017). "Evidence for wave resonance as a key mechanism for generating high-amplitude quasi-stationary waves in boreal summer." In: *Climate Dynamics* 49.5, pp. 1961–1979. DOI: 10.1007/s00382-016-3399-6.

Kretschmer, M. et al. (2016). "Using causal effect networks to analyze different arctic drivers of midlatitude winter circulation." In: *Journal of Climate* 29.11, pp. 4069–4081. DOI: 10.1175/JCLI-D-15-0654.1.

Kumar, D., V. Mishra, and A. R. Ganguly (2015). "Evaluating wind extremes in CMIP5 climate models." In: *Climate Dynamics* 45.1, pp. 441–453. DOI: 10.1007/S00382-014-2306-2/FIGURES/10.

Kunsch, H. R. (1989). "The Jackknife and the Bootstrap for General Stationary Observations." In: *The Annals of Statistics* 17, pp. 1217–1241. DOI: 10.1214/aos/1176347265.

Labe, Z., Y. Peings, and G. Magnusdottir (2020). "Warm Arctic, cold Siberia pattern: role of full Arctic amplification versus sea ice loss alone." In: *Geophysical Research Letters* 47.17. DOI: 10.1029/2020gl088583.

Legras, B. and M. Ghil (1985). "Persistent anomalies, blocking and variations in atmospheric predictability." In: *Journal of Atmospheric Sciences* 42.5, pp. 433–471. DOI: https://doi.org/10.1175/1520-0469(1985)042<0433:PABAVI>2.0.CO;2.

Lehmann, J. and D. Coumou (2015). "The influence of mid-latitude storm tracks on hot, cold, dry and wet extremes." In: *Scientific Reports* 5.1, pp. 1–9. DOI: 10.1038/srep17491.

Lennard, C. and G. Hegerl (2015). "Relating changes in synoptic circulation to the surface rainfall response using self-organising maps." In: *Climate Dynamics* 44.3, pp. 861–879. DOI: 10.1007/S00382-014-2169-6/TABLES/1.

Lenssen, N. J. L. et al. (2019). "Improvements in the GISTEMP Uncertainty Model." In: *Journal of Geophysical Research: Atmospheres* 124.12, pp. 6307–6326. DOI: 10.1029/2018JD029522.

Li, C. and J. J. Wettstein (2012). "Thermally Driven and Eddy-Driven Jet Variability in Reanalysis." In: *Journal of Climate* 25.5, pp. 1587–1596. DOI: 10.1175/JCLI-D-11-00145.1.

Liu, J. et al. (2012). "Impact of declining Arctic sea ice on winter snowfall." In: *Proceedings of the National Academy of Sciences of the United States of America* 109.11, pp. 4074–4079. DOI: 10.1073/PNAS.1114910109.

Lloyd, E. A. and N. Oreskes (2018). "Climate Change Attribution: When Is It Appropriate to Accept New Methods?" In: *Earth's Future* 6.3, pp. 311–325. DOI: 10.1002/2017EF000665.

Lorenz, E. N. (1963). "Deterministic Nonperiodic Flow." In: *Journal of the Atmospheric Sciences* 20.2, pp. 130–141. DOI: 10.1175/1520-0469(1963)020<0130:dnf>2.0.co;2.

Lorenz, E. (1969). "Atmospheric predictability as revealed by naturally occurring analogues." In: *Journal of the Atmospheric Sciences* 26.4, pp. 636–646. DOI: 10.1175/1520-0469(1969)26<636:aparbn>2.0.co;2.

Lorenz, R., Z. Stalhandske, and E. M. Fischer (2019). "Detection of a Climate Change Signal in Extreme Heat, Heat Stress, and Cold in Europe From Observations." In: *Geophysical Research Letters* 46.14, pp. 8363–8374. DOI: 10.1029/2019GL082062.

Luo, D. et al. (2016). "Impact of ural blocking on winter warm Arctic-cold Eurasian anomalies. Part I: Blocking-induced amplification." In: *Journal of Climate* 29.11, pp. 3925–3947. DOI: 10.1175/JCLI-D-15-0611.1.

Lüpkes, C. and V. M. Gryanik (2015). "A stability-dependent parametrization of transfer coefficients for momentum and heat over polar sea ice to be used in climate models." In: *Journal of Geophysical Research: Atmospheres* 120.2, pp. 552–581. DOI: 10.1002/2014JD022418.

MacQueen, J. (1967). "Some methods for classification and analysis of multivariate observations." In: *Proceedings of the fifth Berkeley symposium on mathematical statistics and probability* 1, pp. 281–297.

Machenhauer, B. (1979). "The spectral method." In: *Numerical Methods Used in Atmospheric Models* 2, pp. 121–275.

Madonna, E. et al. (2017). "The link between eddy-driven jet variability and weather regimes in the North Atlantic-European sector." In: *Quarterly Journal of the Royal Meteorological Society* 143.708, pp. 2960–2972. DOI: 10.1002/qj.3155.

Masato, G., B. J. Hoskins, and T. J. Woollings (2012). "Wave-breaking characteristics of midlatitude blocking." In: *Quarterly Journal of the Royal Meteorological Society* 138.666, pp. 1285–1296. DOI: 10.1002/QJ.990.

Matsuno, T. (1971). "A Dynamical Model of the Stratospheric Sudden Warming." In: *Journal of the Atmospheric Sciences* 28.8, pp. 1479–1494. DOI: 10.1175/1520-0469(1971)028<1479:ADMOTS>2.0.CO;2.

Meredith, M. et al. (2019). "Chapter3: Polar Regions." In: *IPCC Special Report on the Ocean and Cryosphere in a Changing Climate*, pp. 203–320. DOI: https://doi.org/10.1017/9781009157964.005.

Michelangeli, P.-A., R. Vautard, and B. Legras (1995). "Weather regimes: Recurrence and quasi stationarity." In: *Journal of the atmospheric sciences* 52.8, pp. 1237–1256.

Miller, G. H. et al. (2010). "Arctic amplification: Can the past constrain the future?" In: *Quaternary Science Reviews* 29.15-16, pp. 1779–1790. DOI: 10.1016/j.quascirev.2010.02.008.

Miralles, D. G. et al. (2014). "Mega-heatwave temperatures due to combined soil desiccation and atmospheric heat accumulation." In: *Nature Geoscience* 7.5, pp. 345–349. DOI: 10.1038/ngeo2141.

Mitchell, J. M. (1961). "Recent secular changes of global temperature." In: *Annals of the New York Academy of Sciences* 95.1, pp. 235–250. DOI: 10.1111/J.1749-6632.1961.TB50036.X.

Molteni, F., S. Tibaldi, and T. N. Palmer (1990). "Regimes in the wintertime circulation over northern extratropics. I: Observational evidence." In: *Quarterly Journal of the Royal Meteorological Society* 116.491, pp. 31–67. DOI: 10.1002/QJ.49711649103.

Nakamura, T. et al. (2015). "A negative phase shift of the winter AO/NAO due to the recent Arctic sea-ice reduction in late autumn." In: *Journal of Geophysical Research: Atmospheres* 120.8, pp. 3209–3227. DOI: 10.1002/2014JD022848.

Nakamura, T. et al. (2016). "The stratospheric pathway for Arctic impacts on midlatitude climate." In: *Geophysical Research Letters* 43.7, pp. 3494–3501. DOI: 10.1002/2016GL068330.

Naveau, P., A. Hannart, and A. Ribes (2020). "Statistical Methods for Extreme Event Attribution in Climate Science." In: *Annual Review of Statistics and Its Application* 7.1, pp. 89–110. DOI: 10.1146/annurev-statistics-031219-041314.

Notz, D. and Coauthors (2020). "Arctic Sea Ice in CMIP6." In: *Geophysical Research Letters* 47.10. DOI: 10.1029/2019GL086749.

Palmer, T. N. (1993). "Extended-range atmospheric prediction and the Lorenz model." In: *Bulletin of the American Meteorological Society* 74.1, pp. 49–65. DOI: 10.1175/1520-0477(1993)074<0049:ERAPAT>2.0.CO;2.

Palmer, T. N. (1999). "A nonlinear dynamical perspective on climate prediction." In: *Journal of Climate* 12.2, pp. 575–591. DOI: 10.1175/1520-0442(1999)012<0575:ANDPOC>2.0.CO;2.

Peings, Y. (2019). "Ural Blocking as a Driver of Early-Winter Stratospheric Warmings." In: *Geophysical Research Letters* 46.10, pp. 5460–5468. DOI: 10.1029/2019GL082097.

Peings, Y., J. Cattiaux, and G. Magnusdottir (2019). "The Polar Stratosphere as an Arbiter of the Projected Tropical Versus Polar Tug of War." In: *Geophysical Research Letters* 46.15, pp. 9261–9270. DOI: 10.1029/2019GL082463.

Peings, Y., Z. M. Labe, and G. Magnusdottir (2021). "Are 100 ensemble members enough to capture the remote atmospheric response to 12°C arctic sea ice loss?" In: *Journal of Climate* 34.10, pp. 3751–3769. DOI: 10.1175/JCLI-D-20-0613.1.

Pelly, J. L. and B. J. Hoskins (2003). "A New Perspective on Blocking." In: *Journal of Atmospheric Sciences* 60.5, pp. 743–755.

Petoukhov, V. and V. A. Semenov (2010). "A link between reduced Barents-Kara sea ice and cold winter extremes over northern continents." In: *Journal of Geophysical Research: Atmospheres* 115.D21. DOI: 10.1029/2009JD013568.

Petoukhov, V. et al. (2013). "Quasiresonant amplification of planetary waves and recent Northern Hemisphere weather extremes." In: *Proceedings of the National Academy of Sciences of the United States of America* 110.14, pp. 5336–5341. DOI: 10.1073/pnas.1222000110.

Pfahl, S. and H. Wernli (2012). "Quantifying the relevance of atmospheric blocking for co-located temperature extremes in the Northern Hemisphere on (sub-)daily time scales." In: *Geophysical Research Letters* 39.12. DOI: 10.1029/2012GL052261.

Pichler, H. (1997). *Dynamik der Atmosphäre*. Spektrum Akademischer Verlag.

Pithan, F. and T. Mauritsen (2014). "Arctic amplification dominated by temperature feedbacks in contemporary climate models." In: *Nature Geoscience* 7.3, pp. 181–184. DOI: 10.1038/ngeo2071.

Pohl, B. and N. Fauchereau (2012). "The southern annular mode seen through weather regimes." In: *Journal of Climate* 25.9, pp. 3336–3354. DOI: 10.1175/JCLI-D-11-00160.1.

Rantanen, M. et al. (2022). "The Arctic has warmed nearly four times faster than the globe since 1979." In: *Communications Earth and Environment* 3.1, pp. 1–10. DOI: 10.1038/s43247-022-00498-3.

Rayner, N. A. et al. (2003). "Global analyses of sea surface temperature, sea ice, and night marine air temperature since the late nineteenth century." In: *Journal of Geophysical Research: Atmospheres* 108.D14. DOI: 10.1029/2002JD002670.

Rex, D. F. (1950). "Blocking Action in the Middle Troposphere and its Effect upon Regional Climate." In: *Tellus* 2.4, pp. 275–301. DOI: 10.3402/tellusa.v2i4.8603.

Riboldi, J. et al. (2020). "On the Linkage Between Rossby Wave Phase Speed, Atmospheric Blocking, and Arctic Amplification." In: *Geophysical Research Letters* 47.19, e2020GL087796. DOI: 10.1029/2020GL087796.

Riebold, J. et al. (2023). "On the linkage between future Arctic sea ice retreat, Euro-Atlantic circulation regimes and temperature extremes over Europe." In: *Weather and Climate Dynamics* 4.3, pp. 663–682. DOI: 10.5194/wcd-4-663-2023.

Robertson, A. W., M. Ghil, and M. Latif (2000). "Interdecadal Changes in Atmospheric Low-Frequency Variability with and without Boundary Forcing." In: *Journal of Atmospheric Sciences* 57.8, pp. 1132–1140. DOI: 10.7916/D8FR06BM.

Romanowsky, E. et al. (2019). "The role of stratospheric ozone for Arctic-midlatitude linkages." In: *Scientific Reports* 9.1, pp. 1–7. DOI: 10.1038/s41598-019-43823-1.

Rossby and C. G. (1939). "Relation between variations in the intensity of the zonal circulation of the atmosphere and the displacements of the semi-permanent centers of action." In: *Journal of Marine Research* 2, pp. 38–55.

Rousi, E. et al. (2020). "Implications of Winter NAO Flavors on Present and Future European Climate." In: *Climate* 8.1. DOI: 10.3390/cli8010013.

Rust, H. W. et al. (2010). "Quantifying Differences in Circulation Patterns Based on Probabilistic Models: IPCC AR4 Multimodel Comparison for the North Atlantic." In: *Journal of Climate* 23.24, pp. 6573–6589. DOI: 10.1175/2010JCLI3432.1.

Rust, H. W. et al. (2015). "Linking teleconnection patterns to European temperature – a multiple linear regression model." In: *Meteorologische Zeitschrift* 24.4, pp. 411–423. DOI: 10.1127/METZ/2015/0642.

Salzmann, M. (2017). "The polar amplification asymmetry: role of Antarctic surface height." In: *Earth System Dynamics* 8.2, pp. 323–336. DOI: 10.5194/ESD-8-323-2017.

Sato, K., J. Inoue, and M. Watanabe (2014). "Influence of the Gulf Stream on the Barents Sea ice retreat and Eurasian coldness during early winter." In: *Environmental Research Letters* 9.8. DOI: 10.1088/1748-9326/9/8/084009.

Savić, S., A. Selakov, and D. Milošević (2014). "Cold and warm air temperature spells during the winter and summer seasons and their impact on energy consumption in urban areas." In: *Natural Hazards* 73.2, pp. 373–387. DOI: 10.1007/S11069-014-1074-Y/TABLES/2.

Scherrer, S. C. et al. (2006). "Two-dimensional indices of atmospheric blocking and their statistical relationship with winter climate patterns in the Euro-Atlantic region." In: *International Journal of Climatology: A Journal of the Royal Meteorological Society* 26.2, pp. 233–249. DOI: 10.1002/joc.1250.

Schwierz, C., M. Croci-Maspoli, and H. C. Davies (2004). "Perspicacious indicators of atmospheric blocking." In: *Geophysical Research Letters* 31.6. DOI: 10.1029/2003GL019341.

Screen, J. A. (2014). "Arctic amplification decreases temperature variance in northern mid- to high-latitudes." In: *Nature Climate Change* 4.7, pp. 577–582. DOI: 10.1038/nclimate2268.

– (2017a). "Simulated Atmospheric Response to Regional and Pan-Arctic Sea Ice Loss." In: *Journal of Climate* 30.11, pp. 3945–3962. DOI: 10.1175/JCLI-D-16-0197.1.

– (2017b). "The missing Northern European winter cooling response to Arctic sea ice loss." In: *Nature Communications* 8.1, pp. 1–9. DOI: 10.1038/ncomms14603.

Screen, J. A. and I. Simmonds (2013). "Exploring links between Arctic amplification and mid-latitude weather." In: *Geophysical Research Letters* 40.5, pp. 959–964. DOI: 10.1002/grl.50174.

Screen, J. A. et al. (2014). "Atmospheric impacts of Arctic sea-ice loss, 1979-2009: Separating forced change from atmospheric internal variability." In: *Climate Dynamics* 43.1-2, pp. 333–344. DOI: 10.1007/s00382-013-1830-9.

Screen, J. A. et al. (2018). "Consistency and discrepancy in the atmospheric response to Arctic sea-ice loss across climate models." In: *Nature Geoscience* 11.3, pp. 155–163. DOI: 10.1038/s41561-018-0059-y.

Sellers, W. D. (1969). "A Global Climatic Model Based on the Energy Balance of the Earth-Atmosphere System." In: *Journal of Applied Meteorology (1962-1982)* 8.3, pp. 392–400. DOI: 10.1175/1520-0450(1969)008<0392:agcmbo>2.0.co;2.

Sellevold, R., S. Sobolowski, and C. Li (2016). "Investigating Possible Arctic–Midlatitude Teleconnections in a Linear Framework." In: *Journal of Climate* 29.20, pp. 7329–7343. DOI: 10.1175/JCLI-D-15-0902.1.

Sempf, M. et al. (2007a). "Circulation Regimes due to Attractor Merging in Atmospheric Models." In: *Journal of the Atmospheric Sciences* 64.6, pp. 2029–2044. DOI: 10.1175/JAS3923.1.

– (2007b). "Toward Understanding the Dynamical Origin of Atmospheric Regime Behavior in a Baroclinic Model." In: *Journal of the Atmospheric Sciences* 64.3, pp. 887–904. DOI: 10.1175/JAS3862.1.

Senf, C. and R. Seidl (2021). "Persistent impacts of the 2018 drought on forest disturbance regimes in Europe." In: *Biogeosciences* 18.18, pp. 5223–5230. DOI: 10.5194/BG-18-5223-2021.

Shepherd, T. G. (2016). "A Common Framework for Approaches to Extreme Event Attribution." In: *Current Climate Change Reports* 2.1, pp. 28–38. DOI: 10.1007/s40641-016-0033-y.

Siew, P. Y. F. et al. (2020). "Intermittency of Arctic–mid-latitude teleconnections: stratospheric pathway between autumn sea ice and the winter North Atlantic Oscillation." In: *Weather and Climate Dynamics* 1.1, pp. 261–275. DOI: 10.5194/wcd-1-261-2020.

Sillmann, J. et al. (2011). "Extreme cold winter temperatures in Europe under the influence of North Atlantic atmospheric blocking." In: *Journal of Climate* 24.22, pp. 5899–5913. DOI: 10.1175/2011JCLI4075.1.

Smith, D. M. et al. (2017). "Atmospheric Response to Arctic and Antarctic Sea Ice: The Importance of Ocean–Atmosphere Coupling and the Background State." In: *Journal of Climate* 30.12, pp. 4547–4565. DOI: 10.1175/JCLI-D-16-0564.1.

Smith, D. M. et al. (2019). "The Polar Amplification Model Intercomparison Project (PAMIP) contribution to CMIP6: investigating the causes and consequences of polar amplification." In: *Geoscientific Model Development* 12.3, pp. 1139–1164. DOI: 10.5194/gmd-12-1139-2019.

Smyth, P. et al. (1999). "Multiple Regimes in Northern Hemisphere Height Fields via MixtureModel Clustering." In: *Journal of the Atmospheric Sciences* 56.21, pp. 3704–3723. DOI: 10.1175/1520-0469(1999)056<3704:MRINHH>2.0.CO;2.

Stevens, B. et al. (2013). "Atmospheric component of the MPI-M Earth System Model: ECHAM6." In: *Journal of Advances in Modeling Earth Systems* 5.2, pp. 146–172. DOI: 10.1002/jame.20015.

Straus, D. M., S. Corti, and F. Molteni (2007). "Circulation Regimes: Chaotic Variability versus SST-Forced Predictability." In: *Journal of Climate* 20.10, pp. 2251–2272. DOI: 10.1175/JCLI4070.1.

Streffing, J. et al. (2021). "Response of northern hemisphere weather and climate to arctic sea ice decline: Resolution independence in polar amplification model intercomparison project (pamip) simulations." In: *Journal of Climate* 34.20, pp. 8445–8457. DOI: 10.1175/JCLI-D-19-1005.1.

Stroeve, J. and D. Notz (2018). "Changing state of Arctic sea ice across all seasons." In: *Environmental Research Letters* 13.10. DOI: 10.1088/1748-9326/AADE56.

Strommen, K. et al. (2019). "The Sensitivity of Euro-Atlantic Regimes to Model Horizontal Resolution." In: *Geophysical Research Letters* 46.13, pp. 7810–7818. DOI: 10.1029/2019GL082843.

Stuecker, M. F. et al. (2018). "Polar amplification dominated by local forcing and feedbacks." In: *Nature Climate Change* 8.12, pp. 1076–1081. DOI: 10.1038/s41558-018-0339-y.

Sulikowska, A. and A. Wypych (2021). "Seasonal Variability of Trends in Regional Hot and Warm Temperature Extremes in Europe." In: *Atmosphere* 12.5. DOI: 10.3390/ATMOS12050612.

Sun, L., C. Deser, and R. A. Tomas (2015). "Mechanisms of Stratospheric and Tropospheric Circulation Response to Projected Arctic Sea Ice Loss." In: *Journal of Climate* 28.19, pp. 7824–7845. DOI: 10.1175/JCLI-D-15-0169.1.

Taylor, K. E. (2001). "Summarizing multiple aspects of model performance in a single diagram." In: *Journal of Geophysical Research: Atmospheres* 106.D7, pp. 7183–7192. DOI: 10.1029/2000JD900719.

Taylor, P. C. et al. (2018). "On the Increasing Importance of Air-Sea Exchanges in a Thawing Arctic: A Review." In: *Atmosphere* 9.2. DOI: 10.3390/ATMOS9020041.

Taylor, P. C. et al. (2019). "Arctic cloud annual cycle biases in climate models." In: *Atmospheric Chemistry and Physics* 19.13, pp. 8759–8782. DOI: 10.5194/ACP-19-8759-2019.

Tibaldi, S. and F. Molteni (1990). "On the operational predictability of blocking." In: *Tellus A* 42.3, pp. 343–365. DOI: 10.1034/J.1600-0870.1990.T01-2-00003.X.

Toreti, A. et al. (2019). "The Exceptional 2018 European Water Seesaw Calls for Action on Adaptation." In: *Earth's Future* 7.6, pp. 652–663. DOI: 10.1029/2019EF001170.

Trenberth, K. E., J. T. Fasullo, and T. G. Shepherd (2015). "Attribution of climate extreme events." In: *Nature Climate Change* 5.8, pp. 725–730. DOI: 10.1038/nclimate2657.

Varotsos, C. (2004). "The extraordinary events of the major, sudden stratospheric warming, the diminutive antarctic ozone hole, and its split in 2002." In: *Environmental Science and Pollution Research* 11.6, pp. 405–411. DOI: 10.1007/BF02979661.

Vautard, R. et al. (2016). "Attribution of human-induced dynamical and thermodynamical contributions in extreme weather events." In: *Environmental Research Letters* 11.11. DOI: 10.1088/1748-9326/11/11/114009.

Vautard, R. et al. (2010). "Northern Hemisphere atmospheric stilling partly attributed to an increase in surface roughness." In: *Nature Geoscience* 3.11, pp. 756–761. DOI: 10.1038/ngeo979.

Vihma, T. et al. (2020). "Effects of the tropospheric large-scale circulation on European winter temperatures during the period of amplified Arctic warming." In: *International Journal of Climatology* 40.1, pp. 509–529. DOI: 10.1002/joc.6225.

Vogel, M. M. et al. (2019). "Concurrent 2018 Hot Extremes Across Northern Hemisphere Due to Human-Induced Climate Change." In: *Earth's Future* 7.7, pp. 692–703. DOI: 10.1029/2019EF001189.

Walker, G. T. (1923). "Correlation in seasonal variation of weather. VIII : A preliminary study of world weather." In: *Memoirs of India Meteorological Department* 24, pp. 75–131.

Wallace, J. M. and D. S. Gutzler (1981). "Teleconnections in the geopotential height field during the Northern Hemisphere winter." In: *Monthly Weather Review* 109.4, pp. 784–812. DOI: 10.1175/1520-0493(1981)109<0784:TITGHF>2.0.CO;2.

Wang, S., A. Xie, and J. Zhu (2021). "Does polar amplification exist in Antarctic surface during the recent four decades?" In: *Journal of Mountain Science* 18.10, pp. 2626–2634. DOI: 10.1007/s11629-021-6912-2.

Wegmann, M. et al. (2015). "Arctic moisture source for Eurasian snow cover variations in autumn." In: *Environmental Research Letters* 10.5. DOI: 10.1088/1748-9326/10/5/054015.

Wegmann, M. et al. (2020). "Eurasian autumn snow link to winter North Atlantic Oscillation is strongest for Arctic warming periods." In: *Earth System Dynamics* 11.2, pp. 509–524. DOI: 10.5194/ESD-11-509-2020.

Wetherald, R. T. and S. Manabe (1975). "The effects of changing the solar constant on the climate of a general circulation model." In: *Journal of the Atmospheric Sciences* 32.11, pp. 2044–2059. DOI: 10.1175/1520-0469(1975)032<2044:TEOCTS>2.0.CO;2.

Wilks, D. S. (2006). *Statistical methods in the atmospheric sciences*. 2nd Editio. Academic Press.

Woollings, T. et al. (2018). "Blocking and its Response to Climate Change." In: *Current Climate Change Reports* 4.3, pp. 287–300. DOI: 10.1007/S40641-018-0108-Z.

World Economic Forum (2021). *The Global Risks Report 2021*. Tech. rep.

Xu, X. et al. (2019). "Strengthened linkage between midlatitudes and Arctic in boreal winter." In: *Climate Dynamics* 53.7, pp. 3971–3983. DOI: 10.1007/s00382-019-04764-7.

Yamanouchi, T. (2011). "Early 20th century warming in the Arctic: A review." In: *Polar Science* 5.1, pp. 53–71. DOI: 10.1016/J.POLAR.2010.10.002.

Ye, K. and G. Messori (2021). "Inter-model spread in the wintertime Arctic amplification in the CMIP6 models and the important role of internal climate variability." In: *Global and Planetary Change* 204. DOI: 10.1016/J.GLOPLACHA.2021.103543.

Yee, T. W. (2015). *Vector generalized linear and additive models: With an implementation in R*. New York, USA: Springer.

Yiou, P. (2014). "AnaWEGE: A weather generator based on analogues of atmospheric circulation." In: *Geoscientific Model Development* 7.2, pp. 531–543. DOI: 10.5194/gmd-7-531-2014.

Yiou, P. et al. (2017). "A statistical framework for conditional extreme event attribution." In: *Advances in Statistical Climatology, Meteorology and Oceanography* 3.1, pp. 17–31. DOI: 10.5194/ascmo-3-17-2017.

Zscheischler, J. et al. (2018). "Future climate risk from compound events." In: *Nature Climate Change* 8.6, pp. 469–477. DOI: 10.1038/s41558-018-0156-3.

Zschenderlein, P. et al. (2019). "Processes determining heat waves across different European climates." In: *Quarterly Journal of the Royal Meteorological Society* 145.724, pp. 2973–2989. DOI: 10.1002/qj.3599.

Zwiers, F. W. and V. V. Kharin (1998). "Changes in the extremes of the climate simulated by CGC GCM2 under CO 2 doubling." In: *Journal of Climate* 11.9, pp. 2200–2222. DOI: 10.1175/1520-0442(1998)011<2200:CITEOT>2.0.CO;2.

ACRONYMS

AA Arctic Amplification

AGCM Atmospheric General Circulation Model

AMIP Atmospheric Model Intercomparison Project

ATL- Pattern with anticyclonic center over East Atlantic in winter

BKS Barents-Kara Sea

CRMSE Centered root-mean-square error

DIP Winter dipole regime pattern

DJFM December, January, February, March

EOF Empirical Orthogonal Function

CMIP Coupled Model Intercomparison Project

futArcSI Experiment forced under present day sea surface temperature and future/reduced Arctic-wide sea ice conditions

futBKSI Experiment forced under present day sea surface temperature and future/reduced sea ice conditions in the Barents-Kara Sea

futSST Experiment forced under present day sea ice and globally raised future sea surface temperature conditions

GEV Generalized Extreme Value distribution

gph500 Geopotential height of the 500 hPa pressure level

IFS Integrated Forecasting System

JJA June, July, August

MNLR Multinomial Logistic Regression

NAO North Atlantic Oscillation

NAO+ Winter regime resembling the positive state of the North Atlantic Oscillation

NAO- Winter regime resembling the negative state of the North Atlantic Oscillation

NH Northern Hemisphere

PAMIP Polar Amplification Intercomparison Project

pdSST/pdSI Experiment forced under present day sea surface temperature and present day sea ice conditions

PC Principal Component

PCA Principal Component Analysis

PDF Probability Distribution Function

S-ATL- Pattern with anticyclonic center over East Atlantic in summer

S-DIP Summer dipole regime pattern

S-NAO+ Summer regime resembling the positive state of the North Atlantic Oscillation

S-NAO- Summer regime resembling the negative state of the North Atlantic Oscillation

SCAN Winter Scandinavian Blocking Pattern

S-SCAN Summer Scandinavian Blocking Pattern

SLP Sea Level Pressure

SH Southern Hemisphere

SI Sea Ice

SIC Sea Ice Concentration

SIA Sea Ice Area

SST Sea Surface Temperature

T2m 2 meter Temperature

T2max Maximum 2 meter Temperature

T2min Minimum 2 meter Temperature

u850 Zonal wind speed at 850 hPa

DANKSAGUNG

Danken möchte ich an erster Stelle meiner Betreuerin Dörthe Handorf für die jederzeit wirklich liebevolle und kompetente Unterstützung während meiner Doktorandenzeit.
Danken möchte ich auch Andy Richling für den jederzeit entspannten Austausch und die unkomplizierte Zusammenarbeit in unserem Projekt.
Zudem möchte ich noch Uwe Ulrich und Henning Rust danken für ihren Input in gemeinsamen Projektreffen.
Ein Dank geht auch an Joaquim Pinto, Uwe Ulbrich und Markus Rex, die sich bereit erklärt haben diese Arbeit zu begutachten.
Danken möchte ich ebenso Tido Semmler für die Durchführung der Modellexperimente.
Ein weiterer Dank geht noch extra raus vor allem an Dörthe, sowie an Andy, Raphael und Ralf für das Korrekturlesen von Teilen der Arbeit, sowie eigentlich auch an das gesamte AWI Team samt aller Post-Docs, Doktoranden und anderen Studenten die mich über die Jahre begleitet haben.
Zum Ende will ich auch noch meinen Eltern und meiner Familie danken, die mich vom Anfang meiner Studienzeit bis zum heutigen Tag stets unterstützt haben.

SELBSTSTÄNDIGKEITSERKLÄRUNG

Hiermit versichere ich, dass ich die vorliegende Dissertation selbstständig verfasst und keine anderen als die angegebenen Quellen und Hilfsmittel verwendet habe, wobei ich alle wörtlichen und sinngemäßen Zitate als solche gekennzeichnet habe.
Diese wissenschaftliche Arbeit hat in gleicher oder ähnlicher Form noch keiner Prüfungsbehörde vorgelegen und wurde auch nicht veröffentlicht.

Potsdam, 14. December 2022

Johannes Riebold